UNIVERSITY OF SOUTHAMPTON

FLOW CHARACTERIZATION IN RESIN TRANSFER MOULDING

Jan Rüdiger Weitzenböck M.Sc.

Doctor of Philosophy

SHIP SCIENCE

NOVEMBER 1996

UNIVERSITY OF SOUTHAMPTON

ABSTRACT

FACULTY OF ENGINEERING AND APPLIED SCIENCE
SHIP SCIENCE

Doctor of Philosophy

FLOW CHARACTERIZATION IN RESIN TRANSFER MOULDING

by Jan Rüdiger Weitzenböck

The aim of this thesis is to determine permeability of fibre reinforcement materials more accurately in Resin Transfer Moulding (RTM). The work presented here focuses on the processing of data obtained from permeability experiments.

A unified approach to permeability measurement is proposed. It unifies seven permeability measurement techniques for one, two and three-dimensional flow currently used in RTM. The unified approach offers significant advantages over current methods. Principal permeability and the orientation of the permeability tensor can be obtained from measurement of pressure or flow front position during experiments. It also offers much greater flexibility in the way data is acquired. Data do not need to be collected at the same instance in time for each measurement axis. The principal permeability and its orientation can be obtained regardless of the measurement direction. In addition it is possible to observe the transient behaviour of permeability in experiments with the help of a convergence graph.

The unified approach for radial flow experiments with constant inlet pressure has been analysed extensively. In particular the effect of the inlet shape and the relative size of the inlet have been studied. Permeability experiments were conducted to verify the unified approach. For constant inlet pressure experiments the proposed new method worked well even for results from another laboratory. In the case of constant flow rate the number of results available was not sufficient to fully validate the unified approach. It was demonstrated that three-dimensional permeability experiments suffer from capillary flow which renders any results meaningless. Finally it was shown that experimental design can help with the interpretation of the permeability results.

Meinen Eltern

List of contents

List of tables

List of figures

Acknowledgements

This PhD was only possible with the support and help of many people.

First of all I would like to thank my supervisors Dr Ajit Shenoi and Mr Philip Wilson for their faith and patience and for their guidance throughout the course of my PhD. I am most grateful to them for having given me the opportunity to carry out research in the Department of Ship Science. It was a very rewarding learning process.

I would also like to thank the members of the Department of Ship Science for all their support and help, particularly Simon Clark and Holly Phillips. Special thanks go to Dr Mingyi Tan whose knowledge of fluid dynamics and mathematics saved me on numerous occasions as well as Leigh Sutherland whose help with the design and analysis of experiments was invaluable. Pierre Boyde, Ben Clothier and Andrew Inglis also need to be mentioned as their M.Eng. project was to build my experimental rig, which they did with great success. I am grateful for that.

Throughout the course of my research I received a lot of support from people throughout the University. I would like to thank Will Smith from Engineering Materials for his help with conducting the compaction tests. Rob Stansbridge helped me to sort out the electrical and electronics problems related to the testing - many thanks for that. And finally I need to thank Dr Colin Please from the Department of Mathematics whose help was most appreciated when I got bogged down in mathematics.

Valuable help also came from peers from other Universities whose critical discussions were most helpful for the development of the ideas presented in this thesis. I would therefore like to thank the following: Dan Morris of the University of Nottingham, Pat Griffin, Tony Fell and Dr Eddy Carter all from the University of Plymouth and Dr Richard Parnas of the National Institute of Standards and Technology in Gaithersburg, USA. Thanks also to Dr Chris Rudd from the University of Nottingham and Dr John Summerscales from the University of Plymouth for allowing me to use experimental results from their laboratories in my thesis.

The financial support of the "Bundeswirtschaftskammer" in Vienna and the Faculty of Engineering and Applied Sciences of the University of Southampton is gratefully

acknowledged. Vetrotex (UK) Ltd with Dr Peter Thornburrow provided most of the raw materials used in my experiments - many thanks for that.

Finally I would like to thank my parents for all the (moral) support and encouragement they have given me throughout these years. And last but not least I need to thank Dr Emily Camilleri for all her wonderful support and encouragement, especially during the less enjoyable stages of this PhD.

Nomenclature

In this section the nomenclature which is used throughout this thesis is listed. Variables which are only of 'local' interest are explained in the relevant sections (e.g. integration constants). In sections 8.2 (The theoretical foundation of the unified approach) and 11.1.3 (Introduction to experimental design) the nomenclature from other sources was adopted. Again this will be explained in the relevant sections. The positive direction for angles is the anti-clockwise direction.

Coordinate systems

x, y, z = arbitrary coordinate system

1, **2**, **3** = principal coordinate system

I, *II*, *III* = orientation in which experiments are carried out (*I* = x, *II* = 45° between x,y, *III* = y)

Letters

a = major axis of the inlet ellipse [m]

A = average of F_I and F_{III}

$\underline{A}$ = rotation matrix

$\underline{A}^T$ = transpose of the rotation matrix

A_n = area normal to the flow direction [m^2]

b = minor axis of the inlet ellipse [m]

C = process term

Ca = capillary number

Ca_{mod} = modified capillary number

D = difference between F_I and F_{III}

D_e = equivalent pore diameter [m]

D_f = pore or fibre diameter [m]

e = error

$\underline{E}$ = unit matrix

F = form factor which depends on fibre alignment and the flow direction

F_i = material term containing flow front and time information (for i = *I*, *II*, *III*)

h = height of the cavity [m]

I_1 = first invariant (also called "trace")

I_2 = second invariant

I_3 = third invariant

k = a scalar

K = isotropic permeability [m^2]

K' = quasi-isotropic permeability [m^2]

$\underline{K}$ = permeability tensor [m^2]

$\underline{K}'$ = rotated tensor [m^2]

K_1, K_2, K_3 = principal permeability

$K_{eff,I}$, $K_{eff,II}$, $K_{eff,III}$ = measured effective permeability at 0°, 45° and 90° [m^2]

K_e^0, K_e^{45}, K_e^{90}, K_e^{135} = effective permeability measured at 0°, 45°, 90° and 135°. (Parnas and Salem (1993) [m^2]

K_{xx}, K_{xy}, K_{xz}, K_{yy} , K_{yz}, K_{zz} = permeability tensor components [m^2]

$K'_{xx}, K'_{xy}, K'_{xz}, K'_{yy}, K'_{yz}, K'_{zz}$, K'_{xy} = components of rotated permeability tensor [m^2]

$K_I = K_{eff,I}$ [m^2]

$K_{II} = K_{eff,II}$ [m^2]

$K_{III} = K_{eff,III}$ [m^2]

L_{cv} = cross-over length [m]

$\underline{n}$ = a vector

$\underline{n}_1$, $\underline{n}_2$, $\underline{n}_3$ = eigenvectors

n_{1x}, n_{1y}, n_{1z} = components of first eigenvector ($\underline{n}_1$)

N = number of layers

N_i = nominator of F_i ($i = I, II, III$)

P = pressure [Pa]

$P(x)_{channel}$ = pressure distribution for channel flow

$P(x)_{radial}$ = pressure distribution for radial flow

$P(x)_{spherical}$ = pressure distribution for spherical flow

P_c = capillary pressure [Pa]

P_f = pressure at the flow front [Pa]

P_o = pressure at the inlet [Pa]

P_1 = pressure at radius 1 [Pa]

P_2 = pressure at radius 2 [Pa]

$P_{1,i}$ = pressure at position 1 in direction i ($i = I, II, III$) [Pa]

$P_{2,i}$ = pressure at position 2 in direction i ($i = I, II, III$) [Pa]

Q = volume flow rate [m^3/s]

r = experimentally measured radius [m]

$\bar{r}$ = radius of the quasi-isotropic system (scaled) [m]

$\bar{r}'$ = radius in the quasi-isotropic system (rotated and scaled) [m]

where r, $\bar{r}$ and $\bar{r}'$ can have the following subscripts (i = *I*, *II*, *III*):

f,i = flow front radius in i-direction

o,i = inlet radius in i-direction

$1,i$ = radius of position 1 in i-direction

$2,i$ = radius of position 2 in i-direction

r_f = radius of the flow front [m]

r_o = radius of the inlet [m]

$r_{o,\mathrm{mod},i}$ = modified inlet radius (i = *I*, *II*, *III*) [m]

r_1 = radius of position 1 [m]

r_2 = radius of position 2 [m]

r_1, r_2, r_3 = inlet radii for test case [m]

Re = Reynolds number

t = time [s]

t_o = start time [s]

t_f = time to reach the current flow front position [s]

t_1 = time to reach position 1 [s]

t_2 = time to reach position 2 [s]

t_i = time passed to reach current flow front position in direction i (i = *I*, *II*, *III*) [s]

$t_{1,i}$ = time taken by flow front to reach position 1 in direction i (i = *I*, *II*, *III*) [s]

$t_{2,i}$ = time taken by flow front to reach position 2 in direction i (i = *I*, *II*, *III*) [s]

T = temperature [C°]

$\underline{u}$ = a vector

v = fluid velocity [m/s]

v_x = velocity in x-direction [m/s]

v_y = velocity in y-direction [m/s]

v_z = velocity in z-direction [m/s]

V_f = fibre volume fraction [%]

W_f = weight per unit area [kg/m^2]

x, y, z = coordinates in the physical domain [m]

$\bar{x}, \bar{y}, \bar{z}$ = coordinates in the quasi-isotropic system (scaled) [m]

x', y', z' = coordinates in the quasi-isotropic system (rotated) [m]

$\bar{x}', \bar{y}', \bar{z}'$ = coordinates in the quasi-isotropic system (rotated and scaled) [m]

x_f, y_f, z_f = flow front coordinates [m]

x_o, y_o, z_o = inlet coordinates [m]

x_1, y_1, z_1 = coordinates of position 1 [m]

x_2, y_2, z_2 = coordinates of position 2 [m]

$x_{f,i}, y_{f,i}, z_{f,i}$ = flow front coordinates measured in i-direction (i = *I, II, III*) [m]

$x_{o,i}, y_{o,i}, z_{o,i}$ = inlet coordinates measured in i-direction (i = *I, II, III*) [m]

$x_{o,\mathrm{mod},i}, y_{o,\mathrm{mod},i}, z_{o,\mathrm{mod},i}$ = modified inlet coordinates measured in i-direction (i = *I, II, III*) [m]

$x_{1,i}, y_{1,i}, z_{1,i}$ = coordinates of position 1 measured in i-direction [m]

$x_{2,i}, y_{2,i}, z_{2,i}$ = coordinates of position 2 measured in i-direction [m]

Greek symbols

α = degree of anisotropy (= K_2/K_1)

γ = surface tension of fluid [N/m]

γ_{LV} = surface tension between wetting and nonwetting fluid [N/m]

ΔL = distance between the inlet and vent [m]

ΔP = pressure difference between inlet and flow front for constant inlet pressure [Pa]

$\Delta P_{L_{cv}}$ = pressure drop across a pore or fibre with diameter D_f [Pa]

ε = porosity

ζ = angle of rotation [°]

θ = contact angle between fluid and fibre [°]

$\lambda_{i'j}$ = direction cosine (cosine of the angle between the i' and j-axis; i,j = x,y,z)

μ = dynamic viscosity [Pa s]

ν = kinematik viscosity [m^2/s]

ρ = density of the fluid [kg/m^3]

ϕ_i = orientation of modified inlet radius (i = *I, II, III*) [°]

φ = orientation of principal axis (angle between x' and x-axis) [°]

$\varphi_2 = \varphi + \pi/2$ (second possible solution) [°]

$\varphi_I = \varphi$

$\varphi_{II} = \varphi - 45°$

$\varphi_{III} = \varphi - 90°$

1. Introduction and objectives

Fibre reinforced plastics (FRP) were first used by the US Navy in the 1940's to build boats. It soon became the most popular building material for pleasure craft. In 1955 4% of all small boats where built from FRP compared to more than 80% in 1972. It has remained at that level since (Smith 1990).

The main reasons for boat builders to use FRP is that the raw materials are easily obtainable at short notice with consistent material properties (no lengthy seasoning process is required). In addition only semiskilled labour is needed to process the materials and build the boats. For larger production runs this offers significant benefits over wood. FRP also allows the building of complex shapes which may by required for hydrodynamic, structural or aesthetic reasons (Smith 1990).

The tradition moulding techniques to produce these boats are hand lay-up and spray-up techniques. However economic pressure and increasingly stringent environmental requirements on styrene emission (GPRMC 1994) make these techniques less acceptable. At the same time high performance craft, such as racing yachts, are built using new techniques such as autoclave. Figure 1.1 shows processes which are available for the manufacture of large FRP structures.

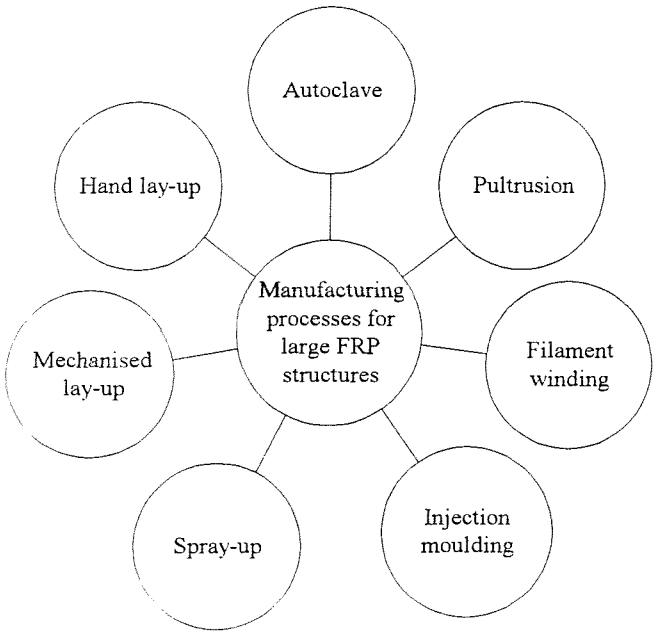

Figure 1.1 Manufacturing processes for large FRP structures

Injection moulding which includes Resin Transfer Moulding (RTM) and vacuum assisted RTM, is receiving increasing attention from manufacturers of large FRP structures in many fields. The main advantages of RTM are that it is a closed moulding process and produces high quality components with smooth surfaces on both sides. Because of the low injection pressures the tooling is quite cheap. It also has potential for a high degree of automation. Foley (1991) found a considerable cost advantage of RTM over conventional hand lay-up. RTM has become a standard process in the automobile industry for high quality low volume production of body panels for sports cars (Rao 1993) and utility vehicles (Harrison 1995). The boat and ship building industry is already taking on some of these new ideas. A ship yard for example is using vacuum assisted RTM to mould bulkheads for mine counter measure vessels and is considering using it to mould the entire hull (The Naval Architect 1995).

Design and production of ships has undergone fundamental changes through the introduction of CAD/CAM in the early 1970's. This has greatly improved the information flow in the ship yard with gains in efficiency, reduced building time and increased competitiveness. The key element of these CAD/CAM systems is a product information model where all information is stored in the form of objects. Even though sophisticated design tools for the economical production of steel and aluminium structures exist, the production of FRP structures is still based on experience and trial and error. For FRP it is crucial that the production process is well understood and controlled since the final material properties depend on it. In fact the material selection and the geometry of a FRP component is inextricably linked with the manufacturing process (Gandhi 1990). Furthermore large structures make a trial and error approach too costly. CAD/CAM software seems to be the ideal tool for achieving design for production of FRP structures. However for a successful example one has to look elsewhere e.g. to the automobile industry (Harrison 1995). Here design optimisation was achieved using structural and flow simulation software only.

To be able to apply simulation software to FRP boat and ship production a number of problems have to be overcome. The RTM process is usually treated as two separate problems: Mould filling which is then followed by the cure of the resin. Resin flow in RTM is described by Darcy's law where permeability characterizes the resistance of the fibres to the flow. As Advani, Bruscke and Parnas (1994) pointed out, the state of the art of flow simulation is far more advanced than the capability in measuring permeability. A number of different permeability measurement techniques exist. However permeability obtained by one method is in many cases different from permeability for the same material but measured using a different

method. Moreover most of the research has been focused on automobile type structures with thin wall thickness. Therefore the aim of this research is to improve current methods of characterizing the permeability of fibre reinforcement materials, not just for two-dimensional flow but also for three-dimensional flow.

2. Literature review

The objectives and aims of the literature review are twofold. Firstly to establish the fluid mechanical foundations of resin flow in RTM and secondly to review the capabilities and limits of current permeability measurement techniques.

2.1 Injection moulding processes for continuous fibres

To limit the scope of this section only injection moulding processes for continuous long fibres and thermosetting resins have been considered (Kötte 1991). In injection moulding the resin is injected into a closed mould in which dry reinforcement fibres or preforms have been placed before. Processes can be distinguished by the way the resin is injected. In Structural Reaction Injection Moulding (S-RIM) the resin is injected at very high pressures (more than 10 bar). Resin Transfer Moulding (RTM) is a very similar process, the main difference is the considerable smaller injection pressure (typically 2 to 5 bar). As a consequence less rigid moulds are required and cheaper materials for building these moulds can be used (e.g. GRP). In the RTM process cycle considerable forces may be required to compress the preform to close the mould which may also cause the mould to deform. This can be overcome by applying a vacuum at the air vents thereby utilising atmospheric pressure to clamp the mould. This process is called Vacuum Assisted Resin Transfer Moulding (VA-RTM). Despite the applied vacuum the resin is still injected under pressure. Another process is vacuum injection moulding which relies entirely on vacuum (Bunney 1994). One of the advantages is that it requires only one rigid mould while the other half can be a plastic film. To wet out the fibres in the mould, resin is sucked into the cavity by the vacuum.

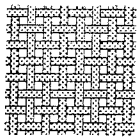

1.) Preform preparation

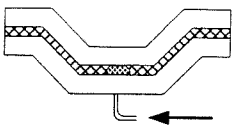

3.) Injection of resin

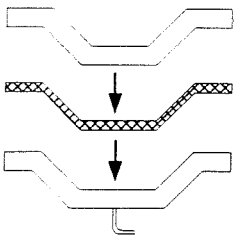

2.) Preform is placed in mould

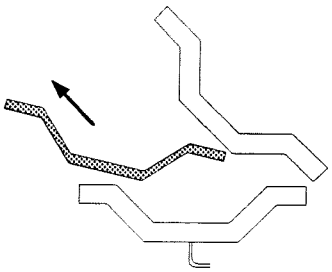

4.) Cured component is removed

Figure 2.1 Typical RTM process cycle

A typical RTM process cycle is shown in Figure 2.1. It comprises a preform preparation stage where the fibre mats are cut to size and if necessary deformed in a press. These preforms increase reproducibility and speed up the lay-up of the fibres. The preform is then placed in a mould which is subsequently closed. The resin is injected into the cavity is left to cure. Accurate metering of the resin components and thorough and complete mixing is a prerequisite for repeatable quality. On completion of the curing stage the component is ejected and deflashed.

2.2 Fluid mechanics of flow in porous media

2.2.1 Fluid and pore structure parameters

In this section the factors and parameters which describe the porous medium and the fluid are being discussed. The section follows the book by Dullien (1979, 1992).

Fluid parameters

A fluid can be described for fluid mechanical purposes by density, viscosity and the surface tension.

Definition of porous media

Porous media can be defined according to Corey (1977), as matter where the non-solid space within the solid matrix is interconnected (not just isolated pockets). Furthermore the pore size has to be large enough to allow fluid flow to occur and at the same time the pore size has to be small enough so that when interfaces between two fluids occur the orientation of interfaces will be controlled by interfacial forces (eliminates a network of pipes).

Pore structure parameters

To characterise the porous material a number of macroscopic and microscopic parameters can be defined. Permeability is that property of a porous medium which characterises the ease with which a fluid may be made to flow through the material by an applied pressure gradient (units: Darcy [$9.87*10^{-11}$ m^2], Gauvin (1986)). Porosity ϕ is the fraction of the bulk volume of the porous sample that is occupied by pores or voids. There are two different types of pores. Effective (or interconnected) pores which form a continuous phase in the porous medium and isolated (or non-interconnected) pores which cannot contribute to the flow. The pore structure parameters discussed so far are macroscopic parameters. There are also a number of microscopic pore structure parameters such as pore size distribution, packing of particles and the topology of the pore structure. Little research has been carried out to study microscopic pore structure parameters. Summerscales (1993) showed the importance of the packing structure of (idealised) fibre clusters while Griffin et al. (1995) demonstrated the influence of

(bound) flow enhancing tows on permeability using quantitative microscopy. While these models and experiments help to explain the flow behaviour qualitatively they are not yet capable of explicitly linking the microstructure of the porous material with observed flow behaviour.

2.2.2 Fluid flow in porous media

Derivation of Darcy's law

The following discussion follows Tucker III and Dessenberger (1994). A volume averaged Navier Stokes equation was derived from a representative unit cell. As a next step simplifications and assumptions were introduced to describe fluid flow in RTM. Normally the solid phase is stationary. There is no exchange of mass between solid and fluid. The fluid is Newtonian with constant density. Furthermore the body forces are due solely to gravity. The drag force is assumed to be independent of the density of the fluid and linear in the velocity difference between solid and fluid. The porous medium is anisotropic. If finally the divergence of the volume averaged viscous stress can be neglected then the Navier Stokes equation reduces to what is known as Darcy's law:

$$\langle v_f \rangle = -\frac{1}{\mu} \underline{K} \nabla \langle P_f \rangle^f \qquad (2.1)$$

where $\langle v_f \rangle$ and $\langle P_f \rangle$ are the volume averaged velocity and pressure. It is common to assume that the permeability tensor $\underline{K}$ is symmetric and as a consequence it is also orthotropic, i.e. there is a set of three mutually orthogonal axis where all the off-diagonal tensor components become zero. Tucker III and Dessenberger quote experiments for general cylindrical channels and layered, randomly deposited particles where this assumption was found to be true. However this does not mean that permeability is symmetric for any porous medium. For example Zijl and Stam (1992) found that for an imperfectly layered porous medium the permeability tensor can become non-symmetric. In fact there is no experimental evidence that permeability for flow in fibres and fabric is a symmetric tensor. The only reference quoted by Tucker III and Dessenberger as evidence for the symmetry of the permeability tensor in RTM (Parnas and Salem 1993) fails to demonstrate these properties. This is because Parnas and Salem calculate principal permeability with degrees of anisotropy and orientation which were averaged for different fibre volume fractions (see section 2.4.2). Hence the results are not independent.

Applicability of Darcy's law to RTM

Up to now it was assumed without proof that resin flow in RTM can be modelled using Darcy's law. Bear (1972) quoted a Reynolds number equal to one as the upper limit for the

validity of Darcy's law. Michaeli et al. (1989) estimated that typically the Reynolds number in RTM is of the order of 10^{-1}. Another important requirement is that the fluid is Newtonian. It has been shown that polyester resin has constant viscosity over a wide range of shear rates and filler content (Lafontaine 1984). And finally fibre mats and fabrics are a porous medium since they contain pores which are permeable by a wide range of fluids. Darcy's law is therefore applicable to RTM.

2.2.3 Immiscible displacement

In RTM resin is injected into a dry preform. The resin displaces the air in the pores. This is known as immiscible displacement which is an unsteady flow process (Corey 1977).

Unsteady flow

Infiltration is a general term for immiscible displacement, regardless of the force which causes it and the type of fluid which is being displaced. During the displacement process there is no capillary equilibrium in the system, since there is a pressure difference between the two sides of the interface which separates the fluids. The difference is called capillary pressure (P_c):

$$P_c = P_{non-wetting} - P_{wetting} \qquad (2.2)$$

Different types of fluid can be distinguished by their wetting behaviour. A wetting fluid tends to spread over a surface ($0° \leq \theta \leq 90°$) while a non-wetting fluid tends run off a surface ($90° < \theta \leq 180°$) where θ is the contact angle between the fluid and the solid.

Infiltration from a constant pressure head source

Most of the theoretical work in the field of infiltration is applied to petroleum engineering where oil is displaced by water or gas. The pressures gradients of the wetting and non-wetting fluids are assumed to be very large so that capillary effects at the flow front can be neglected. This is not true however for injecting resin into a mould with uniform (atmospheric) pressure. Corey (1977) gives an example for vertical infiltration of water into dry soil. First an equation for the total flow rate of air and water was formulated. Then a number of assumptions and simplifications were introduced: The soil is non-deformable. There is a sharp flow front with the soil fully saturated behind the flow front and completely dry ahead of it. At a position behind the flow front the total flow rate (q_t) is equal to the flow rate of the water. The air pressure is atmospheric everywhere. Further it is assumed that the permeability in the saturated region is only dependent on the water. By rearranging the initial formulation the following expression is obtained (Corey):

$$q_t = \frac{K}{\mu} \rho_w g \frac{\left[H + h_f + z_f\right]}{z_f} \qquad (2.3)$$

where z_f is the distance to the flow front, H is the head of the externally applied pressure, h_f is the value of $p_c/\rho_w g$ and ρ_w is the density of water. This equation is also known as the Green and Ampt equation (see Corey). Even though it is only valid for one-dimensional vertical flow it indicates that for RTM in addition to the injection pressure the capillary pressure and static pressure may become important.

Displacement mechanisms

There is a so called primary mechanism which involves flow of a continuous non-wetting phase and a secondary mechanism with a disconnected, so called "trapped" non wetting phase. In RTM the primary mechanism is desired. A dimensionless capillary number is introduced to characterise the displacement (Davé 1990).

$$Ca = \frac{\mu v}{\gamma_{LV}} \qquad (2.4)$$

where v is the interstitial fluid velocity and γ_{LV} is the surface tension between the wetting and non-wetting fluid. The capillary number is the ratio of viscous forces to capillary forces. The transition in macroscopic behaviour depends on the flow rate, configuration of fibres and geometry of pores. After primary displacement the non-wetting phase is discontinuous and secondary displacement will take place only if viscous forces are sufficiently large which means either one has to decrease surface tension (γ_{LV}) or increase viscosity and/ or velocity of resin ("wash out").

2.2.4 Other laminar flow models

The following well known models have also been derived for laminar flow of a uniform incompressible fluid (Batchelor 1973). They will be examined for their suitability for flow modelling in RTM.

Paint brush model

The paint brush model is based on steady unidirectional flow (Batchelor). Rigid, parallel plates slide in the x-direction over a plane. These plates extend over the x, z plane and are spaced evenly in the y-direction with distance b apart. The paint is pulled by the friction of the plane which creates a uniform flow between the plates. There is no external pressure gradient imposed.

Lubrication theory

Lubrication theory is applicable to a liquid film between two moving solid bodies (Batchelor). The inertia forces are assumed to be negligible. Because this film is thin the rate of shear and strain in the liquid is very high. The mathematical solution is based on two-dimensional flow

in a uniform channel. With a known sliding velocity and angle of inclination it is then possible to determine the pressure distribution and volume flux in the fluid.

Hele Shaw cell

The Hele Shaw cell consists of two parallel plates which are spaced closely together (Batchelor). The space between the plates is occupied by fluid and cylindrical obstacles. Flow occurs when an external pressure is applied at the ends of the plates. The layer thickness is small compared with the length of the obstacles hence the flow is assumed to be everywhere approximately the same as if the local pressure gradient extended to infinity. As in lubrication theory, the inertia forces are assumed to be negligible. This equation satisfies the condition of no-flow normal to the solid boundary although not the non-slip condition at the boundary.

In the paint brush model and lubrication theory, flow is generated by the movement of one of the boundaries. This is certainly not a very realistic model for the RTM process. In the case of the Hele Shaw cell there are quite a few similarities. The main obstacle here is that the Hele Shaw cell was derived with the assumption that the gap height is very small which is not acceptable for flow modelling of thick composites. Therefore none of the above mentioned models seem to be a suitable alternative for Darcy's law for describing fluid flow in RTM.

2.3 Modelling of permeability

In the previous section it was established that Darcy's law is the most suitable modelling approach for flow in porous media. The permeability is usually determined as a single constant from experiments while more sophisticated models incorporate additional information about the pore structure. A thorough review of this topic can be found in Dullien (1979, 1992) and Bear (1972).

2.3.1 Empirical permeability models

This is Darcy's law in its simplest form with one parameter describing the flow properties of the porous material. This is the most common approach and requires a single permeability value to be determined experimentally. This characterisation experiment is done for different porosities and the permeability can then be plotted as a graph. These experiments have to be conducted for each type of material and fluid over the whole range of porosity values of interest (Adams 1987, Gauvin 1986). It is then possible to fit a polynomial to the measured permeability data (Gauvin 1994, Kim 1990, Trevino 1991). It was shown by Gauvin et al. (1994) that empirical models yield the most accurate representation of permeability compared with the other modelling approaches discussed in this section. They also found that a single

permeability model for all the different types of mats was not realistic and therefore proposed the following model:

$$K = a + b\exp(c\phi) \quad ; \qquad 0.65 \le \phi \le 0.90 \tag{2.5}$$

where ϕ is the porosity of the fabric. The coefficients a, b and c have to be determined experimentally for each reinforcement material of interest.

2.3.2 Capillaric or geometric permeability models

These permeability models are derived from flow inside capillary tubes or channels. The most widespread representative is the Kozeny-Carman model. It is based on the mean hydraulic radius concept and the Hagen-Poiseuille equation (laminar flow in a pipe).

$$K_i = \frac{D_f^2}{16k_i}\frac{\left(1-V_f\right)^3}{V_f^2} \quad ; \qquad i = 1,2,3 \tag{2.6}$$

where D_f is the diameter of the glass fibres (25 μm for woven fabric, 15 μm for chopped strand mat), V_f is the fibre volume fraction and K_i is the Kozeny constant (Ahn 1995). The Kozeny-Carman equation shows that the permeability is dependent on fibre diameter, porosity and the Kozeny constant which needs to be determined experimentally (Ahn 1995). The Kozeny-Carman equation should only be applied where the mean hydraulic radius concept is applicable, i.e. for fibres which are packed uniformly or completely random (Griffin 1995). Gauvin et al. 1994 showed that the Kozeny-Carman equation correlates badly with permeability data for a random mat while Ahn et al. (1995) reported good agreement for woven and chopped strand mats.

Another attempt to derive permeability from first principle is the model proposed by Gebart (1992). He derived permeability expressions for unidirectional reinforcements based on flow in slowly varying channels. The permeability for flow along the fibres is very similar to the Kozeny-Carman equation while the permeability for flow across the fibres takes account of the fact that there is a maximum fibre volume fraction beyond which no flow is possible. Gebart reported a good fit of the proposed models to experimental data. He also reported that the effective fibre diameter had to be adjusted to about four times the real physical diameter which was attributed to a deviation of the fibre samples from the (assumed) circular geometry.

2.3.3 Flow around solid object permeability model

This model is based on the analysis of the drag and shear forces of flow around circular obstacles. It also takes into account friction forces on the cavity wall (Gauvin 1994). This quite complicated model requires the input of a number of parameters such as the overlaying

density (Chibani 1991). Despite these efforts, it was shown that in comparison with empirical and geometric models it is the least accurate model (Gauvin 1994).

2.3.4 Average in-plane permeability

For a variety of practical applications different types of reinforcement materials or fabrics with different orientations are used within a laminate. For thin laminates an average in-plane permeability is defined by a rule of mixture (Gebart 1991, Michaeli 1989, Rudd 1994, Verheus 1993). This assumes a plug-like flow and works well for different orientations of the same type of fabric (Verheus 1993) and quite well for a stack of mixed types of reinforcements (Gebart 1991). The thickness of each layer has to be calculated for the same compaction pressure which means that the porosity is different for the different reinforcement materials (Gauvin 1986).

However it can be observed that the flow front is advancing at different rates in different layers of the fibre stack which leads to flow in the through-thickness direction. This transverse flow can lead to a decrease in in-plane permeability. This effect is mainly observed at the flow front. It is desirable to model these through-thickness effects without having to resort to full three-dimensional modelling. Bruschke (1992) developed an analytical expression for the effective in-plane permeability at the flow front. This formula is a function of both in-plane and through-thickness permeabilities. Further away from the flow front conventional two-dimensional flow modelling can be used since there the pressure gradient has become constant in the through-thickness direction. Verheus and Peeters (1993) observed this effect for unbalanced twill fabric stacked with different angles of orientation. However they found that the rule of mixture still gave an accurate prediction of the effective in-plane permeability.

2.3.5 Through-thickness effects

The type of material and the stacking sequence also influence the through-thickness permeability while the compressibility appears not to be affected (Wu 1994). The change in permeability is therefore attributed to changes on the interface between layers of different types of materials. Wu et al. (1994) suggested a formula which considers the thickness and a interface permeability of the individual layers. For a mixed lay-up of random mats and bi-directional fibre mats this interface effect was found to be negligible (about 2%).

2.3.6 Deformation of preforms

The permeability models mentioned so far are valid for flat, undeformed fabrics and mats. This is usually not a very realistic condition since most FRP components are shaped with

curvature and corners. To model the mould filling of these components successfully one needs to modify permeability to take into account the changes of fibre architecture due to the preforming process. Two factors cause this change. The porosity changes due to the stretching of the fibres. This causes an increase of permeability in the stretch direction while perpendicular to this direction the permeability is reduced. Therefore orientation is also very important.

Two approaches have been proposed. Fong and Lee (1994) modelled the deformation effects by modifying the Kozeny-Carman equation. They introduced a porosity factor and an orientation function. When fabrics are bent around corners the thickness of the fibre stack, changes which can cause a channel to form. Fong and Lee came up with a simple expression for flow in a channel to take account of this effect. The modified permeability and channel effects were incorporated into a flow modelling code. The flow front prediction were compared with two "short shot" parts. The shape of the flow front is quite well approximated by the simulation. However since no time for each of the flow front steps was reported no quantitative judgement on the accuracy of the model is possible. Rudd et al. (1994) and McGeehin et al. (1994) take a slightly different approach. They first model fibre rotation and shear as caused by the preform deformation. This information is then used as the input to the permeability model instead of the orientation function. The predicted permeabilities correlate reasonably well with experimental permeability data.

2.4 Measurement of permeability

2.4.1 Flow measurement in porous media

There are two different ways to measure permeability. Firstly by measuring the pressure drop or the pressure history at a number of points. Alternatively the progression of the flow front is monitored. The latter requires a reliable technique to measure fluid flow in the mould. In this section the available methods to measure flow in porous media will be discussed.

Visualisation

Observation of the resin flow front progression was pioneered by Adams et al. (1986). The fluid was injected from the top and the flow front observed through a transparent bottom plate. More commonly the experimental apparatus consists of a solid (metal) base plate with a transparent top plate. This enables the recording of the flow front progression with a video camera or frame grabber which can be connected to image processing software to obtain the coordinates of the flow front at a given time step (Carter 1995, Parnas 1993). An important consideration is the stiffness of the transparent plate in order to avoid excessive deflection. For

this reason glass is preferred to acrylic. Another option to measure the flow front (for channel flow) is to use photo diodes (Gauvin 1994). These were positioned underneath a transparent cavity. The advancing flow front changes the light intensity which translates into a change in voltage. Trevino et al. (1991) proposed an edge flow mould to observe flow in the out-of-plane direction. It consisted of a L-shaped acrylic base plate with inlet gate and outlet located close to the edge to make the flow as one-dimensional as possible.

Intrusive

The non-intrusive flow measurement technique discussed in the previous section are not suitable for obtaining detailed information on the spatial flow front position. Several intrusive methods have been proposed to achieve this. Trochu et al. (1993) applied successfully heated thermistors to flow front measurements. The wires of the thermistors were laid so as to minimise the flow disturbance. A similar approach was used by Diallo et al. (1995) where thin electrical wires (0.35mm diameter) were placed at various locations within the mould cavity of a channel flow mould. The wires were arranged in stacks with wires at various heights. Since the fluid was water based the wires would short circuit when the flow front reached the position of the wires. The fluid was injected at a constant flow rate. Hence a linear relation between flow front positions measured in different stacks of wires at the same height exists. This allowed the reconstruction of the shape of the flow front.

Bréard et al. (1995) investigated the use of x-ray radiography to measure the flow front shape. This is a non-intrusive method. However to correlate these two-dimensional images with the three-dimensional flow front shape the partially filled fibre stack was taken apart and photographs were made of the flow front position of each layer. This information could then be used to rebuild the three-dimensional flow front shape. This technique is still being developed. The main question is whether by taking the fibre stack apart accuracy is lost firstly by fluid dripping out of pores and secondly, since time passes between injection and measurement, by allowing the fluid to advance through capillary action.

Ahn et al. (1995) used optical fibres to measure the flow front position. These fibres were placed between reinforcement layers. Short segments (<2mm) of the cladding of the optical fibres were removed. When the fluid reached these "bare spots" a distinct change in the photoelectric output of the sensor was observed. This arrangement worked very well in radial flow tests of thick laminates. The main limitation was the data analysis algorithm (see 2.4.3).

2.4.2 Measurement of in-plane permeability

Channel flow

For channel flow both flow with moving flow front (Gauvin 1990, 1994, Gebart 1991, 1992, Verheus 1993) and stationary flow front (Gauvin 1986, Kim 1990, Parnas 1993, Trevino 1990, 1991) are used to measure permeability. Flow with moving flow front means that the fabric or mat is initially dry and is wetted by the progressing flow front. In the case of the stationary flow front the whole sample is already fully wetted at the start of the experiment. For flow with moving flow front constant inlet pressure results in unsteady flow. Unsteady flow implies that the fluid velocity and the velocity of the progressing flow front change with time. A constant flow rate inlet condition results in steady flow - the fluid velocity remains constant throughout the duration of the experiment. For flow with stationary flow front the two inlet conditions, constant inlet pressure and constant flow rate, both result in steady flow. In all cases is the wetted domain assumed to be fully saturated with test fluid (no air bubbles). For flow with moving flow front the permeability is calculated as follows:

$$K = m\frac{\mu\varepsilon}{2\,\Delta P} \qquad \text{with} \quad m = \frac{x_f^2}{t} \tag{2.7}$$

where x_f is the distance to the flow front, t is the time, ΔP is the pressure difference between inlet and flow front, μ is the viscosity and ε is the porosity. Gebart et al. (1991) and Gebart (1992) found that the above formula gives very reliable results. Plots of x_f^2 versus t show hardly any scatter which can be seen as a proof for the validity of Darcy's law. These tests where carried out on unidirectional reinforcements at various angles of orientation and on a twill fabric. The fluid was a polyester resin. Verheus and Peeters (1993) came to the same conclusion.

To determine permeability from flow with stationary flow front simply Darcy's law is used

$$K = \frac{Q\mu}{A_n\,\Delta P/\Delta L} \tag{2.8}$$

where Q is the flow rate, A_n is the cross-sectional area of the mould, ΔP is the pressure difference between inlet and outlet and ΔL is the distance between the inlet and outlet. Kim et al. (1990) found that permeability is independent of superficial velocity (= Q/A) while Trevino et al. (1991) found the opposite i.e. permeability is dependent on superficial velocity. It has to be mentioned that Kim et al. (1990) tested at considerably lower velocities than Trevino et al. (1991). Because of the curved shape of the plot of the pressure versus superficial velocity Trevino et al. (1991) took the gradient of the lower half to calculate permeability. No

justification was given. A possible explanation for this non-linear behaviour could be the forming of channels in the fabric due to the high inlet pressure. The thickness of the cavity has also a noticeable influence on the permeability of bi-directional cloth while for random mat no effect was observed (Kim 1990). The considerable increase of the permeability of bi-directional cloth is probably due to the increase of the relative proportion of the large interlaminar pores with an increasing number of layers. After about 8 layers an equilibrium was reached (Kim 1990).

Two methods have been suggested to obtain principal permeability and orientation from channel flow experiments. Gebart and Lidström (1996) use flow resistance (the inverse of the permeability) measured from 3 channel flow experiments to calculate principal permeability and its orientation. Gebart and Lidström reported good agreement with radial flow results if the deflection of the radial flow mould was controlled. Parnas and Salem (1993) also calculate principal permeability and orientation of the permeability tensor. By using an average degree of anisotropy and orientation Parnas and Salem reduce the number of experiments. To determine principal permeability for two fibre volume fractions 6 experiments are required to determine the 6 unknowns. With the average degree of anisotropy and orientation only 4 experiments are needed to determine principal permeability and orientation. The calculated orientation compares quite well with the orientation of the flow front ellipse observed in radial flow experiments on the same materials.

Gebart and Lidström (1996) performed channel flow tests for flow with stationary and moving flow front. Their results show that flow with stationary flow front yields lower permeabilities than flow with moving flow front (for a random mat). Kim et al. (1990) found that a sample which was wetted with oil prior to testing would yield a lower permeability than a dry fabric. The test fluid was corn oil. Gauvin et al. (1994) found that the weight per unit area of continuous filament mats can vary quite considerably (up to 25%). It is therefore advisable to weigh the samples prior to testing. They also recommended to use a template for cutting the samples. This ensures an accurate fit into the mould cavity which thus minimises channelling.

Radial flow

The main attraction of the radial flow test is that both the principal permeability values and their orientation can be determined in a single experiment. It is therefore widely used by researchers (Adams 1986, 1988, Carter 1995a, Chan 1991, 1993, Fong 1994, Hirt 1987, Parnas 1993, Rudd 1995, Wang 1994, Wu 1993, Young 1995). Two algorithms to calculate permeability data from flow front measurement have been developed (Adams 1988, Chan 1991). Both have in common, that the orientation of the ellipse needs to be determined visually

since the algorithms apply only to flow front measurements along the principal axes. Radial flow experiments are always unsteady flow experiments with moving flow front (for both constant inlet pressure and constant flow rate).

The method by Chan and Hwang (1991) to calculate the permeability for anisotropic flow will be outlined briefly. For isotropic materials the permeability is defined as:

$$K = \frac{\varepsilon \mu r_o^2}{4t\,\Delta P}\left[\frac{r_f}{r_o}\left(2\ln\left(r_f/r_o\right)-1\right)+1\right] \qquad (2.9)$$

where r_f is the flow front radius, r_o is the inlet radius and t is the time. To compute the anisotropic permeability the problem is transformed into a quasi-isotropic problem by scaling the x and y-coordinates according to the ratio of the principal permeabilities. An identical solution to (2.9) is obtained, the only difference being the dependence of the radius on permeability. Firstly the degree of anisotropy (α) is determined from the square of the ratio of the major and minor axis of the flow front ellipse while the actual permeability value (K_1) is obtained from a plot of the expression in square brackets in (2.9) versus time t. Multiplying K_1 with α yields the second permeability value K_2. The method by Carter et al. (1995b) is based on Chan and Hwang. However they do not scale the inlet diameter. This significantly improves the accuracy of the calculated permeability. Adams et al. (1988) presented a method to calculate principal permeability in elliptical coordinates. It is iterative in the degree of anisotropy. The main difference to Chan and Hwang is the treatment of the inlet which is replaced with an elliptical equivalent. The results obtained with Adams method are very accurate (see section 6.9). For Adams method flow front measurements can be made at different time steps along the two principal axes. In contrast Chan and Hwang and Carter et al. require that the flow front radius in the two directions is measured at the same instance in time.

All the above theories of Adams et al. (1988) and Chan and Hwang (1991) and Carter et al. (1995b) are only applicable in the principal coordinate system. They assume permeability to be a symmetric second rank tensor. However some confusion about the properties of a tensors exist in the literature. Chan (1991, 1993) discuss orthotropic and anisotropic cases when in fact both are orthotropic while in the second case the reference coordinate system has been rotated and is not aligned with the principal axis any more. A lot of effort is spent on deriving the relationship between principal permeability and the general permeability tensor even though this is a general property of a second order tensor (Chan 1991, Carter et al. 1995a).

An interesting comparison was made by Gebart et al. (1991) who compared measurements obtained from channel flow test and radial flow tests. They concluded that the results obtained with the radial flow mould indicated less anisotropy and lower permeability in the direction of the highest permeability (The radial flow test was evaluated according to Adams 1988). Also Parnas and Salem (1993) observed that the degree of anisotropy of the flow front ellipse is time dependent which could not be explained by the influence of the circular inlet hole.

Rudd et al. (1995) discuss the use of the radial flow technique to determine permeability for S-RIM. An algorithm is proposed to determine principal permeability from constant flow rate injection. Pressure is measured in the cavity at various points along two orthogonal axes. Rudd et al. investigated the effect of different inlet diameters on permeability. They found that increasing diameters lead to a decrease in permeability. At about 20mm permeability seem to become independent of the inlet diameter. Furthermore a dependence of permeability on flow rate was observed. For a quasi-unidirectional non-crimp fabric the permeability decreased with increasing flow rate.

Carronnier et al. (1995) have tried to estimate the relative error introduced into the calculation of permeability. Very large values of relative error (up to 80%) were observed. This might be due to the way the relative error was calculated. It was simply the sum of the relative errors of each parameter of the Adams et al. (1988) algorithm. Viscosity and the degree of anisotropy were found to make the largest contribution to the relative error. However it was not possible to determine the source of these errors accurately, mainly because of the complexity of the Adams algorithm. Comparisons with numerical flow simulation confirmed that the algorithm gave accurate results hence the experimental measurements must have been subjected to errors. Carronnier et al. (1995) concluded that because of this it might be advantageous to use a one-dimensional flow measurement technique where errors are easier to analyse.

2.4.3 Measurement of three-dimensional permeability

The most common method to measure permeability in the out of plane direction is to use the one-dimensional channel flow apparatus (transplane measurement device) with constant flow rate (Trevino 1991, Wu 1993, 1994). To calculate the through-thickness permeability Darcy's law for one dimensional flow is used (2.8). The in-plane permeabilities are determined from two-dimensional flow experiments. Trevino et al. (1991) found that through-thickness permeability (K_{zz}) of most reinforcement materials showed a dependence on stack thickness. This is probably due to the fact that only a very small stack thickness was used (permeability values were given for a thickness of 3.2mm!).

In addition to the transplane permeability tests Wu (1993, 1994) performed a three-dimensional radial flow experiment with circular preform (thickness 18mm). Since the in-plane permeability of that particular material was known from two-dimensional tests, a flow simulation program was employed to match the inlet pressure by selecting an appropriate K_{zz} value. It was found that the permeability values obtained from the transplane measurement device were about 10 to 15% larger than the simulated K_{zz} values. This was attributed to edge leaking effects in the transplane measurement device. In the same article the influence of clamping pressure on permeability was investigated. It was found that as soon as the inlet pressure exceeds the clamping pressure the relation between pressure and flow rate becomes non-linear (a violation of Darcy's law). This effect was explained by additional compaction caused by the high flow rates. As long as the injection pressure was less than the clamping pressure this effect was not observed.

Woerdeman et al. (1995) have taken a different approach. Since it was thought that it is "virtually impossible to obtain through-thickness permeability with the radial flow technique" this method utilises the one-dimensional channel flow technique. The approach makes use of the assumption that permeability is a symmetric second order tensor. For six different directions the effective permeability was derived as a function of the rotation angles and the principal permeabilities. A root finder was then used to solve the six equations for the unknowns (three angles and three principal permeabilities). This approach is based on the studies of Parnas and Salem (1993). There are some questions about the formulation of effective permeability. The three-dimensional expression for effective permeability used here seems to be in contrast with the geometry of channel flow moulds which are very thin compared with the width and thickness of the moulds.

The approach suggested by Ahn et al. (1995) is the first to use a single three-dimensional radial flow experiment to measure the three-dimensional permeability tensor. The fibre optics allow the measurement of the flow front within the cavity. This study attempts to compare different measurement approaches, namely the pressure drop (channel flow), flow visualisation (two-dimensional radial flow) and fibre optics (three-dimensional radial flow) techniques. However there are two problems which limit the value of this investigation. Firstly only thin moulds were used (6.4 to 9.5mm) and secondly because of the mould material used (Plexiglas) too much deflection was experienced at higher fibre volume fractions. As a result there is very little overlap between the permeability results from the different tests which makes a meaningful comparison difficult. The analytical formula to calculate permeability for

the three-dimensional radial flow experiment requires a hemispherical inlet. This boundary condition cannot be met in practical permeability experiments where the initial flow front is disk shaped.

2.5 Summary and problem formulation

Darcy's law is used to model resin flow in RTM. The concept of principal permeabilities which is the basis of all the permeability tests and flow simulation programs requires the permeability tensor to be symmetric. This has not yet been demonstrated successfully for typical RTM reinforcements. It was found that a simple permeability model gave the best results. Gauvin's power law and the Kozeny equation were found to describe permeability well. Attempts to take into account detailed information about the pore structure have not been very successful. Analytical expression are only suitable for very simple reinforcement architectures like unidirectional fibres. In the case of permeability models for deformed fabrics more work is required even though promising attempts have been made. The measurement techniques for one and two-dimensional flow are well established and quite reliable. However the question of whether there is a difference between permeability obtained from experiments with stationary or moving flow front remains unanswered. In the literature there is evidence to support either view. Measurement techniques for three-dimensional flow are either cumbersome and difficult to perform or the permeability algorithm is insufficiently developed. It is surprising to note that for none of the measurement techniques their accuracy or reliability has been examined with the exception of one recent study which seems to suggest that the radial flow technique is not very reliable.

A number of possible improvements of current two-dimensional radial flow permeability measurement techniques emerge from this review. Permeability measurement is restricted to measurement of pressure or flow front in the principal coordinates. This is can be difficult to achieve as the flow front shape is not always known prior to the experiment. Furthermore there are no possibilities currently to monitor the transient behaviour of permeability e.g. to observe capillary flow or the effect of the circular inlet. These issues will be addressed in the following chapters. In addition current flow front measurement techniques will be adapted to allow pointwise measurement of the spatial flow front position. This enables the use of the three-dimensional radial flow test to determine permeability in a single experiment.

3. Measurement of permeability

This chapter will give a brief overview about the measurement of permeability. As discussed in the previous chapter flow in porous media can be described by Darcy's law:

$$v = -\frac{K}{\mu}\frac{dP}{dr} \qquad (3.1)$$

The fluid velocity v is a function of the (isotropic) permeability K, the viscosity of the fluid μ and the pressure gradient. The next step is to solve equation (3.1) for the boundary conditions of the experimental set up. The solution is a permeability model which characterizes permeability in terms of flow front radius, time, flow rate and pressure. The fluid is assumed to be Newtonian. Furthermore the experiment is carried out under isothermal conditions. Therefore the viscosity of the test fluid remains constant throughout the experiment.

During the experiment flow will occur not only in the pores between the fibre bundles but also inside the individual fibre bundle. However in permeability measurement these microscopic flow effects in the fibre bundles are ignored. Darcy's law considers only the macroscopic flow in the pores between the bundles. Furthermore it is not yet possible to measure the microscopic flow during a permeability experiment.

Pressure is measured using pressure transducers. For the measurement of the flow front a number of different techniques are available (see section 2.4.1). For the measurement of three-dimensional flow no readily available technique exists. Non-intrusive techniques, like observing flow are not suitable because they fail to give out of plane resolution. An alternative is to measure the flow front progression with an intrusive method. The measurement of pressure instead of flow front is not promising. It was found from simple calculations that pressure variation in out-of-plane direction is very small. Due to the low fluid velocities found in RTM, the dynamic pressure varies very little in the out-of-plane direction. The other pressure component, the static pressure, is also very small because a thickness of 30mm or less is too little to generate a noticeable gravitational pressure component.

There are two basic permeability measurement techniques which can be distinguished by the type of flow experiment used. They are the one-dimensional channel flow technique and the two (and three)-dimensional radial flow technique. The latter utilises flow between two parallel plates with an injection port in the centre of the mould. Because of the difference in

mould geometry the pressure distribution is different for channel flow and two- and three-dimensional radial flow. As a results the formulae to calculate the permeability from the experimental results are different.

In the following chapter an introduction to tensors and principal permeability will be given. Next permeability measurement with channel flow will be discussed and a new approach will be proposed (chapter 5). After that a new approach to radial flow permeability measurement will be derived. First for constant inlet pressure in chapter 6 and then for constant flow rate and for three-dimensional radial flow (chapter 7). Finally the different methods to measure permeability for channel flow and radial flow will be brought together in chapter 8 in a unified approach to permeability measurement which is then compared with current measurement techniques.

4. Symmetric tensors and principal permeability

4.1 Tensor concept

In RTM, permeability is assumed to be a symmetric second rank tensor. This forms the basis of all flow simulation programs and permeability measurement experiments. As pointed out in the literature review this property has not yet been proven successfully for porous media which are typical for RTM. Furthermore it was also found in the literature review that the tensor concept was not always well understood. It seems therefore advisable to outline and define the tensor concept.

Borg (1963) defines a tensor as "a quantity having physical significance which satisfies a certain transformation law". Another definition by Stigant (1964) describes a tensor as "a quantity that remains invariant under any admissible transformation of the reference frame. If a tensor equation holds in one reference frame it holds in all others." The transformation referred to in both definitions is the rotation-of-axis transformation. As Borg (1963) points out it is the transformation behaviour that has to be shown in order to prove that a quantity is a tensor:

$$\underline{K}' = \underline{A}^T \underline{K}\, \underline{A} \qquad (4.1)$$

where $\underline{K}$ is the permeability tensor, $\underline{A}$ is the rotation matrix, $\underline{A}^T$ is the transpose of the rotation matrix and $\underline{K}'$ is the transformed tensor. Important properties of tensors are diagonalisation and invariance (Borg 1963). Diagonalisation of symmetric tensors means that there is an orthogonal set of axes (principal axes) where all off-diagonal terms of the tensor become zero. For any 3x3 tensor there are three invariants or scalars which are quantities whose values do not change when the axes are rotated (e.g. The first invariant: $K_{xx} + K_{yy} + K_{zz} = K_1 + K_2 + K_3$).

Therefore in order to show that the permeability tensor for reinforcement fibres in RTM is a symmetric second order tensor one has to show that the principal permeability values are invariant. Measurements taken in different directions have to yield the same value for principal permeability and its orientation.

4.2 Determining principal permeability

4.2.1 Principal permeability in three dimensions

The relationship between the fluid velocity and the pressure can be written as

$$
\begin{aligned}
v_x &= -\frac{K_{xx}}{\mu}\frac{\partial P}{\partial x} - \frac{K_{xy}}{\mu}\frac{\partial P}{\partial y} - \frac{K_{xz}}{\mu}\frac{\partial P}{\partial z} \\
v_y &= -\frac{K_{xy}}{\mu}\frac{\partial P}{\partial x} - \frac{K_{yy}}{\mu}\frac{\partial P}{\partial y} - \frac{K_{yz}}{\mu}\frac{\partial P}{\partial z} \\
v_z &= -\frac{K_{xz}}{\mu}\frac{\partial P}{\partial x} - \frac{K_{yz}}{\mu}\frac{\partial P}{\partial y} - \frac{K_{zz}}{\mu}\frac{\partial P}{\partial z}
\end{aligned}
\qquad (4.2)
$$

where $K_{i,j}$ $(i,j = x,y,z)$ are components of the permeability tensor $\underline{K}$ which is assumed to be a symmetric second order tensor.

$$
\underline{K} = \begin{bmatrix} K_{xx} & K_{xy} & K_{xz} \\ K_{xy} & K_{yy} & K_{yz} \\ K_{xz} & K_{yz} & K_{zz} \end{bmatrix}
\qquad (4.3)
$$

To determine principal permeability the diagonalisation property of the tensor will be utilised. Multiplying the permeability tensor with a vector $\underline{n}$ yields another vector say $\underline{u}$:

$$
\underline{K}\,\underline{n} = \underline{u}
\qquad (4.4)
$$

If further, $\underline{u}$ is parallel to $\underline{n}$

$$
\underline{u} = k\,\underline{n}
\qquad (4.5)
$$

where k is a scalar then

$$
\underline{K}\,\underline{n} - k\,\underline{n} = 0
\qquad (4.6)
$$

or

$$
(\underline{K} - \underline{E}k)\underline{n} = 0
\qquad (4.7)
$$

where $\underline{E}$ is the unit matrix. And fully expanded:

$$
\begin{aligned}
(K_{xx} - k)\underline{n}_x + K_{xy}\underline{n}_y + K_{xz}\underline{n}_z &= 0 \\
K_{xy}\underline{n}_x + (K_{yy} - k)\underline{n}_y + K_{yz}\underline{n}_z &= 0 \\
K_{xz}\underline{n}_x + K_{yz}\underline{n}_y + (K_{zz} - k)\underline{n}_z &= 0
\end{aligned}
\qquad (4.8)
$$

This is a homogeneous system of linear equations. For a non-trivial solution the determinant of the coefficient matrix has to be zero which leads to the following characteristic equation.

$$
k^3 - I_1 k^2 + I_2 k - I_3 = 0
\qquad (4.9)
$$

with the invariants

$$
\begin{aligned}
I_1 &= K_{xx} + K_{yy} + K_{zz} \\
I_2 &= K_{xx}K_{yy} + K_{yy}K_{zz} + K_{zz}K_{xx} - K_{xy}^2 - K_{yz}^2 - K_{xz}^2 \\
I_3 &= K_{xx}K_{yy}K_{zz} + 2K_{xy}K_{yz}K_{xz} - K_{xx}K_{yz}^2 - K_{yy}K_{xz}^2 - K_{zz}K_{xy}^2
\end{aligned}
\qquad (4.10)
$$

The roots of the characteristic equation ($k = K_{1,2,3}$) are the eigenvalues of this homogeneous system of linear equations. In the case of symmetric tensors all off-diagonal terms become zero; hence the eigenvalues correspond to principal permeability (Duschek and Hochrainer 1948). The eigenvectors ($\underline{n}_1$, $\underline{n}_2$, $\underline{n}_3$) of this system determine the directions of the principal axes. The eigenvectors are obtained by solving the following set of equations (e.g. for $k = K_1$ and $\underline{n}_1^T = [n_{1x}, n_{1y}, n_{1z}]$):

$$
\begin{aligned}
(K_{xx} - K_1)n_{1x} + K_{xy}n_{1y} + K_{xz}n_{1z} &= 0 \\
K_{xy}n_{1x} + (K_{yy} - K_1)n_{1y} + K_{yz}n_{1z} &= 0 \\
K_{xz}n_{1x} + K_{yz}n_{1y} + (K_{zz} - K_1)n_{1z} &= 0
\end{aligned}
\qquad (4.11)
$$

and

$$
n_{1x}^2 + n_{1y}^2 + n_{1z}^2 = 1 \qquad (4.12)
$$

This can be solved for the three components of the eigenvector ($\underline{n}_1$). Four equations are needed because n_{1x}, n_{1y}, n_{1z} are mutually dependent. Routines from software libraries (e.g. NAG) are available which determine the eigenvalues and eigenvectors efficiently and reliably.

4.2.2 Principal permeability in two dimensions

In two dimensions the homogeneous system of linear equations can be written as

$$
\begin{aligned}
(K_{xx} - k)\underline{n}_x + K_{xy}\underline{n}_y &= 0 \\
K_{xy}\underline{n}_x + (K_{yy} - k)\underline{n}_y &= 0
\end{aligned}
\qquad (4.13)
$$

with the characteristic equation:

$$
k^2 - I_1 k + I_2 = 0 \qquad (4.14)
$$

and the invariants

$$
\begin{aligned}
I_1 &= K_{xx} + K_{yy} \\
I_2 &= K_{xx}K_{yy} - K_{xy}^2
\end{aligned}
\qquad (4.15)
$$

The eigenvalues (and the principal permeability, $k = K_{1,2}$) are obtained by solving the characteristic equation (4.14). In two dimensions an explicit solution of the characteristic equation is possible.

$$
K_{1,2} = \frac{K_{xx} + K_{yy}}{2} \pm \sqrt{\left(\frac{K_{xx} - K_{yy}}{2}\right)^2 + K_{xy}^2} \qquad (4.16)
$$

The direction of the principal permeabilities is determined by the eigenvectors (as in (4.11) and (4.12)). The angle which is enclosed by the first eigenvector and the x-axis is given by:

$$2\varphi = \tan^{-1}\left(\frac{2K_{xy}}{K_{xx} - K_{yy}}\right) \qquad (4.17)$$

with $K_{xx} \neq K_{yy}$. There is a second possible solution with $\varphi_2 = \varphi + \pi/2$ because $\tan\varphi$ is only unique in an interval of $\pm \pi/2$. It can also be shown (e.g. Mohr's circle) that the principal values are the maximum and minimum permeabilities (see e.g. Gere and Timoshenko 1987).

4.3 Tensor rotation

As outlined in section 4.1 tensors can be rotated from one coordinate system to another. This is utilised to relate the experimental results obtained in different coordinate systems (e.g. channel flow experiments). The rotation matrix in equation (4.1) is defined as follows:

$$\underline{A} = \begin{bmatrix} \lambda_{x'x} & \lambda_{x'y} & \lambda_{x'z} \\ \lambda_{y'x} & \lambda_{y'y} & \lambda_{y'z} \\ \lambda_{z'x} & \lambda_{z'y} & \lambda_{z'z} \end{bmatrix} \qquad (4.18)$$

where $\lambda_{i'j}$ are the direction cosines (see e.g. Borg 1963 or Zienkiewicz and Taylor 1991). For example $\lambda_{x'x}$ means the cosine of the angle between the x' - axis and the x-axis. Performing the multiplication in equation (4.1) results in the following K' matrix tensor components:

$$\begin{aligned}
K'_{xx} &= K_{xx}\lambda^2_{x'x} + 2K_{xy}\lambda_{x'x}\lambda_{x'y} + 2K_{xz}\lambda_{x'x}\lambda_{x'z} + K_{yy}\lambda^2_{x'y} + 2K_{yz}\lambda_{x'y}\lambda_{x'z} + K_{zz}\lambda^2_{x'z} \\
K'_{xy} &= K_{xx}\lambda_{x'x}\lambda_{y'x} + K_{xy}\left(\lambda_{x'x}\lambda_{y'y} + \lambda_{y'x}\lambda_{x'y}\right) + K_{xz}\left(\lambda_{y'z}\lambda_{x'x} + \lambda_{y'x}\lambda_{x'z}\right) \\
&\quad + K_{yy}\lambda_{y'y}\lambda_{x'y} + K_{yz}\left(\lambda_{y'z}\lambda_{x'y} + \lambda_{y'y}\lambda_{x'z}\right) + K_{zz}\lambda_{y'z}\lambda_{x'z} \\
K'_{xz} &= K_{xx}\lambda_{z'x}\lambda_{x'x} + K_{xy}\left(\lambda_{z'y}\lambda_{x'x} + \lambda_{z'x}\lambda_{x'y}\right) + K_{xz}\left(\lambda_{z'z}\lambda_{x'x} + \lambda_{z'x}\lambda_{x'z}\right) \\
&\quad + K_{yy}\lambda_{z'y}\lambda_{x'y} + K_{yz}\left(\lambda_{z'z}\lambda_{x'y} + \lambda_{z'y}\lambda_{x'z}\right) + K_{zz}\lambda_{z'z}\lambda_{x'z} \\
K'_{yy} &= K_{xx}\lambda^2_{y'x} + 2K_{xy}\lambda_{y'y}\lambda_{y'x} + 2K_{xz}\lambda_{z'y}\lambda_{y'x} + K_{yy}\lambda^2_{y'y} + 2K_{yz}\lambda_{y'z}\lambda_{y'y} + K_{zz}\lambda^2_{y'z} \\
K'_{yz} &= K_{xx}\lambda_{z'x}\lambda_{y'x} + K_{xy}\left(\lambda_{z'y}\lambda_{y'x} + \lambda_{z'x}\lambda_{y'y}\right) + K_{xz}\left(\lambda_{z'z}\lambda_{y'x} + \lambda_{z'x}\lambda_{y'z}\right) \\
&\quad + K_{yy}\lambda_{z'x}\lambda_{y'y} + K_{yz}\left(\lambda_{z'z}\lambda_{y'y} + \lambda_{z'y}\lambda_{y'z}\right) + K_{zz}\lambda_{z'z}\lambda_{y'z} \\
K'_{zz} &= K_{xx}\lambda^2_{z'x} + 2K_{xy}\lambda_{z'y}\lambda_{z'x} + 2K_{xz}\lambda_{z'z}\lambda_{z'x} + K_{yy}\lambda^2_{z'y} + 2K_{yz}\lambda_{z'z}\lambda_{z'y} + K_{zz}\lambda^2_{z'z}
\end{aligned} \qquad (4.19)$$

In the following three chapters the tensor rotation will be employed to determine the principal permeability and its orientation.

5. Channel flow permeability measurement

5.1 Principal permeability for anisotropic materials in two dimensions

5.1.1 Measurement of permeability

In order to determine the full permeability tensor in two dimensions three experiments have to be carried out to measure the three unknowns K_1, K_2 and φ. There are a number of possible experimental configurations. Figure 5.1 shows a schematic of the channel flow experiment and its boundary conditions.

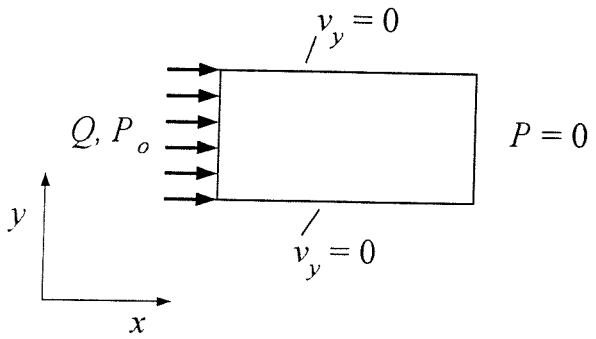

Figure 5.1 One dimensional permeability measurement

The channel flow experiments can be divided into two broad categories: constant flow rate and constant inlet pressure channel flow experiments. For both categories a new experimental configuration is suggested (equations (5.5) and (5.8)).

Constant flow rate

Details on how to calculate permeability from constant flow rate experiments can be found in e.g. Gauvin (1986):

$$K = \frac{\mu Q}{A_n}\frac{x_f}{P_o} \qquad (5.1)$$

For experiments where the flow front is moving, x_f in equation (5.1) is changing with time as well as P_o. In a more general case, permeability can be determined from pressure measurements at two points x_1 and x_2 as follows:

$$K = \frac{\mu Q}{A_n}\frac{(x_2 - x_1)}{(P_1 - P_2)} \qquad (5.2)$$

If x_2 is the flow front x_f and x_1 is set to zero (inlet) then equation (5.2) becomes equation (5.1) again (with zero pressure at the flow front). Another option would be to measure the pressure at a point in the mould rather than the inlet as in equation (5.1). If x_2 is the position of the pressure transducer then the equation (5.2) can be written as:

$$K = \frac{\mu Q}{A_n}\frac{(x_f - x_2)}{P_2} \qquad (5.3)$$

The flow front position x_f can be replaced by an equivalent expression from mass continuity:

$$Q(t - t_2) = A_n(x_f - x_2)\varepsilon \qquad (5.4)$$

where t_2 is the time to reach the position x_2, ε is the porosity while t denotes the time of the current flow front position. Solving equation (5.4) for x_f and substituting it into equation (5.3) yields after rearranging the final expression:

$$K = \frac{\mu Q^2}{\varepsilon A_n^2}\frac{(t - t_2)}{P_2} \qquad (5.5)$$

Constant inlet pressure

For constant inlet pressure experiments permeability can be calculated from (e.g. Gebart (1992)):

$$K = \frac{\mu\varepsilon}{2\Delta P}\frac{x_f^2}{t} \qquad (5.6)$$

The pressure drop between inlet and flow front (ΔP) remains constant throughout the experiment. It is conceivable to measure the pressure drop instead between inlet and flow front between inlet and another fixed point the mould (say x_1). The pressure distribution in a channel flow mould is given by:

$$P(x) = P_o\frac{x_f - x}{x_f - x_o} \qquad (5.7)$$

Solving equation (5.7) for x_f (with $P_1 = P(x_1)$ and $x_o = 0$) and substituting into (5.6) yields permeability in terms of the pressure measured at two points:

$$K = \frac{\mu\varepsilon}{2\Delta P}\frac{\left[\frac{P_o x_1}{P_o - P_1}\right]^2}{t} \qquad (5.8)$$

5.1.2 Determining principal permeability

To determine which permeability tensor component is measured with the channel flow test it is necessary to examine the equation for general flow in three dimensions (equation (4.2)) which is repeated below:

$$v_x = -\frac{K_{xx}}{\mu}\frac{\partial P}{\partial x} - \frac{K_{xy}}{\mu}\frac{\partial P}{\partial y} - \frac{K_{xz}}{\mu}\frac{\partial P}{\partial z}$$

$$v_y = -\frac{K_{xy}}{\mu}\frac{\partial P}{\partial x} - \frac{K_{yy}}{\mu}\frac{\partial P}{\partial y} - \frac{K_{yz}}{\mu}\frac{\partial P}{\partial z} \qquad (5.9)$$

$$v_z = -\frac{K_{xz}}{\mu}\frac{\partial P}{\partial x} - \frac{K_{yz}}{\mu}\frac{\partial P}{\partial y} - \frac{K_{zz}}{\mu}\frac{\partial P}{\partial z}$$

$v_y = 0$ (solid wall)

≈ 0 (thin mould)

In channel flow experiments the gap height is usually very small compared with the width and height of mould (see Table 5.8). It is therefore a reasonable assumption to ignore the flow and pressure gradient in the z-direction. Due to the solid side walls no flow is possible in the y-direction hence $v_y = 0$. As proposed by Parnas and Salem (1993) equation (5.9) can be rearranged to yield the effective permeability, i.e. the permeability which is actually measured in the experiment.

$$K_{eff,1} = \frac{v_x \mu}{-\partial P/\partial x} = K_{xx} + K_{xy}\frac{\partial P/\partial y}{\partial P/\partial x} \qquad (5.10)$$

And from $v_y = 0$ it follows

$$-\frac{K_{xy}}{K_{yy}} = \frac{\partial P/\partial y}{\partial P/\partial x} \qquad (5.11)$$

and finally:

$$K_{eff,1} = K_{xx} - \frac{K_{xy}^2}{K_{yy}} = \frac{K_{xx}K_{yy} - K_{xy}^2}{K_{yy}} \qquad (5.12)$$

Using the tensor rotation scheme it is possible to express the three tensor components in terms of the principal permeability:

$$K_{eff,i} = \frac{K_1 K_2}{K_1 \sin^2\varphi + K_2 \cos^2\varphi} \qquad (5.13)$$

By using the relationship between the second invariant and the principal permeability (equation (4.15)) for the numerator in equation (5.12) it was possible to derive a much more compact expression for the effective permeability than Parnas and Salem. To measure the two principal permeabilities and its orientation three experiments are required which have

to be conducted at different orientations. This is shown schematically in Figure 5.2. These experiments yield $K_{eff,I}$, $K_{eff,II}$ and $K_{eff,III}$ respectively.

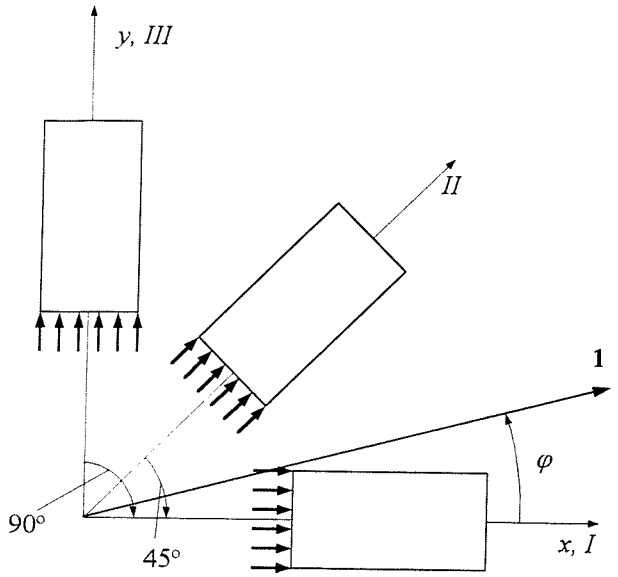

Figure 5.2 Permeability measurement for channel flow

In the following discussion $K_{eff,I}$ is referred to as K_I , $K_{eff,II}$ as K_{II} and $K_{eff,III}$ as K_{III}. K_{II} and K_{III} are measured at 45° and 90° to the first measurement direction. This yields three different equations to determine the principal permeability.

$$K_I = \frac{K_1 K_2}{K_1 \sin^2 \varphi_I + K_2 \cos^2 \varphi_I} \qquad (5.14)$$

with $\varphi_I = \varphi$ (φ is the orientation of the principal axis)

$$K_{II} = \frac{K_1 K_2}{K_1 \sin^2 \varphi_{II} + K_2 \cos^2 \varphi_{II}} \qquad (5.15)$$

with $\varphi_{II} = \varphi - 45°$

$$K_{III} = \frac{K_1 K_2}{K_1 \sin^2 \varphi_{III} + K_2 \cos^2 \varphi_{III}} \qquad (5.16)$$

where $\varphi_{III} = \varphi - 90°$. Equations (5.14) and (5.16) are used to define principal permeability as a function of the angle of rotation. Rearranging (5.14) yields:

$$K_1 = \frac{K_I K_2 \cos^2 \varphi_I}{K_2 - K_I \sin^2 \varphi_I} \qquad (5.17)$$

and (5.16):

$$K_2 = \frac{K_{III} K_1 \sin^2 \varphi_{III}}{K_1 - K_{III} \cos^2 \varphi_{III}} \qquad (5.18)$$

The next step is to substitute (5.17) for K_1 in equation (5.18). Rearranging and using $\sin(\varphi -90^\circ) = -\cos(\varphi)$ and $\cos(\varphi -90^\circ) = \sin(\varphi)$ as well as $(\cos^4\varphi -\sin^4\varphi) = (\cos^2\varphi -\sin^2\varphi)$ yields:

$$K_1 = \frac{K_I K_{III}\left(\cos^2\varphi - \sin^2\varphi\right)}{K_{III}\cos^2\varphi - K_I \sin^2\varphi} \qquad (5.19)$$

Substituting (5.18) for K_2 in equation (5.17) and rearranging yields:

$$K_2 = \frac{K_I K_{III}\left(\cos^2\varphi - \sin^2\varphi\right)}{K_I \cos^2\varphi - K_{III}\sin^2\varphi} \qquad (5.20)$$

To simplify the two equations for K_1 and K_2 the average A and difference D is introduced:

$$A = \frac{K_I + K_{III}}{2} \quad \text{and} \quad D = \frac{K_I - K_{III}}{2} \qquad (5.21)$$

Therefore $K_I = A + D$ while $K_{III} = A - D$. Substituting for K_I and K_{III} in equation (5.19) yields (with $(\cos^2\varphi -\sin^2\varphi) = \cos 2\varphi$):

$$K_1 = K_I \frac{(A - D)}{(A - D/\cos 2\varphi)} \qquad (5.22)$$

and in equation (5.20)

$$K_2 = K_{III} \frac{(A + D)}{(A + D/\cos 2\varphi)} \qquad (5.23)$$

From equation (5.15) the angle φ is computed. Using $\sin^2(\varphi -45^\circ) = (1-\sin 2\varphi)/2$ and $\cos^2(\varphi - 45^\circ) = (1+\sin 2\varphi)/2$ equation (5.15) can be written as:

$$\frac{K_{II}}{2}\left(\frac{(1 - \sin 2\varphi)}{K_2} + \frac{(1 + \sin 2\varphi)}{K_1}\right) = 1 \qquad (5.24)$$

Substituting for K_1 and K_2 and rearranging yields:

$$K_{II}\left(\frac{A - D\tan 2\varphi}{A^2 - D^2}\right) = 1 \qquad (5.25)$$

Equation (5.25) can be solved for φ to obtain an explicit expression for the orientation of the principal permeability.

$$\varphi = \frac{1}{2}\tan^{-1}\left\{\frac{A}{D} - \frac{A^2 - D^2}{K_{II} D}\right\} \qquad (5.26)$$

The permeability in the x,y plane is now fully defined. First the angle of orientation is calculated using equation (5.26). Then the principal permeabilities are computed using equations (5.22) and (5.23). For φ equal to zero equations (5.22) and (5.23) greatly simplify because the effective permeabilities K_I and K_{III} become the principal permeabilities.

5.2 Comparison with published data

Published results for effective permeability for different angles of orientation are limited. Parnas and Salem (1993) published results measured at four different angles. Unfortunately only two experiments where conducted at the same fibre volume fraction. Therefore these results were not suitable for validating the formulae. Gebart and Lidström (1996) conducted similar experiments at 0°, 45° and 90°, all at the same fibre volume fraction. The materials used were Injectex 21091, a highly anisotropic fabric, and Unifilo 812, a continuous filament mat. The measured effective permeabilities are repeated in Table 5.1.

	U 812 (moving flow front)	U 812 (stationary flow front)	Injectex 21091
K_I	$3.81\text{x}10^{-10}$	$3.67\text{x}10^{-10}$	$8.54\text{x}10^{-10}$
K_{II}	$3.98\text{x}10^{-10}$	$3.85\text{x}10^{-10}$	$8.00\text{x}10^{-11}$
K_{III}	$5.12\text{x}10^{-10}$	$4.72\text{x}10^{-10}$	$3.70\text{x}10^{-11}$

Table 5.1 Experimental results (Gebart and Lidström (1996))

Table 5.2 lists the principal permeabilities and its orientation as calculated by equations (5.22), (5.23) and (5.26). Gebart and Lidström propose to use the flow resistance tensor (the inverse of the permeability tensor) to calculate the principal permeability values. This method is equivalent to the method outlined in the previous section and yields identical results. There is good agreement between the orientations of the principal permeability for the two sets of U 812 results with a difference of less than 2° (see Table 5.2). Unfortunately Gebart and Lidström did not report any visual observations from radial flow tests to confirm this rotation of the principal axis. The angle of orientation for the Injectex 21091 fabric is also quite good considering the degree of anisotropy (expected value of $\varphi = 0°$). Small variations in K_{III} (the smallest of the effective permeabilities) cause a noticeable change in the results. For example by increasing K_{III} from $3.70\text{x}10^{-11}$ to $3.80\text{x}10^{-11}$ the angle of orientation becomes $\varphi = 2.82°$ while $K_1 = 9.01\text{x}10^{-10}$ and $K_2 = 3.79\text{x}10^{-11}$. The difference in the permeability values for U 812 was attributed by Gebart and Lidström to the different flow mechanism (stationary and moving flow front). For all three sets of results the principal permeabilities are maximum or minimum values with the measured effective permeability laying in between them. This is another confirmation that equations (5.22), (5.23) and (5.26) work successfully.

	U 812 (moving flow front)	U 812 (stationary flow front)	Injectex 21091
φ	16.83°	15.05°	3.53
K_1	3.71×10^{-10}	3.61×10^{-10}	9.32×10^{-10}
K_2	5.30×10^{-10}	4.83×10^{-10}	3.69×10^{-11}

Table 5.2 Principal permeability and orientation (equations (5.22), (5.23), (5.26))

In Table 5.3 the degree of anisotropy for the effective and principal permeability are compared. As the principal permeability is an extreme value, the degree of anisotropy is slightly less than the degree of anisotropy for effective permeability.

	U 812 (moving flow front)	U 812 (stationary flow front)	Injectex 21091
K_1 / K_2	0.70	0.75	25.29
K_I / K_{III}	0.74	0.78	23.08

Table 5.3 Degree of anisotropy for effective and principal permeability

To test the method further the principal permeability values and its orientation were used to recalculate the effective permeabilities using equation (5.13). The results are shown in Table 5.4. The calculated effective permeabilities are identical to the experimentally measured values in Table 5.1. Hence the method is reversible.

angle of rotation	U 812 (moving flow fr.)	U 812 (stationary flow fr.)	Injectex 21091
0° (= K_1)	3.71×10^{-10}	3.61×10^{-10}	9.32×10^{-10}
$-\varphi$ (= K_I)	3.81×10^{-10}	3.67×10^{-10}	8.54×10^{-10}
$-\varphi+45°$ (= K_{II})	3.98×10^{-10}	3.85×10^{-10}	8.00×10^{-11}
$-\varphi+90°$ (= K_{III})	5.12×10^{-10}	4.72×10^{-10}	3.70×10^{-11}
90° (= K_2)	5.30×10^{-10}	4.83×10^{-10}	3.69×10^{-11}

Table 5.4 Effective permeability calculated from principal permeability

This exercise also shows the relation of the calculated angle φ and principal permeability. Because φ is not unique there are two possible orientations: φ and $\varphi + 90°$. Due to the choice of the reference coordinate system for the experiments of the U 812 continuous filament mat K_I is smaller than K_{III} . This results in K_1 being also smaller than K_2. It is clear from Table 5.4 that a rotation of the reference coordinate system by an angle φ will align the x-axis with the

direction of the smaller value of the principal permeabilities. An additional rotation of + 90° will align the reference coordinate system with the larger permeability value. The usual convention is that K_1 is larger than K_2. To achieve this, the calculated principal values have to be swapped with each other and the reference coordinate system has to be rotated by φ + 90° (see also section 6.6.3). This is not necessary for the principal permeability for Injectex 21091.

As already mentioned the experimental results obtained by Parnas and Salem (1993) were not suitable for the new formulae developed here. The approach by Parnas and Salem uses 4 experimental results to calculate principal permeability and its orientation by using an average degrees of anisotropy and angle of orientation. The results are repeated in Table 5.5.

Fabric type	φ	Set A		Set B	
		K_1	K_2	K_1	K_2
JPS 8-harness satin	115	$3.78\text{x}10^{-08}$	$4.67\text{x}10^{-08}$	$2.00\text{x}10^{-08}$	$2.47\text{x}10^{-08}$
CNF 8-harness satin	75	$6.11\text{x}10^{-07}$	$8.37\text{x}10^{-07}$	$3.84\text{x}10^{-07}$	$5.26\text{x}10^{-07}$
CNF 5-harness satin	121	$8.27\text{x}10^{-07}$	$9.73\text{x}10^{-07}$	$1.34\text{x}10^{-06}$	$1.58\text{x}10^{-06}$
CNF Crowfoot	94	$4.58\text{x}10^{-07}$	$7.51\text{x}10^{-07}$	$7.99\text{x}10^{-07}$	$1.31\text{x}10^{-06}$

Table 5.5 Principal permeability and its orientation (Parnas and Salem 1993)

Since Parnas and Salem and the new approach use the same formulation for effective permeability it is a good test of their accuracy if the effective permeability of the experiments can be expressed by the principal permeabilities. This is demonstrated successfully for the new approach in Table 5.4 where calculated effective permeabilities are shown to be identical to the measured effective permeabilities. Table 5.6 and Table 5.7 show the results for both sets of experiments conducted by Parnas and Salem.

Fabric type	experimental results		calculated effective permeability	
	K_e^0	K_e^{90}	$-\varphi\ (=K_e^{90})$	$-\varphi+90°\ (=K_e^0)$
JPS 8-harness satin	$3.91\text{x}10^{-08}$	$4.49\text{x}10^{-08}$	$4.48\text{x}10^{-08}$	$3.91\text{x}10^{-08}$
CNF 8-harness satin	$4.65\text{x}10^{-07}$	$6.13\text{x}10^{-07}$	$8.16\text{x}10^{-07}$	$6.22\text{x}10^{-07}$
CNF 5-harness satin	$1.39\text{x}10^{-06}$	$1.50\text{x}10^{-06}$	$9.29\text{x}10^{-07}$	$8.61\text{x}10^{-07}$
CNF Crowfoot	$4.57\text{x}10^{-07}$	$7.50\text{x}10^{-07}$	$7.49\text{x}10^{-07}$	$4.59\text{x}10^{-07}$

Table 5.6 Effective permeability calculated from principal permeability ,Set A

Fabric type	experimental results		calculated effective permeability	
	K_e^{45}	K_e^{135}	$-\varphi\ (= K_e^{135})$	$-\varphi+90°\ (= K_e^{45})$
JPS 8-harness satin	$2.04\text{x}10^{-08}$	$2.40\text{x}10^{-08}$	$2.37\text{x}10^{-08}$	$2.07\text{x}10^{-08}$
CNF 8-harness satin	$5.53\text{x}10^{-07}$	$4.74\text{x}10^{-07}$	$5.13\text{x}10^{-07}$	$3.91\text{x}10^{-07}$
CNF 5-harness satin	$8.31\text{x}10^{-07}$	$9.63\text{x}10^{-07}$	$1.50\text{x}10^{-06}$	$1.39\text{x}10^{-06}$
CNF Crowfoot	$1.02\text{x}10^{-06}$	$9.52\text{x}10^{-07}$	$1.31\text{x}10^{-06}$	$8.01\text{x}10^{-07}$

Table 5.7 Effective permeability calculated from principal permeability ,Set B

In all but one case the experimental results differ from the calculated effective permeabilities. This seems to indicate that the mathematical procedure to calculate principal permeability by Parnas and Salem is not very accurate. Using equation (5.13) to recalculate the effective permeability is merely an inversion of the process of finding principal permeability. Parnas and Salem claim that by using all four results of the channel flow tests the accuracy will be improved - the contrary appears to be the case.

Comparing principal permeability (Table 5.5) with the experimentally measured effective permeability (Table 5.6 and Table 5.7) shows that for the CNF 8 and CNF 5-harness satin the principal permeability is not always the maximum or minimum value. This is a contradiction of principal permeability (see section 4.2.2). Also the relation of the calculated angle of orientation and the principal permeability value was not discussed by Parnas and Salem.

Further investigation revealed that some of the results presented in Parnas and Salem (1993) were actually wrong (Parnas 1996). Parnas and Salem use an average orientation and degree of anisotropy to determine permeability from the two sets of results. Therefore a small discrepancy is expected when the process is reversed (with equation (5.13)), which is not an error of the method itself but caused by the averaging process. This is not a problem with the new method outlined here as three results are used to determine the two principal permeability and its orientation. However to determine permeability at two fibre volume fraction six experiments are required while Parnas and Salem only need four experiments. This is a considerable saving for larger experimental programmes. Table 5.2 and Table 5.3 demonstrate (for U812) that the assumption of using a constant orientation and degree of anisotropy is quite reasonable.

Some of the results by Parnas and Salem (Table 5.5, CNF Crowfoot (Set A)) were used by Woerdeman et al. (1995) to compare effective permeability calculated by equation (5.13) and a two-dimensional flow simulation. In both cases the effective permeability was approximately $1x10^{-06}$. It is surprising that the effective permeability is larger than the principal permeability ($7.51x10^{-07}$). Additionally it is not possible to reproduce the value for effective permeability. Using equation (5.13), which is identical to equation 9a used by Woerdeman et al., an effective permeability of $5.69x10^{-07}$ was calculated (using $K_1 = 4.58x10^{-07}$ $K_2 = 7.51x10^{-07}$ and $\varphi = 45°$).

5.3 Principal permeability for anisotropic materials in three dimensions

In some cases the third principal permeability, K_3, is required. This is usually measured using the through-the-thickness permeability test. Woerdeman et al. (1995) proposed a scheme with which the principal permeability can be computed even if the principal coordinates are tilted out-of-plane. To do this Woerdeman et al. use a series of channel flow tests (four in-plane, one through the thickness and one out-of-plane). The proposed effective permeability includes, in contrast to equation (5.10), also the term with the pressure gradient in z-direction:

$$K_{eff,i} = K_{xx} + K_{xy}\frac{\partial P/\partial y}{\partial P/\partial x} + K_{xz}\frac{\partial P/\partial z}{\partial P/\partial x} \qquad (5.27)$$

As a next step Woerdeman et al. express the effective permeability in terms of the principal permeability which leads to six very complex equations. In the discussion here the problem will be broken down into two steps. Firstly the six permeability tensor components need to be determined experimentally which are then resolved for principal permeability and its orientation (using the eigenvalue theorem in section 4.2.1). This separation into two steps makes it easier to understand the proposed method as the mathematics are less complex while the underlying assumptions remain unchanged. Using the boundary conditions of $v_y = v_z = 0$ the ratios of the pressure gradients in equation (5.27) are replaced by tensor components as shown in section 5.1.2.

$$K_{eff,i} = K_{xx} - \frac{K_{xy}^2 K_{zz} - 2K_{xy}K_{yz}K_{xz} + K_{xz}^2 K_{yy}}{K_{yy}K_{zz} - K_{yz}^2} \qquad (5.28)$$

The following discussion focuses on the orientation of the channel flow experiments and the formulation of effective permeability.

5.3.1 Orientation of channel flow experiments

The first channel flow experiment is conducted in an arbitrary coordinate system. If another experiment is carried out in the chosen frame of reference but rotated about an axis (by an angle ζ), say about the z-axis, then the components of the second effective permeability are related to the first permeability measurement as follows (using equations (4.19) on page 45):

$$
\begin{aligned}
K'_{xx} &= K_{xx}\cos^2\zeta + 2K_{xy}\sin\zeta\cos\zeta + K_{yy}\sin^2\zeta \\
K'_{xy} &= \left(-K_{xx} + K_{yy}\right)\sin\zeta\cos\zeta + K_{xy}\left(\cos^2\zeta - \sin^2\zeta\right) \\
K'_{yy} &= K_{xx}\sin^2\zeta - 2K_{xy}\sin\zeta\cos\zeta + K_{yy}\cos^2\zeta \\
K'_{zz} &= K_{zz} \\
K'_{yz} &= -K_{xz}\sin\zeta + K_{yz}\cos\zeta \\
K'_{xz} &= K_{xz}\cos\zeta + K_{yz}\sin\zeta
\end{aligned}
\qquad (5.29)
$$

Equations (5.28) and (5.29) demonstrate that all six tensor component are determined in the experiments. It also shows that the whole permeability tensor can be determined by six in-plane measurements carried out at different angles of rotation about one axis. Hence it is possible to simplify the experimental procedure suggested by Woerdeman et al.. The two out-of-plane experiments can actually be replaced by two additional in-plane experiments which are much easier to perform than the two out-of-plane experiments. This is however only possible if the experimental coordinate system is not aligned with the principal axes.

5.3.2 Effective permeability

Another point worth discussing is the formulation of the effective permeability. Equation (5.27) assumes three-dimensional flow in the channel flow mould which seems to be in contrast with the actual geometry of a channel flow mould. Table 5.8 shows typical dimensions of channel flow moulds. In most cases the thickness is very small compared with the width and length of the mould. As a result the flow in the z-direction becomes negligible and the equation for effective permeability ((5.27)) reduces to the two-dimensional version of it, equation (5.10).

Dimensions of mould cavity [mm]			Reference
length	width	thickness	
930	130	12	Diallo et al. (1995)
870	145	4.3	Gauvin et al. (1994)
2000	200	3	Gebart (1992)
800	200	3	Gebart and Lidström (1996)
150	150	3-12	Parnas and Salem (1993)
500	180	~2	Trevino et al. (1991)

Table 5.8 List of typical mould dimensions

The porous media used for permeability measurement are made up of thin layers of fabrics or fibre mats. By stacking a number of layers of the same material, symmetry is introduced into the porous medium. As a consequence two principal axes are in-plane while the third is normal to the plane. The components of the effective in-plane permeability are related to the principal permeability as follows (again rotation about the z-axis, φ is the angle between the measurement direction and the principal direction):

$$\begin{aligned} K_{xx} &= K_1 \cos^2\varphi + K_2 \sin^2\varphi \\ K_{xy} &= \left(-K_1 + K_2\right)\sin\varphi\cos\varphi \\ K_{yy} &= K_1 \sin^2\varphi + K_2 \cos^2\varphi \\ K_{zz} &= K_3 \\ K_{yz} &= K_{xz} = 0 \end{aligned} \qquad (5.30)$$

Equation (5.30) shows that the K_{yz} and K_{xz} terms are not determined by the experiment. Furthermore if this result is substituted back into equation (5.28) it reduces to equation (5.12) or (5.13).

A third consideration is the magnitude of the permeability terms. The through-thickness permeability is usually considerably smaller than the in-plane permeabilities. As a consequence K_{yz} and K_{xz} are smaller than K_{xy} . A common method in engineering is to simplify problems by linearising them - higher order terms are neglected. Because K_{yz} and K_{xz} are smaller than K_{xy} it is conceivable to ignore quadratic terms of K_{yz} and K_{xz} in equation (5.28). This reduces equation (5.28) to the two-dimensional form of effective permeability (equation (5.12)).

Effective permeability for the above scenarios (thin mould, principal coordinates are in-plane and K_{zz} is very small) depends only on K_1, K_2 and φ. Conducting more than three in-plane experiments will not yield any further permeability information. Therefore in addition to three in-plane experiments three out-of-plane experiments are required to determine the full permeability tensor. This can be achieved by rotating the measurement direction about the x- and y-axes. Of the three out-of plane experiments one is through the thickness. The remaining two out-of-plane experiments are impossible to perform as it requires stacking thin stripes of fabric or mat at an angle (preferably 45°) in the mould cavity.

In this section a number of arguments have been presented that suggest that a two-dimensional formulation of effective permeability is the most appropriate approach for channel flow permeability measurement. Therefore if three-dimensional permeability is required the following procedure seems to be the only solution. The in-plane permeabilities K_1 and K_2 and the orientation φ are measured with channel flow experiments. K_3 is determined in a through-thickness experiment. Hence a total of 4 experiments will be required to determine the permeability tensor.

6. Radial flow permeability measurement - constant inlet pressure

6.1 Introduction

One-dimensional channel flow tests measure effective permeabilities which are then resolved for the principal permeability and its orientation. In two- and three-dimensional radial flow tests the principal permeability is determined directly from experimental measurements. This is because the closed form solutions are only available for isotropic and quasi-isotropic problems.

Radial flow tests are commonly distinguished by their inlet condition which can be either constant flow rate or constant pressure. In both cases the mathematical formulation to describe the flow in the porous medium is Darcy's law (in polar coordinates):

$$v = -\frac{K}{\mu}\frac{dP}{dr} \qquad (6.1)$$

where v is the flow velocity, K is the isotropic permeability, μ is the viscosity and dP/dr is the pressure gradient. The solution of equation (6.1) relates the flow front position, pressure, viscosity, flow rate and porosity to permeability. The solution will vary according to the process conditions (constant flow rate or constant inlet pressure) and the variables which are recorded during the experiment (flow front or pressure). In this chapter constant inlet pressure experiments where the flow front is measured will be discussed. Other experimental configuration such as constant flow rate experiments will studied in chapter 7.

For constant inlet pressure, the pressure distribution has to be determined which is the solution of the Laplace equation in polar coordinates. Upon substituting the new pressure distribution into equation (6.1) the equation is integrated subject to the boundary conditions $\varepsilon\, dr_f/dt = v$ at the flow front and $t = 0$ at $r_f = r_o$:

$$K = \left(r_f^2\left[2\ln\left(r_f/r_o\right) - 1\right] + r_o^2\right)\frac{1}{t}\frac{\mu\varepsilon}{4\,\Delta P} \qquad (6.2)$$

where ε is the porosity, t is the time from the start of the injection to when a specified point in the cavity is reached and r_f and r_o are the radius of the flow front and inlet. ΔP is the difference between the pressure at the flow front P_f and the inlet pressure P_o. The pressure at the flow

front is usually set to zero hence ΔP is equal to the pressure applied at the inlet P_o. The radius r is related to the x, y coordinates as follows:

$$r = \sqrt{x^2 + y^2} \qquad (6.3)$$

Equation (6.2) is the permeability model for radial flow tests for isotropic materials at constant inlet pressure (in two dimensions). The derivation of this equation has been published before, see for example Adams et al. (1988). The derivation for three-dimensional flow is explained in section 7.4.

The aim of this chapter is to propose a new approach to permeability calculation for constant inlet pressure radial flow experiments. After briefly discussing isotropic permeability the new approach will be extended to anisotropic materials (section 6.3). First formulae will be developed to model permeability for flow front measurements taken along the principal axes (section 6.4). In section 6.5 this will be extended to measurements in an arbitrary direction by introducing a third measurement axis. After that the uniqueness of the measured results will be discussed in section 6.6. Radial flow tests are commonly conducted with circular inlet. The effect of the circular inlet on the calculated permeability values will be explained in section 6.7. In section 6.8 the effect of varying the process parameters and inlet diameter will be discussed. This is followed by a comparison of published results with results obtained by the new approach using the same experimental data (section 6.9).

6.2 Isotropic permeability

The equation to calculate permeability from a constant pressure experiment has been derived in the previous section (equation (6.2)). The flow front radius r_f is measured as a function of time during the experiment while the other parameters are kept constant. Having measured the flow front radius it is then possible to plot the term in the round brackets versus time t. The gradient of the straight line is F_{iso}:

$$F_{iso} = \frac{\left(r_f^2\left[2\ln\left(r_f / r_o\right) - 1\right] + r_o^2\right)}{t} \qquad (6.4)$$

Permeability is obtained by multiplying F_{iso} with the viscosity, porosity and the pressure:

$$K = F_{iso}\frac{\mu\varepsilon}{4\,\Delta P} \qquad (6.5)$$

The viscosity, porosity and inlet pressure are assumed to be constant throughout the experiment as well as the permeability. As a consequence the gradient F_{iso} is constant for all flow front positions. In other words a straight line fitted through the individual points will go

through the origin. This will become important when experimental results are analysed later in the thesis.

6.3 Anisotropy

So far only flow in isotropic porous materials has been considered. However for many fabrics commonly used in RTM an elliptical flow front is observed. As a consequence the second order partial differential equation of the pressure distribution is no longer Laplaces equation:

$$K_1 \frac{\partial^2 P}{\partial x^2} + K_2 \frac{\partial^2 P}{\partial y^2} = 0 \qquad (6.6)$$

However it is still possible to obtain an approximate solution. This can be achieved by transforming the physical domain into a quasi-isotropic system by applying the following transformation (Adams et al. 1988, Chan and Hwang 1991):

$$\bar{x} = x \sqrt[4]{\frac{K_2}{K_1}} \quad ; \quad \bar{y} = y \sqrt[4]{\frac{K_1}{K_2}} \qquad (6.7)$$

or

$$\bar{x} = x \sqrt[4]{\alpha} \quad ; \quad \bar{y} = y \sqrt[4]{\frac{1}{\alpha}} \quad \text{with} \quad \alpha = \frac{K_2}{K_1} \qquad (6.8)$$

The quasi-isotropic permeability is defined as

$$K' = \sqrt{K_1 K_2} \qquad (6.9)$$

and the radius in the quasi-isotropic system:

$$\bar{r} = \sqrt{\bar{x}^2 + \bar{y}^2} \qquad (6.10)$$

The governing equation for the quasi-isotropic system is:

$$K' \frac{\partial^2 P}{\partial \bar{x}^2} + K' \frac{\partial^2 P}{\partial \bar{y}^2} = 0 \qquad (6.11)$$

It is important to point out that these transformations introduce errors into the solution the consequences of which will be discussed in section 6.7.

6.4 Anisotropic permeability measurement in the principal direction

6.4.1 Derivation of permeability model

In the radial flow test with constant inlet pressure the radius of the advancing flow front is measured as function of time. A closed form solution for the isotropic permeability has been derived in section 6.1. The task of determining the permeability becomes more difficult when

the fabric or mat is not isotropic. In section 6.3 the system was transformed into a quasi-isotropic system yielding an expression equivalent to equation (6.2):

$$K' = \left(\bar{r}_f^2\left[2\ln\left(\bar{r}_f/\bar{r}_o\right)-1\right]+\bar{r}_o^2\right)\frac{1}{t}\frac{\mu\varepsilon}{4\,\Delta P} \qquad (6.12)$$

where $\bar{r}$ is related to the x and y coordinates by

$$\bar{r} = \sqrt{\left(\frac{K_2}{K_1}\right)^{1/2}x^2+\left(\frac{K_1}{K_2}\right)^{1/2}y^2} \qquad (6.13)$$

The radius $\bar{r}$ has become a quite complex expression, depending on four variables (K_1, K_2, x, y). There are however two preferred orientations where (6.13) simplifies significantly - for either x or y equal to zero. This is along one of the principal axes. K_1 is obtained by evaluating equation (6.12) at y equal zero i.e. for flow front measurements taken along the 1-axis.

$$K_1 = \left(x_f^2\left[2\ln\left(x_f/x_o\right)-1\right]+x_o^2\right)\frac{1}{t}\frac{\mu\varepsilon}{4\Delta P} \qquad (6.14)$$

where x_f is the flow front radius and x_o is the inlet radius. For convenience the following constants are introduced:

$$N_I = x_f^2\left[2\ln\left(x_f/x_o\right)-1\right]+x_o^2 \qquad (6.15)$$

and

$$F_I = \frac{N_I}{t} \qquad (6.16)$$

and finally

$$C = \frac{\mu\varepsilon}{4\Delta P} \qquad (6.17)$$

The next step is to plot the flow front radii versus time t. A regression line is fitted through the data points to obtain the slope and K_1 can then be determined.

$$K_1 = F_I\,C \qquad (6.18)$$

K_2 is obtained in the same way as K_1 by setting x equal to zero.

$$K_2 = \left(y_f^2\left[2\ln\left(y_f/y_o\right)-1\right]+y_o^2\right)\frac{1}{t}\frac{\mu\varepsilon}{4\Delta P} \qquad (6.19)$$

Again the following constants are introduced:

$$N_{III} = y_f^2\left[2\ln\left(y_f/y_o\right)-1\right]+y_o^2 \qquad (6.20)$$

and

$$F_{III} = \frac{N_{III}}{t} \qquad (6.21)$$

and finally K_2 is defined:

$$K_2 = F_{III}\, C \qquad (6.22)$$

C is the same as before. In the next section the application of these equations is explains. Both equation (6.18) and equation (6.22) demonstrate again that the straight line fitted to N_I and N_{III} versus time has a constant gradient. Furthermore both lines go through the origin - hence there is no intercept.

6.4.2 Use of new formulae - example 1

Example 1 will be used to explain the use of equations (6.14) and (6.19). To be able to derive the flow front positions for this example analytically a simplified geometry was used. All flow front ellipses have the same aspect ratio (including the inlet):

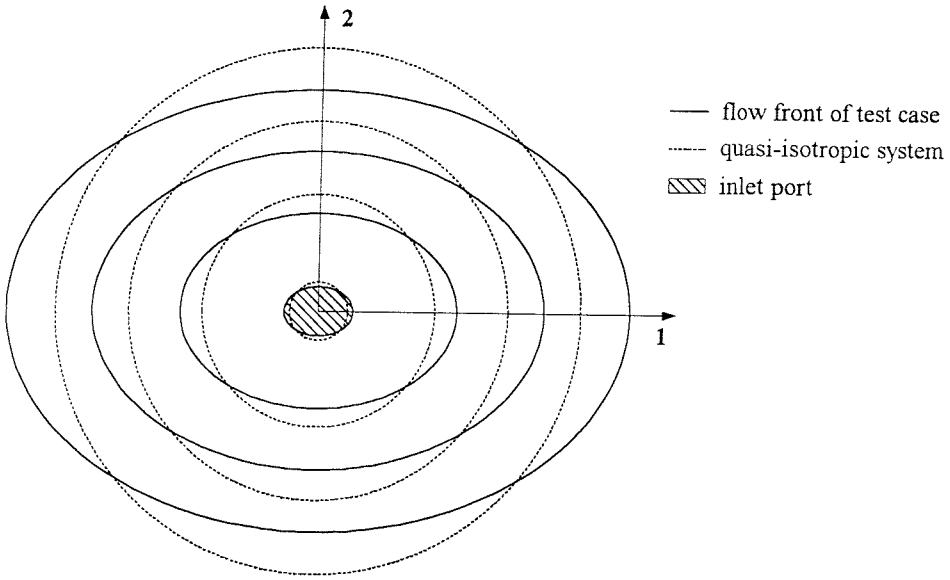

Figure 6.1 Idealised case with elliptical inlet

First the flow front position will be derived. The next step is to apply equations (6.14) and (6.19) to the derived flow front data.

Derivation of flow front position

The quasi-isotropic system and the elliptical flow front are linked by equation (6.13). If this equation is evaluated at y or x equal to zero the following expression is obtained:

$$\bar{r}^{-2} = a^2 \sqrt{\frac{K_2}{K_1}} = b^2 \sqrt{\frac{K_1}{K_2}} \qquad (6.23)$$

where a is the major axis of the flow front ellipse and b is the minor axis of the ellipse. Furthermore the fluid mass has to be conserved in the transformation:

$$\bar{r}^{2}\pi h\rho = ab\pi h\rho \qquad (6.24)$$

where $\bar{r}$ is the radius of the quasi-isotropic system, h is the height of the cavity and ρ is the density of the fluid. If $\bar{r}^{2}$ in equation (6.24) is substituted for by one of the two expression to the right in equation (6.23), then after squaring both sides the following equation is obtained:

$$\frac{b^2}{a^2} = \frac{K_2}{K_1} = \alpha \qquad (6.25)$$

where α was defined in equation (6.8). Equation (6.25) shows the relationship of permeability and elliptical flow front extent. It is possible to define the flow front ellipse in terms of the radius of the quasi-isotropic system. This is done by substituting equation (6.24) for b in equation (6.25):

$$a = \frac{\bar{r}}{\sqrt[4]{\alpha}} \qquad (6.26)$$

and if equation (6.24) is substituted for a in equation (6.25):

$$b = \bar{r}\ \sqrt[4]{\alpha} \qquad (6.27)$$

Alternatively b can be defined in terms of a given major axis of the ellipse by eliminating $\bar{r}$ in equations (6.26) and (6.27):

$$b = a\ \sqrt{\alpha} \qquad (6.28)$$

The following values were used to calculate the major and minor axis of the flow front for example 1. The pressure drop ΔP is 70kPa, the porosity ε is 0.48, the viscosity μ is 0.1 Pa s, and the principal permeabilities are K_1 = 1.0x10^{-9} m^2 and K_2 = 5.0x10^{-10} m^2. Table 6.1 shows the flow front positions which were calculated using equation (6.28). The time was obtained by solving equations (6.14), or (6.19) for time.

a^2/b^2	0.5	0.5	0.5	0.5
a or x_f [m]	0.050	0.100	0.150	0.200
b or y_f [m]	0.035	0.071	0.106	0.141
time [s]	1.01	6.37	17.43	34.93

Table 6.1 Details of example 1

The inlet radii for example 1 are as follows: a = 0.0095 and from equation (6.28) b = 0.0067.

Measuring permeability using the new approach

Figure 6.2 shows the plot of N_I and N_{III} versus time. All the values fit perfectly on a straight line. The gradient of the two lines is F_I or F_{III} respectively. Multiplying F_I and F_{III} with C yields the two principal permeabilities $K_1 = 1.0\text{x}10^{-9}$ m^2 and $K_2 = 5.0\text{x}10^{-10}$ m^2. These are the same as the permeabilities used to derive the example.

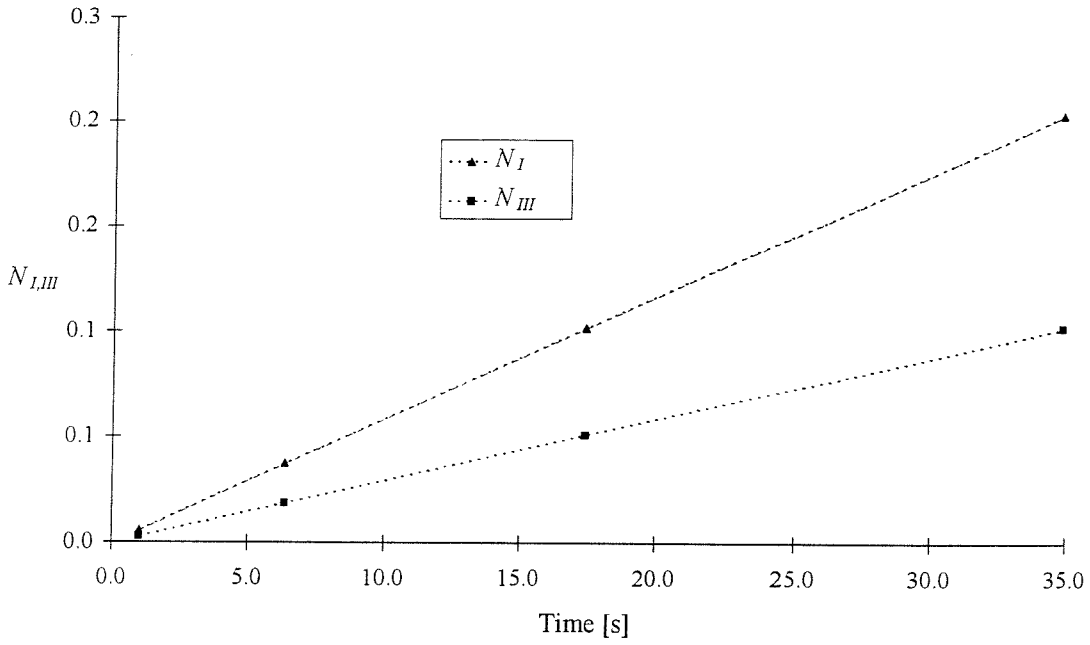

Figure 6.2 Plot of N_I and N_{III} versus time to determine F_I and F_{III} (example 1)

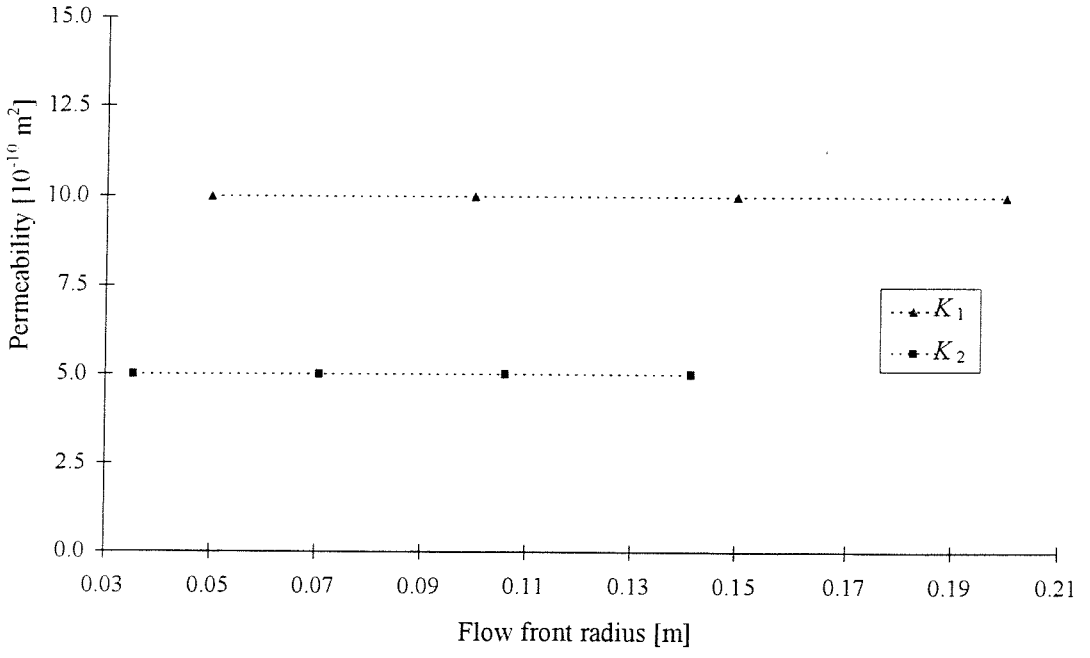

Figure 6.3 Permeability as a function of flow front position (example 1)

It is also possible to calculate F_I and F_{III} for each flow front step individually. By multiplying F_I and F_{III} with C, permeability is obtained for each flow front position as shown in Figure 6.3. All the values are the same as the initial values ($K_1 = 1.0\text{x}10^{-9}$ m^2 and $K_2 = 5.0\text{x}10^{-10}$ m^2).

6.5 Anisotropic permeability measurement in an arbitrary direction

6.5.1 Derivation of permeability model for arbitrary measurement direction

The model for principal permeability derived in the previous section is only applicable if the flow front measurements are taken along the principal axis. This is not always possible to achieve in an experiment. It is therefore desirable to come up with a model which would enable the calculation of the principal permeability regardless of the direction in which the flow front was measured. This would allow the use of a permanent experimental reference coordinate system. The problem arises out of the fact that the principal axes do not align with the reference axes (i). It seems natural to attempt a solution by rotating the coordinate system by an angle φ prior to the transformation of the domain to align it with the principal axes (ii).

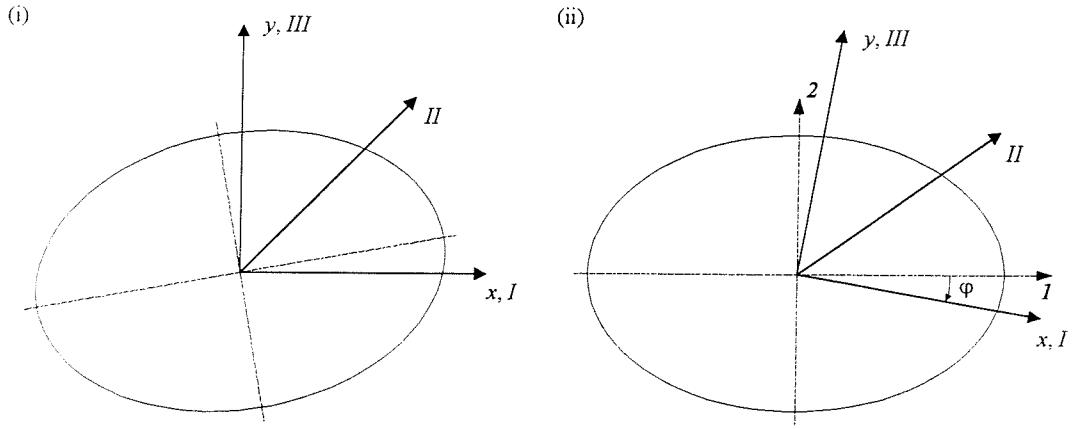

Figure 6.4 Rotation of coordinate system

The axis are rotated according to (e.g. Borg (1963)):

$$\begin{aligned} x' &= x\cos\varphi + y\sin\varphi \\ y' &= -x\sin\varphi + y\cos\varphi \end{aligned} \qquad (6.29)$$

where x', y' are the rotated coordinates and x, y the reference axis for the experiments. If the radii (r) measured along the three measurement axes are considered the expression simplifies to

$$\begin{aligned} x' &= r\cos\varphi \\ y' &= -r\sin\varphi \end{aligned} \qquad (6.30)$$

where

$$r = \sqrt{x^2 + y^2} \qquad (6.31)$$

After this rotation it is possible to transform the shape of the domain and to obtain a solution in the quasi-isotropic system as before.

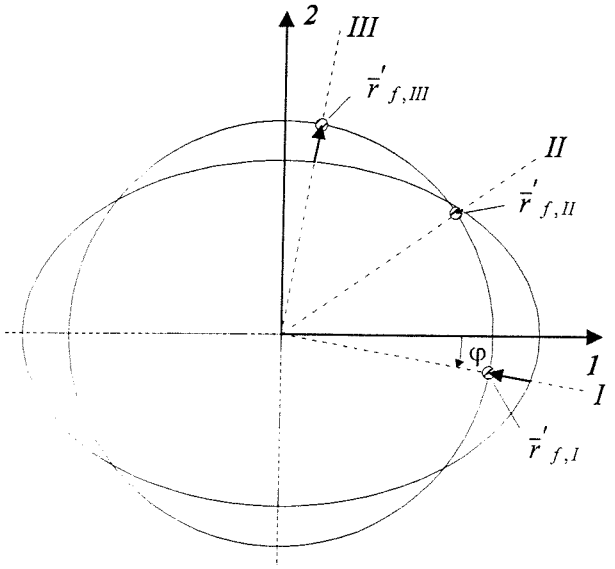

Figure 6.5 Transformation to quasi-isotropic system

For the anisotropic case the governing equation reads as follows:

$$K_{xx}\frac{\partial^2 P}{\partial x^2} + K_{xy}\frac{\partial^2 P}{\partial x \partial y} + K_{yy}\frac{\partial^2 P}{\partial y^2} = 0 \qquad (6.32)$$

Because permeability is assumed to be a symmetric tensor there is an angle for which the mixed permeability term in the above equation becomes zero. Using the tensor rotation scheme the angle of rotation was defined in section 4.2.2 (for K_{xx} not equal K_{yy}):

$$\tan 2\varphi = \frac{2K_{xy}}{\left(K_{xx} - K_{yy}\right)} \quad \text{with} \quad -\frac{\pi}{4} < \varphi < \frac{\pi}{4} \qquad (6.33)$$

The angle φ has to be limited as $\tan 2\varphi$ is defined uniquely only in an interval of ± 45°. If K_{xx} is equal to K_{yy} then φ is defined as:

$$\cos 2\varphi = 0 \qquad (6.34)$$

There are now three unknowns which need to be determined in the flow experiments (K_1, K_2 and φ) hence flow front measurements need to be taken in three directions. Using the same

transformation law as before ((6.7) and (6.9)) but with the additional rotation as defined in equation (6.29) the quasi-isotropic permeability can now be written as:

$$K' = \left(\bar{r}'^{2}_{f}\left[2\ln\left(\bar{r}'_{f}/\bar{r}'_{o}\right)-1\right]+\bar{r}'^{2}_{o}\right)\frac{1}{t}\frac{\mu\varepsilon}{4\,\Delta P} \qquad (6.35)$$

The radius $\bar{r}'$ is related to the x and y coordinates by

$$\bar{r}' = \sqrt{\bar{x}'^{2}+\bar{y}'^{2}} \qquad (6.36)$$

or

$$\bar{r}' = \sqrt{\left(\frac{K_2}{K_1}\right)^{1/2}x'^{2}+\left(\frac{K_1}{K_2}\right)^{1/2}y'^{2}} \qquad (6.37)$$

and fully expanded

$$\bar{r}' = r\sqrt{\left(\frac{K_2}{K_1}\right)^{1/2}\cos^{2}\varphi+\left(\frac{K_1}{K_2}\right)^{1/2}\sin^{2}\varphi} \qquad (6.38)$$

Equation (6.38) is evaluated for the three measurement directions. They are denoted *I*, *II* and *III*. *I* means that y equals zero, for *II* x equals y and for *III* x equals zero. Thus for direction *I* :

$$\bar{r}'_{f,I} = r_{f,I}\sqrt{\left(\frac{K_2}{K_1}\right)^{1/2}\cos^{2}\varphi+\left(\frac{K_1}{K_2}\right)^{1/2}\sin^{2}\varphi} \qquad (6.39)$$

and

$$\bar{r}'_{o,I} = r_{o,I}\sqrt{\left(\frac{K_2}{K_1}\right)^{1/2}\cos^{2}\varphi+\left(\frac{K_1}{K_2}\right)^{1/2}\sin^{2}\varphi} \qquad (6.40)$$

For direction *II* the angle of rotation is φ -45°. The term for $\sin\varphi$ and $\cos\varphi$ can be written as:

$$\cos\left(\varphi-45^{o}\right) = \frac{1}{\sqrt{2}}\left(\cos\varphi+\sin\varphi\right) \qquad (6.41)$$

$$\sin\left(\varphi-45^{o}\right) = \frac{1}{\sqrt{2}}\left(-\cos\varphi+\sin\varphi\right)$$

This yields the following expression (using $2\sin\varphi\cos\varphi = \sin 2\varphi$)

$$\bar{r}'_{f,II} = \frac{r_{f,II}}{\sqrt{2}}\sqrt{\left(\frac{K_2}{K_1}\right)^{1/2}\left(1+\sin 2\varphi\right)+\left(\frac{K_1}{K_2}\right)^{1/2}\left(1-\sin 2\varphi\right)} \qquad (6.42)$$

and

$$\bar{r}'_{o,II} = \frac{r_{o,II}}{\sqrt{2}}\sqrt{\left(\frac{K_2}{K_1}\right)^{1/2}\left(1+\sin 2\varphi\right)+\left(\frac{K_1}{K_2}\right)^{1/2}\left(1-\sin 2\varphi\right)} \qquad (6.43)$$

For direction *III* the angle of rotation is φ -90° which yields the following terms:

$$\bar{r}'_{f,III} = r_{f,III}\sqrt{\left(\frac{K_2}{K_1}\right)^{1/2}\sin^2\varphi + \left(\frac{K_1}{K_2}\right)^{1/2}\cos^2\varphi} \qquad (6.44)$$

and

$$\bar{r}'_{o,III} = r_{o,III}\sqrt{\left(\frac{K_2}{K_1}\right)^{1/2}\sin^2\varphi + \left(\frac{K_1}{K_2}\right)^{1/2}\cos^2\varphi} \qquad (6.45)$$

By evaluating (6.35) for orientations *I*, *II* and *III* and extracting the constant terms the three basic equations to determine the permeability can be set up:

$$K' = F_I\left(\left(\frac{K_2}{K_1}\right)^{1/2}\cos^2\varphi + \left(\frac{K_1}{K_2}\right)^{1/2}\sin^2\varphi\right)C \qquad (6.46)$$

$$K' = \frac{F_{II}}{2}\left(\left(\frac{K_2}{K_1}\right)^{1/2}(1+\sin 2\varphi) + \left(\frac{K_1}{K_2}\right)^{1/2}(1-\sin 2\varphi)\right)C \qquad (6.47)$$

$$K' = F_{III}\left(\left(\frac{K_2}{K_1}\right)^{1/2}\sin^2\varphi + \left(\frac{K_1}{K_2}\right)^{1/2}\cos^2\varphi\right)C \qquad (6.48)$$

where C is

$$C = \frac{\mu\varepsilon}{4\,\Delta P} \qquad (6.49)$$

F_i equals (for i = *I*, *II*, *III*)

$$F_i = \frac{N_i}{t_i} \qquad (6.50)$$

with

$$N_i = r_{f,i}^2\left[2\ln\left(r_{f,i}/r_{o,i}\right) - 1\right] + r_{o,i}^2 \qquad (6.51)$$

and

$$r_{f,i} = \sqrt{x_{f,i}^2 + y_{f,i}^2} \qquad (6.52)$$

and

$$r_{o,i} = \sqrt{x_{o,i}^2 + y_{o,i}^2} \qquad (6.53)$$

where $x_{f,i}$, $y_{f,i}$ and $x_{o,i}$ and $y_{o,i}$ are the coordinates of the flow front (f) and inlet (o) in the physical system.

Equating equations (6.46) and (6.48) and rearranging yields

$$\frac{K_2}{K_1} = \left(\frac{F_{III} \cos^2 \varphi - F_I \sin^2 \varphi}{F_I \cos^2 \varphi - F_{III} \sin^2 \varphi} \right) = B \qquad (6.54)$$

By substituting for K_1/K_2 in (6.46) and K_2/K_1 in (6.48) the principal permeabilities K_1 and K_2 can be written as a function of the angle φ:

$$K_1 = F_I \left(\cos^2 \varphi + B^{-1} \sin^2 \varphi \right) C \qquad (6.55)$$

$$K_2 = F_{III} \left(\cos^2 \varphi + B \sin^2 \varphi \right) C \qquad (6.56)$$

To make the resulting equations more compact the following terms are introduced. The average A

$$A = \frac{F_I + F_{III}}{2} \qquad (6.57)$$

and the difference D

$$D = \frac{F_I - F_{III}}{2} \qquad (6.58)$$

Rearranging (6.57) and (6.58) yields $F_I = A + D$ and $F_{III} = A - D$. Substituting for F_I and F_{III} in equation (6.54) and introducing $\cos^2\varphi - \sin^2\varphi = \cos 2\varphi$ yields

$$B = \frac{A \cos 2\varphi - D}{A \cos 2\varphi + D} \qquad (6.59)$$

Substituting equation (6.59) for B in equation (6.55) and rearranging yields:

$$K_1 = F_I \frac{(A - D)}{(A - D/\cos 2\varphi)} C \qquad (6.60)$$

while substituting equation (6.59) for B in equation (6.56) and rearranging yields

$$K_2 = F_{III} \frac{(A + D)}{(A + D/\cos 2\varphi)} C \qquad (6.61)$$

To find the angle of rotation equation (6.47) is divided by K'

$$1 = \frac{F_{II}}{2} \left\{ \frac{(1 + \sin 2\varphi)}{K_1} + \frac{(1 - \sin 2\varphi)}{K_2} \right\} C \qquad (6.62)$$

Substituting equations (6.60) and (6.61) for K_1 and K_2 in equation (6.62) and rearranging yields

$$1 = F_{II} \left\{ \frac{A - D \tan 2\varphi}{A^2 - D^2} \right\} \qquad (6.63)$$

Solving equation (6.63) for φ yields

$$\varphi = \frac{1}{2}\tan^{-1}\left(\frac{A}{D} - \frac{A^2 - D^2}{F_{II} D}\right) \qquad (6.64)$$

Equations (6.60), (6.61) and (6.64) define the permeability in two-dimensions.

6.5.2 Use of new formulae - example 2

The aim of this section is to demonstrate the use of equations (6.60), (6.61) and (6.64).

Derivation of example 2

For this example flow front measurements are made at an arbitrary angle. Therefore points on the circumference of the flow front ellipse need to be determined at an arbitrary angle. The equation of an ellipse is:

$$\frac{x^2}{a^2} + \frac{y^2}{b^2} = 1 \qquad (6.65)$$

For a point on the circumference of the ellipse the y coordinate can be expressed by

$$y = x \tan\phi \qquad (6.66)$$

Substituting equation (6.66) for y in equation (6.65) and rearranging yields

$$x = \sqrt{\frac{1}{\left(\frac{1}{a^2} + \frac{\tan^2\phi}{b^2}\right)}} \qquad (6.67)$$

Rearranging equation (6.65) yields

$$y = \frac{b}{a}\sqrt{a^2 - x^2} \qquad (6.68)$$

Equations (6.67) and (6.68) where used to calculate the coordinates of the flow front points for different angles of orientation. The same major and minor axes as used in example 1 (Table 6.1) were used. For a rotation of $\phi = 15°$ the following flow front radii were calculated:

time [s]	1.01	6.37	17.43	34.93
radius in *I*-direction	0.048	0.097	0.145	0.194
radius in *II*-direction	0.038	0.076	0.113	0.151
radius in *III*-direction	0.036	0.072	0.108	0.144

Table 6.2 Details of example 2

The inlet radii are as follows: $r_{oI} = 0.0092$, $r_{oII} = 0.0072$ and $r_{oIII} = 0.0068$.

Discussion

The equations of permeability model (equations (6.60), (6.61)and (6.64)) were applied to the test case derived above. First the F_I, F_{II} and F_{III} are calculated as the gradient of N_I, N_{II} and N_{III} plotted versus time (Figure 6.6). Next A and D are determined using equations (6.57) and (6.58). Finally K_1 and K_2 as well as φ are calculated from equations (6.60), (6.61) and (6.64). The following values were obtained: $K_1 = 1.0\text{x}10^{-9}$ m^2, $K_2 = 5.0\text{x}10^{-10}$ m^2 and $\varphi = -15°$. These are the values for which the example was derived. Again permeability can be calculated for individual flow front positions. This time one point on each axis is required to calculate (the two) principal permeability values. Figure 6.7 shows a plot of $K_{1,2}$ versus time. For an arbitrary measurement direction it is more appropriate to plot the principal permeability as a function of time rather than flow front as the principal axes are not usually aligned with the measurement axes. In chapter 11 this method will be applied to experimental data where it is important to know how permeability changes with time (if at all). Therefore Figure 6.7 will also be called convergence graph (as suggested by Ferland et al. 1996).

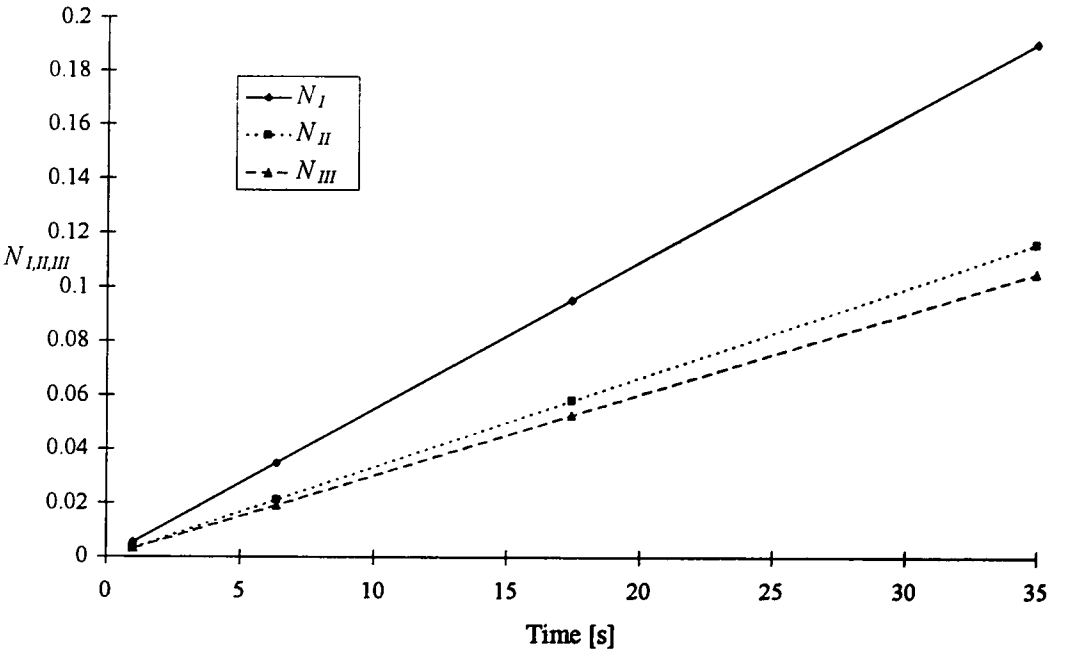

Figure 6.6 Plot of N_I, N_{II} and N_{III} versus time to determine F_I, F_{II} and F_{III}

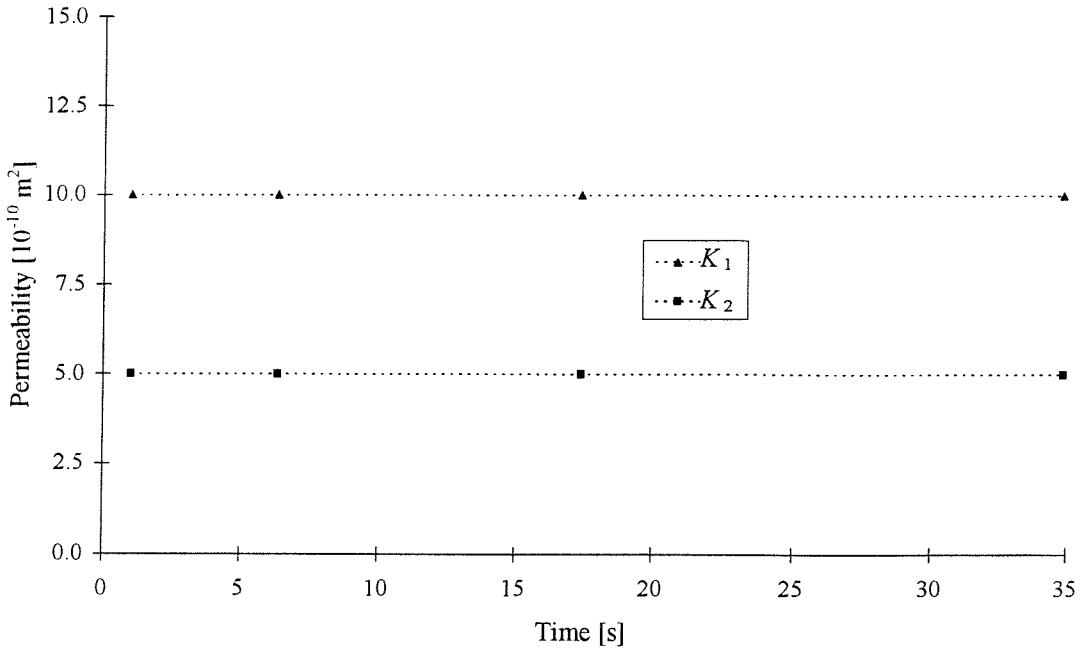

Figure 6.7 Principal permeability as function of time (convergence graph)

6.6 Uniqueness of the solution

In this section the interpretation of the calculated permeability will be discussed. A very important question is how the principal permeabilities are related to the calculated angle of orientation. For the purpose of this investigation the equation for the principal permeability ((6.60)) was divided into three distinct terms:

$$K_1 = F_I \underbrace{\frac{(A-D)}{(A-D/\cos 2\varphi)}} C \qquad (6.69)$$

Permeability value — Material term — Rotation term — Process term

The *process term* contains all the process parameters which can be set independently of the material tested (viscosity, porosity, pressure). The *material term* is specific for the mat or fabric used and its lay-up sequence as it contains the information about the flow front shape and its time dependence. And finally the *rotation term*, which is non-dimensional and is equal to unity if the measurements are taken in the direction of the principal axis. The rotation term multiplied with the material term fully characterises the permeability of a reinforcement material. The equation for K_2 ((6.61)) can be characterized in the same way.

As mentioned in section 6.5.1 the results are only unique in an interval of ± 45° between the measurement direction and the principal axes. First the behaviour in the interval of ± 45° will

be investigated. The next step is to rotate the measurement direction beyond the ± 45° limit. The examples to illustrate the following discussion were all based on example 1. The measurement coordinate system (*I,II,III*) was rotated by an measurement angle ϕ. (ϕ = 0 means that the coordinate system is aligned with the principal axes). The flow front positions were then determined as outlined in example 2 for ϕ, $\phi + 45°$ and $\phi + 90°$ to obtain $r_{f,I}$, $r_{f,II}$ and $r_{f,III}$. The inlet radii were obtained in the same way.

6.6.1 Uniqueness of solution for angles of orientation of less than ± 45°

Figure 6.8 shows the variation of F_I, F_{II} and F_{III} with the measurement angle. Figure 6.9 is a plot of the rotation terms for K_1 and K_2. Figure 6.10 shows the product of the rotation terms and F_I and F_{III} which is independent of the measurement angle. To obtain the principal permeabilities the results in Figure 6.10 need to be multiplied with the process term C which in this example is 1.714×10^{-7} ($K_1 = 1.0 \times 10^{-9}$ m^2, $K_2 = 5.0 \times 10^{-10}$ m^2).

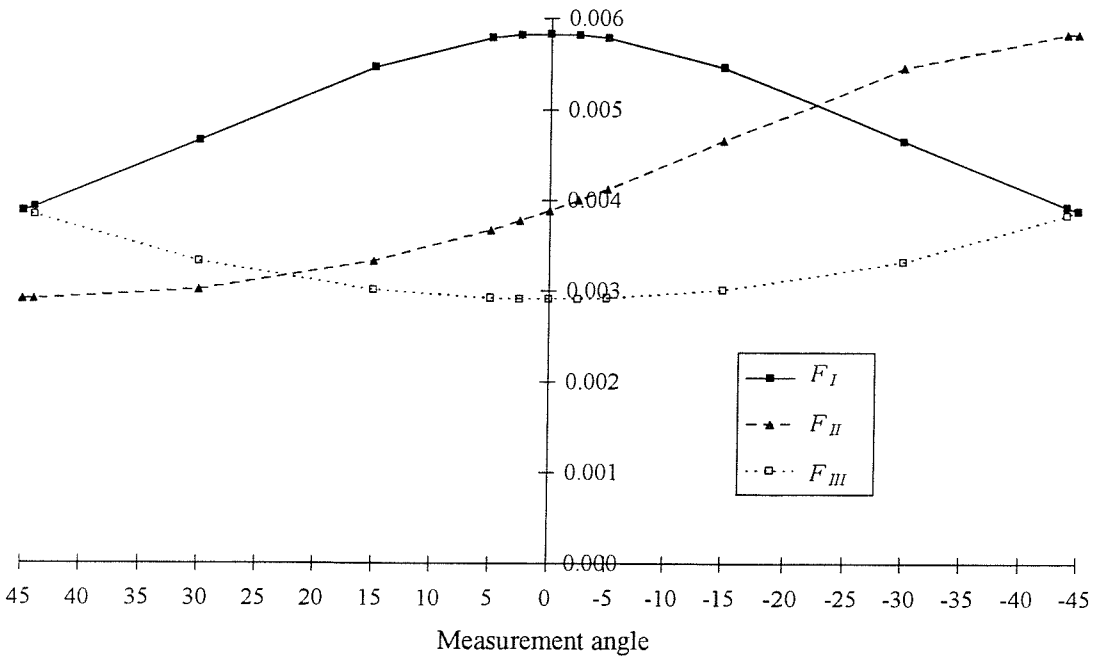

Figure 6.8 Variation of F_I, F_{II} and F_{III} for different measurement angles

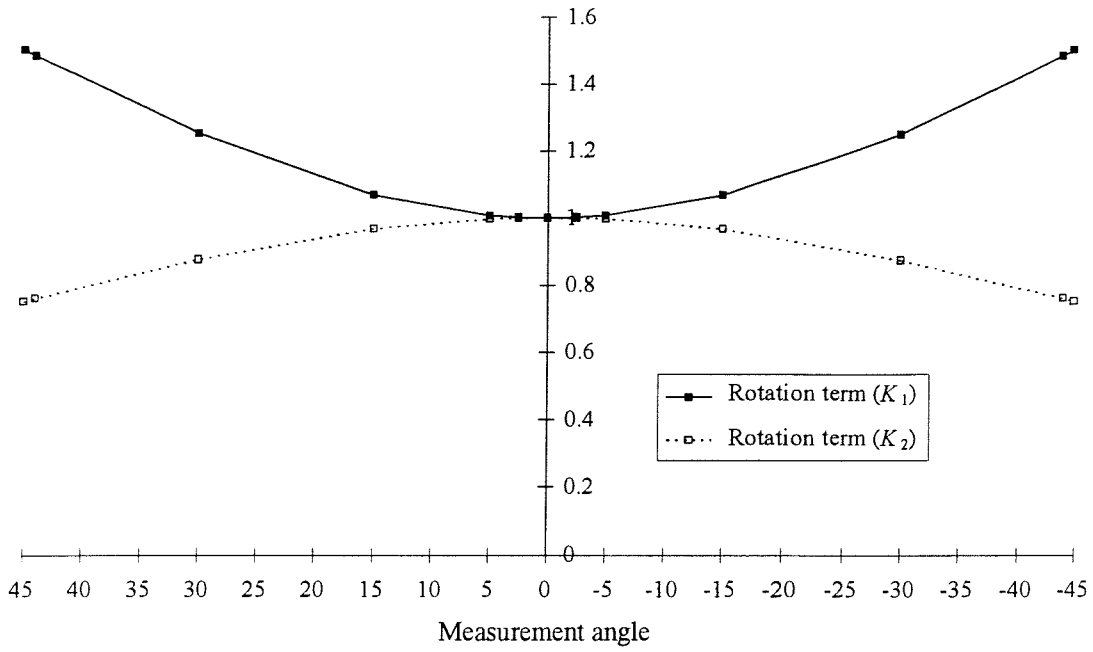

Figure 6.9 Variation of rotation terms

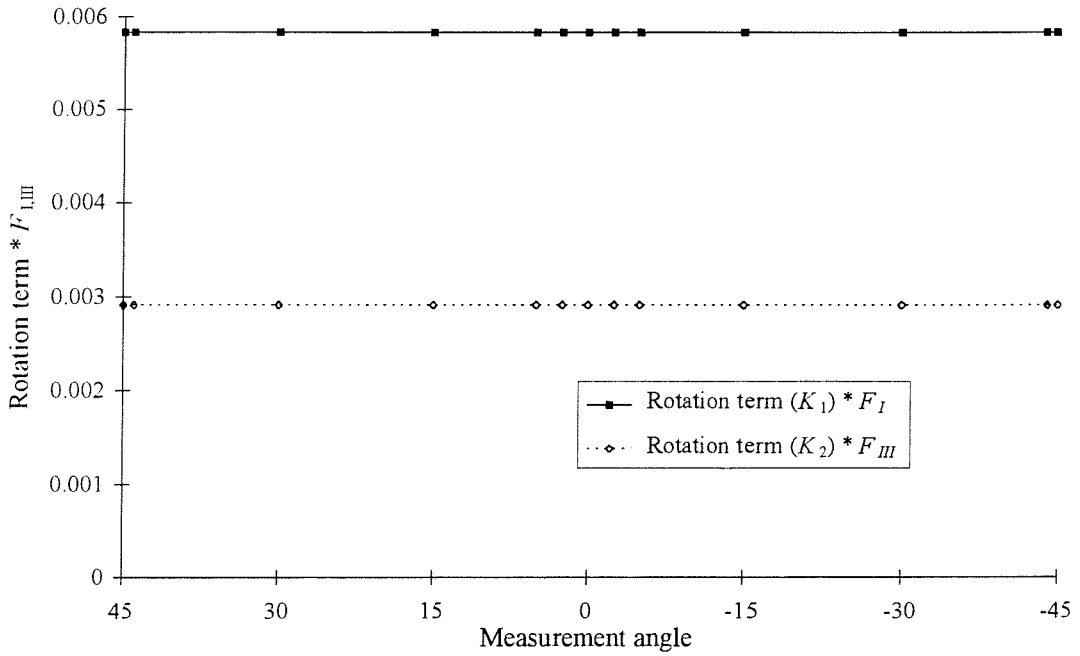

Figure 6.10 Product of rotation terms and F_I and F_{III}

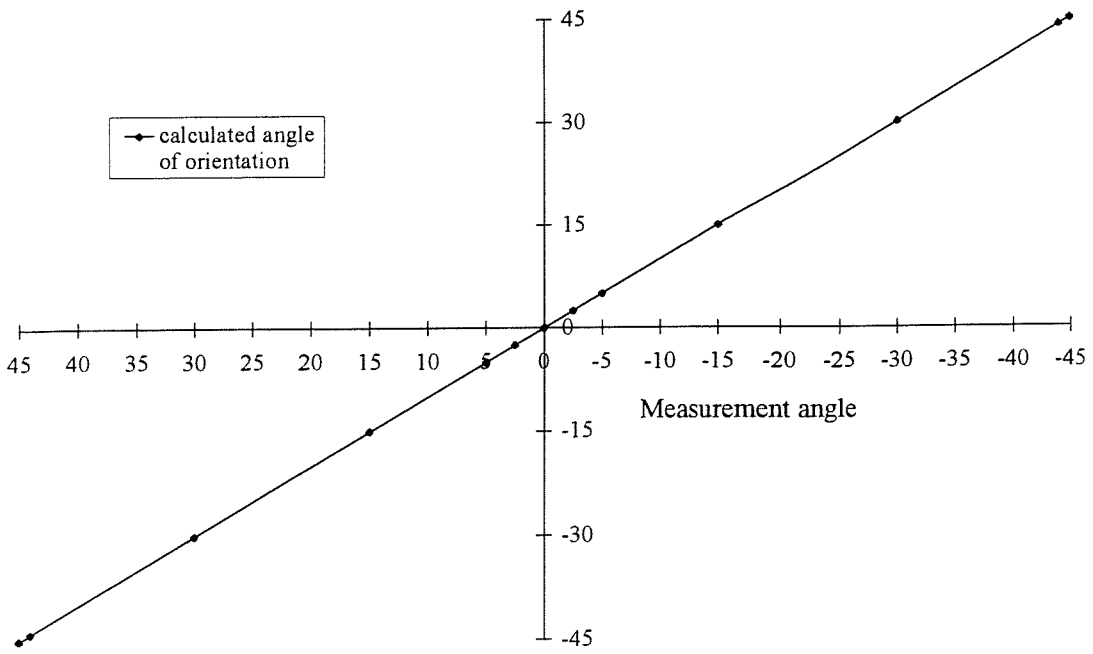

Figure 6.11 Calculated angle of orientation

Figure 6.11 is a plot of the calculated angle of orientation (equation (6.64)) as a function of the measurement angle. This calculated angle is the angle by which the measurement coordinate system has to be rotated to align it with the principal axes. The measurement angle was measured as a rotation away from the principal axes. As it can be seen from Figure 6.11 the calculated angle of orientation reverses this rotation, hence the method predicts the orientation of the principal axes accurately. Furthermore there is a unique solution for each measurement direction. In section 6.6.2 it will be investigated what happens if the measurement coordinate system is rotated by more than ±45°.

6.6.2 Uniqueness of solution for arbitrary measurement directions

In this section the measurement coordinate system is rotated by ± 180°. Figure 6.12 shows a periodic variation of F_I, F_{II} and F_{III} with the measurement angle. The graph shows that at ±90° F_I takes on the same value as F_{III} at 0° and F_{III} becomes F_I (at 0°). At ±180° F_I and F_{III} return to their original values (at 0°).

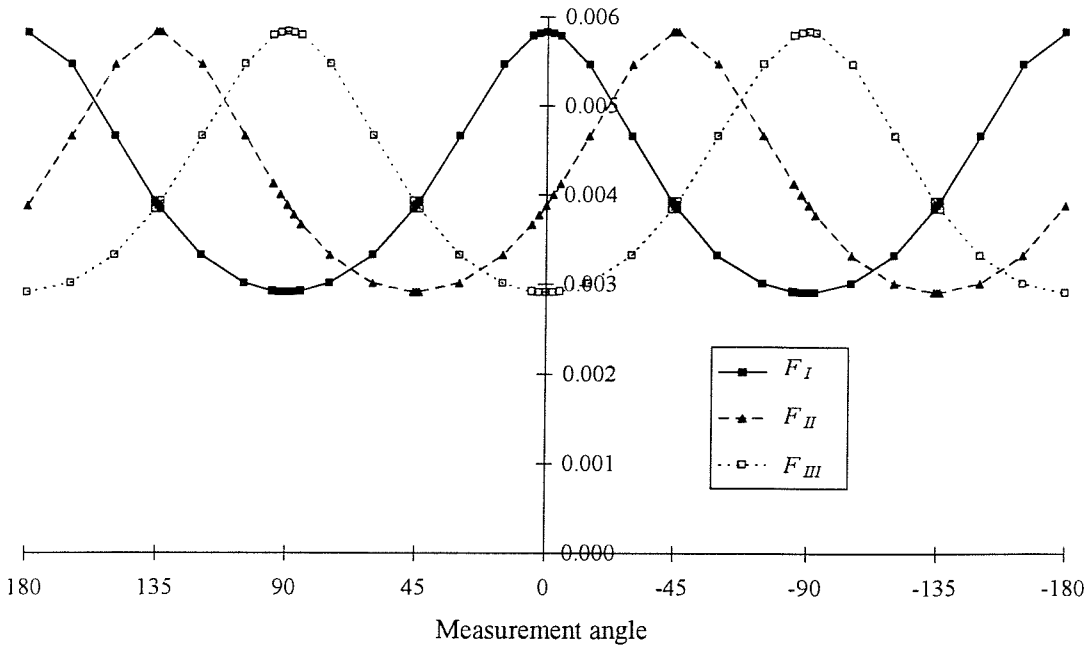

Figure 6.12 Variation of F_I, F_{II} and F_{III} with measurement angle

Figure 6.13 is a plot of the rotation term. It illustrates clearly why in the derivation of the rotation term ((6.33)) a limit of ±45° had been specified. At ±45° (and at ±135°) the value of the rotation term suddenly changes. This is reflected in the calculated angle of orientation in Figure 6.14.

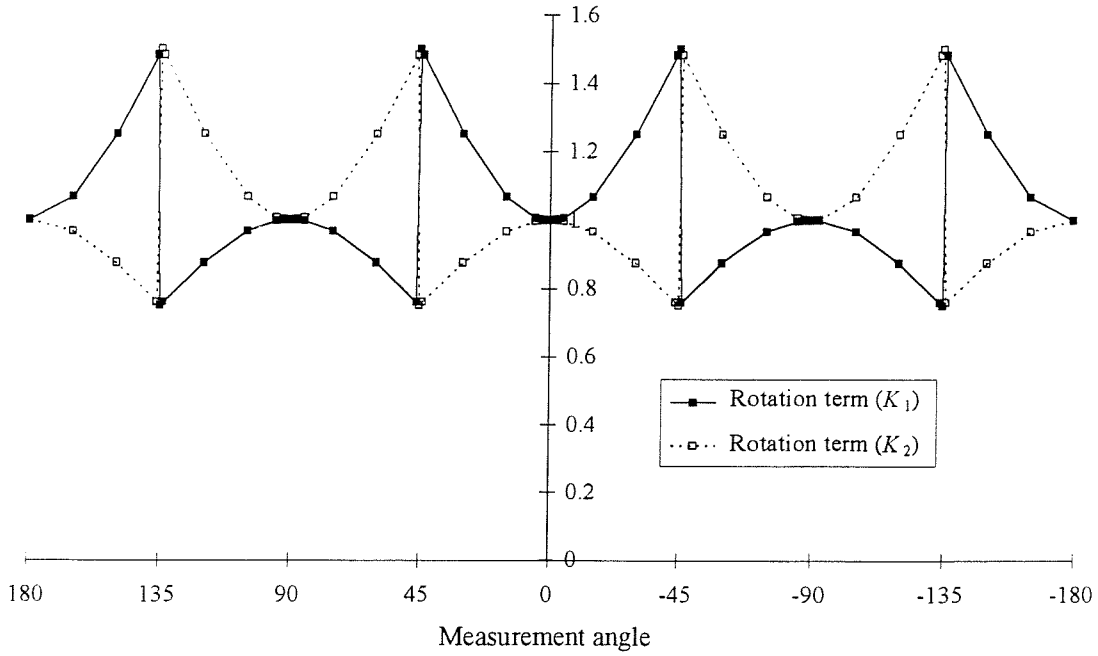

Figure 6.13 Variation of rotation term with measurement angle

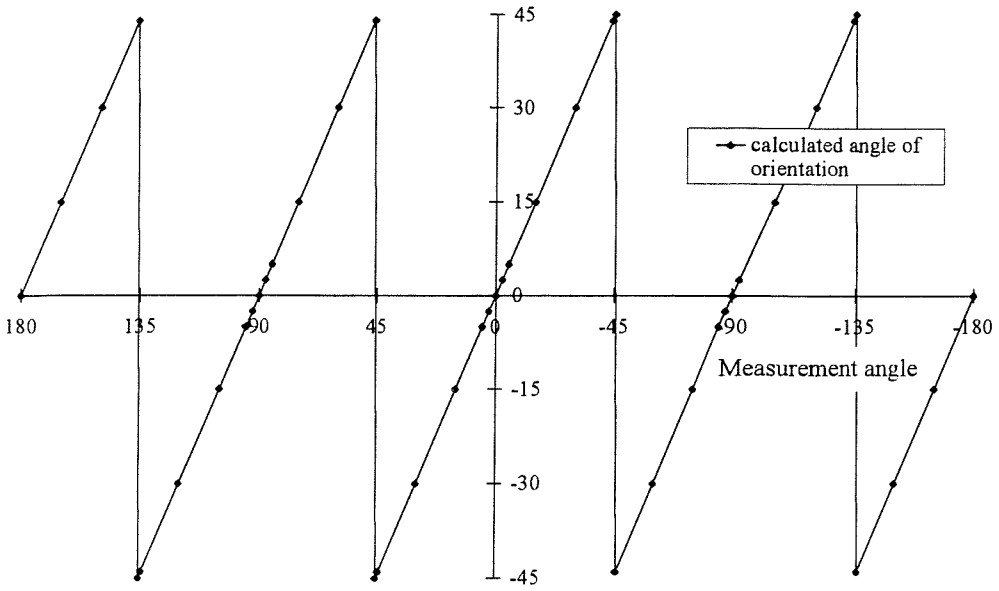

Figure 6.14 Calculated angle of orientation of principal axes

Figure 6.15 is a plot of the product of the rotation terms and F_I and F_{III} (which if multiplied with C is equal to the principal permeability) versus the measurement angle. It shows that where the step changes of the angle of orientation occurred (Figure 6.14) the principal permeability values change as well. There are four intervals (-135° to -45°, ±45°, +45° to +135°, 135° to -135°) where the permeability values are constant. In addition in each of those four intervals the calculated orientation of the principal axes is unique (see Figure 6.14).

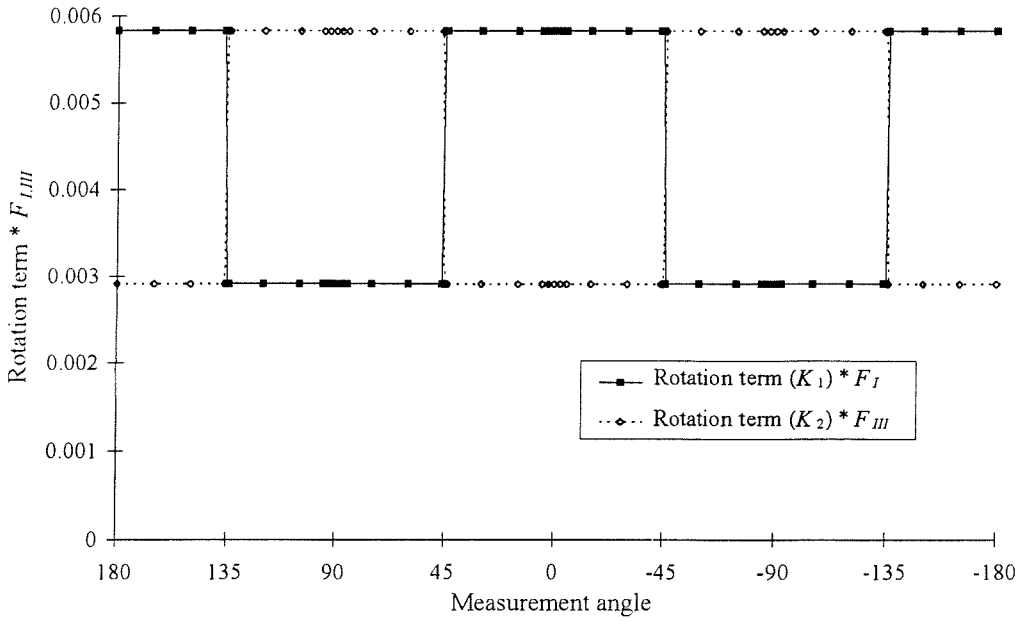

Figure 6.15 Product of rotation term and F_I and F_{III} for different measurement angles

6.6.3 Interpretation of results - example 3

To illustrate the periodic changes of permeability, principal permeability is calculated for two measurement angles: $\phi = 15°$ and 75°. The first case is the same as example 2 in section 6.5.2 ($K_1 = 1.0\text{x}10^{-9}$ m^2, $K_2 = 5.0\text{x}10^{-10}$ m^2 and $\varphi = -15°$). For a rotation by 75° the following values were obtained (in the same way as example 2): $K_1 = 5.0\text{x}10^{-10}$ m^2, $K_2 = 1.0\text{x}10^{-9}$ m^2 and $\varphi = 15°$. As expected the two different measurement orientations yield different values for K_1 and K_2 and φ.

To determine how the permeability values are related to the angle of orientation a further step is required. It will be shown in section 8.2 that the effective permeability which is measured along each axis in the radial flow test can be expressed in terms of the principal permeability:

$$K_{eff} = \frac{K_1 K_2}{K_1 \sin^2 \zeta + K_2 \cos^2 \zeta} \qquad (6.70)$$

The effective permeability measured along an axis "i" in radial flow is $K_{eff,i} = F_i * C$ with $i = I.II.III$. Using the calculated principal permeability values effective permeabilities can be calculated for five different angles of ζ: along the principal axes (0° and 90°) and along the experimental axes ($-\varphi$, $-\varphi$+45° and $-\varphi$+90°). Table 6.3 and Table 6.4 list the effective permeabilities for examples 2 and 3.

angle of rotation	0° (K_1)	15° (K_I)	60° (K_{II})	90° (K_2)	105° (K_{III})
K_{eff}	$1.0\text{x}10^{-9}$	$9.37\text{x}10^{-10}$	$5.71\text{x}10^{-10}$	$5.0\text{x}10^{-10}$	$5.17\text{x}10^{-10}$

Table 6.3 Effective permeabilities for example 2

angle of rotation	-15° (K_I)	0° (K_1)	30° (K_{II})	75°(K_{III})	90° (K_2)
K_{eff}	$5.17\text{x}10^{-10}$	$5.0\text{x}10^{-10}$	$5.71\text{x}10^{-10}$	$9.37\text{x}10^{-10}$	$1.0\text{x}10^{-9}$

Table 6.4 Effective permeabilities for example 3

The results in Table 6.3 are visualised in Figure 6.16. K_I is larger than K_{III}. Furthermore K_1 is larger than K_2. Hence a rotation by 15° will the align the x-axis with the (principal) **1**-axis. In example 3 (Table 6.4) K_{III} is larger than K_I and K_2 is larger than K_1. As shown in Figure 6.17 the calculated angle of rotation is also measured between the x-axis and the **1**-axis. The usual convention is that K_1 is larger than K_2. To achieve this the K_1 has to be renamed K_2 and K_2 becomes K_1 . With this new orientation the angle of rotation is now measured between the **2**-axis and the x-axis (see Figure 6.18).

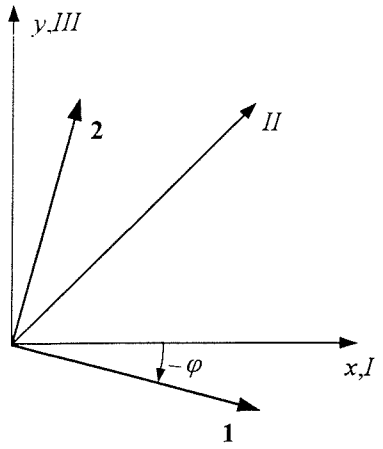

Figure 6.16 Example 2

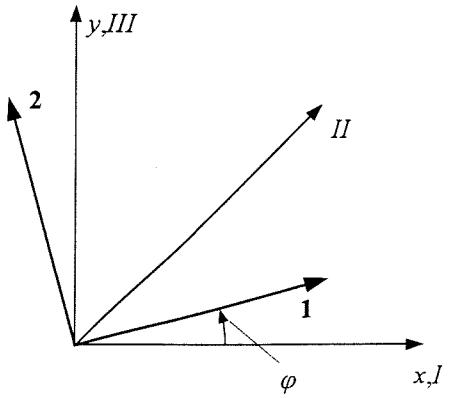

Figure 6.17 Example 3

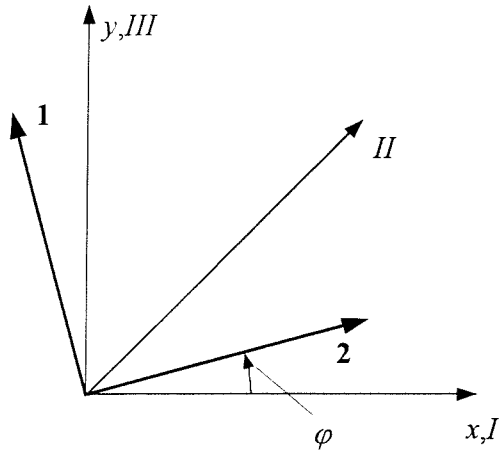

Figure 6.18 Example 3 - modified coordinate system

In summary it can be said that if the principal permeability K_1 is larger than K_2 then φ is measured between the **1**-axis and the x-axis. If on the other hand K_1 is smaller than K_2 then K_1 needs to be renamed K_2, while K_2 becomes K_1. The angle φ is measured between the x-axis and the (new) **2**-axis.

6.7 Circular inlet

The scaling process to obtain a solution for anisotropic materials required an elliptical inlet in the physical domain (section 6.3). This boundary condition is violated in practical experiments where circular inlets are commonly used. The first step is to see whether variations or errors in the inlet diameter are important. Then a modification of the inlet shape is suggested for flow front measurements taken in the principal direction. This is followed by a discussion of effects

of the inlet modification and finally the concept is extended to arbitrary measurement directions.

6.7.1 Influence of inlet diameter

To investigate the influence of the inlet diameter, the nominator N of the material term F_i was more closely inspected as it is the only term of the permeability equation which contains the inlet diameter:

$$r_f^2\left[2\ln\left(r_f/r_o\right)-1\right]+r_o^2 \qquad (6.71)$$

The following inlet radii were used in this investigation:

$$r_1 = r_o\sqrt{\frac{K_1}{K_2}} \;;\quad r_o \;;\quad r_3 = r_o\sqrt{\frac{K_2}{K_1}} \qquad (6.72)$$

To demonstrate the influence of anisotropy N was plotted for three degrees of anisotropy (K_2/K_1 = α = 3/4; 1/2; 1/10) and r_o = 8mm. The results are shown in Figure 6.19. A significant variation of N for the different inlet radii can be observed.

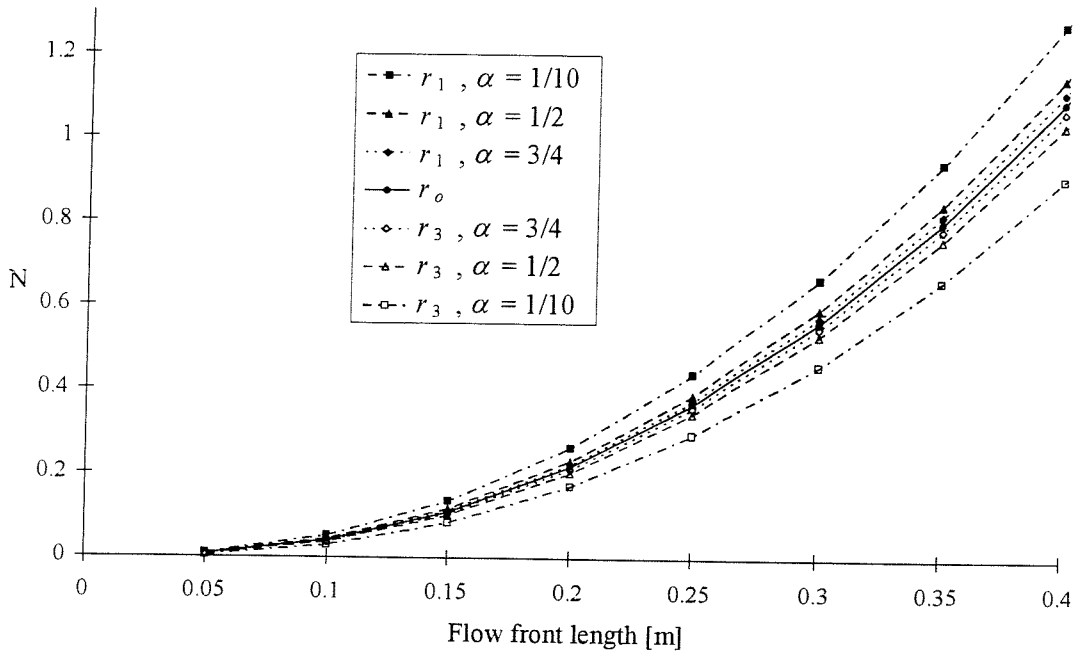

Figure 6.19 Nominator N versus flow front length

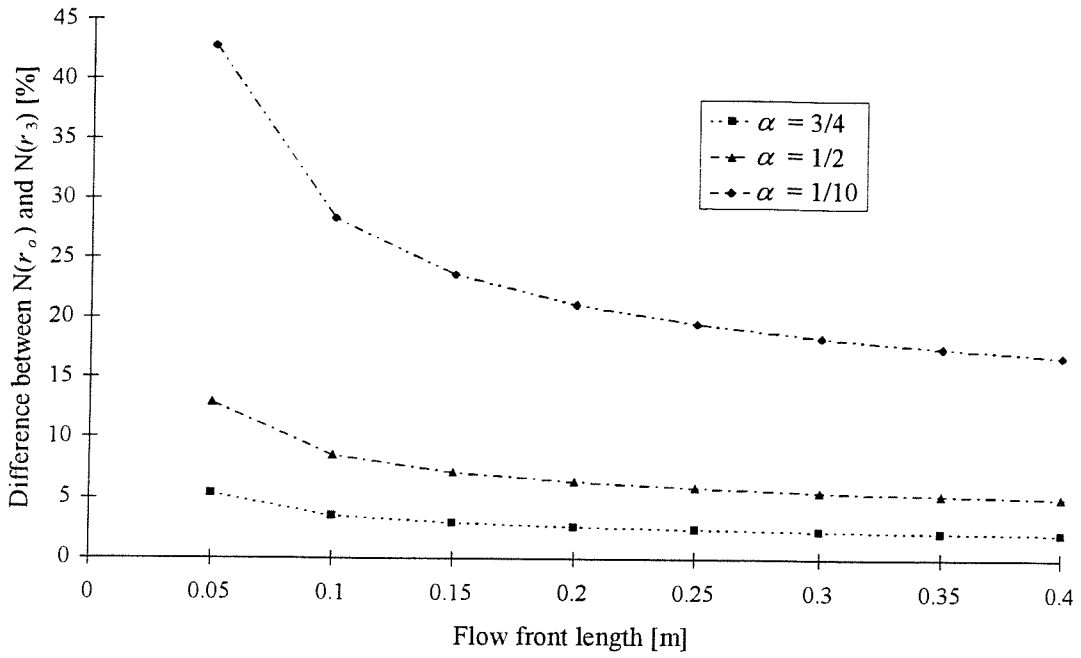

Figure 6.20 Relative difference between N(r_0) and N(r_3)

For Figure 6.20 the same results as in Figure 6.19 were used (but only the lower half because of the symmetry of Figure 6.19). This time the relative differences between the original radius r_o and the scaled radius r_3 are shown. Figure 6.20 clearly shows that the largest differences in the results of equation (6.71) are found close to the inlet. Further away these differences are less significant.

6.7.2 Modification of inlet shape

The investigation in the previous section demonstrated the significance of the inlet radius. In scaling operation to convert the flow front to the quasi-isotropic system the circular inlet is shortened in the x-direction while in the y-direction it is stretched (Figure 6.21). This produces an elliptical inlet in the quasi-isotropic system rather then the required circular inlet. As a result the inlet is too short in the x-direction resulting in higher permeability values while in the y-direction the inlet is too long resulting in an underestimation of permeability.

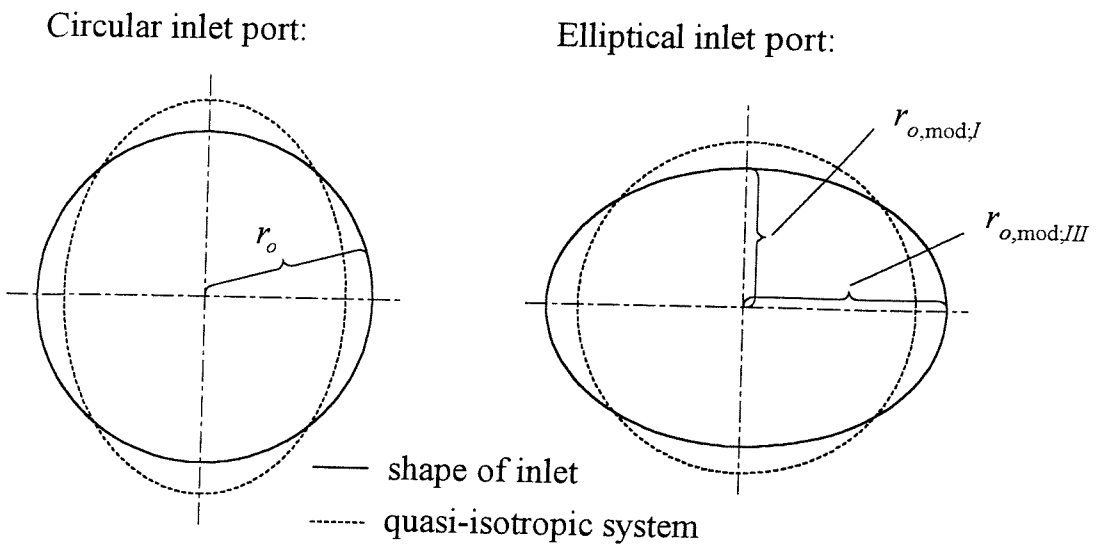

Figure 6.21 Transformation of inlet port shape

To achieve a circular inlet in the quasi-isotropic system the physical inlet diameter has to be stretched in the x-direction prior to the scaling operation by the inverse of the scaling factor:

$$r_{o,\mathrm{mod};I} = r_0 \sqrt[4]{\frac{1}{\alpha}} \qquad (6.73)$$

The diameter in the y-direction is shortened by the inverse of the scaling factor:

$$r_{o,\mathrm{mod};III} = r_0 \sqrt[4]{\alpha} \qquad (6.74)$$

As shown in Figure 6.21 this produces the desired elliptical inlet in the quasi-isotropic system.

To calculate permeability it is now necessary to measure α independently to be able to calculate permeability. This is usually done by plotting flow front measured in y-direction versus flow front measured in x-direction. The square of the gradient of the best fit line is α. It is not always possible however to measure the flow front in x and y-direction at the same instance in time, which is necessary to plot the flow front measurements. Therefore an alternative approach is to use equation (6.8) which defined α as the ratio of the two principal permeabilities. From equations (6.60) and (6.61) α can be written as a function of the measured flow front:

$$\alpha = \frac{F_{III}}{F_I} \qquad (6.75)$$

The correct value for α is found by an iterative approach. Firstly F_I and F_{III} are calculated using the modified inlet radii ((6.73), (6.74)) with α set to 1. The guessed value for α is then reduced until it matches the value for α as calculated by (6.75).

6.7.3 Flow front measurements along the principal axes - example 4

For the case when the inlet is circular it is not possible to derive the progression of the flow front analytically. Therefore a flow simulation program was written to determine the flow front position as a function of time. It is a two-dimensional flow finite difference program which uses the flow analysis network and fill factors to trace the position of the flow front (Tadmor, Broyer and Gutfinger 1974 and Young et al. 1991). The resulting system of linear equations was solved using the SOR method (Kincaid et al. 1982). It was initially intended to be a general purpose flow program hence the square mesh used is not ideally suited for modelling the flow in a radial flow mould. In particular the inlet presented problems. Furthermore some of the boundary conditions used in the program were only first order accurate. Figure 6.22 compares the numerical solution with the analytical solution for isotropic flow.

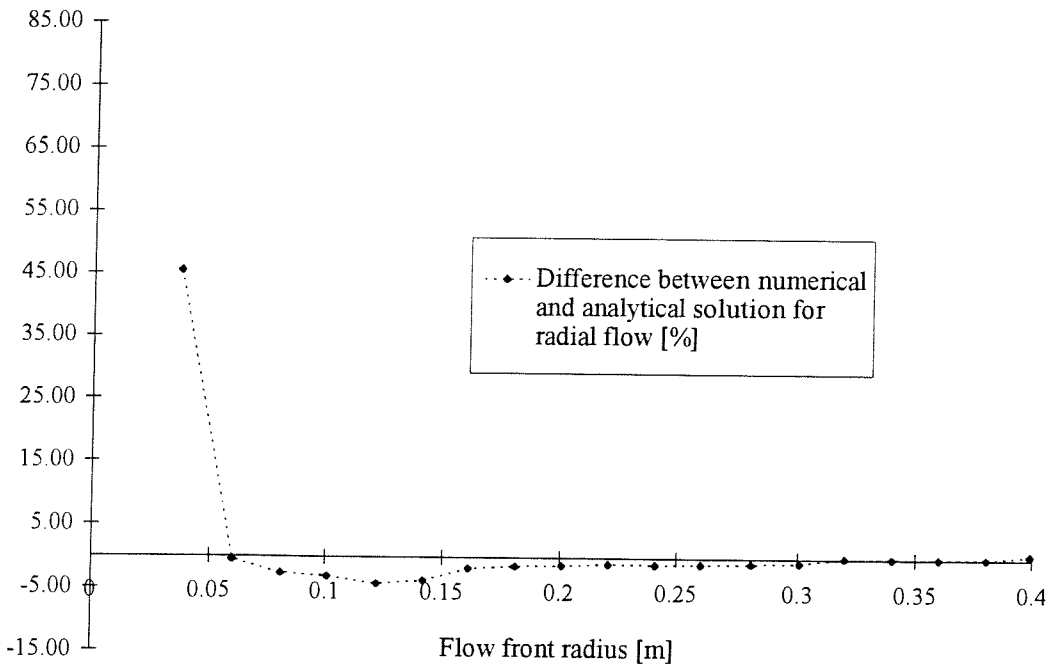

Figure 6.22 Comparison of analytical and numerical solution (r_o = 28mm)

In Figure 6.22 the initial radius is 28mm. Close to the inlet the agreement is not very good. It soon however becomes quite close and towards the end the time predicted by the flow simulation is slightly too short in comparison with the analytical solution. For the large inlet radius in Figure 6.22 the flow front prediction was considered to be acceptable after about one inlet radius away from the inlet (difference is less than 5%). For smaller inlet radii this distance was slightly larger. For example for r_o = 8mm the predictions were acceptable for flow front positions larger than 40mm. Generally speaking the program is not very accurate.

However as the results are used to compare different options this is acceptable since only relative differences are of interest.

The results of the various runs are listed in Appendix B. The results from the flow simulation are used to investigate the effect of the circular inlet on the calculated permeability . For the following example run 2 was used (With the following details: $K_1 = 4.0\text{x}10^{-9}$ m^2, $K_2 = 2.0\text{x}10^{-9}$ m^2, $r_o = 8$mm, $P_o = 70$ kPa, $\varepsilon = 0.48$, $\mu = 0.1$ Pa s).

Figure 6.23 shows the plot of y_f/x_f as a function of the flow front position. It can be seen that the flow front ratio very quickly approaches the square root of the degree of anisotropy (here = 0.707) and remains constant at this value. This means the flow front has become independent of the inlet shape. It behaves like the idealised problem with elliptical inlet. It is therefore permissible to modify the shape of the inlet as suggested in the previous section.

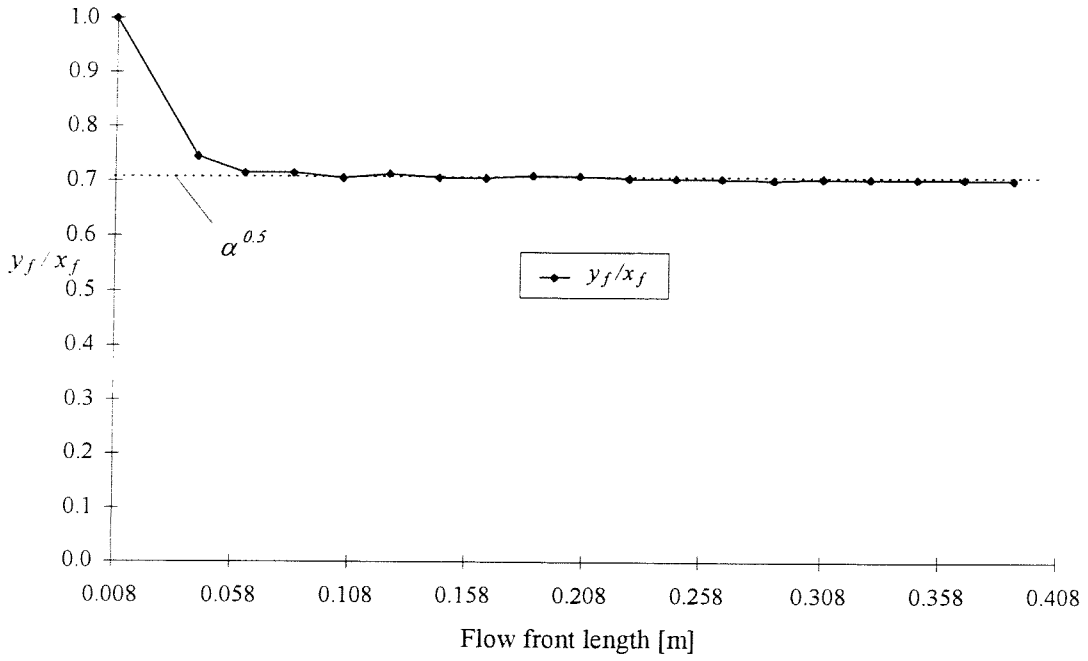

Figure 6.23 Ratio of y_f versus x_f

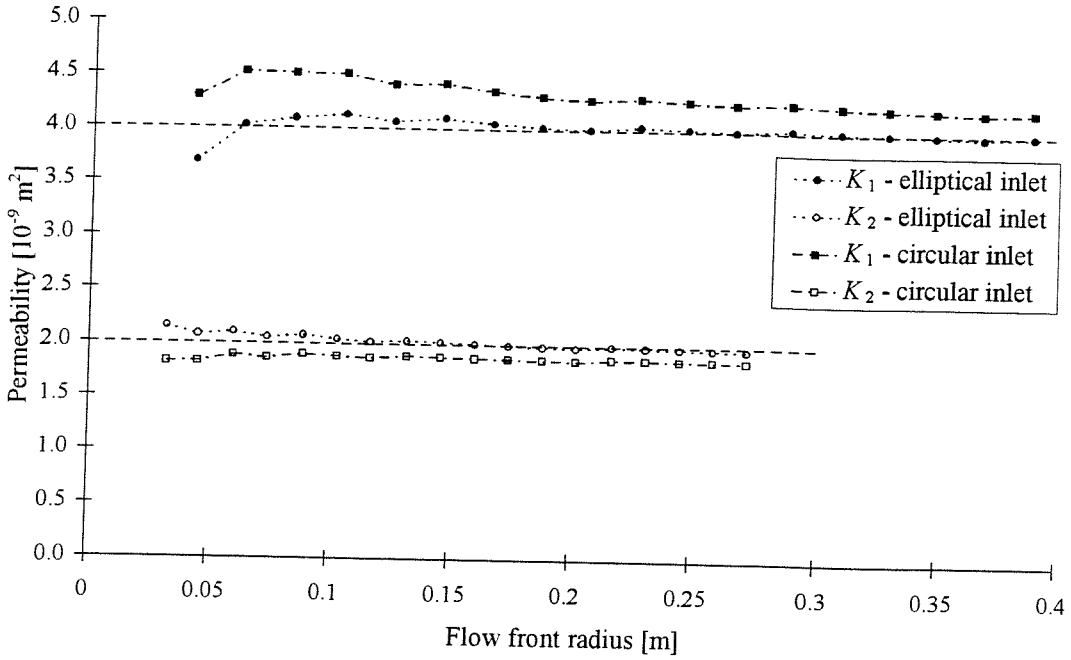

Figure 6.24 Permeability calculated with circular and elliptical inlet (run 2)

Figure 6.24 shows permeability calculated with the circular inlet and the modified elliptical inlet. Both were calculated in the same way as outlined in section 6.4.2. For the elliptical inlet, equation (6.73) was used instead of r_o to determine K_1 and equation (6.74) to find K_2. Initially α is set to 1 for equations (6.73) and (6.74). Next the ratio of F_{III} and F_I is calculated using (6.75). For a circular inlet (α = 1) the value for K_1 is larger than the real value and K_2 is smaller than the real value (see Figure 6.24) hence α is underestimated. Using an iterative procedure (e.g. the *Solver* in Microsoft Excel) the guessed value for α is reduced until it matches the value for α as calculated by (6.75).

The permeability values are different for the two inlet conditions. The results with circular inlet "bracket" the elliptical results. K_1 is larger for the circular inlet while K_2 with the circular inlet is too small. The results with the elliptical inlet agree very well with the permeability values for which the flow front positions were computed. These results confirm the observation that the correct choice of inlet diameter is crucial. They also show that in order to obtain a mathematically correct solution the physical inlet boundary needs to be modified. This is, as Figure 6.23 has shown, acceptable since the flow front becomes independent of inlet shape.

6.7.4 What are the effects of scaling the inlet?

In the previous section it was confirmed that the inlet needs to be modified to calculate permeability accurately. This assures that for flow front measurements further away from the inlet the results become more accurate. But what happens close to the inlet? Figure 6.25 is a schematic diagram to illustrate the transient behaviour of the flow front due to the circular inlet. As shown in Figure 6.23 the initially circular flow front very quickly becomes elliptical. The aspect ratio of this flow front is determined by the degree of anisotropy of the material. Figure 6.25 compares the real mould geometry (circular inlet) with the idealised case which is used to calculate permeability for fully developed flow.

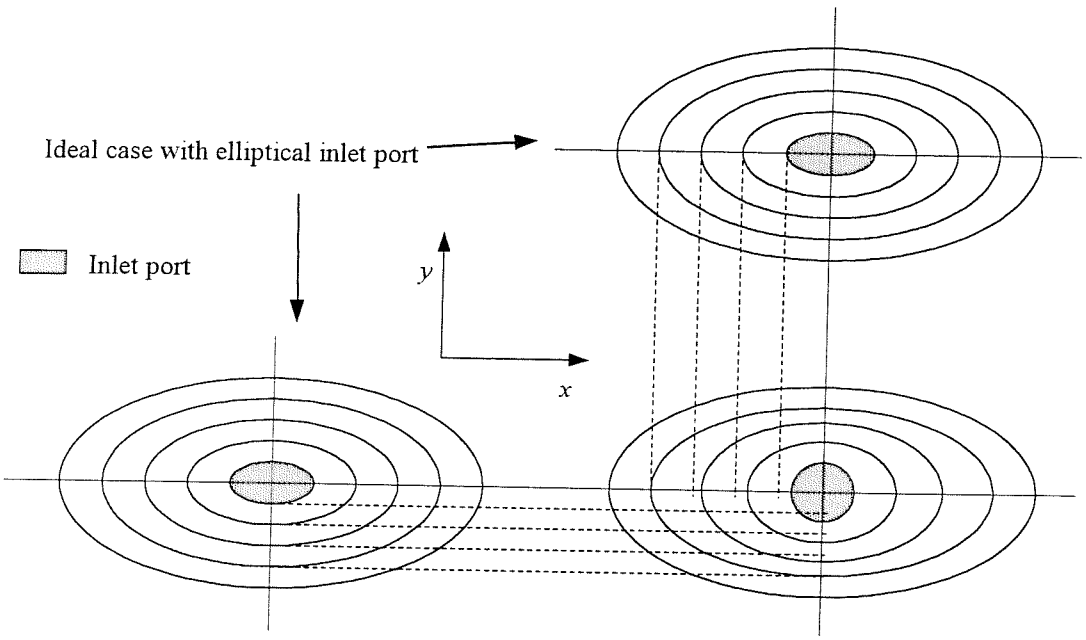

Figure 6.25 Influence of circular inlet port on flow front shape

Initially the flow front in the x-direction is too short in comparison with the ideal flow case while in the y-direction it is too long (see Figure 6.25). This can be illustrated with an example. Using the same input data as for run 2 of the computer simulation (see Appendix B) the equivalent idealised problem (with elliptical inlet port) can be calculated in the same way as for example 1 (see section 6.4.2). The circular inlet of run 2 is converted to the elliptical port using equations (6.73) and (6.74) (a = 0.0095 m, b = 0.0067 m). The results are listed in Table 6.5.

x_f [m]	0.050	0.100	0.150	0.200
y_f [m]	0.035	0.071	0.106	0.141
time [s]	0.25	1.59	4.36	8.73

Table 6.5 Flow front for anisotropic flow (elliptical inlet)

To estimate the initial flow front it was assumed that initially the flow behaves like flow in an isotropic material which quickly develops into fully anisotropic flow with an elliptical flow front shape (see Figure 6.25). The isotropic permeabilities were taken to be the principal permeabilities K_1 and K_2 of the anisotropic material. Table 6.6 lists the flow front steps of the two isotropic systems (in x and y-direction) using the same time steps as in Table 6.5.

$x_{\text{isotropic}}$ [m]	0.048	0.097	0.145	0.195
$y_{\text{isotropic}}$ [m]	0.037	0.073	0.110	0.146
time [s]	0.25	1.59	4.36	8.73

Table 6.6 Flow front for isotropic flow in x and y-direction (using same the time steps as in Table 6.5)

Table 6.7 shows the results for the flow time of the two isotropic systems using the same flow front steps as in Table 6.5.

x_f [m]	0.050	0.100	0.150	0.200
$t_{x,\text{isotropic}}$ [s]	0.29	1.74	4.69	9.32
y_f [m]	0.035	0.071	0.106	0.141
$t_{y,\text{isotropic}}$ [s]	0.22	1.44	4.03	8.14

Table 6.7 Flow time for isotropic flow in x and y-direction (using the same flow front steps as in Table 6.5)

Firstly it is interesting to note the way anisotropy changes the flow behaviour. Comparing Table 6.5 with Table 6.6 reveals that for the same time steps the flow front in x-direction of the isotropic system is lagging behind the anisotropic flow front even though both permeabilities are the same. The opposite is observed for flow in the y-direction where the isotropic flow front is leading the anisotropic flow front (again both having identical permeability values). This can be explained as follows. In the anisotropic case K_2 is smaller

than K_1. Therefore the preferred flow direction is the x-direction which explains the lead over the isotropic flow front in the x-direction. Because most of the fluid is flowing into the x-direction the flow front is slowed down in the y-direction - for this reason is the isotropic flow front leading the anisotropic flow front in the y-direction.

In Figure 6.26 N_I and N_{III} are plotted versus time. It shows that despite the different flow front lengths $K_{(x)}$, the isotropic permeability in x-direction and $K_{(y)}$, the isotropic permeability in y-direction, yield the same gradient and hence permeability value as K_1 and K_2 (as expected). If on the other hand anisotropic permeability is calculated using the isotropic flow front steps ($x_{\text{isotropic}}$) or flow times ($t_{x,\text{isotropic}}$) from Table 6.6 and Table 6.7 then N_I is for both cases lower than N_I obtained for $K_{(x)}$ or K_1. The opposite is true for N_{III}. N_{III} for $t_{y,\text{isotropic}}$ or $y_{\text{isotropic}}$ is larger than N_{III} for $K_{(y)}$ or K_2 .

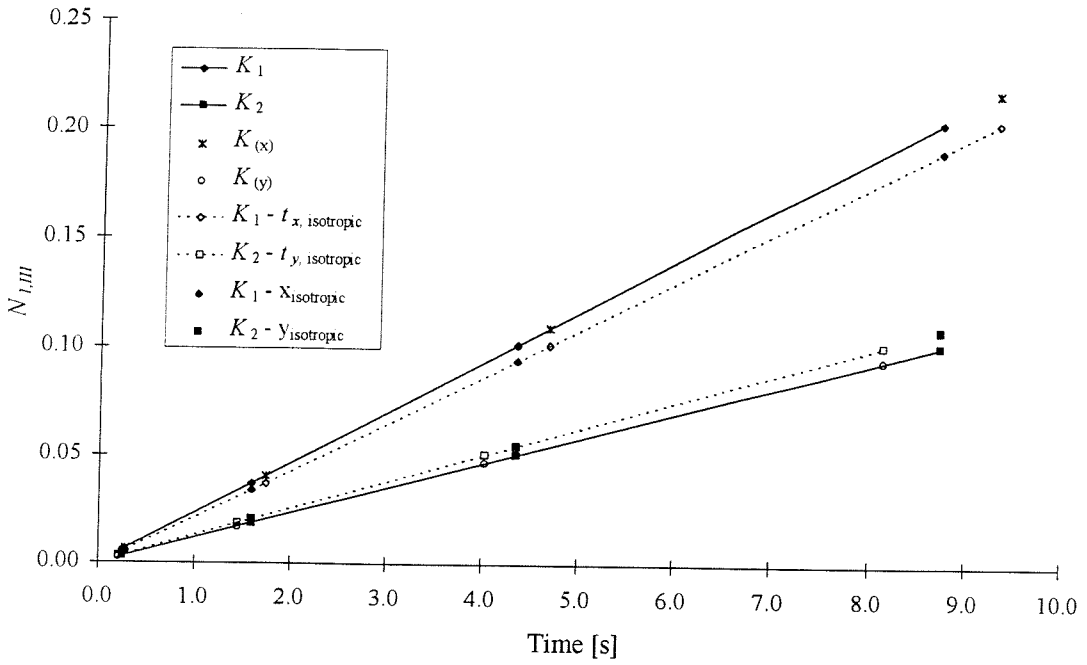

Figure 6.26 N_I and N_{III} for isotropic and anisotropic flow

It was assumed that very close to the inlet the flow front behaves like flow in an isotropic medium and then quickly changes to the elliptical shape of the anisotropic flow front. It can therefore be expected that when plotting N_I and N_{III} versus time the points close to the inlet will not fit the regression line. For F_I they should initially be slightly smaller while for F_{III} they should be slightly larger. However N_I and N_{III} close to the inlet are very small which makes it quite difficult to observe any deviation from the straight line. It is much better to look at the convergence behaviour of the calculated permeability values. Figure 6.24 and Figure 6.30

clearly show that K_1 is initially too low while K_2 is too high before converging to the expected value thus confirming the explanation of the transient nature of the flow front.

6.7.5 Arbitrary measurement direction

For an arbitrary measurement direction some changes have to be introduced to the concepts outlined in the previous sections. The degree of anisotropy (calculated from (6.75)) has to be modified to take into account the fact that the axes are not aligned with the principal directions. Using equations (6.8), (6.60) and (6.61) α can be written as a function of the measured flow front:

$$\alpha = \frac{K_2}{K_1} = \frac{F_{III}\dfrac{(A+D)}{(A+D/\cos 2\varphi)}}{F_I\dfrac{(A-D)}{(A-D/\cos 2\varphi)}} \qquad (6.76)$$

and after some rearranging

$$\alpha = \frac{A-D/\cos 2\varphi}{A+D/\cos 2\varphi} \qquad (6.77)$$

For φ equal to zero the above equation is the same as (6.75). The correct value for α and φ is found by an iterative approach. Firstly F_I and F_{III} are calculated with α set to 1 and φ set to 0. Then the ratio of F_{III} and F_I is calculated using (6.77) while φ determined from (6.64). First φ is set to the calculated angle φ. Then α is reduced until it matches the value for α as calculated by (6.77). After that φ is corrected again and then α. After this second iteration loop the two values usually have converged.

The equations for the modified inlet need some modifications as well. The radius of the inlet ellipse is now required at an arbitrary angle. This was already derived for the example in section 6.5.2. Hence the modified inlet radius may now be defined as:

$$r_{o,\mathrm{mod};i} = \sqrt{x_{o,\mathrm{mod};i}^2 + y_{o,\mathrm{mod};i}^2} \qquad (6.78)$$

with $i = I,II,III$. $x_{o,\mathrm{mod};i}$ is

$$x_{o,\mathrm{mod};i} = \sqrt{\frac{1}{\left(\dfrac{1}{a^2} + \dfrac{\tan^2\phi_i}{b^2}\right)}} \qquad (6.79)$$

where $\phi_I = -\varphi$, $\phi_{II} = -\varphi + 45°$ and $\phi_{III} = -\varphi + 90°$. ϕ and φ have opposite signs because the radius of the inlet ellipse is measured from the major axis while φ is the angle by which the

measurement coordinate system has to be rotated towards the principal axes. $y_{o,\mathrm{mod};i}$ is defined as:

$$y_{o,\mathrm{mod};i} = \frac{b}{a}\sqrt{a^2 - x_{o,\mathrm{mod};i}^2} \qquad (6.80)$$

In both equations a and b are the major and minor axis of the flow front ellipse which are defined in the same way as (6.73) and (6.74):

$$a = r_0 \sqrt[4]{\frac{1}{\alpha}} \qquad (6.81)$$

$$b = r_0 \sqrt[4]{\alpha} \qquad (6.82)$$

6.7.6 Arbitrary measurement direction - example 5

To calculate permeability in an arbitrary direction the same procedure is followed as outlined in section 6.5.2. To find F_I, F_{II} and F_{III} the inlet radius r_o is replaced with equation (6.78). The additional steps which are required to determine principal permeability are as follows. First F_I, F_{II} and F_{III} are calculated with α set to 1 and φ set to 0. Then the ratio of F_{III} and F_I is determined from equation (6.77) and φ is calculated from equation (6.64). First φ is set to the calculated angle φ . Then α is reduced until it matches the value for α as calculated by (6.77). After that φ is corrected again and then again α . At this stage the two values of φ and α should have converged to an accuracy of 10^{-5}. As before these iterations are conveniently performed on a spread sheet with the help of a numerical fitting procedure (e.g. *Solver* in Microsoft Excel). If the material is very anisotropic it may be necessary to set α to 0.5 or even 0.2 (or 2 or even 4) rather than 1 in order to help the convergence of the iterative solution.

Figure 6.27 shows the principal permeability calculated for circular inlet and the modified elliptical inlet for run 2. The principal permeability was calculated for different measurement angles. The results for the modified inlet port are independent of orientation while the permeability for the circular port varies considerably with orientation. Figure 6.27 also shows that the principal permeability calculated with circular inlet is not symmetric about the principal axis (Measurement angle 0°). For example a measurement angle of +/-30° does not yield identical permeability values. This can be explained by looking at the way the flow front is measured. Measurements are taken along two mutually orthogonal axes and a third axis which is at 45° between the two axes. For rotations of +/-30° identical flow front radii for the two orthogonal axes are obtained because the rotation takes place about the symmetry axes of

the ellipse. However for the middle axis the measurement angles are 75° and 15° for the two directions resulting in two different flow front radii. Since the inlet radius is constant (circular) the calculated principal permeability varies for the two orientations. Figure 6.27 shows that this is not a problem for permeability calculated with an elliptical inlet as the inlet radius is corrected automatically to take account of this effect.

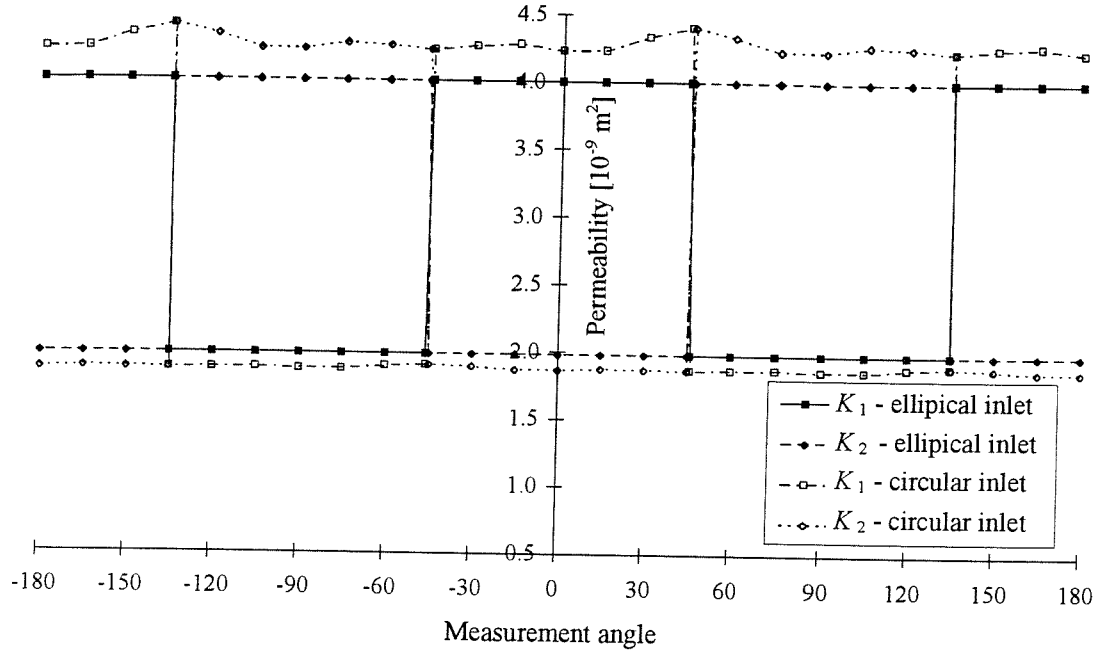

Figure 6.27 Principal permeability for circular and elliptical inlet for different measurement angles (run 2)

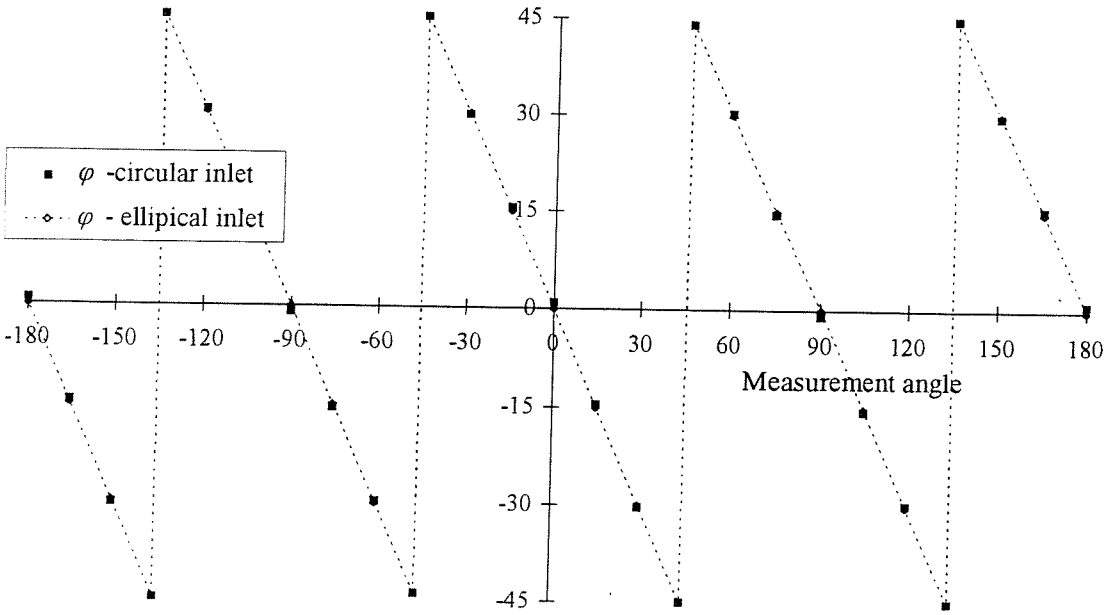

Figure 6.28 Comparison of calculated angles of orientation for circular and elliptical inlet

Figure 6.28 shows the calculated angle of orientation for circular and elliptical inlets. The agreement is quite good hence the angle of orientation for the circular inlet is a very good initial estimate to find the orientation of the modified inlet ellipse. The agreement is best for angles close to ±45°.

6.8 Other issues

6.8.1 Variation of process parameters

As explained in section 6.3 the scaling of the physical system to obtain the quasi-isotropic system involves only the degree of anisotropy. Variation in pressure or magnitude of permeability do not influence the relative dimensions of the flow front. For example changing the permeability by a factor of ten results in an tenfold increase of the filling time for identical flow front positions (see for results Appendix B; run 1: $K_1 = 4.0\text{x}10^{-9}$, $K_2 = 3.0\text{x}10^{-9}$ and run 6: $K_1 = 4.0\text{x}10^{-10}$, $K_2 = 3.0\text{x}10^{-10}$). Increasing the injection pressure leads to a reduction of the filling time by the ratio of the pressures (run 2 = 70kPa, run 10 = 250kPa). To summarise the shape of the flow front is only dependent on the ratio of the two principal permeabilities.

6.8.2 Relative size of circular inlet

In this section the influence of varying the inlet diameter on principal permeability is studied. All other parameters are kept constant ($K_1 = 4.0\text{x}10^{-9}$ m^2, $K_2 = 2.0\text{x}10^{-9}$ m^2, $P_o = 70$ kPa, $\varepsilon = 0.48$, $\mu = 0.1$ Pa s). For the following discussion the results of runs 14 to 16 of the flow simulation are utilised (run 14: $r_o = 8$mm, run 15: $r_o = 16$mm, run 16: $r_o = 28$mm; Appendix B). Figure 6.29 and Figure 6.30 show principal permeability calculated with circular and elliptical inlet. As before the results with the circular inlet do not agree very well with the target values (Figure 6.29). In Figure 6.30 the effect of the increasing inlet diameter size can be observed. K_1 is increasing initially while K_2 is decreasing at the same time. This is caused by the circular inlet as discussed in section 6.7.4. Once the flow front has fully developed permeability becomes constant. Figure 6.30 also shows that the larger the inlet diameter the longer it takes for permeability to settle. In Figure 6.31 the same permeability results as in Figure 6.30 are plotted against time. This figure seems to indicate that the relative flow behaviour of the flow front is not effected by the size of the inlet. Permeability takes about the same time for all three diameters to reach its steady state value.

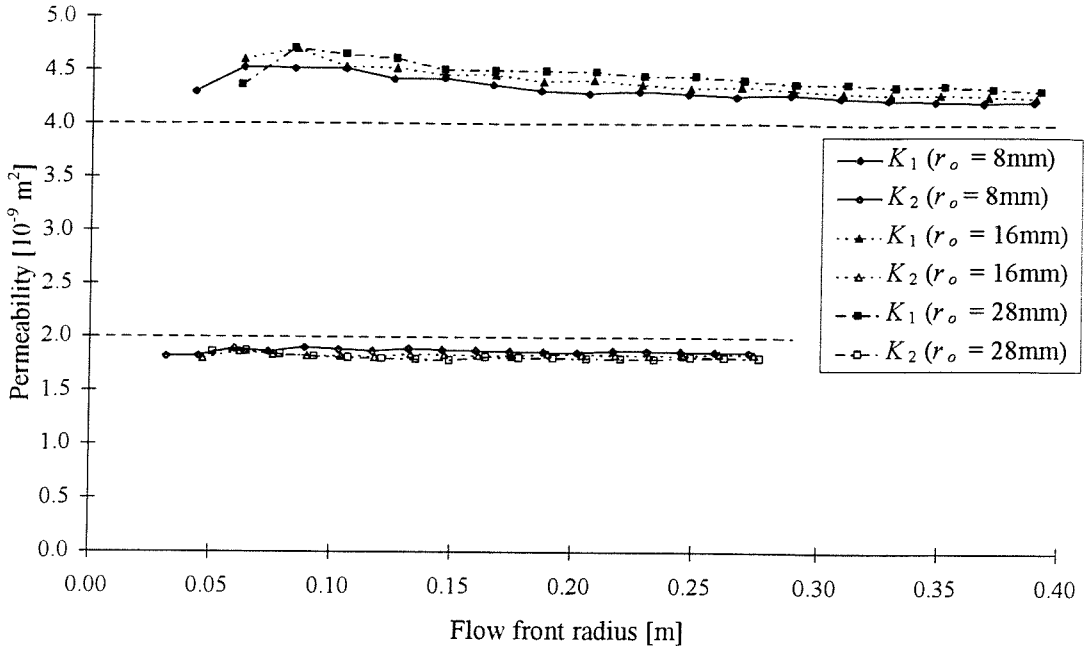

Figure 6.29 Permeability calculated with circular inlet (runs 14 to 16)

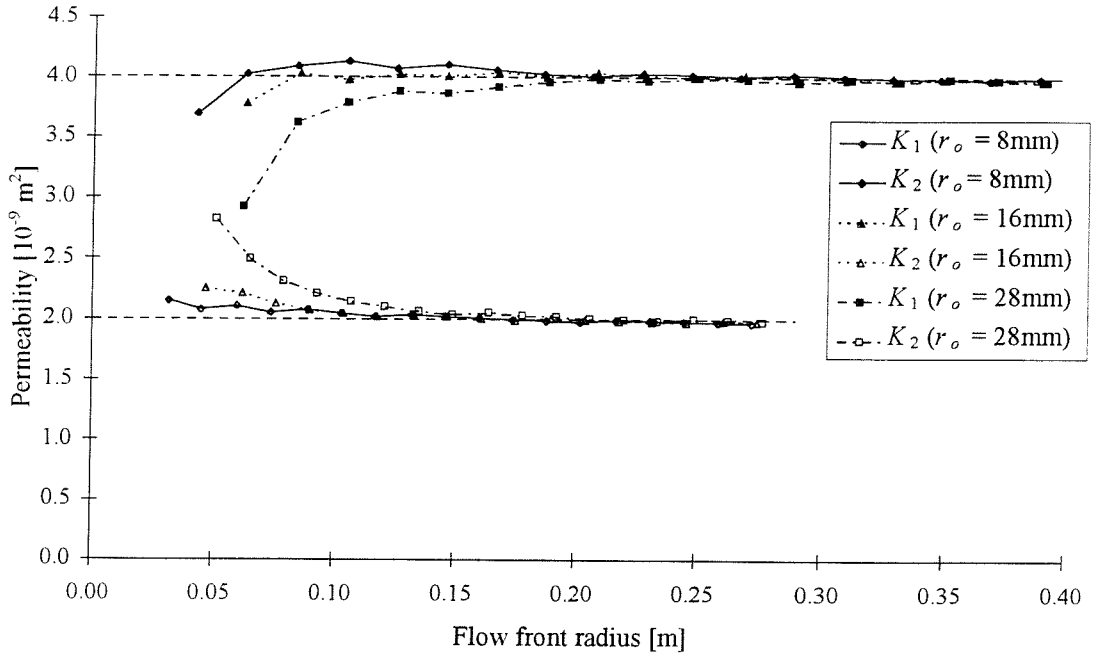

Figure 6.30 Permeability calculated with elliptical inlet (runs 14 to 16)

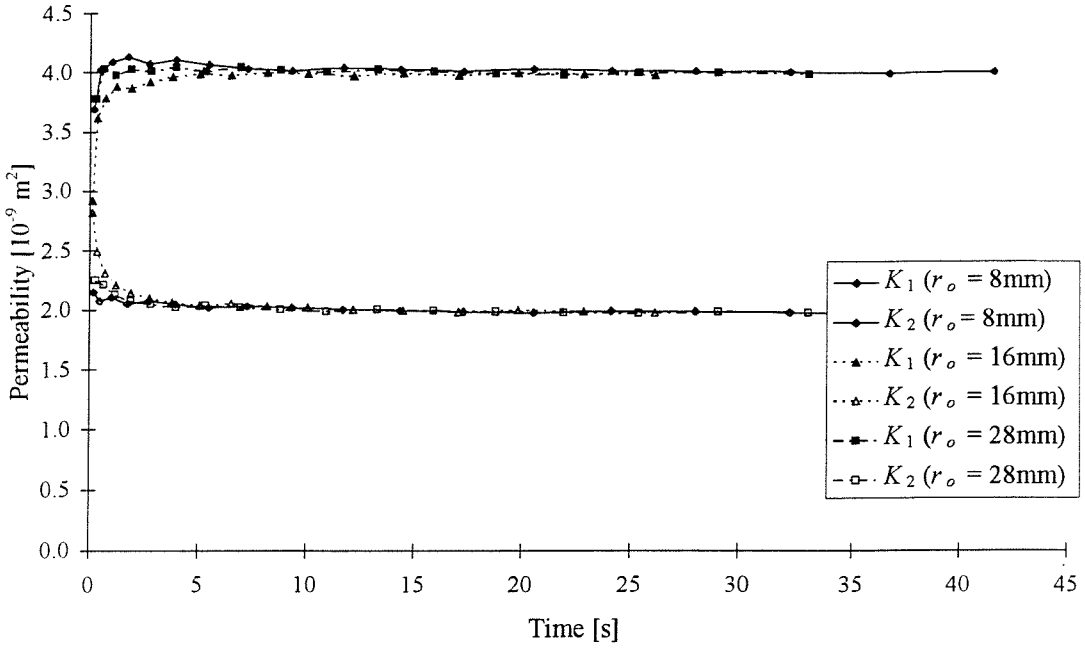

Figure 6.31 Permeability calculated with elliptical inlet versus time (runs 14 to 16)

6.8.3 Size of mould

In a recent paper by Gauvin et al. (1996) results for radial flow experiments carried out with different inlet diameters are reported. The results are repeated in Figure 6.32. Permeability was measured with three different inlet diameters: 13, 25 and 50 mm.

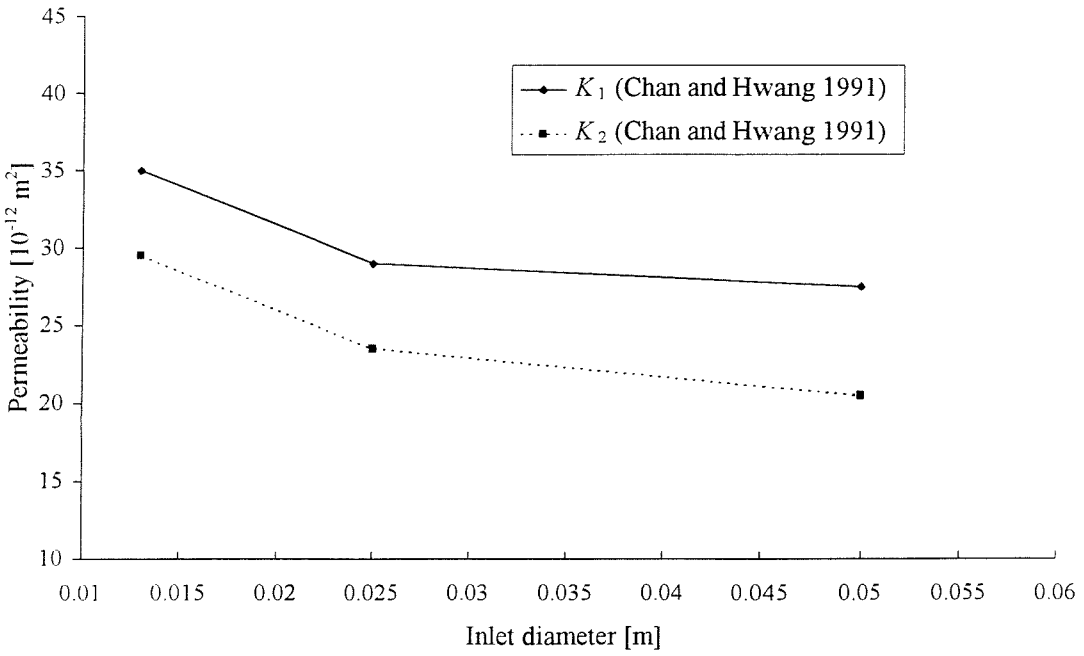

Figure 6.32 Permeability as a function of the inlet diameter (Gauvin et al. 1996)

It appears that Gauvin et al. used a sample size of less than 300x300mm. Therefore an inlet diameter of 50mm is about one sixth of the sample size. As Figure 6.32 demonstrates there is a large variation of permeability for the different inlet diameters. To study the effect of varying inlet diameter in a small mould the flow simulation results obtained for runs 14 to 16 were re-examined. The results were used for flow front radii of up to 165mm length. First of all the convergence behaviour of the ratio of the flow front radii was looked at. Figure 6.33 shows that the larger the inlet radius the longer it takes for the flow front to converge to a steady state value. In fact for run 16 (r_o = 28mm) the flow front is only converging beyond the limit of 165mm.

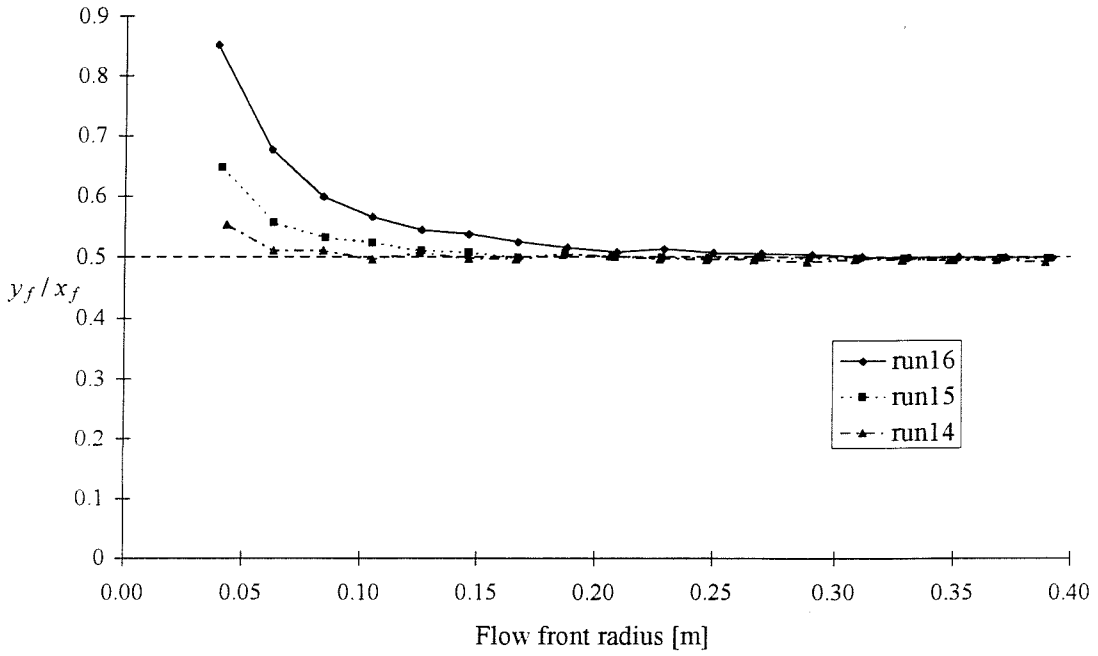

Figure 6.33 Convergence of the ratio of y_f versus x_f (runs 14 to 16)

In Figure 6.34 permeability calculated with Chan and Hwangs method (as used by Gauvin et al. 1996) is compared with the new approach with elliptical inlet. Chan and Hwang uses a circular inlet to calculate K_1. K_1 is therefore offset from the target value. K_2 is found by multiplying K_1 with the degree of anisotropy which in turn is obtained from plotting y_f versus x_f. It can be seen from Figure 6.34 that K_1 is almost constant while K_2 is increasing with increasing inlet diameter. The larger the inlet diameter the less anisotropic the flow becomes (at a fixed point of measurement) hence the difference between K_1 and K_2 is reducing. As shown in Figure 6.33 the flow front is not fully developed yet - the ratio of the flow front radii in x and y-direction is still changing. The same effect can be observed for the new approach.

Here both K_1 and K_2 are decreasing and increasing respectively. This is due to the fact that both permeability values depend on the degree of anisotropy. (K_1 and K_2 were calculated only from flow front points which already had converged or had almost reached a steady state value).

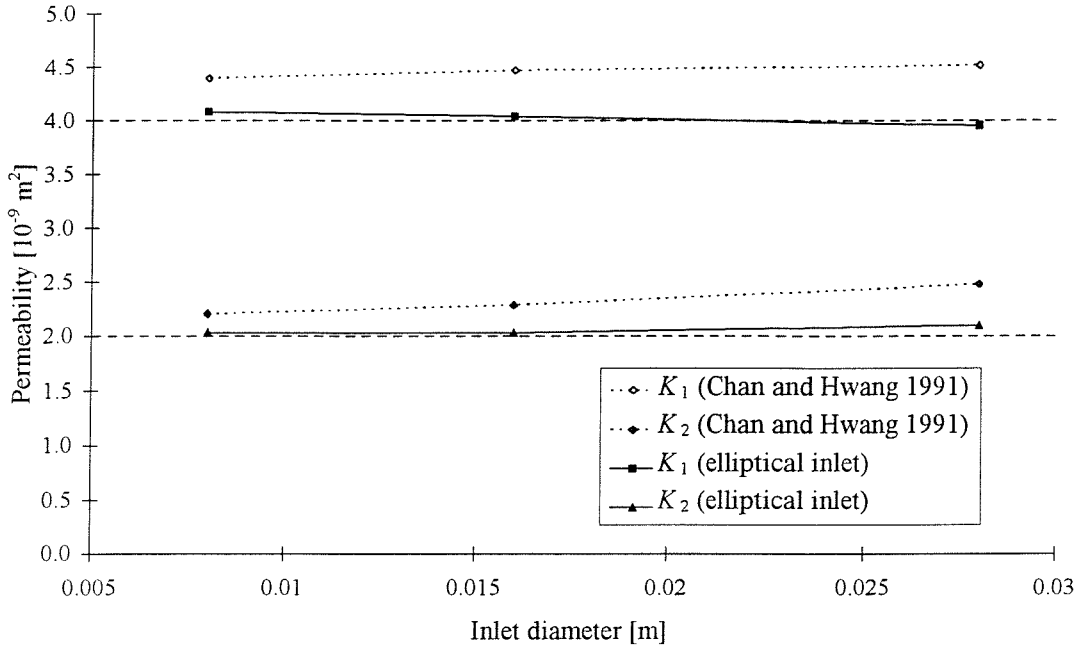

Figure 6.34 Permeability for short experiments, $x_{f,max}$ = 165mm (runs 14 to 16)

The results obtained from Chan and Hwang's method in Figure 6.34 are in complete contrast to the results reported by Gauvin et al. (repeated in Figure 6.32). Small discrepancies arise due to the fact that the numerical input values are not identical (e.g. inlet radii). The main problem however is that the general trends are disagreeing. There is some indication that the experimental results might be suspect. Firstly the permeability values are decreasing with increasing inlet diameter. In addition the difference between K_1 and K_2 is increasing. This means that the flow is becoming more anisotropic the larger the inlet diameter becomes! This is a contradiction of the (experimentally and numerically) observed flow pattern where the flow front becomes less anisotropic with increasing inlet diameter and constant observation point (for example in Figure 6.33). A possible explanation of the experimental results could be that the mould deflected during injection. Gebart and Lidström (1996) showed that deflection of the radial flow mould can have a noticeable impact on the measured permeability values. The mould used by Gauvin et al. has a cavity thickness of only 2.36mm while the transparent top plate was 25mm thick (half the thickness of the top plate used by Gebart and Lidström !). Therefore more experimental work is required to confirm the results of the numerical study

carried out in this section as the experimental results by Gauvin et al. seem to be effected by mould deflection.

6.9 Comparison with published results

Some experimental data for radial flow has been published in the literature. Table 6.8 and Table 6.9 compare the results published by Adams et al. 1988 and Chan and Hwang 1991 with results obtained by applying equations (6.14) and (6.19) to the published experimental data. One set of results is calculated using the circular inlet while for the elliptical inlet the radius was modified according to equations (6.73) and (6.74). The experimental data published by Chan and Hwang is based on Adams 1988 but with added points (by interpolating) as the algorithm by Chan and Hwang requires the knowledge of the flow front positions in the x and y-direction for each time step. The *published* columns in Table 6.8 and Table 6.9 refer to the values in the respective papers while *actual* is the recalculated values using the published experimental details. Surprisingly they do not always agree.

For both sets of data the results for the elliptical inlet are "bracketed" by the results for circular inlet. Table 6.8 shows that the agreement between the results published by Adam et al. and equations (6.14) and (6.19) is very good for the elliptical inlet. Furthermore the results calculated with the elliptical inlet are very similar for both sets of data (see Table 6.8 and Table 6.9). Table 6.9 shows that K_1 calculated by Chan and Hwang is identical to K_1 obtained by equations (6.14) with circular inlet. K_2 is calculated by Chan and Hwang by multiplying K_1 with the degree of anisotropy. Therefore K_2 by Chan and Hwang is larger than K_2 with the circular inlet.

	published	actual	circular inlet	elliptical inlet
K_1	$5.27x10^{-10}$	$5.19x10^{-10}$	$5.39x10^{-10}$	$5.15x10^{-10}$
K_2	$3.90x10^{-10}$	$3.88x10^{-10}$	$3.74x10^{-10}$	$3.91x10^{-10}$

Table 6.8 Comparison with published data (Adams, Russel and Rebenfeld 1988)

	published	actual	circular inlet	elliptical inlet
K_1	$5.38x10^{-10}$	$5.34x10^{-10}$	$5.34x10^{-10}$	$5.09x10^{-10}$
K_2	$4.01x10^{-10}$	$4.01x10^{-10}$	$3.67x10^{-10}$	$3.86x10^{-10}$

Table 6.9 Comparison with published data (Chan and Hwang 1991)

In summary it can be said that the method by Adams et al. (1988) is taking account of the shape of the inlet. Hence there is excellent agreement with the results obtained with equations (6.14) and (6.19) for the elliptical inlet. Chan and Hwang (1991) do not modify the inlet. Therefore the agreement between permeability obtained with Chan and Hwangs method and permeability for the other two methods is not very good.

6.10 Summary

A new approach to permeability calculation for radial flow tests with constant inlet pressure was developed. With flow front measurements taken in three directions it is possible to calculate the principal permeability and its orientation. Problems associated with the inlet boundary condition have been discussed. In order to obtain a mathematically correct solution for principal permeability and its orientation the inlet is modified (made elliptical). To show that the permeability is converging to a constant value it is possible with the new approach to plot the principal permeability as a function of time or position for each flow front measurement. It was also shown how the calculated angle of orientation is related to the principal permeabilities. Furthermore it was shown that the inlet diameter can have a noticeable effect on the results if the mould is small. Finally a comparison with published data showed good agreement with other methods.

7. Radial flow permeability measurement - other test configurations

7.1 Introduction

In this chapter permeability measurement for other radial flow tests will be discussed. The first case is for constant inlet pressure where the pressure drop between the inlet and a point in the mould is measured. Then permeability models for constant flow rate will be derived. There are three different test configurations: measurement of flow front, measurement of pressure drop and measurement of pressure at a point. Finally a permeability model for three-dimensional radial flow will be developed.

7.2 Constant inlet pressure - measure pressure drop

7.2.1 Isotropic permeability

If the flow front radius r_f is kept constant in equation (6.2) on page 59 (now called r_1), then the pressure drop measured between the inlet and the fixed radial position will change with time (because the inlet pressure is constant). For isotropic flow the pressure distribution in the mould can be written as (see e.g. Adams et al. 1986):

$$P(r) = P_f + (P_o - P_f)\frac{\ln(r/r_f)}{\ln(r_o/r_f)} \qquad (7.1)$$

Assuming P_f is atmospheric and can be set to zero, r is equal to r_1 and $P(r)$ is equal to P_1

$$P_1 = P_o \frac{\ln(r_1/r_f)}{\ln(r_o/r_f)} \qquad (7.2)$$

rearranging yields

$$\ln(r_f)(P_o - P_1) = P_o \ln(r_1) - P_1 \ln(r_0) \qquad (7.3)$$

and finally

$$r_f = \exp\left(\frac{P_o \ln(r_1) - P_1 \ln(r_0)}{P_o - P_1}\right) \qquad (7.4)$$

Substituting for r_f in equation (6.2) yields the permeability model for measuring the pressure difference for isotropic radial flow with constant inlet pressure:

$$K = \left(\exp\left(2\frac{P_o \ln(r_1) - P_1 \ln(r_0)}{P_o - P_1} \right) \left[2\ln\left(\frac{\exp\left(\frac{P_o \ln(r_1) - P_1 \ln(r_0)}{P_o - P_1} \right)}{r_o} \right) - 1 \right] + r_o^2 \right) \frac{1}{t} \frac{\mu\varepsilon}{4\,\Delta P}$$

(7.5)

From equation (7.5) the permeability is obtained from the measured pressure history at a point with radius r_1 and the constant inlet pressure P_o.

7.2.2 Anisotropic permeability

For anisotropic permeability the same approach as in section 6.5.1 is adopted. Only the flow front radius is replaced with an equivalent expression which includes pressure measurement at a point. The radius for the quasi-isotropic system is equation (6.38) on page 68. For the general anisotropic case with an arbitrary measurement direction the pressure at a the radius $\bar{r}'_1$ can be expressed by (equivalent to equation (7.2)):

$$P_{1,i} = P_o \frac{\ln\left(\bar{r}'_{1,i} / \bar{r}'_{f,i} \right)}{\ln\left(\bar{r}'_{o,i} / \bar{r}'_{f,i} \right)} \qquad (7.6)$$

with $i = I$, II and III as defined in section 6.5.1 (Figure 6.4). For i equal to I the pressure $P_{1,I}$ can be expressed as

$$P_{1,I} = P_o \frac{\ln\left(r_{1,I} / r_{f,I} \right)}{\ln\left(r_{o,I} / r_{f,I} \right)} \qquad (7.7)$$

Rearranging yields the flow front radius

$$r_{f,I} = \exp\left(\frac{P_o \ln(r_{1,I}) - P_{1,I} \ln(r_{o,I})}{P_o - P_{1,I}} \right) \qquad (7.8)$$

For i = to II the following expression for the flow front radius can be derived:

$$r_{f,II} = \exp\left(\frac{P_o \ln(r_{1,II}) - P_{1,II} \ln(r_{o,II})}{P_o - P_{1,II}} \right) \qquad (7.9)$$

and for i = to III:

$$r_{f,III} = \exp\left(\frac{P_o \ln(r_{1,III}) - P_{1,III} \ln(r_{o,III})}{P_o - P_{1,III}} \right) \qquad (7.10)$$

It is now possible to define N_I, N_{II} and N_{III} by substituting for $r_{f,i}$ in equation (6.51) on page 69.

$$N_i = \exp\left(2\frac{P_o \ln(r_{1,i}) - P_{1,i} \ln(r_{o,\mathrm{mod},i})}{P_o - P_{1,i}}\right)\left[2\ln\left(\frac{\exp\left(\frac{P_o \ln(r_{1,i}) - P_{1,i} \ln(r_{o,\mathrm{mod},i})}{P_o - P_{1,i}}\right)}{r_{o,\mathrm{mod},i}}\right) - 1\right] + r_{o,\mathrm{mod},i}^2$$

where $i = I$, II and III (7.11)

The inlet radius $r_{o,\mathrm{mod},i}$ was defined in section 6.7.5. The radius of the pressure measurement location is defined as:

$$r_{1,i} = \sqrt{x_{1,i}^2 + y_{1,i}^2} \qquad (7.12)$$

The radius $r_{1,i}$ is assumed to be in the region of fully developed flow. The principal permeability and its orientation can now be determined from pressure measurements made on the three axes *I,II,III* and the constant inlet pressure. The procedure is the same as outlined in section 6.7.6. The only difference is that N_i in section 6.5.1 (equation (6.51)) is substituted for by equation (7.11).

7.3 Constant flow rate

Instead of conduction experiments with an constant inlet pressure it is also possible to set a constant flow rate. This changes the mathematical formulation of the (flow) problem and its solution slightly. There are three ways to obtain permeability. By measuring (i) the progression of the flow front, (ii) the pressure drop along a radius and (iii) the pressure at a point. All three approaches will be discussed in this section for both isotropic and anisotropic flow.

7.3.1 Isotropic permeability

By multiplying Darcy's law for radial flow (equation (6.1), page 59) with the area normal to the flow the basic equation for constant flow rate is set up

$$Q = -\frac{K}{\mu}\frac{dP}{dr}A_n \qquad (7.13)$$

For radial flow the area A_n is equal to $2\,\pi h\, r$ thus

$$Q\frac{dr}{r} = -\frac{K}{\mu}dP\,2\pi h \qquad (7.14)$$

Integrating yields

$$Q\ln(r) = -\frac{K}{\mu}2\pi h\, P + E \qquad (7.15)$$

The integration constant E is determined for $P = P_f$ at $r = r_f$:

$$E = Q\ln(r_f) + \frac{K}{\mu}2\pi h\, P_f \qquad (7.16)$$

Substituting for E in (7.15) yields:

$$Q\ln(r/r_f) = \frac{K}{\mu}2\pi h(P_f - P) \qquad (7.17)$$

For $r = r_o$ and $P = P_o$ isotropic permeability for constant flow rate can be modelled as follows:

$$K = \frac{Q\mu}{2\pi h}\frac{\ln(r_f/r_o)}{(P_o - P_f)} \qquad (7.18)$$

Measurement of flow front

Assuming zero pressure at the flow front equation (7.18) becomes

$$K = \frac{Q\mu}{2\pi h}\frac{\ln(r_f/r_o)}{P_o} \qquad (7.19)$$

From continuity considerations an equivalent expression for the flow rate Q can be found:

$$Q(t_f - t_o) = (r_f^2 - r_o^2)\pi h\varepsilon \qquad (7.20)$$

Setting t_o to zero and t_f to t yields

$$Q = \frac{(r_f^2 - r_o^2)\pi\, h\varepsilon}{t} \qquad (7.21)$$

Substitute for Q:

$$K = \frac{\varepsilon\,\mu}{2}\frac{(r_f^2 - r_o^2)\ln(r_f/r_o)}{t\,P_o} \qquad (7.22)$$

Measurement of pressure drop

To measure the pressure drop across two points, r_o and r_f in equation (7.18) are set to r_1 and r_2 respectively while P_o and P_f are set to P_1 and P_2 (the pressures at the two radii r_1 and r_2).

$$K = \frac{Q\mu}{2\pi h}\frac{\ln(r_2/r_1)}{(P_1 - P_2)} \qquad (7.23)$$

Note that the pressure difference P_1 - P_2 is constant throughout the experiment which will be shown below. The radial pressure distribution can be written as (see section 7.2.1):

$$P = P_f + (P_o - P_f)\frac{\ln(r/r_f)}{\ln(r_o/r_f)} \qquad (7.24)$$

and with atmospheric pressure at the flow front

$$P = P_o \frac{\ln(r/r_f)}{\ln(r_o/r_f)} \qquad (7.25)$$

The pressure at r equal to r_1 is P_1

$$P_1 = P_o \frac{\ln(r_1/r_f)}{\ln(r_o/r_f)} \qquad (7.26)$$

while at r equal to r_2 the pressure is P_2

$$P_2 = P_o \frac{\ln(r_2/r_f)}{\ln(r_o/r_f)} \qquad (7.27)$$

The pressure difference P_1 - P_2 can now be written as

$$P_1 - P_2 = P_o \frac{\ln(r_1/r_f)}{\ln(r_o/r_f)} - P_o \frac{\ln(r_2/r_f)}{\ln(r_o/r_f)} \qquad (7.28)$$

and after rearranging

$$P_1 - P_2 = P_o \frac{\ln(r_1/r_2)}{\ln(r_o/r_f)} \qquad (7.29)$$

By rearranging equation (7.18) P_o can be expressed in terms of the inlet and flow front radius:

$$P_o = \frac{Q\mu}{2\pi hK} \ln(r_f/r_o) = C \ln(r_f/r_o) \qquad (7.30)$$

Substitute for P_o in equation (7.29)

$$P_1 - P_2 = C \ln(r_f/r_o) \frac{\ln(r_1/r_2)}{\ln(r_o/r_f)} \qquad (7.31)$$

and after some rearranging

$$P_1 - P_2 = -C \ln(r_1/r_2) \qquad (7.32)$$

As all the terms in equation (7.32) are constant it follows that the pressure difference P_1 - P_2 is also constant.

Measurement of pressure at a point

If the pressure is measured at a point which is located at r_2 then r_o in equation (7.18) is equal to r_2 and P_o equal to P_2. Again the pressure at the flow front is assumed to be atmospheric

$$K = \frac{Q\mu}{2\pi h} \frac{\ln(r_f/r_2)}{P_2} \qquad (7.33)$$

The flow front radius r_f is replaced by an equivalent expression by rearranging (7.20) .

$$r_f = \sqrt{\frac{Q(t-t_2)}{\pi h \varepsilon} + r_2^2} \qquad (7.34)$$

where t_2 is the time the flow front took to reach the radius r_2. Equation (7.33) can now be written as:

$$K = \frac{Q\mu}{2\pi h} \frac{\ln\left(\sqrt{\frac{Q(t-t_2)}{\pi h \varepsilon} + r_2^2} \Big/ r_2\right)}{P_2} \qquad (7.35)$$

and after rearranging:

$$K = \frac{Q\mu}{2\pi h} \frac{\frac{1}{2}\ln\left(\frac{Q(t-t_2)}{\pi h \varepsilon r_2^2} + 1\right)}{P_2} \qquad (7.36)$$

7.3.2 Anisotropic permeability measurement in the principal direction

Anisotropy

So far only isotropic flow cases have been considered. However many fabrics commonly used in RTM are anisotropic. As a consequence the flow is no longer just a function of the radius but also of its orientation. Hence the equations presented in section 7.3.1 are no longer valid. However it is still possible to obtain an approximate solution by transforming the physical domain into a quasi-isotropic system as shown in section 6.3. This allows to formulate the basic equation for anisotropic permeability which is very similar to equation (7.18).

$$K' = \frac{Q\mu}{2\pi h} \frac{\ln\left(\bar{r}_f / \bar{r}_o\right)}{\left(P_o - P_f\right)} \qquad (7.37)$$

where $\bar{r}_o$ and $\bar{r}_f$ were defined section 6.3. This transformation is only valid if the pressure and flow front measurements are carried out in the principal coordinate system **1,2**.

Measurement of flow front

With P_f equal to zero equation (7.37) can be written as:

$$K' = \frac{Q\mu}{2\pi h} \frac{\ln\left(\bar{r}_f / \bar{r}_o\right)}{P_o} \qquad (7.38)$$

In the quasi-isotropic system equation (7.21) becomes

$$Q = \frac{\left(\bar{r}_f^{-2} - \bar{r}_o^{-2}\right)\pi h \varepsilon}{t} \qquad (7.39)$$

Substituting for Q in (7.38) yields

$$K' = \frac{\varepsilon \mu}{2} \frac{\left(\bar{r}_f^{-2} - \bar{r}_o^{-2}\right) \ln\left(\bar{r}_f / \bar{r}_o\right)}{t P_o} \qquad (7.40)$$

As in section 6.4.1 $\bar{r}_o$ and $\bar{r}_f$ has two preferred orientations where $\bar{r}_o$ and $\bar{r}_f$ greatly simplify. If equation (7.40) is evaluated for y equal to zero i.e. for measurements taken along the **1**-axis then it is possible to write an explicit expression for K_1.

$$K_1 = \frac{\varepsilon \mu}{2} \frac{\left(x_f^2 - x_o^2\right) \ln\left(x_f / x_o\right)}{t P_o} \qquad (7.41)$$

Similarly for x equal to zero i.e. measurements taken along the **2**-axis K_2 may be obtained:

$$K_2 = \frac{\varepsilon \mu}{2} \frac{\left(y_f^2 - y_o^2\right) \ln\left(y_f / y_o\right)}{t P_o} \qquad (7.42)$$

Measurement of pressure drop

As in the isotropic case $\bar{r}_o$ and $\bar{r}_f$ in equation (7.37) are set to $\bar{r}_1$ and $\bar{r}_2$ and P_o and P_f are set to P_1 and P_2.

$$K' = \frac{Q\mu}{2\pi h} \frac{\ln\left(\bar{r}_2 / \bar{r}_1\right)}{\left(P_1 - P_2\right)} \qquad (7.43)$$

Since Q does not contain any directional information it needs to be replaced by an equivalent expression in terms of the flow front radii.

$$Q\left(t_2 - t_1\right) = \left(\bar{r}_2^{-2} - \bar{r}_1^{-2}\right) \pi h \varepsilon \qquad (7.44)$$

where t_1 and t_2 are the time the flow front took to reach the radial positions $\bar{r}_1$ and $\bar{r}_2$ respectively. This leads to the following basic equation:

$$K' = \frac{\varepsilon \mu}{2} \frac{\left(\bar{r}_2^{-2} - \bar{r}_1^{-2}\right) \ln\left(\bar{r}_2 / \bar{r}_1\right)}{\left(t_2 - t_1\right)\left(P_1 - P_2\right)} \qquad (7.45)$$

Evaluating equation (7.45) for two pressure measurements at x_1 and x_2 along the **1**-axis (y = 0) yields the principal permeability K_1:

$$K_1 = \frac{\varepsilon \mu}{2} \frac{\left(x_2^2 - x_1^2\right) \ln\left(x_2 / x_1\right)}{\left(t_2 - t_1\right)\left(P_1 - P_2\right)} \qquad (7.46)$$

For x equal to zero K_2 is obtained:

$$K_2 = \frac{\varepsilon \mu}{2} \frac{\left(y_2^2 - y_1^2\right) \ln\left(y_2 / y_1\right)}{\left(t_2 - t_1\right)\left(P_1 - P_2\right)} \qquad (7.47)$$

Measurement of pressure at a point

The equation for measurement of pressure at a point (7.36) reads for the quasi-isotropic as follows:

$$K' = \frac{Q\mu}{2\pi h} \frac{\frac{1}{2}\ln\left(\frac{Q(t-t_2)}{\pi h \varepsilon \bar{r}_2^{-2}} + 1\right)}{P_2} \qquad (7.48)$$

To obtain directional information, Q in the first fraction of equation (7.48) is replaced by an equivalent expression as in the previous section (equation (7.44) with $t_1 = 0$ and $\bar{r}_1 = \bar{r}_o$):

$$K' = \frac{\varepsilon\mu}{2} \frac{\left(\bar{r}_2^{-2} - \bar{r}_o^{-2}\right)}{t_2} \frac{\frac{1}{2}\ln\left(\frac{Q(t-t_2)}{\pi h \varepsilon \bar{r}_2^{-2}} + 1\right)}{P_2} \qquad (7.49)$$

Evaluating the previous equation along the **1**-axis yields

$$K_1 = \frac{\varepsilon\mu}{2} \frac{\left(x_2^2 - x_o^2\right)}{t_2} \frac{\frac{1}{2}\ln\left(\frac{Q(t-t_2)}{\pi h \varepsilon x_2^2 \sqrt{K_2/K_1}} + 1\right)}{P_2} \qquad (7.50)$$

and along the **2**-axis:

$$K_2 = \frac{\varepsilon\mu}{2} \frac{\left(y_2^2 - y_o^2\right)}{t_2} \frac{\frac{1}{2}\ln\left(\frac{Q(t-t_2)}{\pi h \varepsilon y_2^2 \sqrt{K_1/K_2}} + 1\right)}{P_2} \qquad (7.51)$$

It can be seen that equations (7.50) and (7.51) are mutually dependent and therefore do not define the principal permeabilities uniquely. This can be overcome by introducing the degree of anisotropy as a third condition.

$$\alpha = \frac{K_2}{K_1} \qquad (7.52)$$

Equations (7.50) and (7.51) can then be written as

$$K_1 = \frac{\varepsilon\mu}{2} \frac{\left(x_2^2 - x_o^2\right)}{t_2} \frac{\frac{1}{2}\ln\left(\frac{Q(t-t_2)}{\pi h \varepsilon x_2^2 \sqrt{\alpha}} + 1\right)}{P_2} \qquad (7.53)$$

and

$$K_2 = \frac{\varepsilon\mu}{2} \frac{\left(y_2^2 - y_o^2\right)}{t_2} \frac{\frac{1}{2}\ln\left(\frac{Q(t-t_2)}{\pi h \varepsilon y_2^2 \sqrt{1/\alpha}} + 1\right)}{P_2} \qquad (7.54)$$

A solution for the principal permeabilities is obtained iteratively. First a value for α is guessed (say 1). Then K_1 and K_2 are calculated using equations (7.53) and (7.54). With the results for K_1 and K_2 α is obtained from equation (7.52). With an iterative procedure the guessed value of α is reduced until it matches the calculated value for α obtained from equation (7.52).

Alternatively it would be possible to use equations (7.48) and (7.52) to define principal permeability as follows:

$$K_1 = \frac{Q\mu}{2\pi h\sqrt{\alpha}} \frac{\frac{1}{2}\ln\left(\frac{Q(t-t_2)}{\pi h\varepsilon x_2^2\sqrt{\alpha}}+1\right)}{P_2} \qquad (7.55)$$

and:

$$K_2 = \frac{Q\mu}{2\pi h}\sqrt{\alpha} \frac{\frac{1}{2}\ln\left(\frac{Q(t-t_2)}{\pi h\varepsilon y_2^2\sqrt{1/\alpha}}+1\right)}{P_2} \qquad (7.56)$$

The procedure to calculate principal permeability is identical to the one outlined above.

7.3.3 Anisotropic permeability measurement in an arbitrary direction

The formulae to calculate principal permeability can be extended to arbitrary measurement directions as shown for constant inlet pressure in section 6.5. This is a geometrical problem where the only measurement technique specific terms are C and F_I, F_{II} and F_{III}. For simplicity only the F_i's for each measurement technique are listed in this section without detailed derivation (which is identical to section 6.5 and). The process term C is the same for all three constant flow rate measurement techniques:

$$C = \frac{\varepsilon\,\mu}{2} \qquad (7.57)$$

F_i for the three measurement directions i = *I,II,III* is shown below. For measurement of the flow front F_i is equal to

$$F_i = \frac{\left(r_{f,i}^2 - r_{o,\mathrm{mod};i}^2\right)\ln\left(r_{f,i}/r_{o,\mathrm{mod};i}\right)}{t_i P_o} \qquad (7.58)$$

while for measurement of the pressure drop between two points :

$$F_i = \frac{\left(r_{2,i}^2 - r_{1,i}^2\right)\ln\left(r_{2,i}/r_{1,i}\right)}{\left(t_{2,i} - t_{1,i}\right)\left(P_{1,i} - P_{2,i}\right)} \qquad (7.59)$$

For the measurement of pressure at a point:

$$F_i = \frac{\left(r_{2,i}^2 - r_{o,\mathrm{mod};i}^2\right)\frac{1}{2}\ln\left(\frac{Q\left(t_i - t_{2,i}\right)}{\pi h \varepsilon r_{2,i}^2\left(\sqrt{\alpha}\cos^2\varphi + \sqrt{1/\alpha}\sin^2\varphi\right)} + 1\right)}{t_i P_{2,i}} \qquad (7.60)$$

with $r_{1,i}$:

$$r_{1,i} = \sqrt{x_{1,i}^2 + y_{1,i}^2} \qquad (7.61)$$

and $r_{2,i}$:

$$r_{2,i} = \sqrt{x_{2,i}^2 + y_{2,i}^2} \qquad (7.62)$$

F_i for measurement of the pressure drop can be determined explicitly. It is important however that the two pressure measurements are made in the fully developed region of the flow (to get a constant pressure drop). Please note that in the equations (7.58) and (7.60) the modified inlet diameter $r_{o,\mathrm{mod},i}$ has been used with out proof. However it was demonstrated in section 6.8.1 that the shape of the flow front only depends on the ratio of the principal permeabilities. It is therefore a reasonable assumption that the inlet has to be scaled in the same way as for constant inlet pressure (see sections 6.7.5 and 6.7.6). The degree of anisotropy α and the orientation φ are determined iteratively as shown in section 6.7.6.

7.4 Radial flow measurements in three dimensions

The derivation of a permeability model for three-dimensional flow follows the same pattern as in two dimensions. First the pressure distribution (for a sphere) is determined. Then the isotropic permeability is developed and finally flow domain scaling is introduced to deal with anisotropy.

7.4.1 Isotropic permeability measurement

Laplace's equation in spherical coordinates is given as (Moon and Eberle Spencer (1969)):

$$\nabla^2 P(r,\theta,\psi) = \frac{\partial^2 P}{\partial r^2} + \frac{2}{r}\frac{\partial P}{\partial r} + \frac{1}{r^2}\frac{\partial^2 P}{\partial \theta^2} + \frac{\cot\theta}{r^2}\frac{\partial P}{\partial \theta} + \frac{1}{r^2\sin^2\theta}\frac{\partial^2 P}{\partial \psi^2} \qquad (7.63)$$

In the isotropic case the pressure is only a function of the radius r hence

$$\nabla^2 P(r) = \frac{\partial^2 P}{\partial r^2} + \frac{2}{r}\frac{\partial P}{\partial r} \qquad (7.64)$$

With the boundary conditions of P equal to P_f at $r = r_f$ and P equal to P_o at $r = r_o$ (this assumes the inlet is hemispherical) it is possible to determine the solution for the pressure distribution:

$$P(r) = P_f + \frac{(P_o - P_f) r_o r_f}{r_f - r_o} \left\{ \frac{1}{r} - \frac{1}{r_f} \right\} \qquad (7.65)$$

and

$$\frac{dP}{dr} = -\frac{1}{r^2} \frac{(P_o - P_f) r_o r_f}{r_f - r_o} \qquad (7.66)$$

Next equation (7.66) is substituted for the pressure gradient in Darcy's law (equation (6.1) on page 59). Then the Darcy velocity at the flow front is replaced with the progression of the flow front (as in section 6.1) yielding:

$$\frac{dr_f}{dt} = \frac{K \Delta P}{\mu \varepsilon} \frac{r_o}{r_f (r_f - r_o)} \qquad (7.67)$$

where ΔP is equal to P_o - P_f. In order to obtain an expression of permeability in terms of flow front radius and time passed this equation has to be integrated thus

$$\frac{K \Delta P}{\mu \varepsilon} t = \frac{r_f^3}{3 r_o} - \frac{r_f^2}{2} + \frac{r_o^2}{6} \qquad (7.68)$$

After rearranging the final expression for permeability is obtained:

$$K = \frac{\mu \varepsilon}{6 \Delta P} \left[\frac{2 r_f^3}{r_o} - 3 r_f^2 + r_o^2 \right] \frac{1}{t} \qquad (7.69)$$

The spherical coordinate system is related to the Cartesian coordinate system by

$$r = \sqrt{x^2 + y^2 + z^2} \qquad (7.70)$$

7.4.2 Anisotropic permeability measurement in the principal direction

If the porous material is anisotropic the governing equation needs to be transformed to a quasi-isotropic system as described in section 6.3 in order to obtain an analytical solution. Using the same definition for the quasi-isotropic permeability as is section 6.3 ($K' = \sqrt{K_1 K_2}$) the coordinates are transformed as follows:

$$\bar{x} = x \sqrt[4]{\frac{K_2}{K_1}} \quad ; \quad \bar{y} = y \sqrt[4]{\frac{K_1}{K_2}} \quad ; \quad \bar{z} = z \sqrt[4]{\frac{K_1 K_2}{K_3}} \qquad (7.71)$$

The governing equation for the quasi-isotropic system becomes:

$$K' \frac{\partial^2 P}{\partial \bar{x}^2} + K' \frac{\partial^2 P}{\partial \bar{y}^2} + K' \frac{\partial^2 P}{\partial \bar{z}^2} = 0 \qquad (7.72)$$

while solution for quasi-isotropic permeability can be written as:

$$K' = \frac{\mu\varepsilon}{6\Delta P}\left[\frac{2\bar{r}_f^{-3}}{\bar{r}_o} - 3\bar{r}_f^{-2} + \bar{r}_o^{-2}\right]\frac{1}{t} \qquad (7.73)$$

where $\bar{r}$ is the radius of the quasi-isotropic system:

$$\bar{r} = \sqrt{\bar{x}^{-2} + \bar{y}^{-2} + \bar{z}^{-2}} \qquad (7.74)$$

During the radial flow permeability test measurements are taken along the x, y and z-axis. As for two-dimensional flow equation (7.74) is simplified by setting two out of the three coordinates to zero. To determine K_2 for example x and z are set to zero (flow front measurements are made along the 2-axis). This simplifies (7.74) to

$$\bar{r} = y\sqrt[4]{\frac{K_1}{K_2}} \qquad (7.75)$$

Equation (7.75) is substituted into equation (7.73):

$$K' = \sqrt{K_1 K_2} = \frac{\mu\varepsilon}{6\Delta P}\sqrt{\frac{K_1}{K_2}}\left[\frac{2y_f^3}{y_o} - 3y_f^2 + y_o^2\right]\frac{1}{t} \qquad (7.76)$$

After rearranging an explicit expression for K_2 is obtained:

$$K_2 = \frac{\mu\varepsilon}{6\Delta P}\left[\frac{2y_f^3}{y_o} - 3y_f^2 + y_o^2\right]\frac{1}{t} \qquad (7.77)$$

K_1 is obtained for y and z equal to zero

$$K_1 = \frac{\mu\varepsilon}{6\Delta P}\left[\frac{2x_f^3}{x_o} - 3x_f^2 + x_o^2\right]\frac{1}{t} \qquad (7.78)$$

And finally K_3 can be calculated by setting x and y equal to zero

$$K_3 = \frac{\mu\varepsilon}{6\Delta P}\left[\frac{2z_f^3}{z_o} - 3z_f^2 + z_o^2\right]\frac{1}{t} \qquad (7.79)$$

In practice considerable difficulty arises from the fact that z_o is required to evaluate the expression. It is not possible to measure z_o directly in the experiment. As soon as the flow front reaches the top plate of the mould equations (7.77), (7.78) and (7.79) cease to be valid as the flow is no longer three dimensional.

The flow front in the mould is measured using thermistors (see section 9.3.2). K_1 and K_2 are obtained from the x or y coordinate of thermistors placed on the second layer. The height of the thermistor is ignored. It is therefore interesting to know what the difference is between the in-plane coordinate (say x_f) and the effective in-plane coordinate ($x_{f,eff}$) taking into account the height of the thermistor (z_{therm}):

$$x_{f,eff} = \sqrt{x_f^2 + z_{therm}^2} \qquad (7.80)$$

A limit for z_{therm} can be derived for a specified error e:

$$e \geq 1 - \frac{x_f}{x_{f,eff}} \qquad (7.81)$$

substituting for $x_{f,eff}$:

$$e \geq 1 - \frac{x_f}{\sqrt{x_f^2 + z_{therm}^2}} \qquad (7.82)$$

Resolving for z_{therm} yields:

$$z_{therm} \leq x_f \left(\frac{\sqrt{1-(1-e)^2}}{1-e} \right) \qquad (7.83)$$

For an error e of less than 1% z_{therm} has to equal $0.143*x_f$ and for an error of 0.1% z_{therm} equals $0.045*x_f$. Therefore the influence of the height of the thermistors on the thermistor position is very small.

7.4.3 Anisotropic permeability measurement in an arbitrary direction

As discussed in section 5.3 the out-of-plane permeability should be in almost all cases normal to the x,y plane. It is mainly the in-plane principal permeability which can have different orientations. In this case the rotation takes place about the z-axis. The coordinate transformation can be written as (an extension of equation (6.30) on page 67):

$$\begin{aligned} x' &= r\cos\varphi \\ y' &= -r\sin\varphi \\ z' &= z \end{aligned} \qquad (7.84)$$

The radius for the quasi-isotropic system can written in three dimensions (in the same way as in section 6.5):

$$r' = \sqrt{r\left[\left(\frac{K_2}{K_1}\right)^{1/2}\cos^2\varphi + \left(\frac{K_1}{K_2}\right)^{1/2}\sin^2\varphi\right] + z\left(\frac{K_1K_2}{K_3}\right)^{1/2}} \qquad (7.85)$$

For in-plane permeability measurement only the x,y-coordinates are required (z is set to zero). Equation (7.85) then becomes identical to equation (6.38) (on page 68) - hence the rotation behaviour is exactly as in the two-dimensional case. Only F_i and C are different. For three-dimensional radial flow C becomes:

$$C = \frac{\mu\varepsilon}{6\Delta P} \qquad (7.86)$$

while F_i (for $i = I,II,III$) is:

$$F_i = \left[\frac{2r_{f,i}^3}{r_{o,\mathrm{mod};i}} - 3r_{f,i}^2 + r_{o,\mathrm{mod};i}^2 \right] \frac{1}{t_i} \qquad (7.87)$$

In-plane permeability is obtained as described in sections 6.7.5 and 6.7.6.

8. Formulation of a unified approach to permeability measurement

8.1 Introduction

In the literature each permeability measurement technique is treated as a separate approach with no connection to other measurement techniques. However permeability is a parameter of the porous material which should be independent of the technique used. Hence all measurement techniques must be related if they have Darcy's law as their basis. In this chapter a unified approach to permeability measurement is proposed which unifies most of the current permeability measurement techniques. First the theoretical justification for the unified approach will be given. This is followed by a detailed description of the unified. After that, current permeability measurement techniques are classified according to the new unified approach and differences to the unified approach are discussed.

8.2 The theoretical foundation of the unified approach

This section follows section 5.6 in Bear (1972). Please note that for this section Bear's notation is adopted which is different to the notation used in this thesis. Bear defines Darcy's law as follows:

$$\mathbf{q} = \frac{\underline{\mathbf{k}}}{\mu}\mathbf{J} \qquad (8.1)$$

where $\mathbf{q}$ is the specific discharge (the discharge per unit cross-sectional area), $\mathbf{J}$ is the hydraulic gradient (e.g. $J_x = -\partial P/\partial x$), μ is the viscosity and $\underline{\mathbf{k}}$ is the permeability tensor. From (8.1) it follows that the vectors $\mathbf{q}$ and $\mathbf{J}$ are only collinear when they are in the direction of one of the principal axes. The angle θ between the vectors $\mathbf{q}$ (components: q_x, q_y) and $\mathbf{J}$ (components: J_x, J_y) is given by (Bear):

$$\cos\theta = \frac{\mathbf{qJ}}{qJ}; \qquad q \equiv |\mathbf{q}|, \qquad J \equiv |\mathbf{J}| \qquad (8.2)$$

When x, y are the principal direction of the permeability, we have

$$\cos\theta = \frac{k_x J_x^2 + k_y J_y^2}{\mu q J} \qquad (8.3)$$

Following the definition of permeability in Darcy's law for an isotropic medium, the directional permeability can be defined as the ratio of the specific discharge at a point and the

component of the gradient in the direction of **q**. The directional permeability in the direction of the flow can be written:

$$k_q = \frac{\mu q}{J\cos\theta} \qquad (8.4)$$

From (8.2) and (8.3) it follows that:

$$k_q = \frac{\mu q}{J\cos\theta} = \frac{\mu q^2}{\mathbf{qJ}} = \frac{\mu^2 q^2}{(\underline{\mathbf{k}}\mathbf{J})\mathbf{J}} = \frac{k_x^2 J_x^2 + k_y^2 J_y^2}{k_x J_x^2 + k_y J_y^2} \qquad (8.5)$$

Let β_1 and β_2 denote the angles between the direction of **q** and the two principal axes x and y respectively (see Figure 8.1). Then:

$$q_x = \frac{k_x}{\mu} J_x = q\cos\beta_1 \; ; \quad q_y = \frac{k_y}{\mu} J_y = q\cos\beta_2 \qquad (8.6)$$

By combining (8.5) and (8.6)

$$\frac{1}{k_q} = \frac{\cos^2\beta_1}{k_x} + \frac{\cos^2\beta_2}{k_y} \qquad (8.7)$$

Rearranging equation (8.7) with $\cos^2\beta_2 = \sin^2\beta_1$ yields:

$$k_q = \frac{k_x k_y}{k_x \sin^2\beta_1 + k_y \cos^2\beta_1} \qquad (8.8)$$

This defines the directional permeability in terms of the principal permeabilities and their orientation. For simplicity the directional permeability is shown here only in two dimensions. Bear also derived directional permeability for three dimensions.

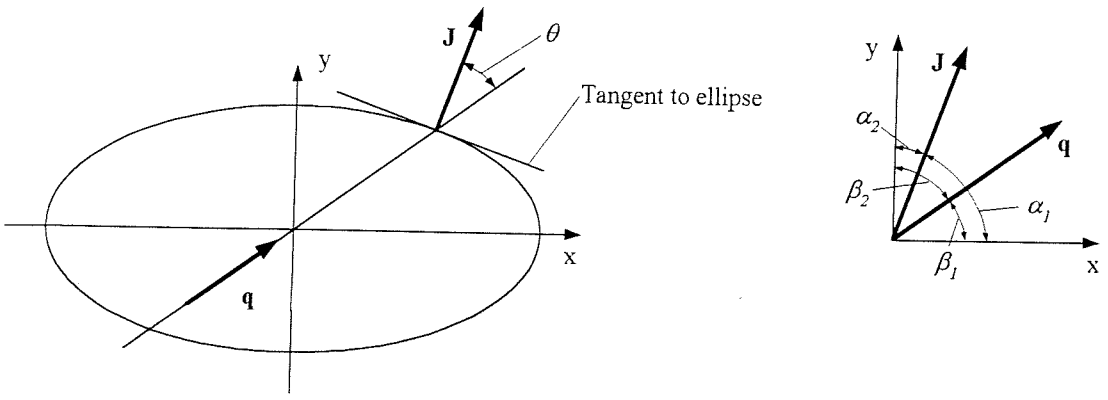

Figure 8.1 Directional permeability for flow in anisotropic porous media (Bear 1972)

For completeness the other possible definition of directional permeability is listed here. For the case where the directional permeability is measured in the direction of the gradient **J** permeability can be written as follows (Bear):

$$k_J = k_x \cos^2 \alpha_1 + k_y \sin^2 \alpha_1 \qquad (8.9)$$

Comparing equation (8.8) with the effective permeability for channel flow (equation (5.13) on page 48) shows that both are identical. The same is possible for radial flow. For example if equation (6.46) on page 69 is multiplied with $K' = \sqrt{K_1 K_2}$ and divided by the expression in the round bracket then $F_1 * C$ is equal to the directional permeability as defined in equation (8.8). This demonstrates that both channel flow and radial flow are based on the same directional permeability.

Equation (8.8) is the theoretical justification for proposing a single set of standard equations to calculate permeability for all the experimental configurations discussed in chapters 5, 6 and 7. The derivations for channel flow and radial flow differ because the former is derived from the effective permeability while the latter uses the quasi-isotropic permeability of the scaled domain as the starting point. The details of the standard equations will be outlined in the next section.

8.3 Standard equations for permeability calculation

8.3.1 Schematic and basic equations

Figure 8.2 shows schematically the different configurations of the permeability experiments for channel flow and radial flow. All five configurations are based on Darcy's law. For constant inlet pressure there is no pressure measurement at a point. This is because for constant inlet pressure the flow front radius can only be expressed in terms of the pressure at the point of interest and the inlet pressure (equation (7.4), page 100). Therefore it is impossible to come up with two different expressions for measurement of pressure drop or pressure at a point. It is conceivable to derive the five different configurations shown in Figure 8.2 also for three-dimensional radial flow. However at the moment only constant inlet pressure with measurement of the flow front has been implemented (for reasons which become apparent in chapter 11).

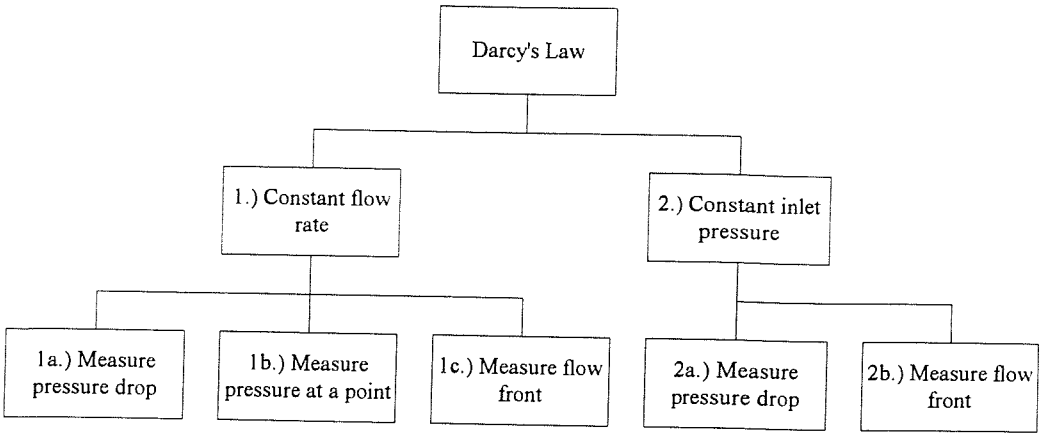

Figure 8.2 Schematic of permeability measurement techniques

All the equations on the last level of the schematic (1a, 1b, 1c, 2a and 2b in Figure 8.2) have a common structure which is due to the fact that the measured effective permeability is the same for both channel flow and radial flow as shown in the previous section. The standard equations for permeability measurement in an arbitrary direction are introduced below. This is followed by an simplified subset for measurements along the principal axes.

Measurement in an arbitrary direction

For the case where the measurement axis are not aligned with the principal axis the following equations are utilised. The angle of rotation is obtained from

$$\varphi = \frac{1}{2}\tan^{-1}\left(\frac{A}{D} - \frac{A^2 - D^2}{F_{II}D}\right) \qquad (8.10)$$

K_1 can be written as

$$K_1 = F_I \frac{(A-D)}{(A - D/\cos 2\varphi)}C \qquad (8.11)$$

while K_2 can be written as

$$K_2 = F_{III} \frac{(A+D)}{(A + D/\cos 2\varphi)}C \qquad (8.12)$$

where A is defined as:

$$A = \frac{F_I + F_{III}}{2} \qquad (8.13)$$

and D

$$D = \frac{F_I - F_{III}}{2} \qquad (8.14)$$

Measurement parallel to principal axes

If the measurements are taken along the principal axes then φ becomes zero and the rotation terms in equations (8.10) and (8.11) are equal to unity. Therefore K_1 can be simplified to:

$$K_1 = F_I C \tag{8.15}$$

while K_2 can be written as

$$K_2 = F_{III} C \tag{8.16}$$

and finally K_3

$$K_3 = F_{IV} C \tag{8.17}$$

In the next two sections C, F_I, F_{II} and F_{III} will be listed for each type of experiment and their use will be explained. F_{IV} is used only for three-dimensional radial flow and for channel flow.

8.3.2 Modules of the unified approach

Channel flow

For channel flow the modules of the standard equation are defined below (as derived in section 5.1.1). For constant flow rate C is defined as follows:

$$C = \frac{\mu Q}{A_n} \tag{8.18}$$

while for constant inlet pressure the following term is used:

$$C = \frac{\mu \varepsilon}{2\Delta P} \tag{8.19}$$

The F_i's are listed in Table 8.1. Please note that in section 5.1.2 principal permeability and its orientation was derived in terms of the effective permeability rather than F_i * C. This was because experimental data was only available as effective permeability. However both approaches are identical.

Two-dimensional radial flow

The equations for C and F_i from chapters 6 and 7 which are summarised below. For constant flow rate C is defined as follows:

$$C = \frac{\mu \varepsilon}{2} \tag{8.20}$$

while for constant inlet pressure the following term is used:

$$C = \frac{\mu \varepsilon}{4\Delta P} \tag{8.21}$$

F_i for each type of experiment is listed in Table 8.2.

Type	F_i
1a	$\dfrac{\left(x_{2,i}-x_{1,i}\right)}{\left(P_{1,i}-P_{2,i}\right)}$
1b	$\dfrac{Q\left(t_i-t_{2,i}\right)}{P_{2,i}A_n\varepsilon}$
1c	$\dfrac{x_{f,i}}{P_o}$
2a	$\dfrac{\left[\dfrac{P_o x_{1,i}}{P_o-P_{1,i}}\right]^2}{t_i}$
2b	$\dfrac{x_{f,i}^2}{t_i}$

Table 8.1 F_i modules for channel flow

Type	F_i
1a	$\dfrac{\left(r_{2,i}^2-r_{1,i}^2\right)\ln\left(r_{2,i}/r_{1,i}\right)}{\left(t_{2,i}-t_{1,i}\right)\left(P_{1,i}-P_{2,i}\right)}$
1b	$\dfrac{\left(r_{2,i}^2-r_{o,\mathrm{mod};i}^2\right)\dfrac{1}{2}\ln\left(\dfrac{Q\left(t_i-t_{2,i}\right)}{\pi h\varepsilon r_{2,i}^2\left(\sqrt{\alpha}\cos^2\varphi+\sqrt{1/\alpha}\sin^2\varphi\right)}+1\right)}{t_i P_{2,i}}$
1c	$\dfrac{\left(r_{f,i}^2-r_{o,\mathrm{mod};i}^2\right)\ln\left(r_{f,i}/r_{o,\mathrm{mod};i}\right)}{t_i P_o}$
2a	$\dfrac{\exp\left(2\dfrac{P_o\ln\left(r_{1,i}\right)-P_{1,i}\ln\left(r_{o,\mathrm{mod},i}\right)}{P_o-P_{1,i}}\right)\left[2\ln\left(\dfrac{\exp\left(\dfrac{P_o\ln\left(r_{1,i}\right)-P_{1,i}\ln\left(r_{o,\mathrm{mod};i}\right)}{P_o-P_{1,i}}\right)}{r_{o,\mathrm{mod};i}}\right)-1\right]+r_{o,\mathrm{mod};i}^2}{t_i}$
2b	$\dfrac{r_{f,i}^2\left[2\ln\left(r_{f,i}/r_{o,\mathrm{mod};i}\right)-1\right]+r_{o,\mathrm{mod};i}^2}{t_i}$

Table 8.2 F_i modules for two-dimensional flow

Three-dimensional radial flow

As already mentioned, for three-dimensional flow only constant inlet pressure with measurement of flow front have been derived. The two equations for C and F_i ((7.86) and (7.87)) are repeated below:

$$C = \frac{\mu\varepsilon}{6\Delta P} \qquad (8.22)$$

$$F_i = \left[\frac{2r_{f,i}^3}{r_{o,\mathrm{mod};i}} - 3r_{f,i}^2 + r_{o,\mathrm{mod};i}^2 \right] \frac{1}{t_i} \qquad (8.23)$$

Radii

The inlet radius $r_{o,\,\mathrm{mod};i}$ was defined in section 6.7.2 for measurements along the principal axes while in section 6.7.5 the inlet radius was defined for an arbitrary measurement direction. The flow front radius r_f was defined in equation (6.52) on page 69. The definitions of the radii r_1 and r_2 can be found on page 109 (equations (7.61) and (7.62)). The two radii r_1 and r_2 have to be selected far away enough from the inlet to ensure that the flow at r_1 and r_2 is fully developed.

8.3.3 Application of the new approach

First the permeability measurement technique is chosen. Then the appropriate modules (C, F_I and F_{III} or C, F_I, F_{II} and F_{III} and for three-dimensional flow also F_{IV}) can be selected to assemble the equations to determine permeability. First it will be shown how principal permeability is determined when the measurements are carried out along the principal axes. This is followed by the general case where measurements are conducted in an arbitrary direction.

Measurement along principal axis

It is helpful to divide the permeability measurement techniques into two groups. The measurement techniques which do not require the knowledge of the degree of anisotropy and those which do. All channel flow measurement techniques and the radial flow with measurement of pressure drop (1a) do not require previous knowledge of the degree of anisotropy. For these measurement techniques C, F_I and F_{III} are calculated and K_1 and K_2 are obtained from equations (8.15) and (8.16).

The remaining radial flow techniques (1b, 1c, 2a, 2b) are iterative in the degree of anisotropy because the inlet radius $r_{o,\,mod,i}$ depends on α (see section 6.7.2). Therefore F_I and F_{III} are computed with an estimated value for the degree for anisotropy (say 1). Then K_1 and K_2 are calculated and the degree of anisotropy is determined according to:

$$\alpha = \frac{K_2}{K_1} \qquad (8.24)$$

In an iteration loop the guessed value for α is reduced until it matches α calculated according to equation (8.24). For three-dimensional flow the inlet radius for K_3 is assumed not to depend on α . It is assumed to be a tenth of r_o as there is no way to measure the inlet radius directly. Furthermore the flow front radius is simply the z-coordinate of the thermistor.

Arbitrary measurement direction

Again it is useful to separate the permeability measurement techniques into the two groups. For the arbitrary measurement direction in the case of channel flow measurement and radial flow with pressure drop measurement (1a) K_1, K_2 and φ are determined simply by calculating C, F_I, F_{II} and F_{III} .

For the remaining radial flow measurement techniques the inlet radius depends on the degree of anisotropy and the orientation of the principal axes. In addition to the condition that the guessed and calculated degree of anisotropy have to be equal, the guessed and the calculated orientation (equation (8.10)) also have to be the same. Therefore α and φ are initially set to 1 and 0 and F_I, F_{II} and F_{III} are determined. Then α is determined from equation (8.24) and φ is calculated from equation (8.10). First the guessed φ is set to the calculated angle φ . Then the guessed α is reduced until it matches the value for α as calculated by (8.24). After that φ is corrected again and then again α . At this stage the two values of φ and α should have converged to an accuracy of 10^{-5}. If the material is very anisotropic it may be necessary to set α to 0.5 or 0.2 (or 2) rather than 1 in order to help with the convergence of the iterative solution.

8.4 Classification of current permeability measurement techniques

8.4.1 Channel flow

In this section channel flow measurement techniques published in the literature are classified according to Figure 8.2. The main measurement techniques will be discussed in section 8.5.

Author(s)	Comment
Gauvin and Chibani (1986)	-
Kim et al. (1990)	-
Parnas and Salem (1993)	calculate principal permeability and orientation
Trevino et al. (1991)	-
Verheus and Peeters (1993)	vary also thickness of mould

Table 8.3 Channel flow - measure pressure drop for constant flow rate (1a)

Author(s)	Comment
Ferland et al. (1996)	see Table 8.5
Gauvin and Chibani (1990)	-
Gauvin, Kerachni and Fisa (1994)	-

Table 8.4 Channel flow - measure flow front for constant flow rate (1c)

Author(s)	Comment
Ferland et al. (1996)	take into account variation of inlet pressure
Gebart et al. (1991)	-
Gebart (1992)	-
Gebart and Lidström (1996)	calculate principal permeability and orientation
Verheus and Peeters (1993)	-

Table 8.5 Channel flow - measure flow front for constant inlet pressure (2b)

8.4.2 Radial flow

It is possible to classify almost all radial flow permeability measurements techniques published in the literature according to the schematic in Figure 8.2. Only 2a (Constant inlet pressure, measure pressure drop) has not yet been mentioned in the literature. Three-dimensional radial flow is not listed separately as there are so few examples in the literature.

Author(s)	Comment
Bruschke, M. V., (1992)	iterative fitting procedure to measured pressure history
Chick, J. P. et al., (1996)	-
Parnas, R. S., et al. (1995)	see Bruschke
Rudd, C. D., et al., (1995)	see Chick
Steenkamer, D. A., et al., (1995)	see Bruschke

Table 8.6 Radial flow - measure pressure drop and pressure at a point for constant flow rate (1a, 1b)

Author(s)	Comment
Chan, A. W., et al., (1993)	-
Lekakou, C., et al., (1996)	see Chan 1993

Table 8.7 Radial flow - measure flow front for constant flow rate (1c)

Author(s)	Comment
Adams, K. L., et al., (1986)	First paper to mention the radial flow test, formula for isotropic permeability
Adams, K. L., et al., (1987)	anisotropic permeability, elliptical coordinates
Adams, K. L., et al., (1988)	more comprehensive discussion than Adams 1987
Adams, K. L., et al., (1991)	see Adams 1987
Ahn, S. H., et al., (1995)	see Chan and Hwang 1991, also developed three-dimensional permeability measurement technique
Carronnier, D., et al., (1995)	see Adams 1987
Carter, E. J., et al. (1995)	see Carter 1995a
Carter, E. J., et al. (1995a)	modified version of Chan and Hwang 1991
Chan, A. and Hwang, S., (1991)	anisotropic permeability, polar coordinates
Gauvin (1996)	Chan and Hwang 1991
Gebart 1996	see Adams 1988
Hammami, A., et al. (1995)	see Chan and Hwang 1991
Hirt, D. E., et al., (1987)	see Adams 1987
McGeehin, P. M., et al., (1994)	see Rudd 1992
Rudd, C. D., et al., (1992)	modified version of Adams 1987

Table 8.8 Radial flow - measure flow front for constant inlet pressure(2b)

Author(s)	Comment
Greve and Soh, (1990)	Constant flow rate; anisotropic permeabilities are calculated from area of flow domain and the flow front ratio
Wang, T. J., et al., (1992)	Constant flow rate; circular fibre samples. Having measured the ratio of the flow front and the orientation of major axis a flow simulation is used to find the K_1 and K_2.
Wang, T. J., et al., (1994)	Constant flow rate; the authors suggest two algorithms which do not require observation of the flow front. However these algorithms are only of theoretical interest as they give accurate results only for isotropic materials. Furthermore circular fibre samples are required which is difficult to produce in practice.
Wu, C.-S., (1993)	see Wang
Young and Wu, (1995)	Constant flow rate; steady flow with circular inlet and square edges. Use observed angle of orientation of flow front ellipse, flow front ratio and numerically calculated shape factor to find permeabilities.

Table 8.9 Radial flow - other measurement techniques

In section 8.6 the most important radial flow permeability measurement techniques will be discussed and compared with the unified approach. For constant flow rate this will be Bruschke (1992), Chick et al. (1996) and Chan et al. (1993). The following constant inlet pressure techniques will be discussed: Adams et al. (1988), Chan and Hwang (1991) and Carter et al. (1995b).

The discussion will focus on two-dimensional flow measurement techniques as only one three-dimensional permeability measurement technique was mentioned in the literature. Ahn et al. (1995) has independently derived equations identical to (7.77), (7.78) and (7.79).

8.5 Discussion of channel flow measurement techniques

There are three measurement techniques which are widely used. The constant flow rate technique with stationary flow front where the pressure drop is measured. There are also the

constant inlet pressure or constant flow rate techniques where the progression of the flow front is measured. All three techniques are reported to give reliable results. Ferland et al. (1996) propose a interpolation method which takes into account variations of the inlet pressure (Concurrent Permeability Measurement Procedure, CPMP). The results suggest that this method works well. However in the derivation of this method Ferland did not included the porosity (as e.g. in C of the unified approach, equation (8.19)). Permeability calculated by CPMP is therefore always too low (by a factor equal to the inverse of porosity).

Only two methods exist (Gebart and Lidström 1996, Parnas and Salem 1993) for determining principal permeability and orientation in channel flow. The method proposed by Gebart and Lidström was shown to be identical to the approach proposed here (section 5.2). Parnas and Salem reduce the number of experiments by using an average degree of anisotropy and angle of orientation of the permeability tensor for different fibre volume fractions (see chapter 5). The other possible configuration suggested in section 5.1 (1b and 2a in Figure 8.2) have not been verified experimentally. Results from numerical studies reported by Woerdeman et al. (1995) seem to suggest that the pressure distribution in the channel flow mould for anisotropic flow is not linear any more. The pressure varies widthways. It may therefore be possible that measurement of pressure at a point in the mould will not yield very accurate results. More work is required to investigate this. It might be possible that by using narrow moulds these effects may become negligible.

8.6 Discussion of radial flow measurement techniques

8.6.1 Constant flow rate

Bruschke (1992)

Bruschke proposed a constant flow rate permeability measurement technique. It utilises three pressure measurements with one pressure transducer located at the inlet and the other two transducers positioned on the two principal axes. A least square method is used to fit equations to the measured pressure history using K_1 and K_2 as the fitting parameters. However the derivation of this algorithm contains a number of shortcomings. Firstly there is no explicit porosity term in Bruschke's method. The porosity was left out in equation 2.88 of Bruschke (1992) where the flow rate is related to the flow front progression. Furthermore the formulation for the expression which is substituted for the flow front radius is not correct (equation 2.91 in Bruschke (1992)). It contains as the fixed radius the inlet radius. This is true only for pressure measurement at the inlet. For the measurements at the principal axes this leads to an error in the mass balance. Instead of taking into account the volume of the fluid

which has flown past the transducer from the time the flow front reached the transducer location, the total fluid volume is taken into account. The further away the pressure transducer is positioned from the inlet the larger the discrepancy becomes. Other than that, the equations suggested by Bruscke are identical to equations (7.55) and (7.56) on page 108.

And finally a remark about using a numerical fitting algorithm to find the principal permeabilities. It was shown in section 7.3.1 that the pressure drop between two points for constant inlet pressure remains constant. It is therefore possible to use the formulae for measurement of the pressure drop of the unified approach (1a in Table 8.2) However at the same time it was demonstrated in section 6.7 (for constant inlet pressure) that the flow front displayed a transient behaviour due to the circular inlet. For constant flow rate it can therefore be expected that the inlet pressure deviates from the usual logarithmic distribution. This is supported by experimental results presented in section 10.3 were the pressure measured at the inlet is not parallel to the pressure measurements along the principal axes (Figure 10.3). Hence the pressure drop is not constant. The numerical fitting algorithm will not overcome this discrepancy as this is due to a violation of the boundary condition of the underlying model. The solution is therefore to use the equation for pressure measurement at a point (1b in Table 8.2) and determine the degree of anisotropy iteratively. The pressure measured at the inlet is ignored.

Chick et al. (1996)

Chick et al. (1996) present formulae to calculate permeability from pressure drop measurements and pressure at a point measurements for constant flow rate. However the derivation of this method contains severe limitations. For both cases the principal permeability is derived separately for each direction. In the case of the measurement of pressure drop both equations contain the degree of anisotropy which need to be determined in a separate experiment (or iteratively). However it was demonstrated (see e.g. 1a in Table 8.2) that the principal permeabilities for pressure drop measurements can be written explicitly without the degree of anisotropy. For pressure measurement at a point, by looking only at flow in one direction an error is introduced into the mass continuity. In equations 20 of Chick et al. (1996) the flow rate is expressed as a function of the flow front radius, time, gap height, π, porosity and the degree of anisotropy: $r_f = \sqrt{Qt/\pi h\beta\varepsilon}$ However with this formulation the total fluid volume which has been injected since the start of the experiment is used for the calculations rather than, as intended, the volume of fluid which has flown past the pressure transducer. This difference only becomes apparent when the second point of criticism is considered.

To determine permeability Chick et al. (1996) define a constant λ which is obtained by plotting pressure versus ½ln(time). This relation is obtained by rearranging equation 23 in Chick et al. (1996): $p_x = \frac{1}{2}\lambda \ln(t) + \frac{1}{2}\lambda \ln(Q/\pi h\beta\varepsilon) - \lambda \ln(r_x)$. The right hand side of equation 23 has three terms which all contain λ. However in the process of rearranging terms 2 and 3 of the right hand side are simply ignored. Therefore λ (in Chick et al. (1996)) is only a function of time and pressure with no reference to the location of the pressure measurement. That is why the error in the mass balance did not effect the calculated permeability values.

Chan et al. (1993).

Chan et al. (1993) developed a permeability measurement technique for constant flow rate and measurement of the progression of the flow front. For the case of anisotropic flow, the flow front is scaled in the same way as in Chan and Hwang (1991). The equation presented by Chan for the isotropic case is identical to the one developed in section 7.3.1. The equivalent equation for anisotropic flow however, only contains the flow front radius as argument for the natural logarithm rather than the ratio of the flow front and inlet radii (see e.g. 1c in Table 8.2). In addition an intercept is calculated when F_i is determined. This is not correct if the permeability is assumed to be constant. Hence the regression line has to go through the origin.

8.6.2 Constant inlet pressure

Adams et al. (1988)

Adams et al (1986) were the first to propose the radial flow technique for permeability measurement in RTM. Adams et al (1988) published a set of equations to determine anisotropic permeability from flow front measurements made along the principal axes for constant inlet pressure. The method was developed using elliptical coordinates. It is iterative in the degree of anisotropy. Also the flow front measurements made along the two principal axes can be made at different time steps. These attributes are the same as for the unified approach. As the comparison in section 6.9 showed the agreement between the two methods is very good.

The only question about Adams' method is that in the experiment the stop watch is only started after the flow front in the x-direction has advanced by 5mm (see Adams and Rebenfeld (1987)). It is not quite clear from the derivations published in Adams et al. (1988) how this has been taken into account in the formulae for permeability calculation. However for typical injection times of 500 to 1500 seconds a small error of a few seconds (which the flow front will take to cover the first 5mm) is negligible.

Chan and Hwang (1991)

The procedure to determine permeability by Chan and Hwang (1991) uses polar coordinates as in the unified approach. The formula to calculate principal permeability uses ratios of flow front and inlet radii. Both radii are scaled by equation (6.8) on page 61. Because ratios of radii are used these scaling factors cancel. This is tantamount to using a circular inlet. The effect on the accuracy of the calculated permeability has been discussed in sections 6.7 and 6.8.3. A comparison with other methods in section 6.9 revealed that Chan and Hwang's method yields results which are noticeably different from the unified approach and Adams et al. (1988).

Carter et al. (1995b)

The method proposed by Carter et al. (1995b) is very similar to the method suggest by Chan and Hwang (1991). However a very important difference exists between the two methods. Carter does not scale the inlet diameter prior to calculating F_1 (Carter (1996)). Hence a ratio of the scaled flow front radius and unscaled circular inlet radius is used to obtain F_1. Careful comparison of the unified approach for flow front measurement along the principal axes (see sections 6.7.2 and 6.7.3) with Carter reveals that the methods are identical. However the calculated principal permeabilities are not always the same. This is because Carter et al. (1995b) do not force the regression line of N_1 versus time through the origin as required for constant permeability. Some difference arises from the fact that Carter et al. obtain α from plotting the flow front radius in the direction of the **2**-axis versus the flow front radius along the **1**-axis. This is not always the same as α obtained by the unified approach where not only the flow front radius but also time is taken into account (F_{111}/F_1).

In summary it can be said that the method by Carter et al. (1995b) is almost identical to the unified approach. The only differences are the way the degree of anisotropy is determined and how F_1 is obtained. In practice these differences are very small. The application of Carter et al. (1995b) is restricted to measurements along the principal axes and for flow front measurements taken at the same instance in time for both directions.

9. Experimental philosophy

9.1 Aim of experiments

The aim of the experiments has been to verify the unified approach to permeability measurement. In particular the effect of varying the thickness, the fibre volume fraction, inlet pressure and measurement angle on the measured permeability were studied. An additional aim was to explore whether three-dimensional permeability measurement (with thermistors) is feasible.

9.2 Analysis of experimental data

Permeability is calculated from the flow front position or pressure measured at various time steps. The theory of calculating permeability from the experimental data has been presented in chapter 8. The standard equations of the unified approach can be found in section 8.3.1. The necessary modules for each selected experimental configuration are listed in section 8.3.2. The usage of the standard equations is explained in section 8.3.3.

9.3 Experimental procedure

9.3.1 Radial flow mould

The test rig is of modular design and is suitable for radial and channel flow tests (see for more details Appendix C). It has an aluminium work surface with a supporting steel structure and maximum working section of 400 x 1300 mm. There are 5 possible alternative injection ports. For the radial flow experiments a glass top plate of 400 x 400 x 25 mm is used. The glass is soda-lime toughened float glass. A pressure transfer frame made of steel box sections is used to compress the fibre stack using four M16 bolts. The fluid is injected from a pressure vessel into the mould using compressed air from an air line. A PC is utilised to record and process inlet pressure transducer and thermistor readings.

9.3.2 Flow front detection

Thermistor sensors have been developed to detect the flow front (Figure 9.1). The initial idea by Trochu et al. (1993) was further developed by Weitzenböck et al. (1995a), (1995b) and (1996). The main aim of this work had been to minimise the flow disturbance caused by the presence of the thermistors.

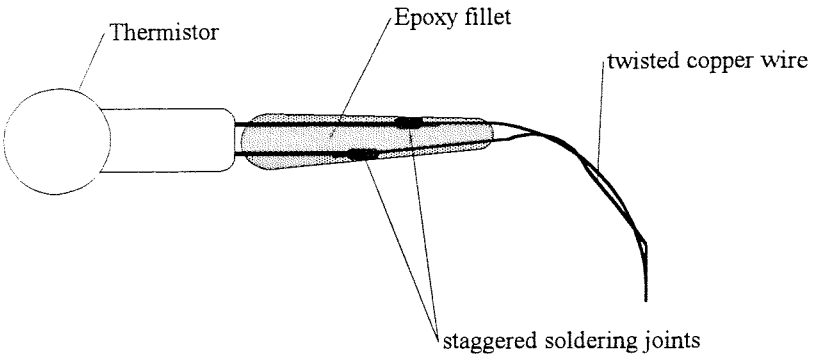

Figure 9.1 Thermistor sensor for flow front measurement

These thermistor sensors are placed at different locations through the depth and width of the mould lay-up (Figure 9.2).

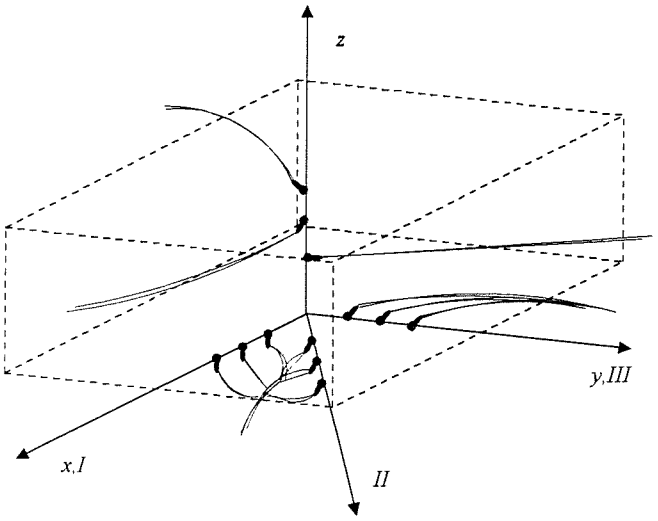

Figure 9.2 Lay-up of thermistors in mould

To measure the in-plane flow front position six thermistors are linked together with thin (less than 1mm wide) strips of masking tape. Figure 9.3 shows a schematic of the multiple flow sensor. In addition fibre bundles are twisted around every wire but the last one to stop unwanted channelling along the wires. This helped to simplify the lay-up process considerably.

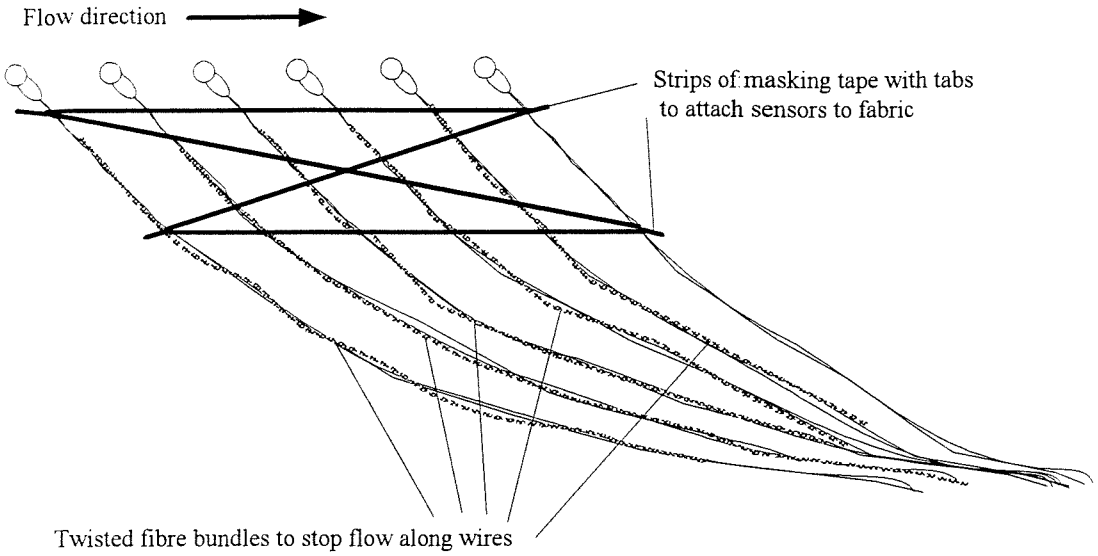

Figure 9.3 Multiple flow sensor

The x, y coordinates of each thermistor head are measured using a tape measure while the through-thickness coordinate is calculated from the ratio of the layer on which the thermistor has been placed to the total number of layers in the stack. This assumes a homogeneous compaction of the fibre mats.

9.3.3 Materials used and lay-up procedure

All the tests were radial flow tests with constant pressure injection. The test fluid was Shell Vitrea M100 oil with a viscosity of 330 mPa at 18^{0}C. The fabrics tested were a continuous filament mat (U750-450) and the twill fabric RC 600 both from Vetrotex and the quasi-unidirectional non crimp fabric E-LPb 567 from Tech Textiles. The thickness of the cavity was 4.65mm for the two-dimensional test and 20mm for the three-dimensional flow tests. To ensure a uniform inlet condition for the two-dimensional tests a 12.7mm diameter hole was punched at the centre of each layer. The diameter of the inlet is 10.5mm. For some of the two-dimensional and three-dimensional constant inlet pressure experiments the measurement coordinate system was rotated by 15°.

10. Results

10.1 Introduction

In this chapter the results from constant inlet pressure and constant flow rate experiments are reported. The first three series of constant inlet pressure experiments were conducted in the Ship Science Laboratory of the University of Southampton. To test more aspects of the unified approach experimental results from other researchers were used as well. Some constant inlet pressure results from the University of Plymouth (Fell and Summerscales 1996) and also results from constant flow rate experiments from the University of Nottingham (Morris and Rudd 1996). In the next chapter these results will then be discussed.

10.2 Constant inlet pressure experiments

10.2.1 Initial experiments

The permeability of radial flow tests on a continuous filament mat from Vetrotex (U750-450) are summarised in Table 10.1. They show the permeability for different fibre volume fractions and injection pressures. It is interesting to note that the permeability is slightly lower when injecting at a higher pressure; for instance at a fibre volume fraction of 22.7% (run 7), K_1 is 1636 at 114 kPa and 1488 at 214 kPa (run 6) [both 10^{-12} m^2]. Another observation is that the calculated orientation is not very consistent. Table 10.1 also gives some results from injection tests into thick laminates. For run 9 a gap height of 20.5mm (35 plies) was used while for runs 11 and 12 the gap height was 25.1mm (43 plies). A small dependence on pressure is noticed here as well. The through-thickness permeability K_3 is higher than the in-plane permeabilities.

Run No.	Results				Factors	
	K_1	K_2	K_3	orientation	V_f [%]	P_o [kPa]
5	358	364		9.99°	45.5	91
6	1488	1594		-0.68°	22.7	214
7	1636	1593		-2.20°	22.7	114
8	321	297		15.83°	45.5	255
9	1320	1273		-	29.5	167
11	538	539	1462	-	29.8	124
12	323	455	987	40.01°	29.8	127

Table 10.1 Permeability for continuous filament mat U750-450 [10^{-12} m^2]

10.2.2 Three-dimensional flow

The results of the permeability tests on twill fabric (RC600 from Vetrotex) are shown in Table 10.2. Runs 1 to 4 are two-dimensional flow experiments with a gap height of 4.65mm which are used for control purposes. Runs 5 and 7 are the results from tests with 20mm gap height and 44 layers of twill fabric. Run 5 compares well with the two-dimensional results. This is not the case for run 7 which is at least one order of magnitude larger than the other results.

Run No.	Results				Factors		
	K_1	K_2	K_3	orientation	angle	V_f [%]	P_o [kPa]
1	50.5	24.5		5.90°	0°	50.4	110
2	22.2	13.6		6.60°	15°	60.5	106
3	48.4	43.5		-11.49°	15°	50.4	200
4	26.1	12.2		1.68°	0°	60.5	195
5	39.9	20.9	1.27	-14.68°	15°	51.6	101
*7**	*5562*	*1609*	*13.0*	*-24.08°*	*0°*	*51.6*	*185*

Table 10.2 Permeability for twill fabric RC600 [10^{-12} m^2]

** permeability values are too high due to channelling, see discussion below*

It was observed in most experiments that the flow front was quite irregular, in particular for small radii. In many cases the flow front was hexagonal which later became elliptical (it followed the diagonal of the crossover points of the twill fabric). In one case (run 3) the flow front was almost circular! Also, for large flow front radii, the flow front sometimes developed a "sharp tooth" at various points along the flow front (run 2 and 4). The calculated angle of orientation is quite consistent for the two-dimensional experiments (except run 3) while for three-dimensional flow it varies considerably. Please note that the orientation is always measured from the (unrotated) x-axis (0°). The results obtained in the rotated coordinate system have been corrected for the rotation.

For run 5 it was observed that the flow front velocity was very slow - it took three hours to complete the experiment. There seemed to be no sharp flow front any more further away from the inlet. This could be seen when the flow front reached the glass plate. Initially only the fibre bundles were wetted with oil - the pores were filled later (after four to five minutes). As a consequence the thermistor readings do not give a very distinct reading any more. The voltage changes very slowly with a total voltage drop of the same order as for faster fluid velocities. The other three-dimensional flow test (run 7) showed a completely different behaviour. The

test was completed in less than 8 minutes. After about one minute oil was emerging from one side. It appeared that the oil had formed a channel between the base plate of the mould and the fibres hence accelerating the flow. The wet out in the vertical direction was then taking place over virtually the whole area of the sample hence the remarkable difference in the fill time (and permeability).

In general it was observed that the flow front in the part of the mould where the thermistor sensors had been placed was lagging behind compared with other undisturbed parts of the mould. Furthermore when oil started to emerge from the side of the mould in run 7 it first appeared in a region with no thermistors. The reason for that is probably local compaction due to the presence of the thermistors. The efforts to try to reduce the channelling along the thermistor wires increases the thickness of the whole sensor which invariably reduces the fibre volume fraction. It appears that the balance between these two opposing factors has yet to be found. For future tests it seems advisable to use smaller fibre bundles and to increase the thermistor spacing.

10.2.3 Two-dimensional flow

The results of the two-dimensional flow permeability experiments are shown in Table 10.3. They were obtained for the quasi-unidirectional non-crimp fabric E-LPb 567 from Tech Textiles. For all experiments the gap height was 4.65mm.

Run No.	Results			Factors		
	K_1	K_2	orientation	angle	V_f [%]	P_o [kPa]
1	109	32.8	0.59°	15°	49.9	55
2	140	33.1	2.84°	0°	49.9	50
3	152	42.0	5.88°	0°	49.9	245
4	298	61.4	-13.64°	0°	44.3	54
5	177	36.8	1.16°	15°	49.9	243
6	324	90.7	3.07°	15°	44.3	245
7	280	61.7	-0.59°	15°	44.3	57
8	316	82.9	-3.12°	0°	44.3	246

Table 10.3 Permeability for quasi-unidirectional non crimp fabric E-LPb 567 [10^{-12} m^2]

Permeability for all 8 runs is not quite as anisotropic as expected which is probably due to the thermistors as discussed below. For runs 1 and 8 the initial flow front was jagged which soon

became smooth and regular again. Despite the low injection pressure for runs 1, 2, 4 and 7 no (or very little) capillary flow was observed in the fibre bundles. Only when the injection pressure was switched off developed a noticeable capillary flow. Some variation of the orientation can be observed (this time orientation is measured between the x-axis and the minor axis (2-axis) of the flow front ellipse, see Figure 10.1).

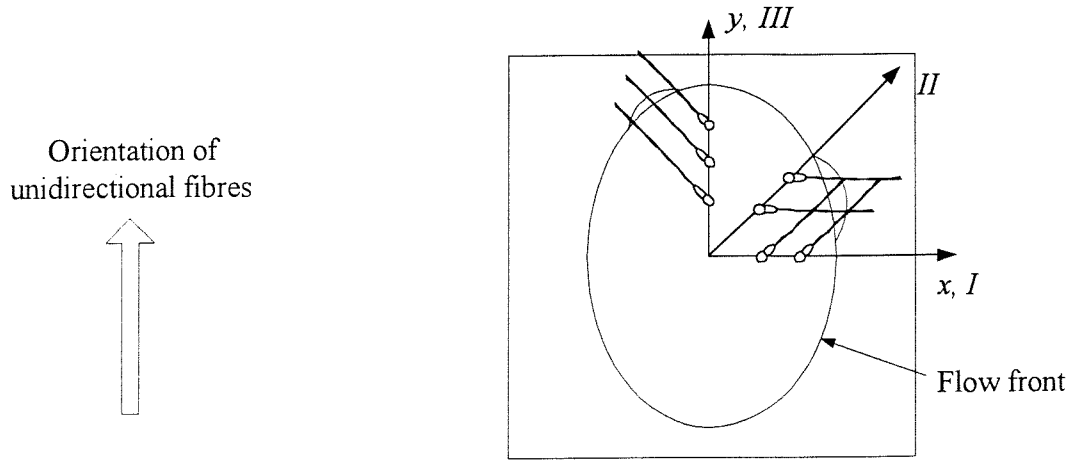

Figure 10.1 Lay-up of thermistors in mould

As in the previous section the thermistors influenced the flow of the fluid. In particular where the wires were led to the data acquisition system out of the mould a "bulge" formed in the flow front (see Figure 10.1). Depending on the orientation of the flow, the thermistors and their wires influenced the flow in a different way. For flow along the x-axis the flow front was ahead of the undisturbed flow front in x-direction. This was observed mainly at high inlet pressure (runs 3,6,7 and 8). The opposite effect was observed for flow along the y-axis. For runs 4 and 7 (low injection pressure) the flow front was lagging behind the flow in the y-direction.

10.2.4 Other experimental results

The following test results were made available by the University of Plymouth (Fell and Summerscales (1996)). The tests were carried out in a constant inlet pressure apparatus with a square glass top plate. The aluminium base plate can be heated if required. The flow front was recorded using a frame grabber. The images were processed to find the flow front coordinates at 15° intervals for each time step. Further details can be found in Carter et al. (1995). The fabrics used were for set 1 a balanced satin weave, for set 2 a twill weave with flow-enhancing weft threads and for set 3 a quasi-unidirectional fabric. The fluid used was an epoxy resin.

set 1			set 2			set 3		
K_1	K_2	orientation	K_1	K_2	orientation	K_1	K_2	orientation
16.0	15.3	-1.4	59.3	16.0	2.1	18.5	3.5	1.4

Table 10.4 Average principal permeability [10^{-12} m^2] and orientation

set 1		set 2		set 3	
K_1	K_2	K_1	K_2	K_1	K_2
17.9	17.8	61.9	15.2	18.5	3.7

Table 10.5 Principal permeability [10^{-12} m^2] (Fell and Summerscales 1996)

Table 10.4 lists the permeability results and orientation for the three different test calculated according to the unified approach. Table 10.5 gives principal permeability calculated by Fell and Summerscales (1996) using Carter et al. (1995b). For set 2 and 3 the results are in close agreement. Only for set 1 there are small differences. This is possibly due to the fact that the flow front of set 1, the balanced satin weave, was not symmetric. The flow seemed to be off-set as shown in Figure 10.2. This is also reflected in the calculated permeability values which do vary depending on measurement direction. Also the calculated measurement direction fluctuates. The results for set 2 and 3 are very consistent.

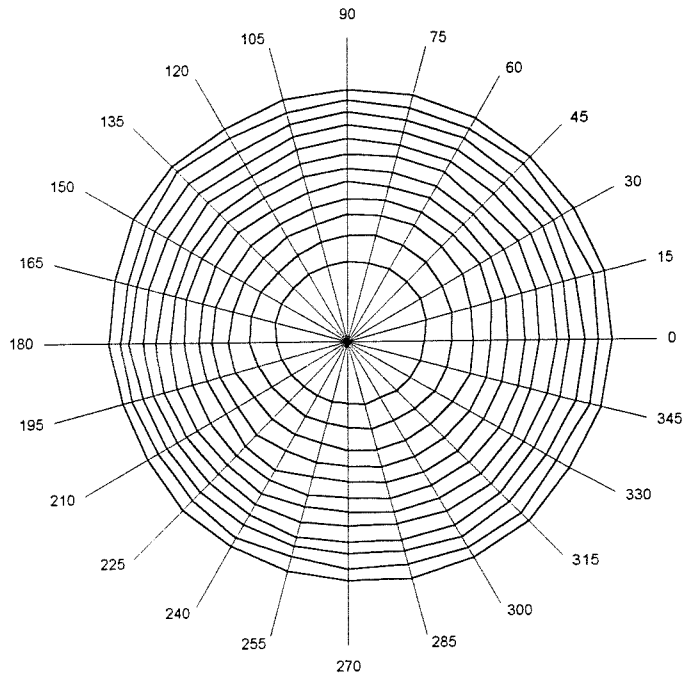

Figure 10.2 Measured flow front positions for satin weave (Fell and Summerscales 1996)

10.3 Constant flow rate experiments

The experimental results in this section were provided by the University of Nottingham (Morris and Rudd 1996). These results are for Tech Textile E-LPb 567 quasi-unidirectional non-crimp fabric. For the experiments a bench-top experimental rig was used with pressure transducers located along a pair of orthogonal axes. To generate the constant fluid flow rate a cylinder was placed in an Instron Universal testing machine. More details can be found in Rudd, Morris, Chick and Warrior (1995). During the experiments the pressure as a function of time was measured for each transducer location. Figure 10.3 shows a typical result. P_{Centre}, P_{Xin}, P_{Xmid}, and P_{Y28} are pressure measurements at various locations in the mould (inlet and x,y-axis).

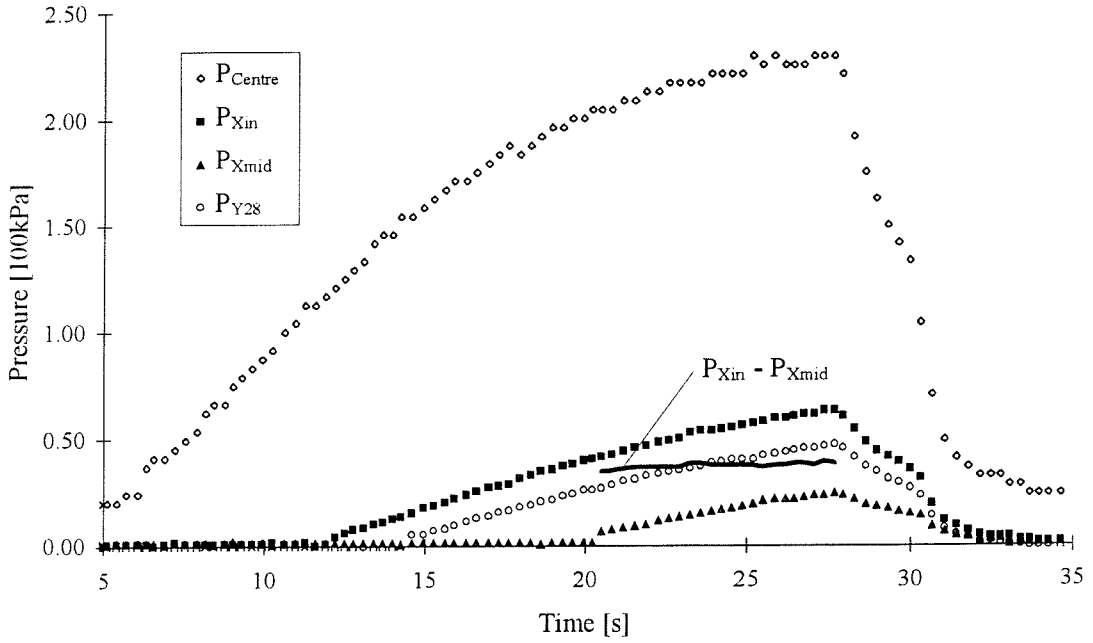

Figure 10.3 Typical pressure history of an experiment (Morris and Rudd 1996)

11. Discussion of results

11.1 Constant inlet pressure experiments

11.1.1 Initial experiments

Runs 5 to 8 where conducted without thermistors. The flow front was measured from video images. The results agree reasonably well for each fibre volume fraction. However the orientation varies between for the two fibre volume fractions. For the three-dimensional flow results larger scatter can be observed. Only the results for run 9 are reasonably consistent with the two-dimensional results. The permeability obtained for runs 11 and 12 is considerably lower than for runs 6 and 7 even though the fibre volume fractions are similar. One explanation is that by placing the thermistors in the fibre stack the fibre volume fraction was increased (or the porosity was reduced). When these (initial) experiments were conducted the thermistor sensors and test procedures where still under development. That might be another reason for the inconsistency of the results.

11.1.2 Three-dimensional permeability

Thermistor signal

By analysing the variation of the thermistor voltage as a function of time, it is possible to extract more information than the time the flow front takes to reach the thermistor position. Figure 11.1 shows voltage readings of four thermistors positioned along the x-axis (run 5). It is interesting to observe how the thermistor response changes with time (and increasing distance away from the inlet). First there is a very sharp drop (thermistor 3) which slowly starts to become more rounded (6 and 9). In addition a second hump is forming in the lower part of the voltage drop curve (black arrow, 9 and 12). A possible explanation could be that initially there is only macroscopic flow in the pores resulting in the sharp drop of thermistor 3. Capillary flow develops as well, but this is still part of the macroscopic flow front (6). As time progresses, capillary flow is leading the macroscopic flow front by several minutes (observed in run 5) so that the initial curve is caused by capillary flow while the second hump marks the arrival of macroscopic flow front (thermistors 9 and 12).

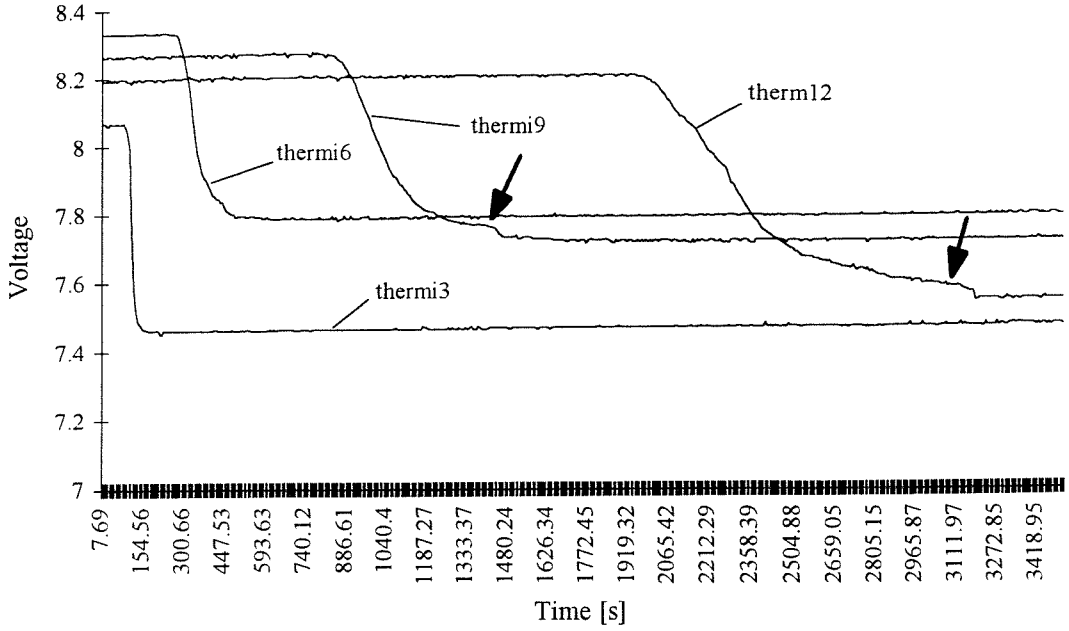

Figure 11.1 Change of thermistor response (run 5)

It is possible to combine point-wise measurements of flow front to obtain an estimate of the orientation of the flow front. Figure 11.2 shows the lay-up which was used in run 7. The flow front first reached thermistor 28 (t = 31.31s), then thermistor 31 (t = 36.80s) and finally thermistor 34 (t = 39.55s). The result for the third thermistor is probably not very accurate as it lies in the wake of the thermistors 28 and 31. The flow times for the first two thermistors indicate that the flow front has more advanced in the *y*-direction than in the *x*-direction. This agrees well with the flow patterns which were observed in the experiment. Oil was emerging at the left hand side (negative *x*-direction) first and last on the right hand side (positive *x*-direction) where most of the thermistors were placed. This is another indication that a series of thermistors does increase the fibre volume fraction.

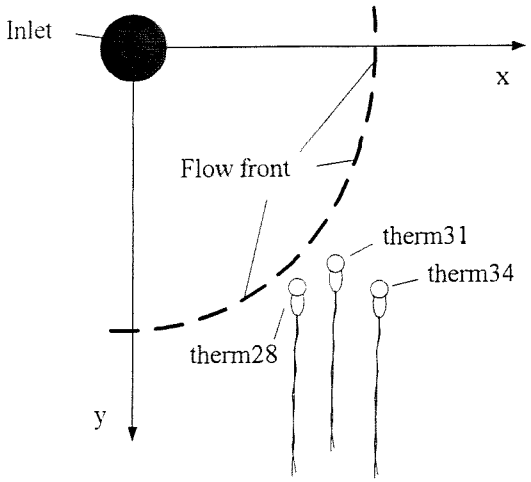

Figure 11.2 Measurement of flow front orientation (run7)

It was also observed that there is some correlation between the fluid velocity and the voltage reading of the thermistor in the wetted domain. Figure 11.3 shows the voltage versus time plot for a thermistor close to the inlet. It clearly shows that the voltage increases with time indicating a drop in velocity (in accordance with the theory). More work is required to correlate voltage measurements with fluid velocity.

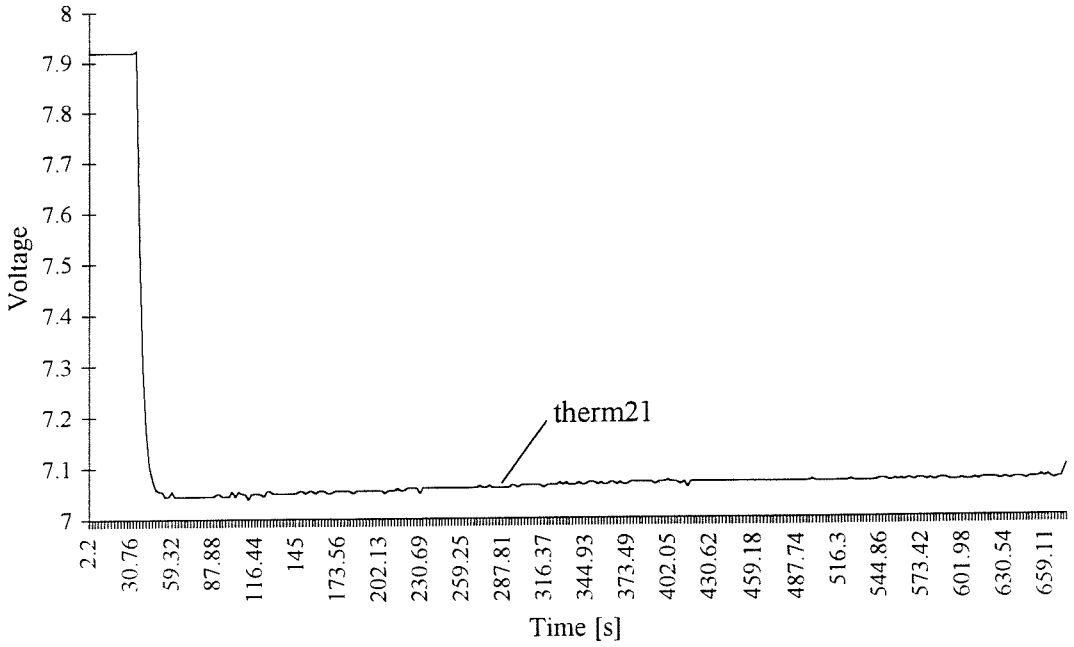

Figure 11.3 Velocity dependence of thermistor reading (run 3)

Figure 11.4 shows the voltage readings of the thermistors which were placed directly above the inlet (run 7). Soon after the start of the injection (~1.5 seconds) a drop in the voltage of all thermistors can be observed. This is clear evidence that with the start of injection the fabric was compacted further, resulting in a channel forming between the fibres and the bottom of the mould. Comparing the thermistor voltage readings for runs 1 to 4 reveal similar voltage drops between the two fibre volume fractions used.

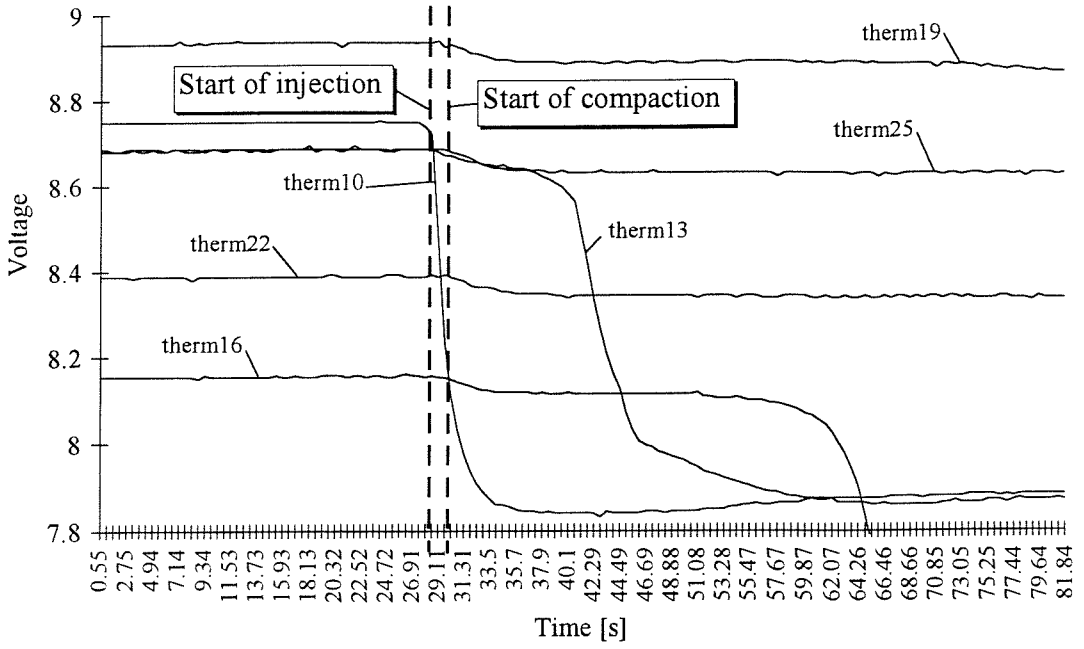

Figure 11.4 Flow induced compaction (injection starts at 28.01s, run 7)

Capillary effects

One way to explain the observed flow patterns is by comparing the pressure distribution of three-dimensional spherical flow with one-dimensional channel flow and two-dimensional radial flow. The pressure distributions are given by the following equations (assuming atmospheric pressure at the flow front):

$$P(x)_{channel} = P_o \frac{x_f - x}{x_f - x_o} \qquad (11.1)$$

$$P(x)_{radial} = P_o \frac{\ln(x/x_f)}{\ln(x_o/x_f)} \qquad (11.2)$$

$$P(x)_{spherical} = P_o \frac{x_f x_o}{x_f - x_o}\left(\frac{1}{x} - \frac{1}{x_f}\right) \qquad (11.3)$$

where P_o is the inlet pressure, x_o is the inlet radius and x_f is the flow front length. In Figure 11.5 the pressure distributions are compared for a given flow front length. This reveals great differences both in magnitude and gradient of the spherical flow compared with the other two tests. This observation is confirmed by plotting the pressure gradient at the flow front for various flow front lengths (Figure 11.6). The small pressure gradient and the low absolute

pressure value at the flow front for the spherical flow case suggest strongly that capillary pressure could be more important than the externally applied inlet pressure.

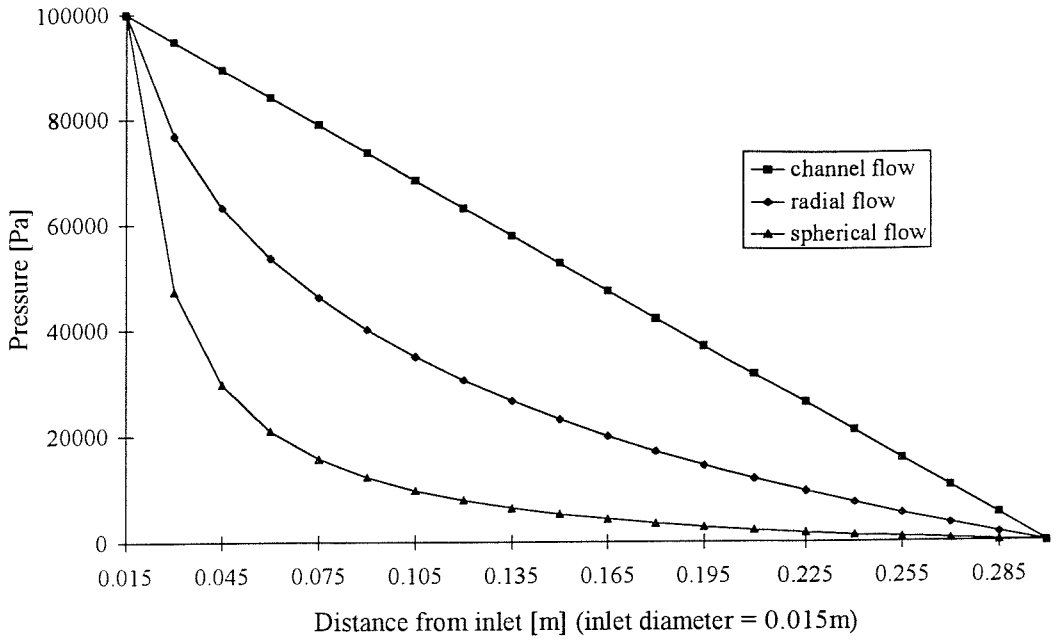

Figure 11.5 Pressure distribution for a given flow front length

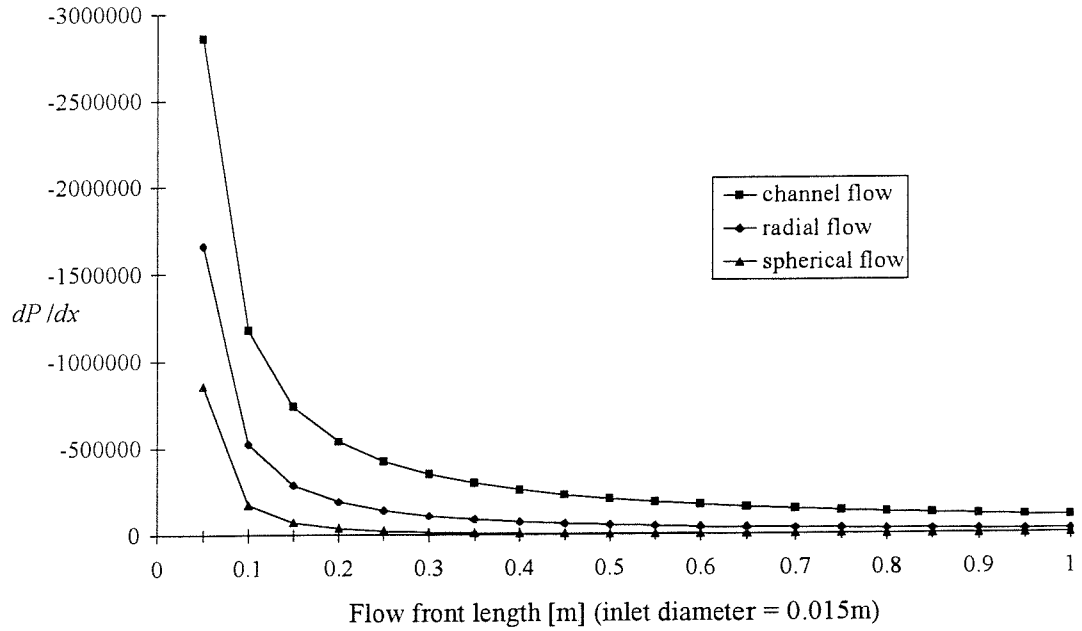

Figure 11.6 Pressure gradient at flow front

Analysis of the flow pattern can be performed using the cross-over length L_{cv}, which is a measure of the importance of capillary pressure. This concept was introduced by Wong (1994). First the ratio of the applied pressure and capillary pressure is determined; this entity, Ca_{mod}, is termed the modified capillary number.

$$Ca_{\text{mod}} = \frac{\Delta P}{P_c} \qquad (11.4)$$

ΔP is defined as the pressure drop across a pore or fibre with diameter D_f, and P_c is the capillary pressure. Wong (1994) then defines the cross-over length as follows:

$$L_{cv} = \frac{D_f}{Ca_{\text{mod}}} \qquad (11.5)$$

In order to minimise the capillary effects one has to ensure that the fabric samples used in the flow experiments are larger than L_{cv} . Equation (11.5) has been derived for one-dimensional flow with constant flow rate. In this case the pressure gradient is constant through-out the experiment. However this is not true for constant inlet pressure experiments where L_{cv} becomes a function of the flow front radius.

The capillary pressure P_c can be defined for a fibrous preform as (Ahn et. al. (1991)):

$$P_c = \frac{F}{D_e}\gamma\cos\theta \qquad (11.6)$$

and

$$D_e = D_f \frac{\varepsilon}{(1-\varepsilon)} \qquad (11.7)$$

where γ is the surface tension of the fluid, θ is the contact angle between fluid and fibre, F is the form factor which depends on fibre alignment and the flow direction, D_e is the equivalent pore diameter and ε is the porosity. For flow along a bundle of fibres F = 4, while, for flow across a fibre bundle F = 2. For flow in the through-thickness direction Ahn et. al. (1991) determined experimentally F = 1.8 for a plain weave fabric. In three-dimensional flow all these flow situations are present. Hence F = 3 is assumed for the following calculations. Capillary flow occurs at the flow front hence pressure needs to be evaluated at $x = x_f - D_e$ to obtain Ca_{mod}. This is done using equations (11.1) to (11.3). Note that to reflect the fibrous structure of the material D_e is used instead of D_f to calculate ΔP and L_{cv}. The following values have been used: P_o = 100kPa, ε = 0.484, D_f = 3.36x10^{-5} m (Carleton and Nelson (1994)), γ = 0.0322 N/m (oil, Steenkamer et. al. (1995)) and θ = 0° (oil, Steenkamer et. al. (1995)).

The cross-over lengths for the one, two and three-dimensional flow have been compared in Figure 11.7. It can be seen from this figure that L_{cv} for spherical flow is about one order of magnitude larger than L_{cv} for both the radial and channel flow. A plot of the ratio of L_{cv} versus flow front illustrates these observations better (Figure 11.8). It shows that L_{cv} for spherical flow very quickly becomes the same order of magnitude as the flow front, making reliable

tests impossible as observed in the experiments. To reduce L_{cv} one has to increase Ca_{mod} either by increasing the inlet pressure or by increasing the radius of the inlet. However increasing the inlet pressure will increase the risk of flow induced compaction rendering any measurement results useless for permeability calculation. Increasing the inlet radius will make the diameter of the inlet larger than the thickness of the mould. The interpretation of the results will be more difficult as the analytical formulae used here, equations (11.1) to (11.3), assume a hemispherical inlet which is violated in the experiment.

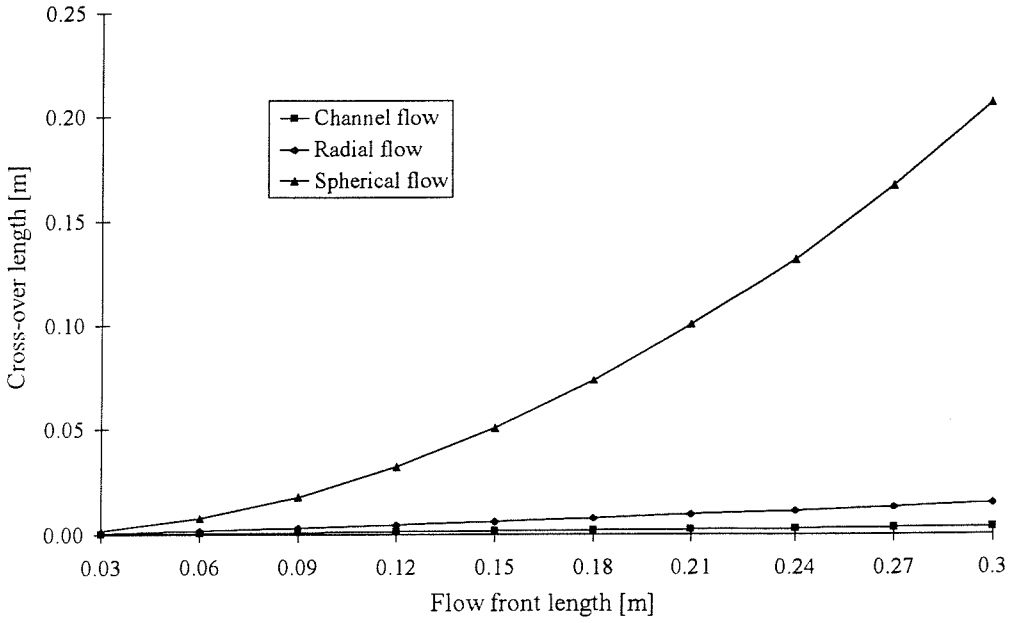

Figure 11.7 Cross-over length

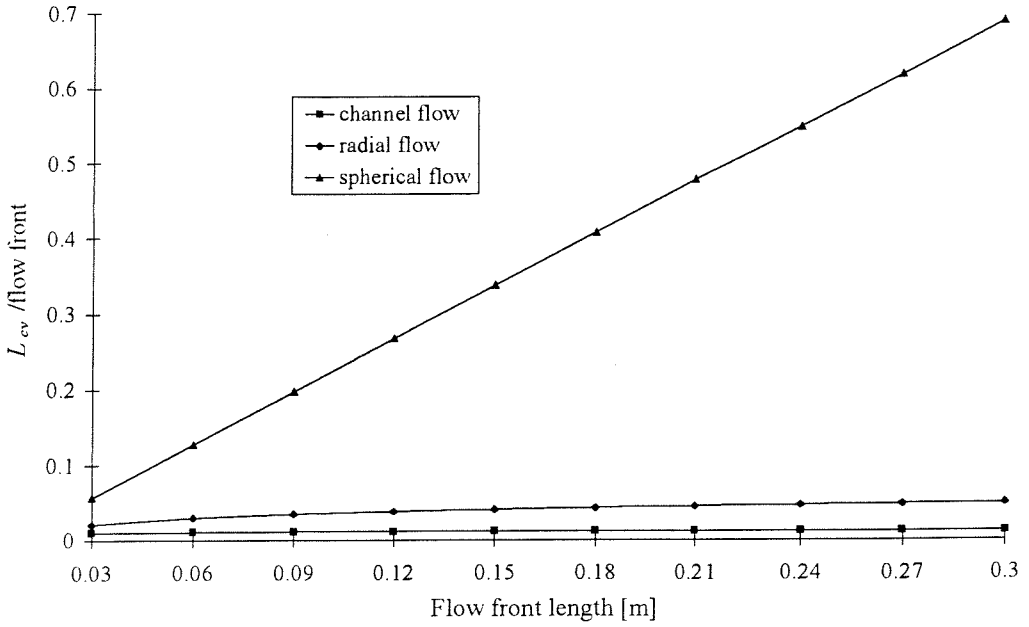

Figure 11.8 Ratio of cross-over length to flow front position

Comparison with literature

The importance of capillary pressure as observed here seems to be in contrast with the results reported for the initial experiments (see section 11.1.1) where the three-dimensional radial flow technique was used successfully to measure permeability of continuous filament random mat (Vetrotex U750-450). This can be explained by the difference in the structure of the random mat and the twill fabric used in this paper. The twill fabric consists of tightly woven bundles of fibres while in the case of random mat thin strands of fibres are laid up in circular loops. As a consequence the effective pore diameter of the random mat is considerably larger than the effective pore diameter for the twill fabric. More importantly this leads to a reduction of the capillary pressure and at the same time increases ΔP. These two effects reduce L_{cv}. Hence it is possible to measure permeability of random mat with the three-dimensional radial flow technique though not that of twill fabric.

The results presented in this section do tie in with observations made by other researchers. Ahn et al. (1995) only uses a 9.5mm thick mould. Over this distance the thermistors gave useful results. At the same time as Figure 11.5 has shown small disturbances will have a profound effect on the pressure distribution and hence permeability results. This will tend to make the test not very reliable and repeatable. Similar observations were made by Trevino et al. (1991). They found that for the one-dimensional channel flow test, a dependence of the through-thickness permeability on the stack thickness if the thickness was small. In later publications (Wu et al. 1994) a three-dimensional radial flow experiment was introduced where the through-thickness permeability was calculated numerically. For reliable permeability measurement a stack thickness of at least 15mm was specified. As this was a steady flow experiment with stationary flow front, no problems with capillary pressure were encountered. It has to be noted however that in this experiment the outside boundary of the fabric samples is also the boundary of the flow domain. Therefore dimensional accuracy is most important. This is very difficult to achieve for circular fabric samples, which are required for this experiment.

11.1.3 Two-dimensional flow

Figure 11.9 shows the permeability results for two-dimensional flow as listed in Table 10.3.

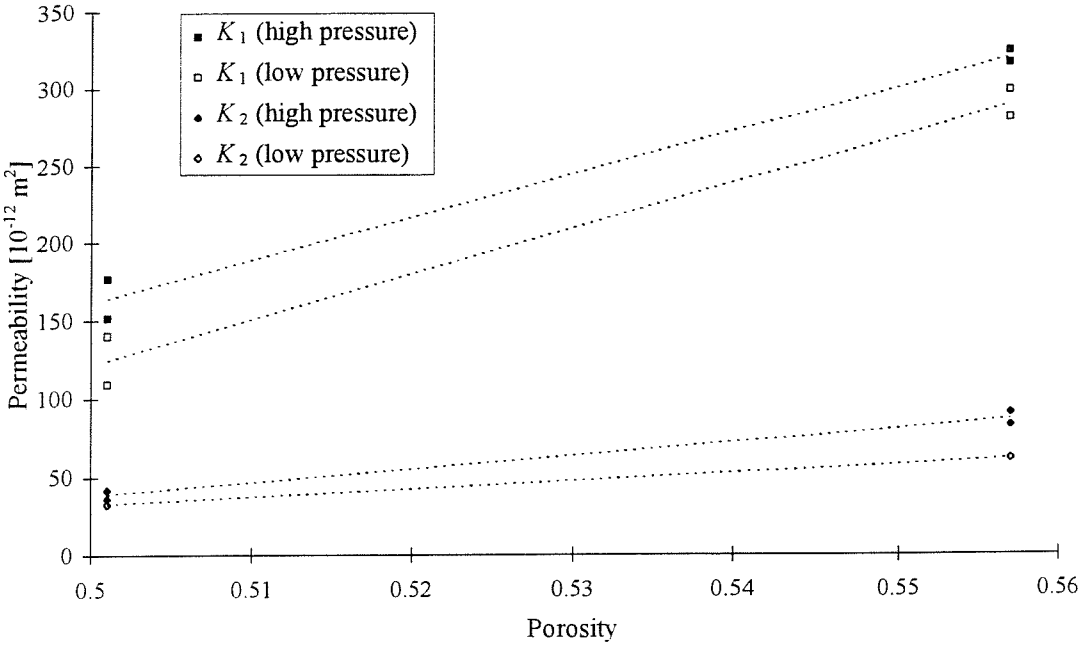

Figure 11.9 Permeability for quasi-unidirectional non crimp fabric E-LPb 567 (high pressure: runs 3,5,6,8; low pressure: runs 1,2,4,7)

As observed during the experiments the flow front in the x-direction was faster than the undisturbed flow front at high pressures (see Figure 10.1). This is also reflected in the results. Figure 11.9 shows that K_2 is larger for higher pressure which increases with higher fibre volume fraction. For flow in the y-direction it was observed that at low pressures with low fibre volume fraction the flow front was lagging behind the undisturbed flow front. Again Figure 11.9 shows that the difference for K_1 at low fibre volume fraction is larger than at high fibre volume fraction. These phenomena could be explained as follows: The permeability for the unidirectional non-crimp fabric in the y-direction is far greater than the permeability in the x-direction where the flow goes across the fibre bundles. Therefore the thermistors along the x-axis create a small channel which particularly at high pressure accelerates the flow. In the y-direction however the thermistors act as an of obstacle which obstructs the flow in the channels between the fibre bundles. It also decreases the porosity locally. These factors cause the flow to slow down. This accelerating of flow in x-direction and slowing down of flow in y-direction by the thermistors might also explain why permeability is not as anisotropic as expected.

It appears that both principal permeability values are dependent on pressure which seems to be caused by the presence of the thermistors in the fabric (even though it does not fully explain the differences for K_1 for high and low pressure). The orientation of the principal permeability, listed in Table 10.3, varies quite a lot. Furthermore no clear trend can be observed. In an attempt to gain a better understanding of the factors causing these variations a new way of conducting and analysing experiments was explored. It is called experimental design.

Introduction to experimental design

The following section is based on the book by Grove and Davis (1992). Some basic concepts and ideas of experimental design will be briefly discussed. Many experiments are conducted where only one factor at a time is changed while keeping everything else fixed. This will lead to an insufficient understanding of the response of a system to changes made to parts of it. In particular interactions will not be discovered. In contrast statistical design of experiments means making many design changes at once and conducting several experiments evaluations before decisions about the next steps are made. In statistically designed experiments, also known as factorial experiments, factors (the "things" which are changed) are set to certain values or levels. For an initial design two levels are common. An important aspect in the design of an experiment is that an experiment is balanced with regards to the design changes. The levels of the factors are arranged in such a way that for each factor which is set at a particular level the levels of the other factors will occur at the low and high settings for the same number of times. Effect is the influence of a factor on the response e.g. permeability. If the effect of one factor depends on the setting of another factor then those two factors exhibit interaction.

Grove and Davis show that the method of multiple regression can be used as a short-cut to some of the statistical output. It provides the coefficients for the prediction equation and the standard deviation for each coefficient. This can then be used to find the t-ratio which is the ratio of the coefficient over the standard deviation. The t-ratios are used to divide the measured effects into two sets, those which are treated as random and those which are treated as real. The effect is "statistically significant" if its t-ratio lies on one of the tails of a t distribution. As a rough rule of thumb in most cases the critical value of the t-ratio is 2. This means that a coefficient has to be bigger than twice its standard error before it is considered likely to represent a real effect.

The method of multiple regression is a general method for fitting an equation of the form (Grove and Davis):

$$y = b_o + b_1 x_1 + b_2 x_2 + b_3 x_3 + \ldots\ldots \qquad (11.8)$$

where x_1, x_2, x_3 etc., are variables and b_o, b_1, b_2, b_3, etc., are the coefficients to be determined. Values of the coefficients are usually chosen by the method of least squares. The selected equation is then the one for which the sum of squares of the residuals is minimised. The method can also cope with dependence between some of the x-variables.

One possible experimental design is the full factorial design (Table 11.1, Grove and Davis). The three factors in Table 11.1 correspond to fibre volume fraction (A), measurement angle (B) and inlet pressure (C) of the two-dimensional flow experiment. The "+" and "-"denote the two settings (levels) of the factors where "+" means high and "-" low. To avoid systematic errors due to factors which cannot be controlled (e.g. temperature variation in the laboratory) the order of the runs of the experiments should be randomised. The two-dimensional flow experiment was designed as a full factorial experiment which can be verified by comparing Table 11.1 with Table 10.3. For example run 1 in Table 10.3 is equivalent to run 5 in Table 11.1, run 2 is equivalent to run 7 etc.. In the next section the results from the regression analysis of the permeability data listed in Table 10.3 is discussed.

Factors	Run number							
	1	2	3	4	5	6	7	8
A	+	-	+	-	+	-	+	-
B	+	+	-	-	+	+	-	-
C	+	+	+	+	-	-	-	-

Table 11.1 2-level full factorial design (Grove and Davis (1992))

Results from regression analysis

In this regression analysis the principal permeabilities and their orientation (K_1, K_2, and φ) are the responses. The measurement angle ϕ, the fibre volume fraction V_f and the inlet pressure P_o are the variables or predictors. To perform the regression analysis a statistical software package called MINITAB was used. The resulting regression equation for K_1 is:

$$K_1 = 360 + 0.038\,\phi - 6.75\,V_f + 0.000083\,P_o \qquad (11.9)$$

with $R^2 = 93.9\%$. R^2 is the coefficient of determination and measures how well the regression equation fits the data. R^2 for the above equation indicates a good fit. Table 11.2 lists the coefficients, standard deviation and t-ratio for the above regression equation. The last column lists the probability that the coefficient is not significant (calculated by the software from the

value for the t-ratio and the degree of freedom). In engineering a 95% probability of something to be important is acceptable. Therefore the coefficients of V_f and P_o are significant (the probability for it not to be significant is very low) while the measurement angle ϕ is not significant.

Predictors	Coefficients	Standard deviation	t-ratio	p for t-ratio
ϕ	0.0375	0.3509	0.11	0.920
V_f	-6.7464	0.9399	-7.18	0.002
P_o	0.00008291	0.00002761	3.00	0.040

Table 11.2 Regression analysis for K_1

The regression equation for K_2 is:

$$K_2 = 1542 - 0.271\,\phi - 28.5\,V_f + 0.000183\,P_o \qquad (11.10)$$

with R^2 = 98.1%. Again this indicates a very good fit of the regression equation to the experimental data. Table 11.3 lists the t-ratio and the corresponding probability values. The coefficients of V_f and P_o are significant while there seems to be a weak influence of ϕ. It is not possible however to make a definite judgement whether or not ϕ is significant. Further experiments are required (with e.g. a non-intrusive flow front measurement technique).

Predictors	Coefficients	Standard deviation	t-ratio	p for t-ratio
ϕ	-0.2713	0.7622	-0.36	0.740
V_f	-28.513	2.042	-13.97	0.000
P_o	0.00018260	0.00005997	3.04	0.038

Table 11.3 Regression analysis for K_2

The final predictor to be looked at is the calculated angle of orientation φ. The regression equation is:

$$\varphi = -58 + 0.202\,\phi + 1.11\,V_f + 0.000023\,P_o \qquad (11.11)$$

The R^2 value for this equation is 54.5% which indicates a very poor fit of the regression equation. This is confirmed by looking at the t-ratios and probabilities in Table 11.4. For all three predictors it is not possible to determine whether they are real effects or random noise.

Predictors	Coefficients	Standard deviation	t-ratio	p for t-ratio
ϕ	0.2023	0.2504	0.81	0.464
V_f	1.1142	0.6708	1.66	0.172
P_o	0.00002340	0.00001970	1.19	0.301

Table 11.4 Regression analysis for φ

In summary it can be said that K_1 clearly was only dependent on V_f and P_o. For K_2 a weak dependence also on ϕ was found while for φ it was impossible to make a definite statement about the significance of any of the coefficients of its regression equation. Further experiments are required to better understand the relationship between the predictors V_f , P_o , ϕ and the responses φ and to some degree K_2. This series of experiments demonstrated the strength of experimental design. It gives an objective measure to asses whether a response is real or just random noise.

11.1.4 Other experimental results

In section 10.2.4 only average permeability values were reported. To investigate how permeability varies with different measurement angles ζ, results are presented for permeability calculated at 15° intervals as shown in Figure 11.10.

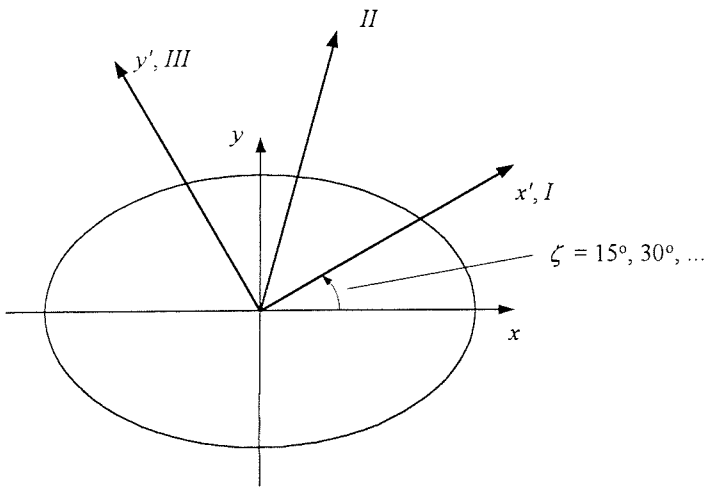

Figure 11.10 Definition of measurement angle for permeability calculation

The calculated orientation φ is always measured relative to the x-axis. Therefore ζ is always added to φ. If ζ is larger than ±45° then K_1 and K_2 switch values and the orientation is measured between the **2**-axis and the x'-axis (see section 6.6). To take this effect into

account 90° have to be added or subtracted to the sum of ζ and φ. If ζ is larger than ±135° then 180° have to be added or subtracted to the sum of ζ and φ. To see whether principal permeability is constant in space or time some convergence graphs are presented here as well (see also section 6.5.2).

Balanced satin weave

As already discussed in section 10.2.4 the measured flow front was not symmetric. This is confirmed by permeability calculated for different measurement angles which is quite irregular as shown in Figure 11.11. The permeability does not show any of the signs of the rotation behaviour of an symmetric second order tensor like the swapping of values of K_1 and K_2 every 90° (see e.g. Figure 6.15 or Figure 6.27). Figure 11.11 also shows the orientation calculated for different measurement directions. The angle of orientation fluctuates widely and is not constant as expected.

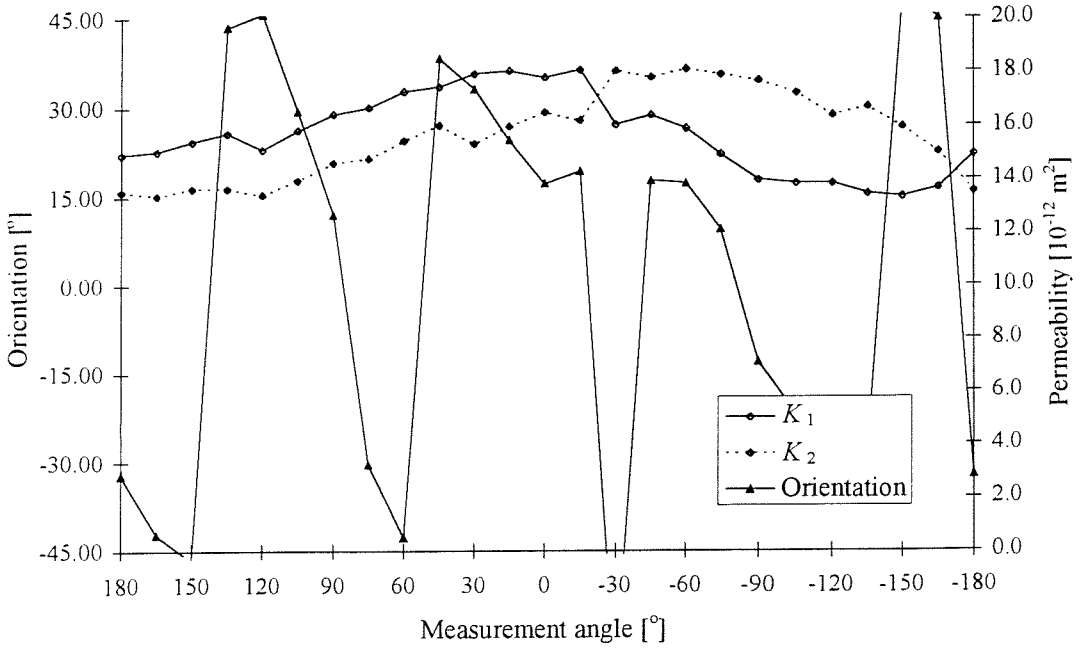

Figure 11.11 Permeability for different measurement angles for the balanced satin weave

To investigate the convergence behaviour of the permeability N_I, N_{II} and N_{III} are plotted versus time for $\zeta = 0°$. A regression line is fitted through the individual points of N_I, N_{II} and N_{III} in Figure 11.12. F_I, F_{II} and F_{III} 's are the slope of these straight lines. It can be seen from Figure 11.12 that the regression lines do not represent the individual points very well. This is confirmed by plotting the convergence graph in Figure 11.13. The dotted line is the principal permeability calculated from F_I, F_{II} and F_{III} . The solid lines are permeabilities calculated from the slopes of each individual point in Figure 11.12. Again the average value does not correlate well. It is obvious that permeability is not constant as assumed! The further the flow front

progresses the higher the permeability value becomes. This is a sign of capillary action. This shows that a convergence graph can give valuable additional information which is not available if only F_I, F_{II} and F_{III} are used. Figure 11.13 also shows that the average permeability (dashed line) is much closer to the permeability values calculated for large flow front values than for flow front steps close to the inlet. This is because the fitted straight line to determine F_I, F_{II} and F_{III} from its gradient is forced through the origin. Hence the influence on the slope by flow front measurement taken further away is much greater.

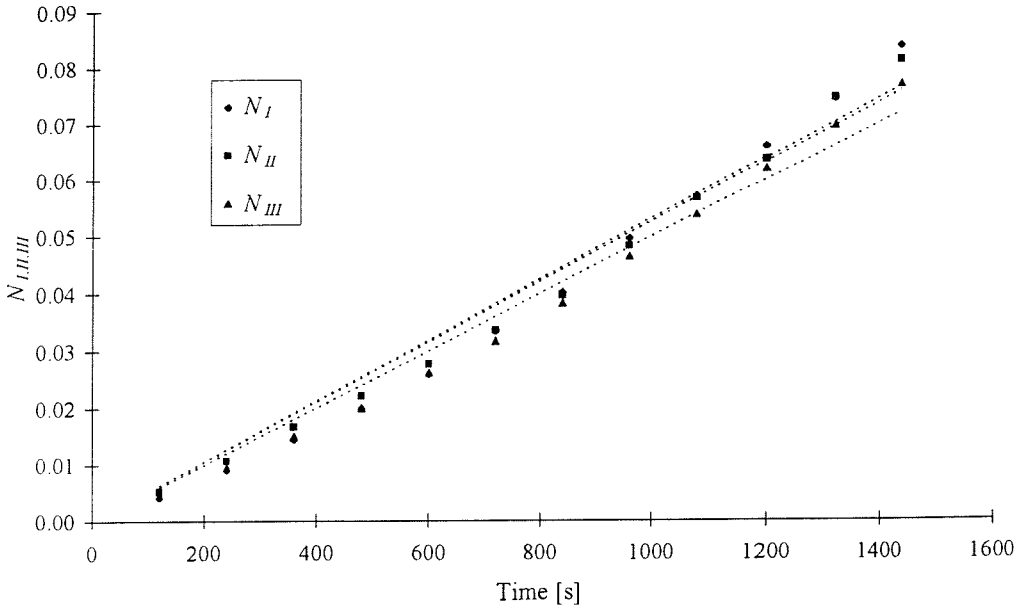

Figure 11.12 Plotting N_I, N_{II} and N_{III} versus time ($\zeta = 0°$)

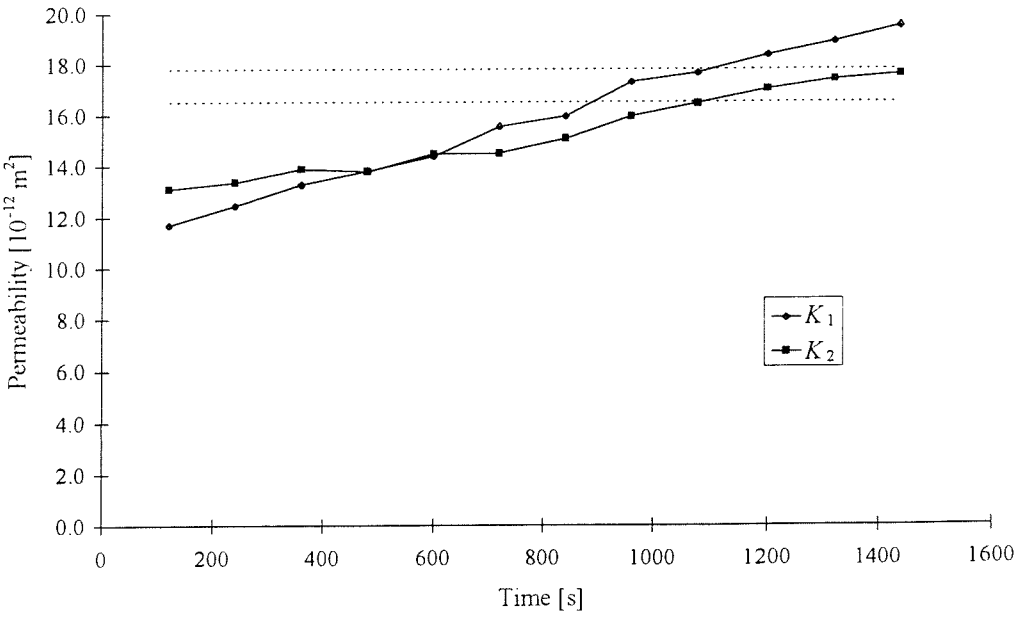

Figure 11.13 Convergence of principal permeability ($\zeta = 0°$)

Twill weave with flow-enhancing weft threads

The twill weave showed much more consistent and regular results than the satin weave in the previous section. Permeability calculated for different measurement angles is quite regular as shown in Figure 11.14. The permeability varies in a very similar way as shown for the ideal examples in Figure 6.15 or Figure 6.27. Also the orientation is quite consistent for the different measurement angles (see Figure 11.14). In Figure 11.15 the calculated average permeability presented in Table 10.4 are compared with Figure 11.14. The variation is quite small. Furthermore the calculated angle of orientation seems to be a very good representation of the actual situation. Figure 11.16 shows the measured flow front position at various time steps. From observation it is clear that the major and minor axis are slightly off-set from the 0° and 90° position. They are rotated by a small angle anti-clockwise - in the positive direction. This was successfully predicted.

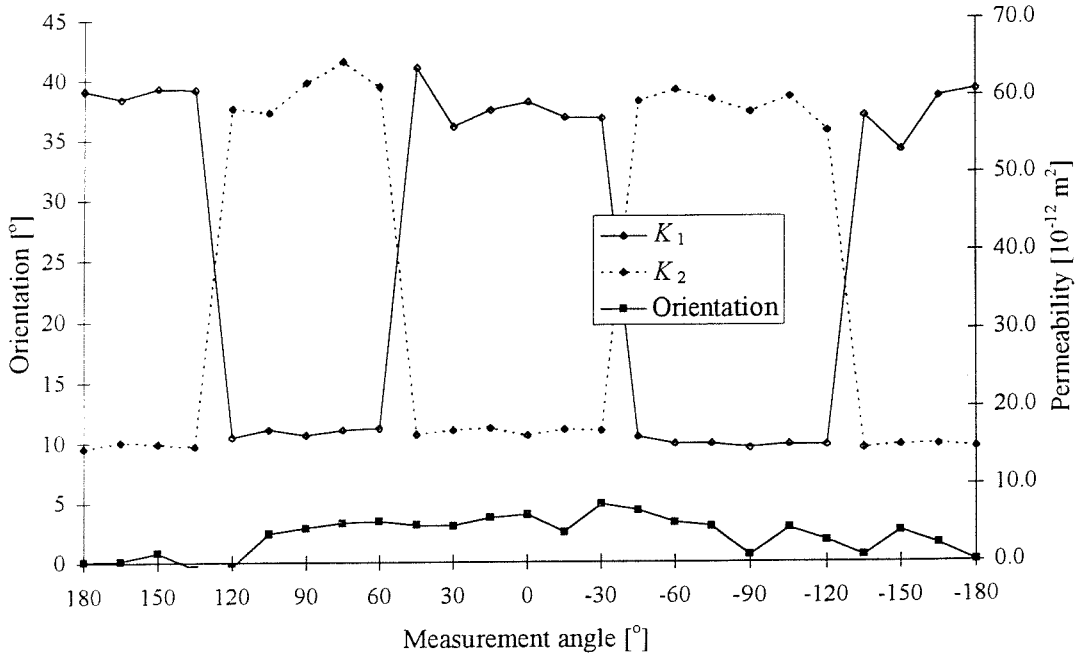

Figure 11.14 Permeability for different measurement angles for twill fabric

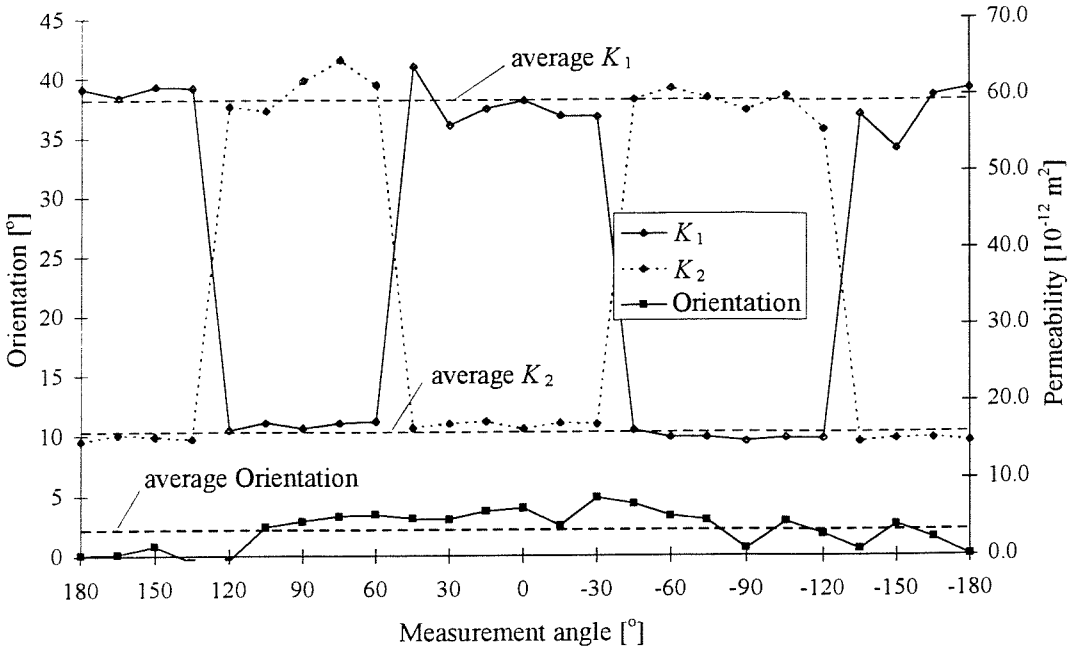

Figure 11.15 Permeability for different measurement angles compared with average permeability (twill fabric)

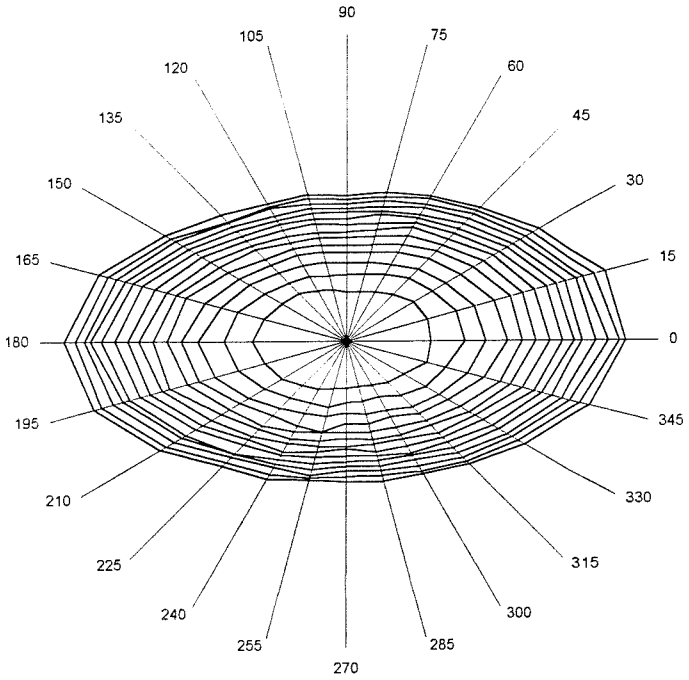

Figure 11.16 Measured flow front positions for twill fabric (Fell and Summerscales 1996)

It is also interesting to know how permeability converges for the twill fabric. As in the previous section N_I , N_{II} and N_{III} are plotted versus time (Figure 11.17). This time the regression line fits the experimental results much closer. This is confirmed by the convergence graph (Figure 11.18). The agreement of principal permeability (dashed line) and permeability calculated for individual flow front points is very good for K_2 and quite good for K_1.

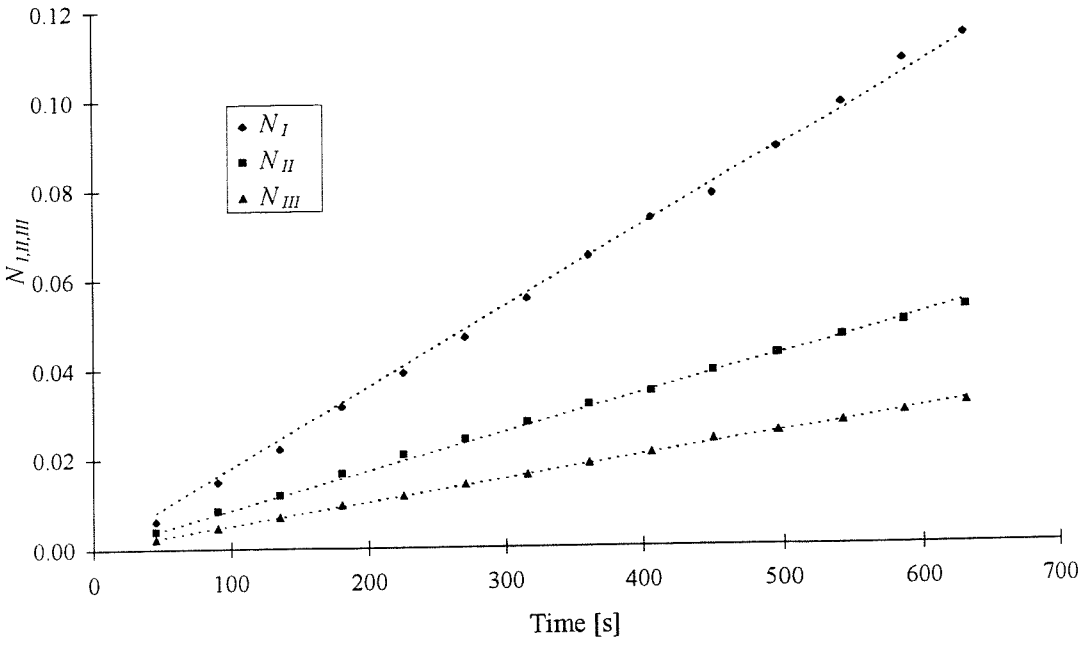

Figure 11.17 Plotting N_I, N_{II} and N_{III} versus time ($\zeta = 0^o$)

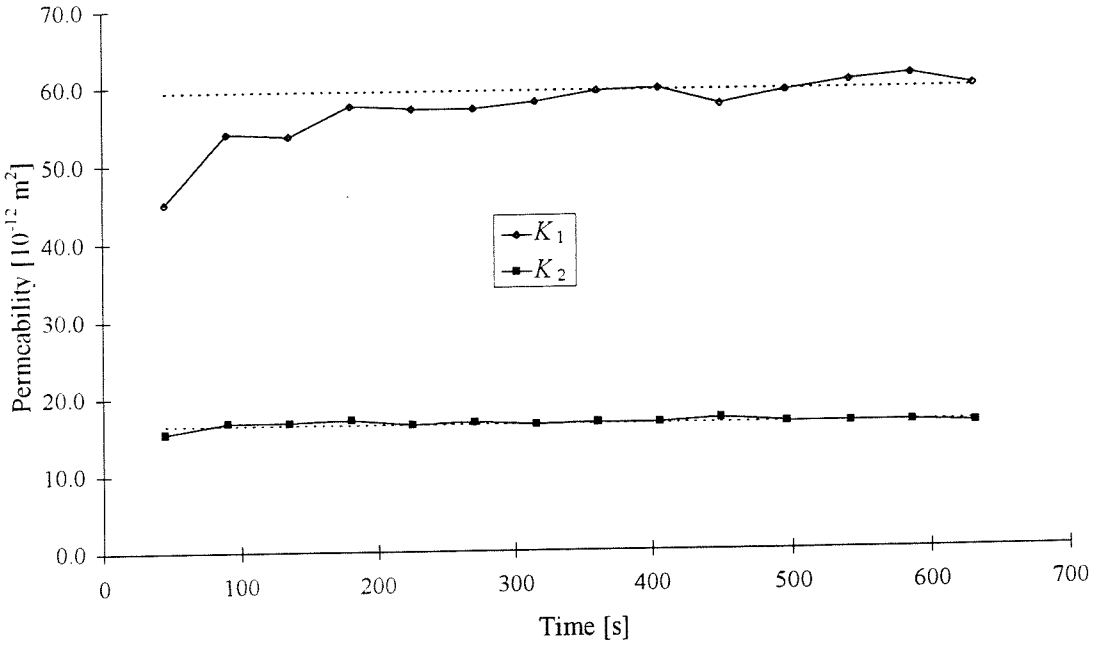

Figure 11.18 Convergence of principal permeability ($\zeta = 0^o$)

Quasi-unidirectional fabric

This is the set of results for the most anisotropic material of the three experiments. Figure 11.19 shows that K_1 varies slightly more than K_1 for the twill fabric. In Figure 11.20 the directional results are compared with the averaged values. K_2 agrees very well while there is

some fluctuation in K_1. The calculated angle of rotation is a small positive value and agrees well with the observed flow front (see Figure 11.21).

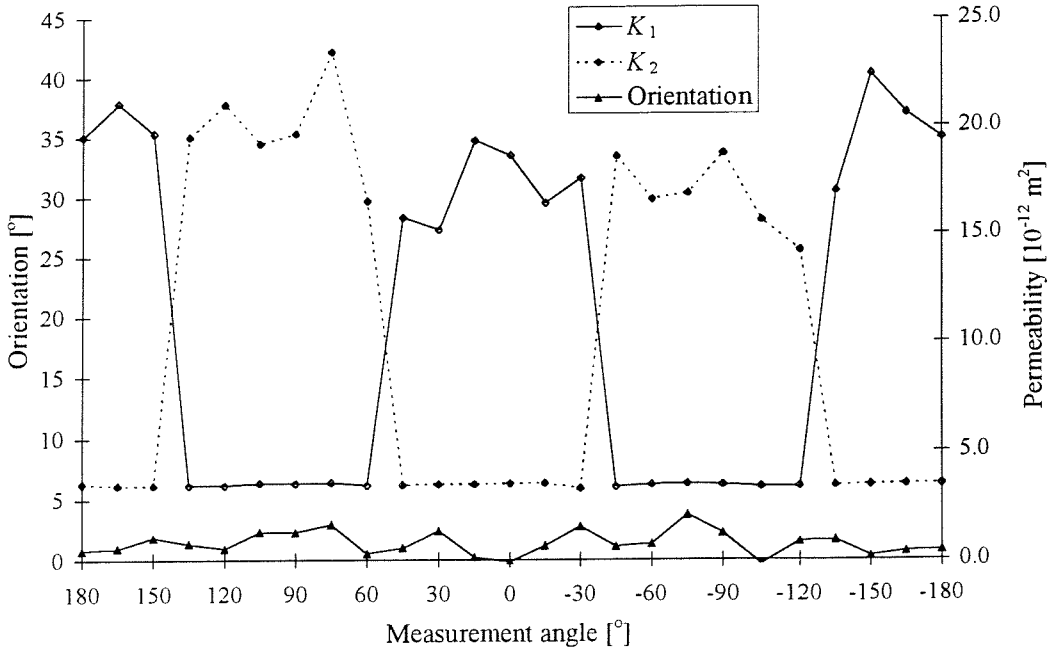

Figure 11.19 Permeability for different measurement angles for unidirectional fabric

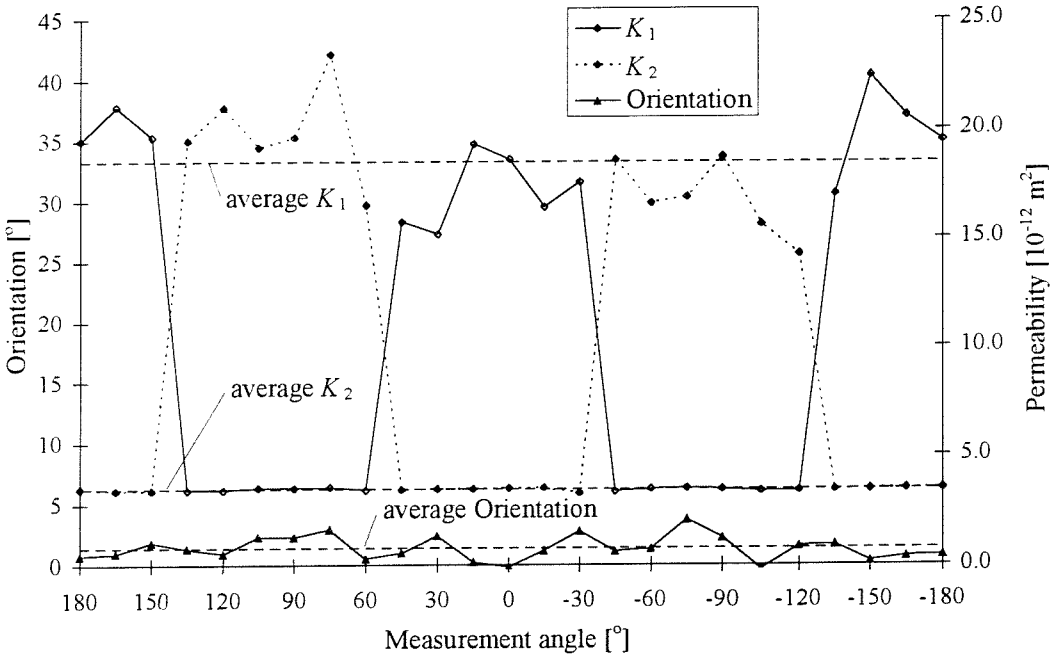

Figure 11.20 Permeability for different measurement angles compared with average permeability (unidirectional fabric)

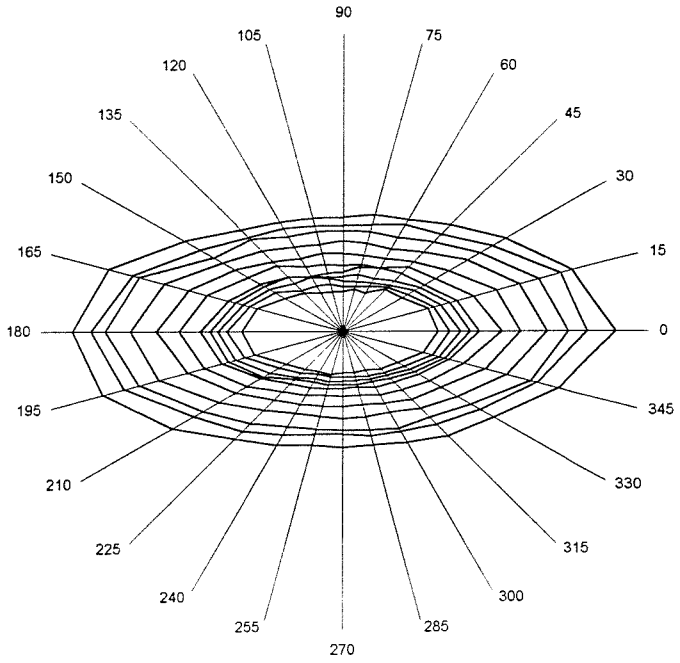

Figure 11.21 Measured flow front positions for UD fabric (Fell and Summerscales 1996)

The plot of N_I, N_{II} and N_{III} versus time is shown in Figure 11.22. F_I, F_{II} and F_{III} are slightly overestimated by the regression line for large flow front radii. This is confirmed in the convergence graph (Figure 11.23). Permeability calculated for each flow front point seems to drop slightly the further the flow front progressed.

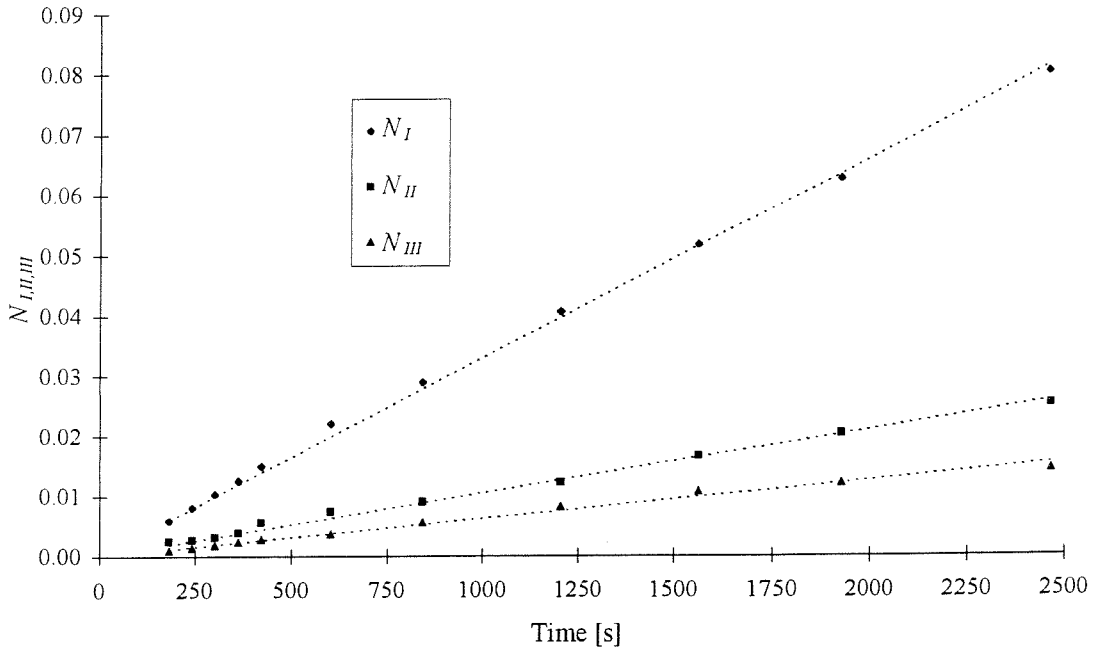

Figure 11.22 Plotting N_I, N_{II} and N_{III} versus time ($\zeta = 0^0$)

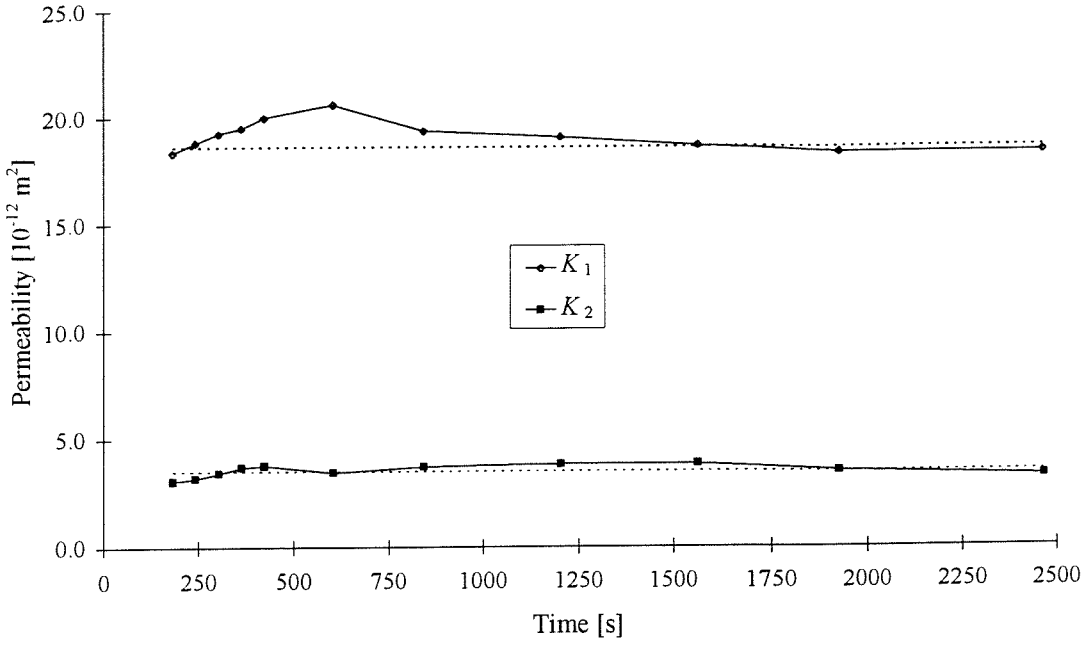

Figure 11.23 Convergence of principal permeability ($\zeta = 0^{\circ}$)

11.2 Constant flow rate experiments

In this section the principal axes are denoted x, y as used by Morris and Rudd (1996). In Table 11.5 the results for permeability calculated from pressure measurements at a point are listed for the highest available porosity value. K_{Xin} , K_{Xmid} , K_{Yin} and K_{Ymid} denote the permeabilities calculated at the different pressure transducer locations. Permeability was calculated using the method by Chick et al. (1996). K_1 and K_2 were obtained by applying equations (7.55) and (7.56) on page 108 to pressure measured at x_{in} and y_{mid}. Even though large scatter is observed, there is reasonable correlation between the results obtained by the different methods. However K_1 and K_2 agree well for the two runs. The permeability values are not as anisotropic as expected for a unidirectional fabric. This is because the porosity is very large which results in a low compaction pressure and easy flow paths during the experiment.

Run No.	K_1	K_2	K_{Xin}	K_{Xmid}	K_{Yin}	K_{Ymid}
1	3219.81	1426.94	2333.25	2859.31	1433.67	1116.66
2	3151.10	1322.27	2857.18	3202.05	1189.25	1332.80

Table 11.5 Permeability for pressure at a point [10^{-12} m^2], ($\varepsilon = 0.728$)

Alternatively permeability can be calculated from pressure drop measurement. It was quite difficult to get two valid pressure measurements in the y-direction for this highly anisotropic

material. K_1 was 3064.48 and 2552.77 for run 1 and 2 respectively while K_2 was 1195.60 and 1177.36 for run 1 and 2 (all results are 10^{-12} m^2). The results are similar to the pressure at a point measurement results in Table 11.5.

Figure 11.24 summarises the results obtained for all the experiments analysed (8 runs in total). At high porosities the results obtained with Chick et al. (1996) and the unified approach agree reasonably well. However with decreasing porosity K_1 is deviating quite significantly from the results obtained with Chick's method while K_2 is quite close. Some differences in the results of the two methods would be expected because of the different ways the two methods have been derived (see section 8.6.1). However the degree of anisotropy for the principal permeability is increasing steadily to a value of α which is noticeably smaller than α observed in other types of experiments.

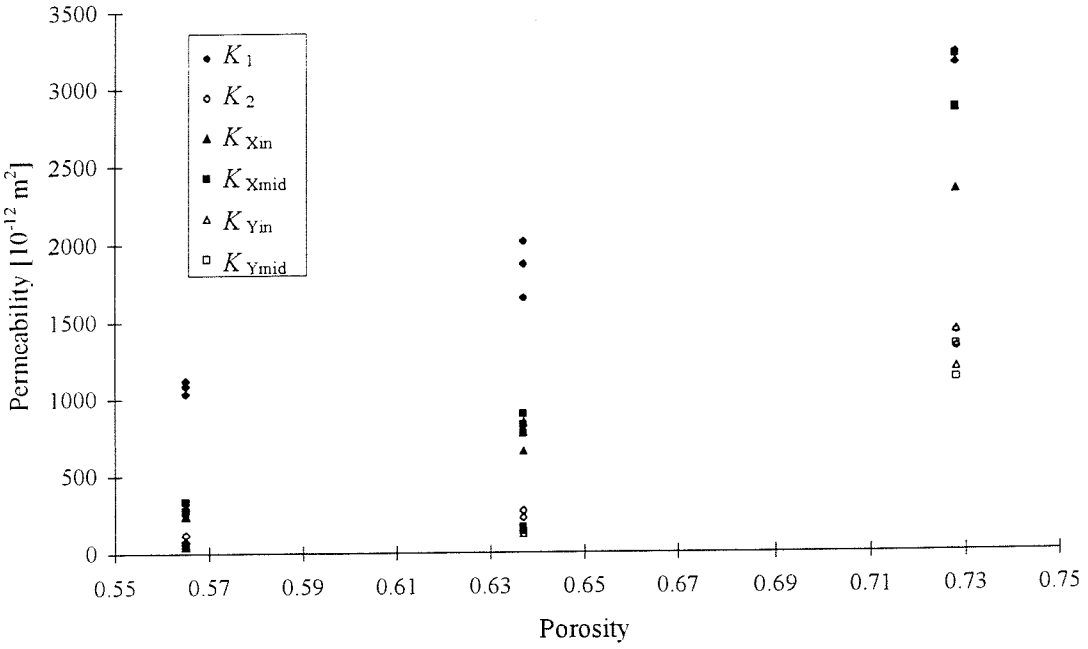

Figure 11.24 Permeability for quasi-unidirectional fabric (E-LPb 567)

A better understanding of this problem is gained by plotting F_I and F_{III} versus time (Figure 11.25 to Figure 11.27). For equations (7.55) and (7.56) F_I and F_{III} take a slightly different form to module 1b of the unified approach (Table 8.2):

$$F_I = \frac{\frac{1}{2}\ln\left(\frac{Q(t-t_2)}{\pi h \varepsilon x_2^2\sqrt{\alpha}}+1\right)}{P_2} \text{ and } F_{III} = \frac{\frac{1}{2}\ln\left(\frac{Q(t-t_2)}{\pi h \varepsilon y_2^2\sqrt{1/\alpha}}+1\right)}{P_2} \quad (11.12)$$

For permeability to be constant F_I and F_{III} are constant too. In addition F_I and F_{III} are also equal (see equations (7.55) and (7.56) on page 108). This can be confirmed for high porosity (Figure 11.25). However the smaller porosity becomes the shorter are the horizontal portion of F_I and F_{III} (see Figure 11.26 and Figure 11.27). For these cases F_I and F_{III} were computed only from the horizontal portions of the graph.

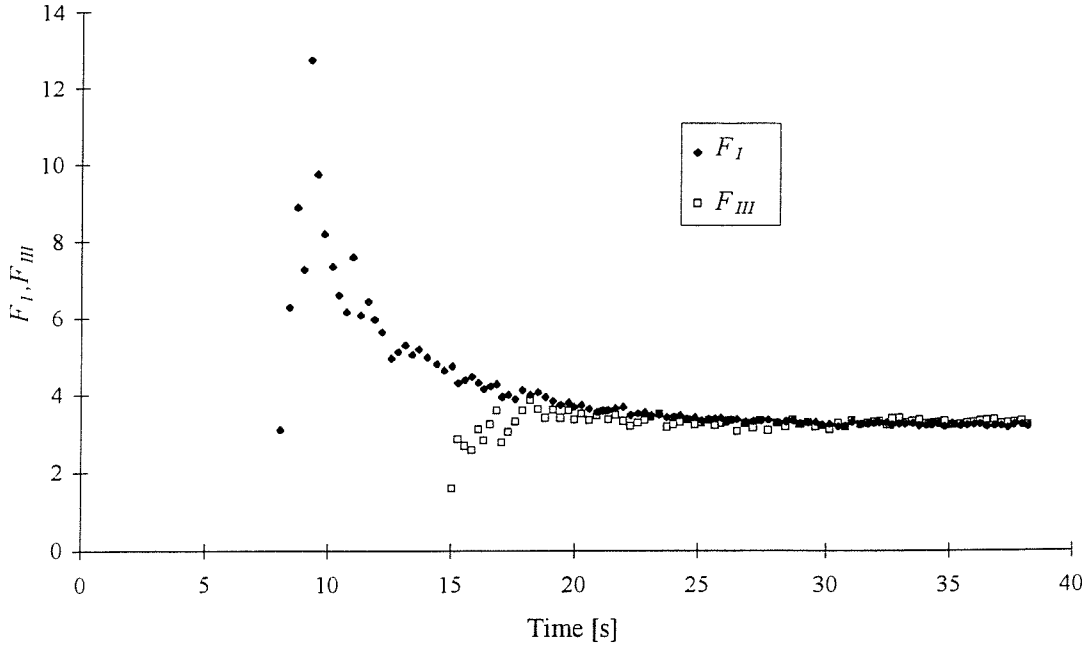

Figure 11.25 F_I and F_{III} ($\varepsilon = 0.728$)

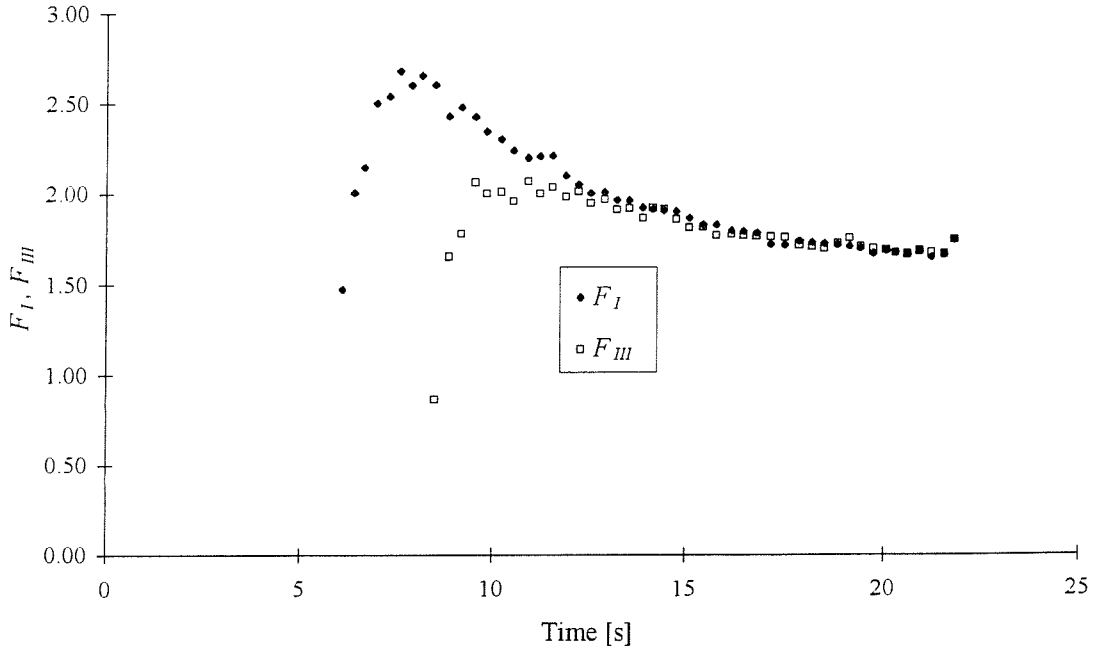

Figure 11.26 F_I and F_{III} ($\varepsilon = 0.637$)

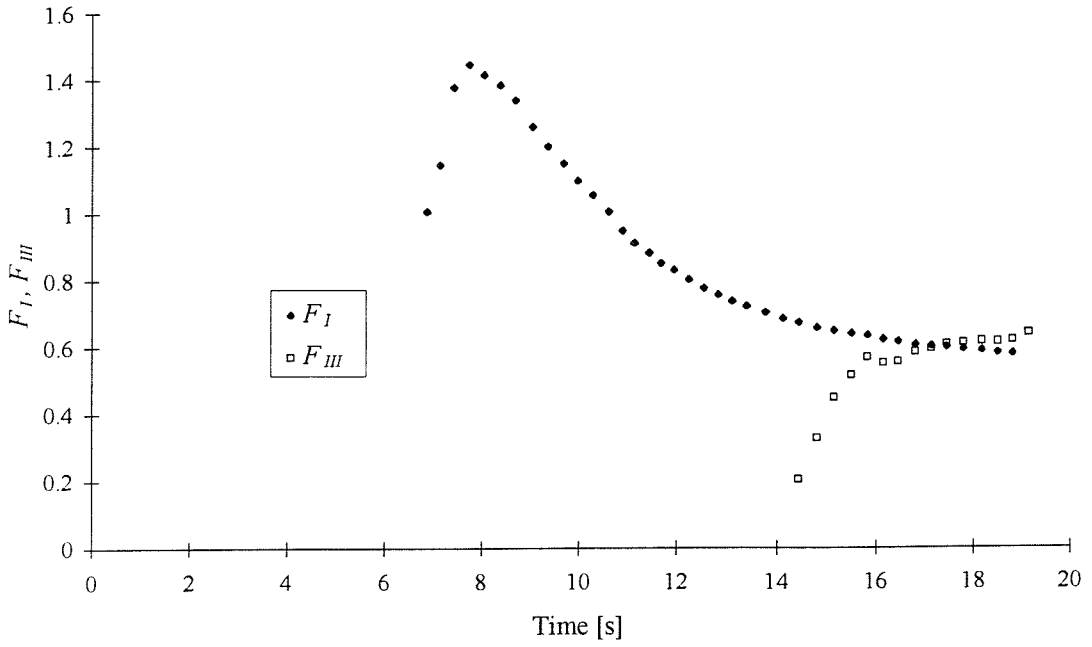

Figure 11.27 F_I and F_{III} ($\varepsilon = 0.565$)

The observed behaviour of F_I and F_{III} may be explained by differences of the expected and actual shape of the inlet. For the derivation of equations (7.55) and (7.56) it was assumed that the flow front and inlet are elliptical with identical aspect ratios. This boundary condition is violated in practice because a circular inlet is used in experiments. Figure 11.28 shows that this leads to an underestimation of pressure in the x-direction which becomes less significant the further the flow front progresses. In the y-direction pressure is overestimated. Therefore F_I is too large initially while F_{III} is too small at the beginning. This can be observed for all three F_I and F_{III} graphs (for F_I an initial build-up of pressure can be observed for the first second). At the same time the horizontal section of F_I and F_{III} versus time remains constant for shorter periods of time. At the lowest porosity value there is virtually no overlap. This is because with decreasing porosity permeability decreases as well. Therefore the maximum injection pressure for this constant flow rate experiment is reached much earlier and the flow front advances less than compared with higher porosities. As a consequence the difference between the expected and the actual pressure is relative larger for lower porosities which leads to the observed increase in anisotropy. Further evidence of this is that the value of F_I and F_{III} is decreasing steadily for decreasing porosity (see Figure 11.25 to Figure 11.27).

In conclusion it seems doubtful whether the constant flow rate technique combined with pressure measurement is actually suitable for measurement of permeability of highly anisotropic fabrics. Due to practical limitations (maximum injection pressure, mould

deflection) it is very difficult to ensure that the flow front radius is large enough to be able to neglect the error in the pressure reading due to the circular inlet. However for less anisotropic flow this method seems to work very well (see K_1 and K_2 in Table 11.5).

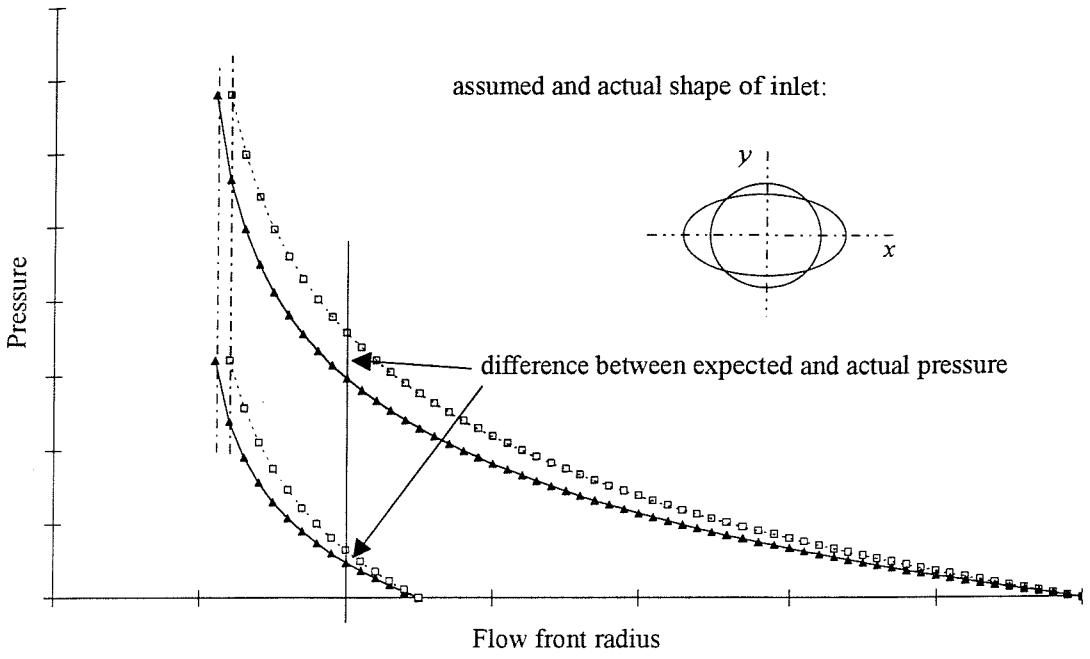

Figure 11.28 Schematic of pressure distribution for circular and elliptical inlet diameter

12. Summary and Discussion

Permeability is a measure of the flow resistance of the porous medium. It is determined by measuring flow front or pressure during experiments. The fluid in these experiments is assumed to be Newtonian and the experiments are carried out under isothermal conditions. Also the permeability is assumed to be constant. It can vary with orientation however (anisotropy). Furthermore permeability is assumed to be a symmetric tensor. Current permeability measurement techniques have been reviewed in chapter 2. Channel flow and two-dimensional radial flow techniques are widely used to measure principal permeability. Radial flow measurement techniques are restricted as they can only measure permeability in the principal coordinate system. In addition variation of permeability during the experiment cannot be detected. Furthermore permeability obtained for channel flow and radial flow does not always agree. In some cases this is due to limitation of the apparatus (e.g. mould deflection). But in many cases the methods which are used to process experimental data are insufficiently developed or flawed. To overcome these problems a unified approach to permeability measurement was proposed in this thesis. First the underlying theory will be discussed. Secondly results from experiments to validate the unified approach are reported and discussed.

12.1 Permeability measurement

The main features of the unified approach are that principal permeability and its orientation can be determined regardless of the measurement direction. For each type of experiment permeability models have been derived which relate permeability to flow rate, flow front position and pressure. Principal permeability is calculated from three different measurements of flow front or pressure (along three axes). For the different boundary conditions of the channel flow experiment 5 different permeability models have been derived. These are then resolved for the principal permeability and its orientation. The formulae were applied to results from the literature. It was found that there was good agreement between the two published sets of results (for stationary and moving flow fronts). The method proposed here is a more general than the method by Parnas and Salem (1991) as it allows the independent determination of the orientation and principal permeability for each fibre volume fraction. In contrast Parnas and Salem average anisotropy and orientation for two fibre volume fractions with the advantage that fewer experiments are required.

The method by Woerdeman et al. (1995) to determine three-dimensional permeability from channel flow tests was reviewed. It was possible to simplify the experimental procedure by Woerdeman et al. by replacing the two out-of-plane experiments with two additional in-plane experiments. Furthermore it was concluded that for layered materials and thin moulds commonly used for channel flow experiments a three-dimensional formulation of effective permeability is not appropriate. As a practical solution to measuring three-dimensional permeability it was suggested to determine the full in-plane permeability tensor (three experiments) and perform one through-thickness test to determine K_3.

Radial flow test are widely used as the full (in-plane) permeability tensor can be found in a single experiment. Permeability models for two-dimensional radial flow with constant inlet pressure or constant flow rate have been developed. In the case of constant inlet pressure this was extended to three-dimensional flow. For two-dimensional radial flow with constant inlet pressure a very detailed study was carried out. In particular it was looked at how the calculated angle of orientation is related to the calculated permeabilities and some simple rules were suggested. Furthermore the influence of the circular inlet was examined. The circular inlet used in experiments is a violation of the boundary condition of the analytical solution which assumes an elliptical inlet. The circular inlet was found to have a noticeable effect on the calculated permeability and a modified (elliptical) inlet shape was suggested with which a mathematically exact solution for permeability is obtained. Other issues which were studied was the relative size of the inlet and the size of the mould. It was concluded that the larger the inlet diameter the longer the flow front takes to develop fully. If at the same time the mould is small it might introduce an error into the solution because the flow front is still developing. The new approach presented here has been compared with examples published in the literature. There is almost perfect agreement between Adam's method (who pioneered radial flow) and the new approach. Chan and Hwang applied their method to the same data set. The results do not match the results obtained with Adam's method or the new approach because Chan and Hwang fail to address the scaling of the inlet shape.

It was demonstrated that channel flow and radial flow can actually be unified. This is because for both types of experiment the effective permeability which is measured during the experiment is the same. Three standard equations (for K_1, K_2 and φ) were proposed. For measurements taken in the principal directions there are two standard equations (for K_1, and K_2). These equations have a modular structure to incorporate the different boundary conditions of the various permeability models. Modules are selected depending on the type of the experiment. Most current permeability measurement techniques can be classified

according to the categories of the unified approach. The discussion revealed that many measurement techniques contain weaknesses. Bruschke (1992) and Ferland et al. (1996) did not include porosity in their models. Chick et al. (1996) obtain permeability from plotting pressure versus time without taking into account the position of the pressure transducer. Chan and Hwang (1991) do not incorporate the scaling of the inlet. Carter et al. (1995b) do not force the regression line for determining F_1 through the origin. The unified approach has established a framework for permeability measurement techniques. It allows the linkage of techniques which have previously been thought to be totally independent.

12.2 Permeability experiments

To verify the unified approach a number of permeability experiments were conducted. In addition results from other researchers were used to verify different options of the unified approach. A series of three-dimensional flow experiments was conducted for twill fabric. It was observed that capillary flow became the dominant flow pattern which rendered any permeability results useless. There was no sharp flow front any more. This could not be overcome by increasing the pressure as this led to fluid induced compaction and easy flow paths. At the same time it was found that thermistors give much more insight into the flow process than expected as they give information about compaction, fluid velocity and the type of impregnation process and flow front orientation.

Next a series of two-dimensional radial flow experiments was conducted. The fabric used was a quasi-unidirectional non-crimp fabric. It became apparent that the thermistors influenced the flow, despite all the precautions. Flow parallel to the unidirectional fibres was slowed down while across the fibres flow was accelerated. The new approach worked well with consistent results for principal permeability while the orientation showed some variation. For these experiments the method of experimental design was used. It was shown that experimental design and its statistical analysis is a very powerful tool for interpreting the experimental results. It was possible to distinguish between random effects and real effects. A dependence of the permeability on the inlet pressure was discovered while orientation seemed to have been affected by inlet pressure and measurement angle. This is probably due to the disturbances caused by the thermistors. More experiments with a non-intrusive flow front measurement technique are required to clarify these observations.

Experimental results were also used from the University of Plymouth. The results for satin weave are very irregular - probably caused by a shift of the measurement coordinate system. However permeability for twill and unidirectional fabric showed only small variability for

different measurement directions. This supports the idea that permeability is a symmetric second rank tensor. It was also demonstrated that the unified approach gives a better understanding of the results. It was possible to show capillary effects for the satin weave with the help of a convergence graph. Some results from constant flow rate experiments were provided by the University of Nottingham. The permeability obtained with the unified approach became more anisotropic with increasing fibre volume fraction. This was explained by the fact that the flow front was less developed. With increasing fibre volume fraction the flow front advances less for a given maximum injection pressure. It is doubtful whether the constant flow rate experiment with pressure measurement is suitable for highly anisotropic fabrics - it works well though for fabrics with a moderate degree of anisotropy.

13. Recommendations for future work

13.1 Verification of unified approach

Much of the verification in chapter 6 was done using the output of a flow simulation program. As discussed, the accuracy of the program near the inlet was reduced due to the inadequate discretisation of the domain. It is therefore recommended to improve the program by using a better discretisation of the domain such as elliptical coordinates or numerically generated boundary fitted curvilinear coordinates. This would then allow to better define limits when the flow front is fully developed (as a function of the inlet diameter and degree of anisotropy). Furthermore the program should be modified to be able to model constant flow rate problems as well.

As a general remark all parts of the unified approach except for the case with constant inlet pressure and measurement of flow front need to be verified in more detail. For example for anisotropic channel flow the pressure distribution is not linear in the mould (indicated by Woerdeman et al. 1995). How does this affect the permeability and flow front shape in the channel flow mould? And following on from that, are current channel flow moulds designed properly - is the width of the moulds too wide in comparison with the length? There are moulds which are square (Parnas and Salem 1993). In this case the flow is not one-dimensional any more.

For constant flow rate experiments the pressure drop between two points is constant. The results in section 11.2 show that this is only true for pressure measurements in the flow domain. The pressure difference between inlet and a pressure transducer along one of the axes is not constant (probably due to the circular inlet). Steenkamer et al. (1995) published experimental results for constant flow rate experiments and showed a typical plot of the pressure history of an experiment. This graph suggests that the pressure difference between the inlet and a point in the flow domain is constant. Because of these conflicting observations it is important to study the effect of the circular inlet in more detail. A flow simulation program would be an ideal tool for this task (as demonstrated in section 6.7 for constant inlet pressure). In section 11.2 it was concluded that pressure measurement along one of the axes is also effected by the circular inlet and developing flow front for highly anisotropic flow. Again a flow program could help to explain this in more detail.

It was demonstrated in section 11.1.3 that experimental design gives a more objective measure to decide whether a result is random or a real physical effect. It is therefore recommended that experimental design should be used much more widely for permeability measurement. This will be particularly useful in establishing whether mould thickness, inlet pressure, type of fluid, measurement angle, flow rate and inlet diameter really effect permeability.

13.2 Possible extensions to unified approach

It is possible to extend the unified approach to include the case where the origin of the experimental coordinate system is not aligned with the origin of the flow front (the inlet). This would require two additional flow front or pressure measurements to determine the x,y offset. For experiments where the inlet pressure varies considerably during the experiment it might be advisable to introduce a pressure averaging scheme similar to the one suggested by Ferland et al. (1996) for channel flow.

For the derivation of the unified approach it was assumed that permeability is constant. The results in chapter 11 did show some variation for different measurement directions and also between runs with identical process conditions. It seems that a statistical approach might be more appropriate to describe permeability. It could also take into account factors like for example the pore size distribution (as determined e.g. by Griffin et al. 1995).

13.3 Interfacial effects

For permeability measurement a sharp flow front is required. As shown in section 11.1.2 the measurement of flow front becomes impossible when capillary flow occurs. The flow front has become a flow front "zone" which creates problems not only for thermistors but also if the progression of the flow front is recorded visually. It is therefore important to define the conditions for which macroscopic flow occurs or alternatively suggest new methods to measure the capillary effects in radial flow experiments. In section 11.1.4 it was demonstrated that a convergence graph can show the effect of capillary action. It may be possible to use the gradient of this graph to quantify capillary pressure (in a similar way to Ahn et al. 1991). In addition to flow front measurement, pressure could be measured at various locations in the radial flow mould (along the *I*, *II* and *III*-axes). Permeability could be calculated using modules 1a, 1b or 2a of the standard equations. If there is capillary flow then permeability obtained from flow front measurements should be higher than permeability obtained from pressure measurements. The difference between the two permeability values is a measure of the capillary effect.

Another possible experiment to investigate capillary flow would be to perform a channel flow experiments at very low inlet pressure or flow rate. First the position of the marching flow front in the dry fabric would be measured. Once the flow front has reached the end of the mould the pressure for the steady state flow is recorded. Any differences between the permeability for flow with stationary flow front or moving flow front would be a measure of capillary flow.

13.4 Flow sensor

In section 11.1.2 the different shapes of the thermistor response was explained by the change of the flow mechanisms from predominantly macroscopic to mainly microscopic flow. This needs to be demonstrated experimentally. Furthermore the overheat ratio of the thermistor should be increased to increase the resolution for velocity measurement. At the same time a calibration procedure is required if thermistors are to be used for quantitative velocity and compaction pressure measurement. Finally the effects of reactive fluids and the heat generated during cure on the thermistor need to be studied.

13.5 New possible test configurations

The unified approach allows to have a fixed measurement coordinate system in the mould . This may be used to design an (almost) fully automated permeability test rig using pressure transducers or diodes to measure flow front (Gauvin et al. 1994). The fabric samples are laid up in the mould always aligned with the experimental coordinate system. The principal permeability and the orientation of the principal axes can be determined on-line during the experiment using the unified approach.

For radial flow experiments with a transparent top plate another way of measuring permeability is conceivable. In radial flow experiments the progression of the flow front is traced along an axis. Instead a point on the flow front could be traced in the direction normal to the flow front (see Figure 8.1). The path of this particle is not necessarily a straight line! As discussed in section 8.2 the effective permeability would be different to the one currently used. This new approach could yield more reliable results as the measurements are now taken in the direction of the pressure potential.

14. Conclusions

The work presented in this thesis is concerned with processing experimental data obtained from permeability experiments. New permeability models have been developed. As a result a unified approach to permeability measurement has been proposed. It establishes a framework for one, two and three-dimensional radial and channel flow experiments and unifies seven different permeability measurement techniques currently used. As inlet conditions it is possible to use constant inlet pressure or constant flow rate. Furthermore it is possible to calculate permeability for an arbitrary direction even if the flow front measurements or pressure measurements along the three measurement axes are not made at the same instance in time. These features make the new approach much more flexible than current methods. A comparison with existing methods was carried out. In one case there was very good agreement while for the second case there was a noticeable difference between the two methods. This was attributed to the fact that the second measurement technique models the inlet incorrectly. A number of other methods have been examined and differences have been discussed. It has been demonstrated that some permeability measurement techniques contain errors.

A number of constant flow rate and constant inlet pressure experiments were conducted to verify the unified approach. In most cases the unified approach was found to work well. Problems occurred when the underlying assumptions were violated in the experiments. It was possible to demonstrate this with the help of a convergence graph. It was possible to show that permeability can be affected by capillary flow. For the constant flow rate experiments the convergence graph also showed that the flow front was still developing for high porosities which lead to permeability values which were more anisotropic than expected. It was further demonstrated that the assumption that permeability is a symmetric second rank tensor is reasonable for the tested combinations of fluid and fabrics. Experimental design helped to detect a pressure dependence of permeability which was attributed to the presence of the thermistors which used to measure the flow front.

The possibility of using a three-dimensional radial flow test to determine the full permeability tensor in a single experiment was investigated. For the three-dimensional permeability tests with flow with a moving flow front it was noticed that capillary flow was the dominant flow pattern. The only way to overcome this was by increasing the inlet pressure. However this led to flow-induced compaction and easy flow paths that rendered any results useless. It was

therefore concluded that three-dimensional permeability measurement with moving flow front was not possible.

The use of thermistors for permeability measurement purposes is questionable as the reduction in local channelling along the wires leads to an increase in fibre volume fraction. However it was demonstrated that using a smaller number of thermistors is ideal for process control and validation of flow simulations as they yield information about the impregnation process, the orientation of the flow front, compaction of the fibres and possibly the fluid velocity.

Appendices

A Compaction tests

The purpose of the compression tests has been to measure the compaction pressure as a function of fibre volume fraction for various fabrics. At the same time the time-dependence of the compaction pressure was investigated to ensure that the flow experiment would be carried out at the desired compaction pressure (to avoid fluid-induced compaction).

1 Background theory

Wu et al. (1993) and (1994) investigated the influence of clamping pressure on permeability. It was found that as soon as the inlet pressure exceeds the clamping pressure, the relation between pressure and flow rate became non-linear (a violation of Darcy's law). This effect was explained by additional compaction caused by the high flow rates. As long as the injection pressure was less than the clamping pressure this effect was not observed. Hence an understanding of the compaction behaviour is essential for successful permeability measurement.

Toll and Månson (1994) derived a power law from micromechanical analysis which describes the compaction of woven fabrics and random mats well. Pearce and Summerscales (1995) investigated the time dependence of the compaction pressure for a plain weave fabric. It was shown that once the target peak load was reached and the crosshead of the testing machine was stopped the load started to relax. It was then possible to reduce the gap height further. Pearce and Summerscales found that it was possible to describe this relaxation with an exponential equation. It was demonstrated that a single layer yields a higher fibre volume fraction for the given pressure while three, four or five layers yield (almost) identical results.

Compressed at the same compaction pressure different types of reinforcement fabrics or mats yield different compressed thickness and hence fibre volume fractions. As a consequence the average fibre volume fractions of a stack of different reinforcement fibres is not the same as fibre volume fractions of the constituent materials if measured separately. It is therefore important to know the compaction behaviour of the individual fabrics and mixed lay-ups. One approach for thin laminates is to calculate the average (in-plane) permeability from a rule of mixtures (Gebart et al. 1991, Kim et al. 1990, Trevino et al. 1990). Batch and Cumiskey (1990) proposed a more complex model for multi-layered composites which also takes into

account the interlayer packing of different types of reinforcement materials. However to measure flow front with thermistors a smooth flow front is required. Therefore permeability measurement with thermistors is restricted to mixed lay-up sequences where the individual layers in the stack are very thin. The resulting porous medium can then be considered a quasi-homogeneous medium. For these cases the compaction behaviour and average porosity can be determined directly from compaction tests of the stacking sequence of interest.

2 Experimental apparatus and materials

The fibre volume fraction is calculated according to Pearce and Summerscales (1995)

$$V_f = \frac{N W_f}{d \rho} \qquad \text{(A.1)}$$

where V_f is the fibre volume fraction, N is the number of layers, W_f is the weight per unit area of the fabric, d is the height of the cavity and is ρ the density of the fibres. Materials tested were a continuous filament mat (Unifilo U750-450), a woven roving (RT600), a twill fabric (RC600) all from Vetrotex and a quasi-unidirectional non crimp fabric from Tech Textiles (E-LPb 567). The tests were done in a universal testing machine (JJ Instruments; 30 kN load cell) which was fitted with a compression jig. The size of the platens was 55 mm by 78 mm.

Run No.	Type of fabric	Lay-up sequence (orientation)	Crosshead speed
2	U750-450	-	0.5 mm/min
4	Woven Roving	-	0.1 mm/min
6	UD	0/0	0.1 mm/min
8		0/90	0.1 mm/min
10	WR/UD	WR/UD/WR/UD (0/0)	0.1 mm/min
12		WR/UD/WR/UD (0/90)	0.1 mm/min
14		WR/WR/UD/UD (0/0)	0.1 mm/min
16		WR/WR/UD/UD (0/90)	0.1 mm/min
A		WR/UD/WR/UD (0/0)	0.1 mm/min
B		WR/UD/WR/UD (0/0)	0.5 mm/min
C		WR/UD/WR/UD (0/0)	2.0 mm/min
D	Twill/UD	Twill/UD/Twill/UD (0/0)	0.1 mm/min
E		Twill/Twill/UD/UD (0/0)	0.1 mm/min
F	Twill	-	0.1 mm/min

Table A.1 Details of compaction experiments

All tests were carried out with four layers of fabric. The crosshead speed and the lay-up sequence for each experiment are shown in Table A.1. "0" means the unidirectional fibres are aligned with the longer side of the platens while "90" denotes that the fibres are aligned at 90 degrees to this direction. To calculate the weight per unit area the side lengths of the samples were measured with a vernier calliper while the weight of the samples was measured using a top pan balance.

3 Discussion of results

Weight per unit area

The results of this investigation are summarised in Table A.2. It shows that for all materials a difference to the nominal weight can be observed. During this investigation it was found that for the woven fabrics, in particular twill fabric, it was very difficult to obtain an accurate measure of the size and weight since these fabrics tend to fray very easily even if handled carefully. All samples are taken from the first metre of each roll.

In the case of the random mat and the twill fabric, the number of samples is very small. Furthermore the deviation from the nominal weight is small too. Hence it was decided to use the nominal weight for random matt (450 g/m^2) and twill fabric (600 g/m^2) to determine the fibre volume fraction. The weight of the woven roving is based on a larger population. Also the standard deviation is quite small which increases the confidence in the measured value. Therefore 588 g/m^2 was used for woven roving for the subsequent calculations. Most surprising was the weight for the unidirectional material of 660 g/m^2 which is a significant deviation from the 567 g/m^2 as quoted by the manufacturer. However consulting Tech Textiles revealed that the quoted weight only applies to the unidirectional tows. The weight for the weft (60-80 g/m^2) and the powder coating has to be added to the nominal weight.

	U750	Woven Roving	UD	Twill
nominal weight	450	600	567	600
mean	458.77	588.47	660.80	616.05
standard deviation	26.97	15.43	9.98	36.09
number of samples	4	18	26	8

Table A.2 Weight per unit area [g/m^2]

Compaction behaviour

For all experiments the samples were compacted at the given crosshead speed until the target pressure of 200kPa was reached. The crosshead was then stopped and a relaxation of the load

was observed. After about 8 minutes the crosshead was moved again to reach the target pressure. The second compaction changed the thickness of the sample very little. Therefore only the initial compaction is reported for the following experiments. A typical result is shown in Figure A.1. For the woven and non-crimp fabric the initial relaxation after 8 min was about 10% while after the second compaction a relaxation of 5-7% was noted. For the random mat it was 25 and 15% respectively. For the purpose of designing the permeability experiments 1% was added to the fibre volume fraction value (which was measured after the initial compaction) to compensate for the relaxation.

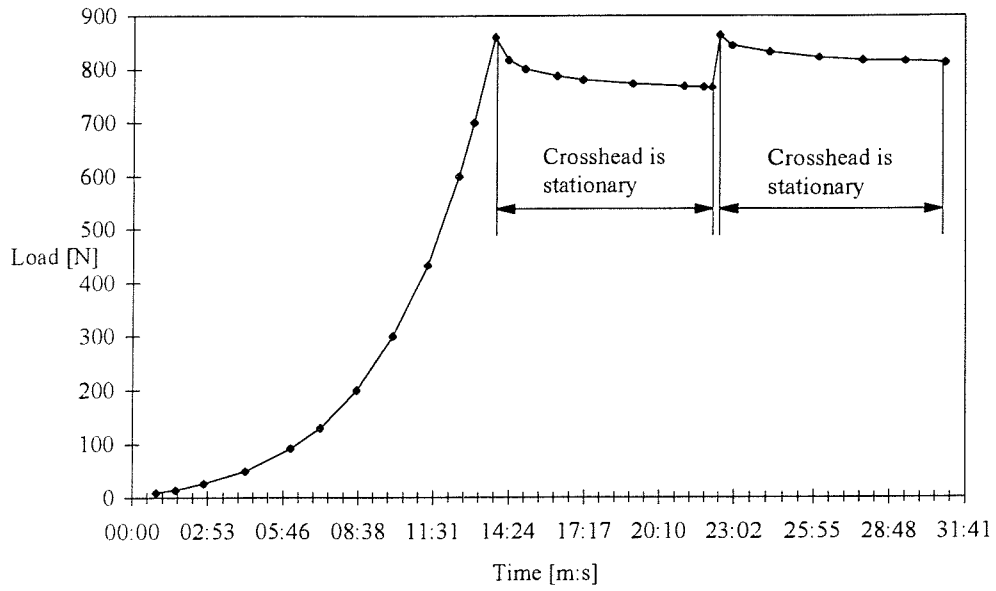

Figure A.1 Load versus time

Important for the planning of injection experiments is the variation of the compaction pressure with fibre volume fraction which is shown for unidirectional (UD) and woven roving (WR) in Figure A.2. It was interesting to note that the unidirectional fabric in the 0/90 lay-up showed a slightly higher fibre volume fraction than the 0/0 lay-up. This could be observed for single and mixed lay-ups (UD and WR, WR/UD/WR/UD). The same effect was not observed for the WR/WR/UD/UD lay-up sequence which yielded slightly lower fibre volume fractions for a given pressure. It was observed that the fibre volume fraction of the mixed lay-ups was higher than the fibre volume fractions of the individual fabrics (WR and UD with 0/0 and 0/90 orientation). This is in agreement with trends observed by Batch and Cumiskey (1990). The fibre volume fraction of the mixed lay-up was calculated from equation (A.1) using the average weight per unit area of the two fabrics.

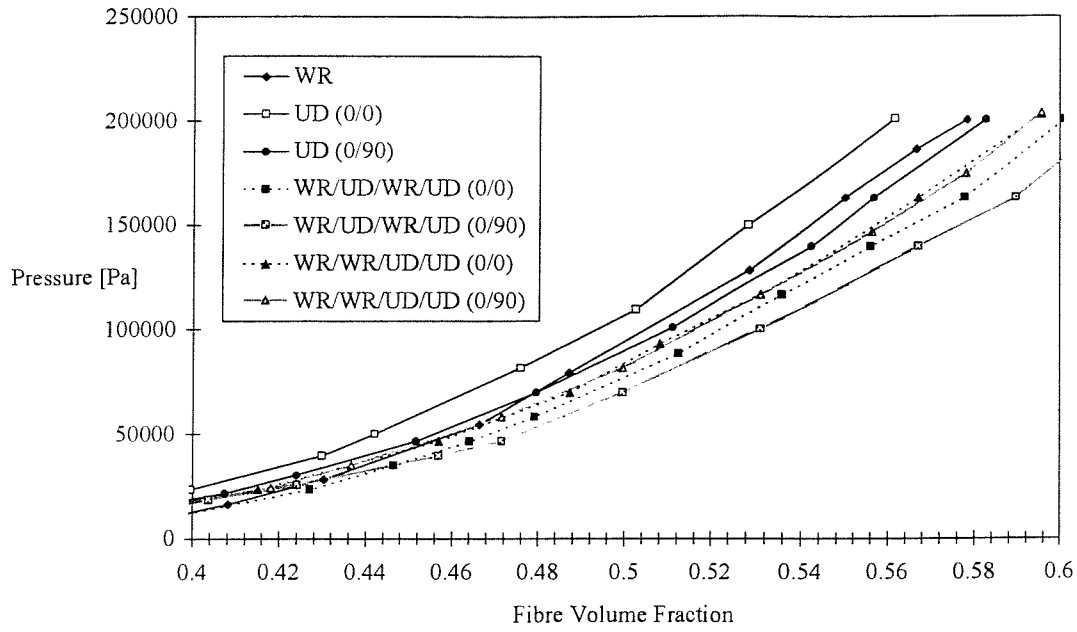

Figure A.2 Compaction pressure versus fibre volume fraction (UD = quasi-unidirectional fabric, WR = woven roving, (0/90) means that the first layer of the UD material is aligned with the longer side of the platens while the second layer is at 90° to that direction)

Figure A.3 shows compaction pressure versus fibre volume fraction for unidirectional and twill fabric (T). As before the combination of single layers of each fabric (T/UD/T/UD) yielded a higher fibre volume fraction than the T/T/UD/UD lay-up sequence. However in comparison with the woven roving results the values obtained here are slightly smaller (about 1% V_f). The fibre volume fraction for four layers of twill fabric had to be estimated since the final compaction thickness was too low (perhaps as a result of a reading error). The thickness of 1 mm compared with 1.6 to 1.7 mm for all the other experiments would have yielded a fibre volume fraction of about 90%. It was found that the compression jig was not ideal for testing the twill fabric. Because of its design the specimens had to be cut to size which allowed only very little overhang to make up for the frayed edges.

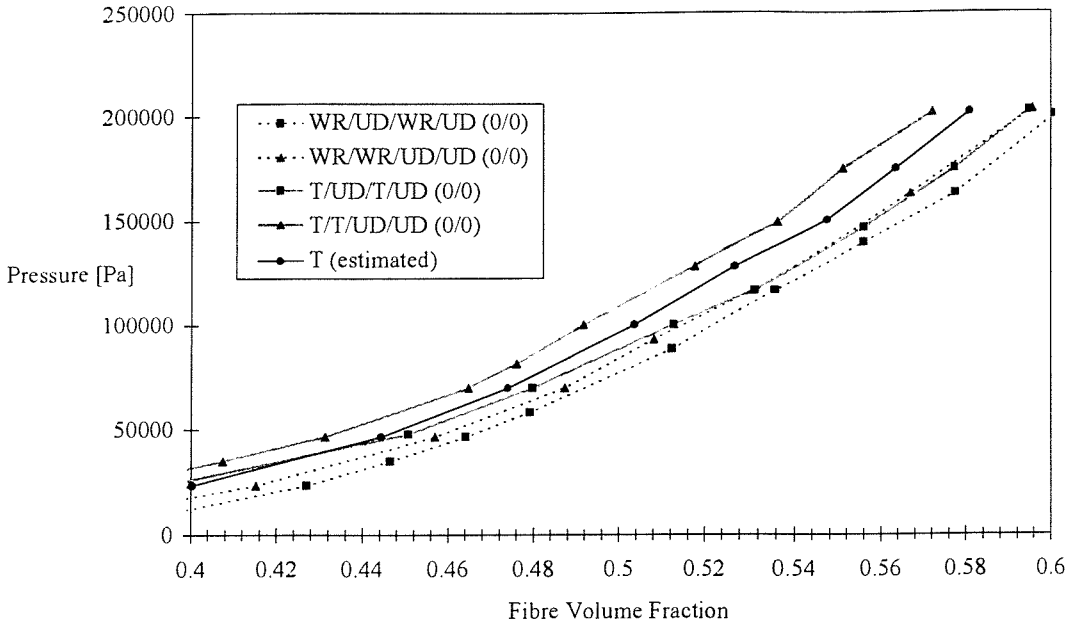

Figure A.3 Compaction pressure versus fibre volume fraction (UD = quasi-unidirectional fabric, T = twill fabric, WR = woven roving, all layers of the UD material are aligned with the longer side of the platens)

In addition to the above investigation the effect of various closing speeds of the crosshead on the compaction behaviour was examined (see Figure A.4). The results indicate that although the speed was increased by a factor of 20 (0.1 mm/min, 0.5 mm/min and 2 mm/min) the effect on the pressure versus fibre volume fraction curve was minimal. It has to be noted however that even though 2mm/min is higher than closing speeds used in other investigations on compaction behaviour, it is still very slow compared with stamping processes used for mass preform fabrication.

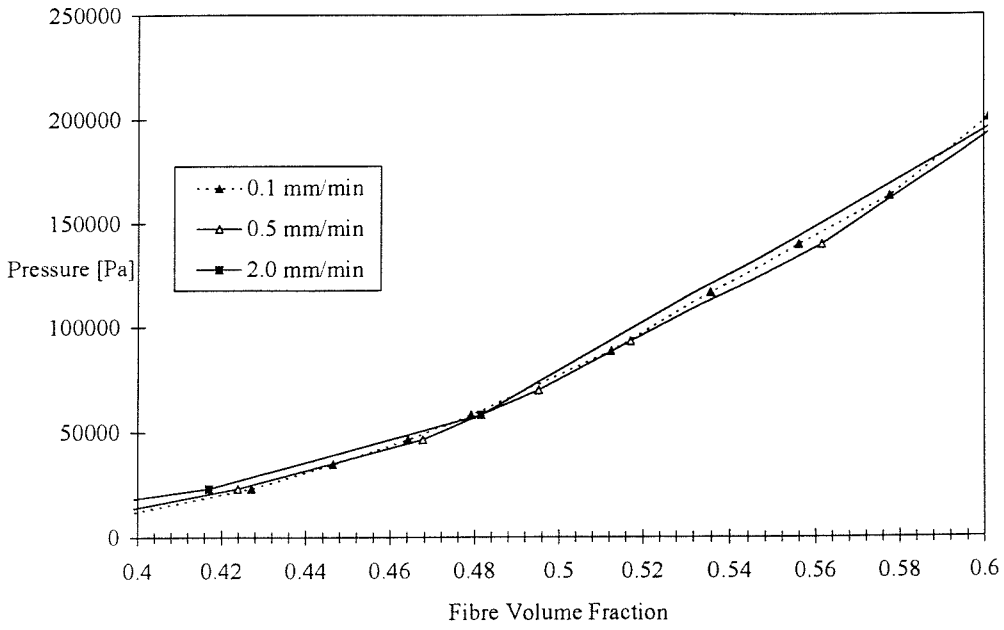

Figure A.4 Compaction pressure for different closing speeds (WR/UD/WR/UD (0/0))

4 Summary

Table A.3 summarises the fibre volume fraction for different lay-ups at selected compaction pressures. The values for 100 kPa and 150 kPa were read of the pressure versus fibre volume fraction graph. Pearce and Summerscales (1995) found that the relaxation behaviour was similar at all pressure ranges. Therefore one percent has to be added to the fibre volume fraction for unidirectionals, woven roving and twill and three percent for the random mat to account for the relaxation (as observed in the experiments).

Type of material	Compaction pressure (no relaxation)			Thickness of each layer [mm]
	100 kPa	150 kPa	200 kPa	
U750	20	23	26	0.69
UD	50/51*	53/55*	56/58*	0.46/0.44*
Woven Roving	50	54	58	0.40
WR/UD/WR/UD	52/53*	56/57*	60/61*	0.41/0.40*
WR/WR/UD/UD	51	56	59	0.41
Twill (estimated)	*50*	*54*	*58*	*0.40*
T/UD/T/UD	51	55	59	0.41
T/T/UD/UD	49	53	57	0.43

Table A.3 Recommended fibre volume fractions [%]

* the first value is for a 0/0 lay-up while the second value is for 0/90 lay-up

B Results from flow simulation

For the case when the inlet is circular it is not possible to derive the progression of the flow front analytically. Therefore a flow simulation program was used to determine the flow front position as a function of time (see section 6.7.3). Table B.1 lists the details of the various runs with the program.

Run No.	K_1 [10^{-9} m^2]	K_2 [10^{-9} m^2]	r_o [mm]	P_o [kPa]	ε	μ [Pa s]
1	4.0	3.0	8	70	0.48	0.1
2	4.0	2.0	8	70	0.48	0.1
6	0.4	0.3	8	70	0.48	0.1
10	4.0	2.0	8	250	0.48	0.1
14	4.0	2.0	8	70	0.48	0.1
15	4.0	2.0	16	70	0.48	0.1
16	4.0	2.0	28	70	0.48	0.1

Table B.1 Details of flow simulations

The tables below show the flow front position at a given time step. The flow front is measured along the **1** and **2**-axis (denoted 0° and 90° respectively) and in between the two axes at 45°.

time [s]	radius [m]		
	0°	45°	90°
0.03	0.014	0.014	0.014
0.16	0.040	0.037	0.035
0.48	0.061	0.058	0.053
0.99	0.081	0.076	0.071
1.75	0.102	0.094	0.089
2.74	0.122	0.115	0.106
3.99	0.142	0.133	0.123
5.48	0.162	0.150	0.141
7.27	0.182	0.170	0.158
9.33	0.202	0.190	0.175
11.68	0.222	0.206	0.192
14.33	0.242	0.225	0.209
17.28	0.262	0.245	0.227
20.55	0.282	0.263	0.244
24.11	0.302	0.280	0.261
27.99	0.322	0.300	0.278
32.22	0.342	0.320	0.296
36.74	0.362	0.337	0.313
41.60	0.382	0.354	0.330
46.81	0.402	0.374	0.347

Table B.2 Run 1

time [s]	radius [m]		
	0°	45°	90°
0.03	0.014	0.010	0.010
0.18	0.043	0.037	0.032
0.47	0.063	0.053	0.045
1.00	0.084	0.070	0.060
1.74	0.105	0.087	0.074
2.73	0.125	0.104	0.089
3.97	0.146	0.120	0.103
5.49	0.166	0.136	0.117
7.28	0.186	0.153	0.132
9.34	0.206	0.169	0.146
11.69	0.227	0.185	0.160
14.33	0.247	0.202	0.174
17.28	0.267	0.218	0.188
20.54	0.288	0.235	0.202
24.11	0.308	0.252	0.217
27.99	0.328	0.269	0.231
32.21	0.348	0.286	0.245
36.74	0.368	0.303	0.259
41.63	0.389	0.319	0.273

Table B.3 Run 2

time [s]	radius [m]		
	0°	45°	90°
0.27	0.014	0.014	0.014
1.60	0.040	0.037	0.035
4.77	0.061	0.058	0.053
9.92	0.081	0.076	0.071
17.46	0.102	0.094	0.089
27.38	0.122	0.115	0.106
39.88	0.142	0.133	0.123
54.79	0.162	0.150	0.141
72.71	0.182	0.170	0.158
93.32	0.202	0.190	0.175
116.81	0.222	0.206	0.192
143.29	0.242	0.225	0.209
172.78	0.262	0.245	0.227
205.46	0.282	0.263	0.244
241.06	0.302	0.280	0.261
279.94	0.322	0.300	0.278
322.22	0.342	0.320	0.296
367.38	0.362	0.337	0.313
416.00	0.382	0.354	0.330
468.07	0.402	0.374	0.347

Table B.4 Run 6

time [s]	radius [m]		
	0°	45°	90°
0.01	0.014	0.010	0.010
0.05	0.043	0.037	0.032
0.13	0.063	0.053	0.045
0.28	0.084	0.070	0.060
0.49	0.105	0.087	0.074
0.77	0.125	0.104	0.089
1.11	0.146	0.120	0.103
1.53	0.166	0.136	0.117
2.04	0.186	0.153	0.132
2.61	0.206	0.169	0.146
3.27	0.227	0.185	0.160
4.01	0.247	0.202	0.174
4.84	0.267	0.218	0.188
5.75	0.288	0.235	0.202
6.75	0.308	0.252	0.217
7.84	0.328	0.269	0.231
9.02	0.348	0.286	0.245
10.29	0.368	0.303	0.259
11.66	0.389	0.319	0.273

Table B.5 Run 10

time [s]	radius [m]		
	0°	45°	90°
0.03	0.014	0.010	0.010
0.18	0.043	0.037	0.032
0.47	0.063	0.053	0.045
1.00	0.084	0.070	0.060
1.74	0.105	0.087	0.074
2.73	0.125	0.104	0.089
3.97	0.146	0.120	0.103
5.49	0.166	0.136	0.117
7.28	0.186	0.153	0.132
9.34	0.206	0.169	0.146
11.69	0.227	0.185	0.160
14.33	0.247	0.202	0.174
17.28	0.267	0.218	0.188
20.54	0.288	0.235	0.202
24.11	0.308	0.252	0.217
27.99	0.328	0.269	0.231
32.21	0.348	0.286	0.245
36.74	0.368	0.303	0.259
41.63	0.389	0.319	0.273

Table B.6 Run 14

time [s]	radius [m]		
	0°	45°	90°
0.07	0.041	0.037	0.033
0.27	0.063	0.054	0.047
0.63	0.085	0.071	0.062
1.16	0.105	0.088	0.076
1.89	0.126	0.105	0.090
2.82	0.146	0.122	0.104
3.97	0.167	0.139	0.118
5.35	0.187	0.155	0.133
6.96	0.208	0.171	0.147
8.81	0.228	0.188	0.161
10.92	0.248	0.204	0.175
13.27	0.269	0.220	0.190
15.89	0.289	0.236	0.204
18.77	0.309	0.253	0.218
21.92	0.329	0.269	0.232
25.36	0.350	0.286	0.246
29.05	0.370	0.303	0.261
33.03	0.390	0.320	0.275

Table B.7 Run 15

time [s]	radius [m]		
	0°	45°	90°
0.018	0.039	0.037	0.036
0.12	0.062	0.055	0.051
0.34	0.084	0.072	0.065
0.70	0.105	0.089	0.079
1.22	0.126	0.106	0.093
1.90	0.146	0.122	0.107
2.76	0.167	0.139	0.121
3.82	0.188	0.156	0.135
5.07	0.209	0.173	0.149
6.52	0.229	0.190	0.164
8.18	0.250	0.206	0.178
10.05	0.270	0.223	0.192
12.15	0.290	0.240	0.206
14.47	0.311	0.257	0.220
17.04	0.331	0.273	0.234
19.82	0.352	0.289	0.249
22.86	0.372	0.305	0.263
26.13	0.392	0.321	0.277
29.67	0.438	0.338	0.291

Table B.8 Run 16

C Permeability measurement rig

In this appendix a brief description of the rig used to measure permeability is given. This rig was the result of a Master of Engineering group design project. All the figures in this appendix were taken from the final report by Boyde, Clothier and Inglis (1995).

The permeability rig consists of a aluminium base plate which is stiffened by a steel grillage supported by a steel frame. A number of possible injection ports are located along the centre line of the base plate. The fibre samples are placed on the base plate. The fibre stack is then compressed by a glass plate and a pressure transfer frame which are placed on top of the fibre stack. In the remainder of this appendix the grillage and base plate, the glass plate, the pressure transfer frame and the fluid supply will be discussed. Finally the results from commissioning experiments will be presented.

1 Grillage and base plate design

For the base plate a cast aluminium tool plate (Alumax MiC-6) was chosen for its flatness (to 0.25mm) and solvent resistance. Standard BS 4 mild steel channel sections were selected for the structural members due to their availability in a wide variety of sizes.

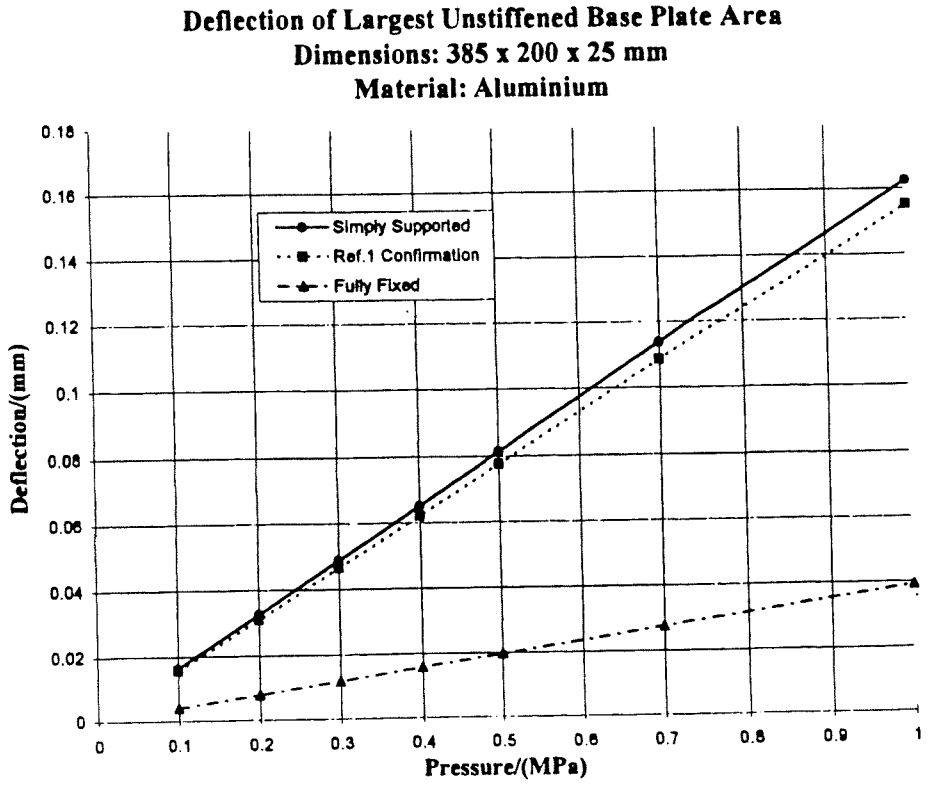

Figure C.1 Deflection of unstiffened plate

The dimensions of the mould working area are 1.4m x 0.5m. The maximum deflection was specified to be less than 2% for a 10mm thick mould cavity at 7 bar working pressure. The base plate thickness is determined by considering the maximum unsupported area of the plate using simple plate bending theory. Figure C.1 shows that a 25mm thick plate would give negligible deflection for the maximum unstiffened area.

Once the number of stiffeners had been decided their dimensions could be determined using stiffened plate bending theory. The results are illustrated in Figure C.2. The chosen dimension was a 127x64mm stiffener.

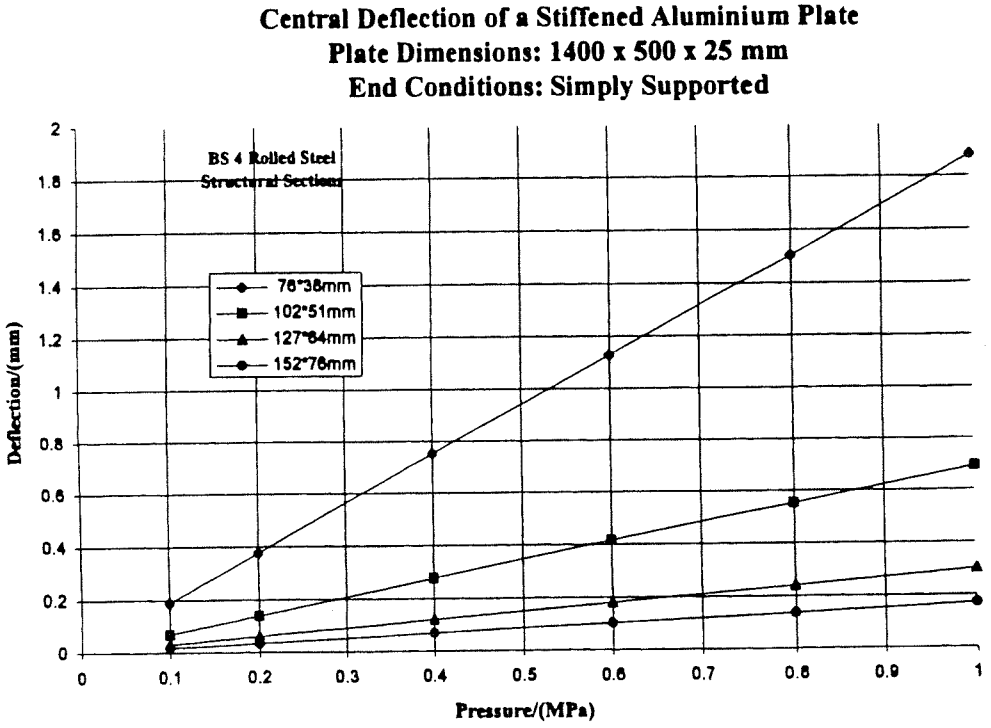

Figure C.2 Deflection of stiffened plate

Figure C.3 and Figure C.4 show the production drawings of the base plate and the grillage. To achieve an acceptable flatness the surface of the grillage had to be planned after welding. The aluminium base plate is fixed to the steel grillage with 4 bolts which allow some movement of the aluminium plate due to thermal expansion. Figure C.5 shows the production drawing of the support structure for both the grillage and the pressure transfer frame.

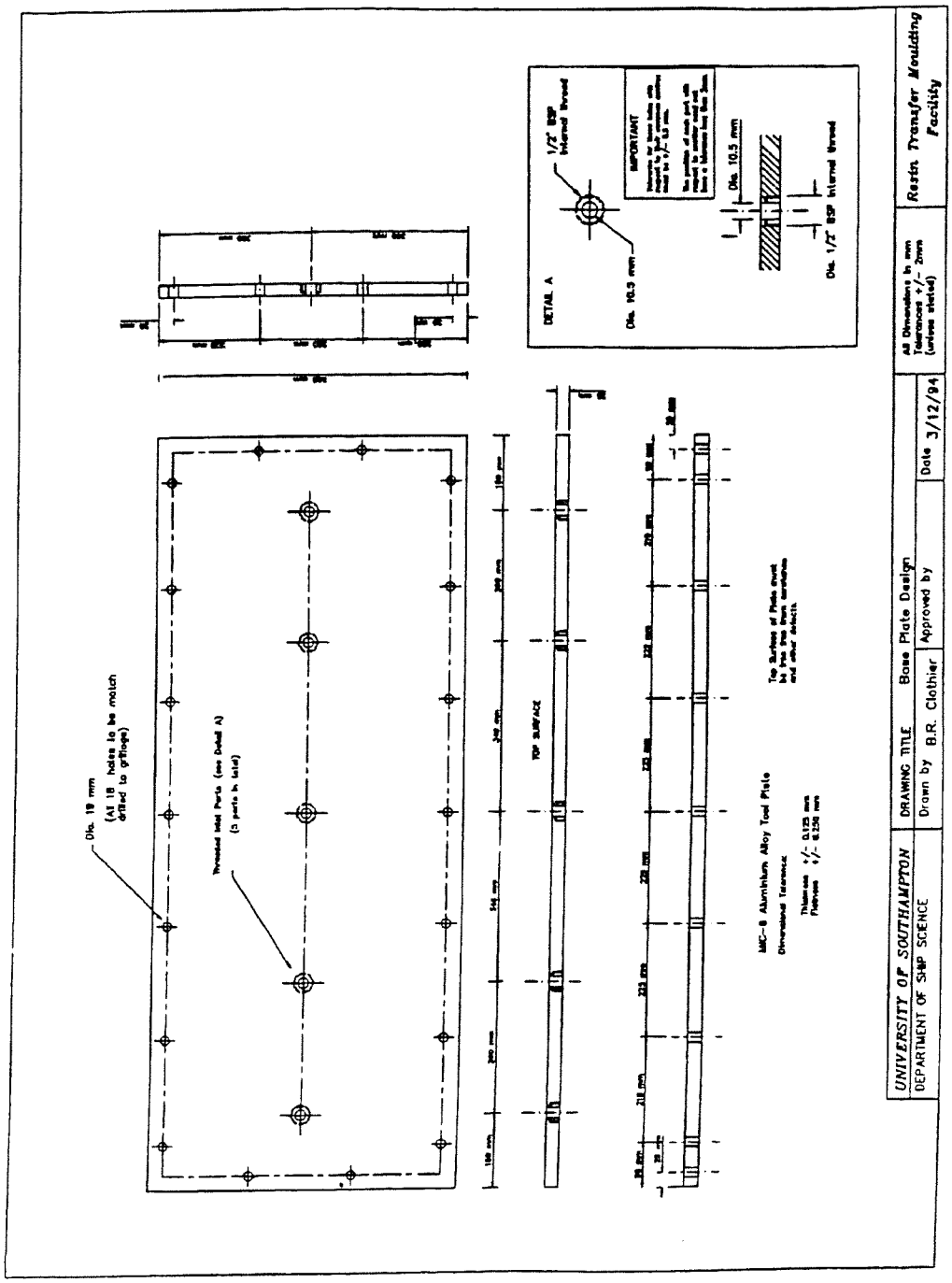

Figure C.3 Base plate

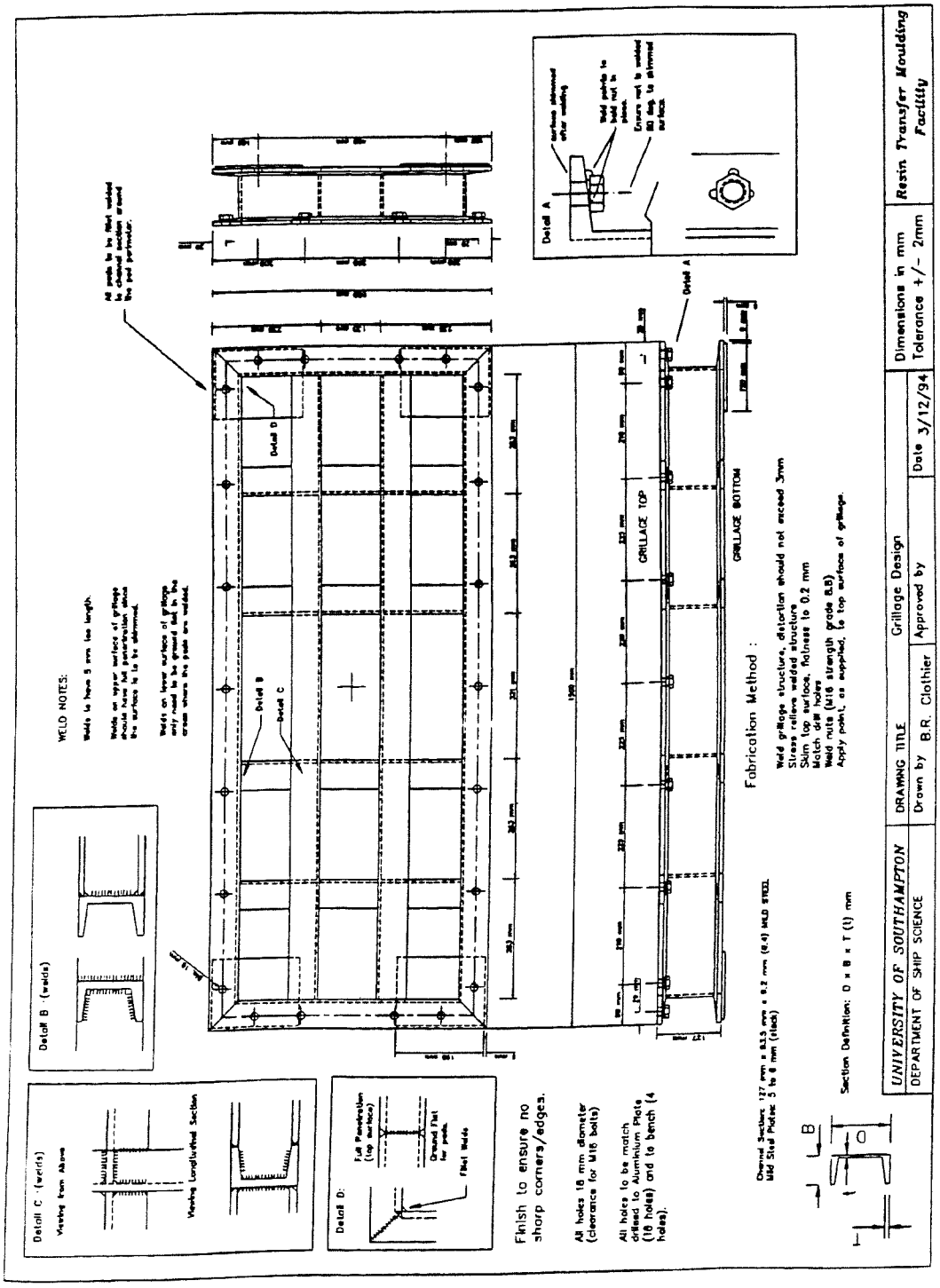

Figure C.4 Grillage

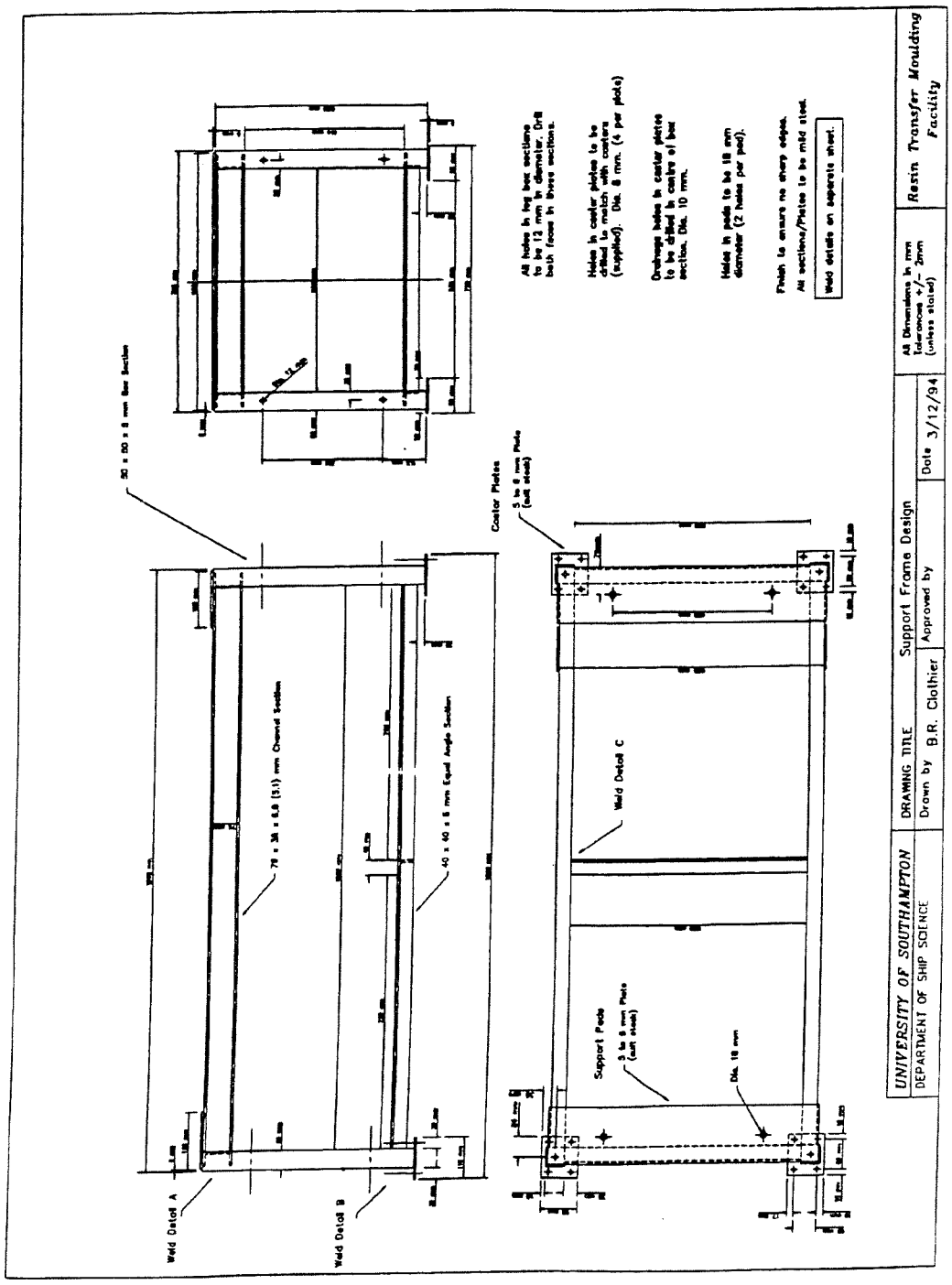

Figure C.5 Support structure

2 Glass plate

The top plate of the radial flow mould is a glass plate. For economical reasons it was decided to use soda-lime toughened float glass. The glass is manufactured to BS 6206 Class A. For this type of glass the safe design stress is 35MPa. Using plate bending theory the stresses and the deflection of the glass plate have been calculated.

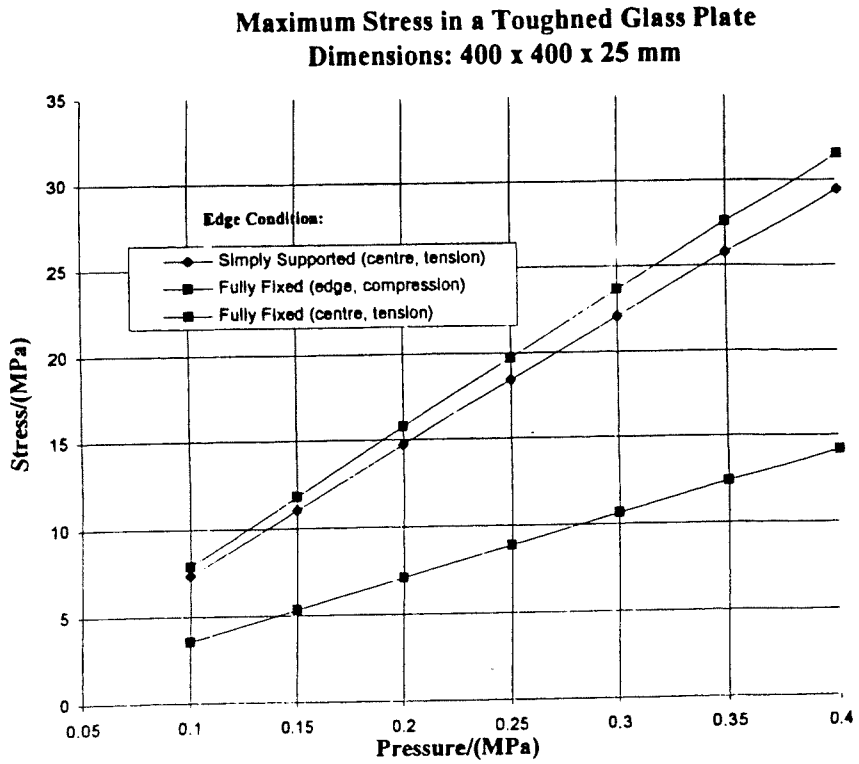

Figure C.6 Stress in glass plate

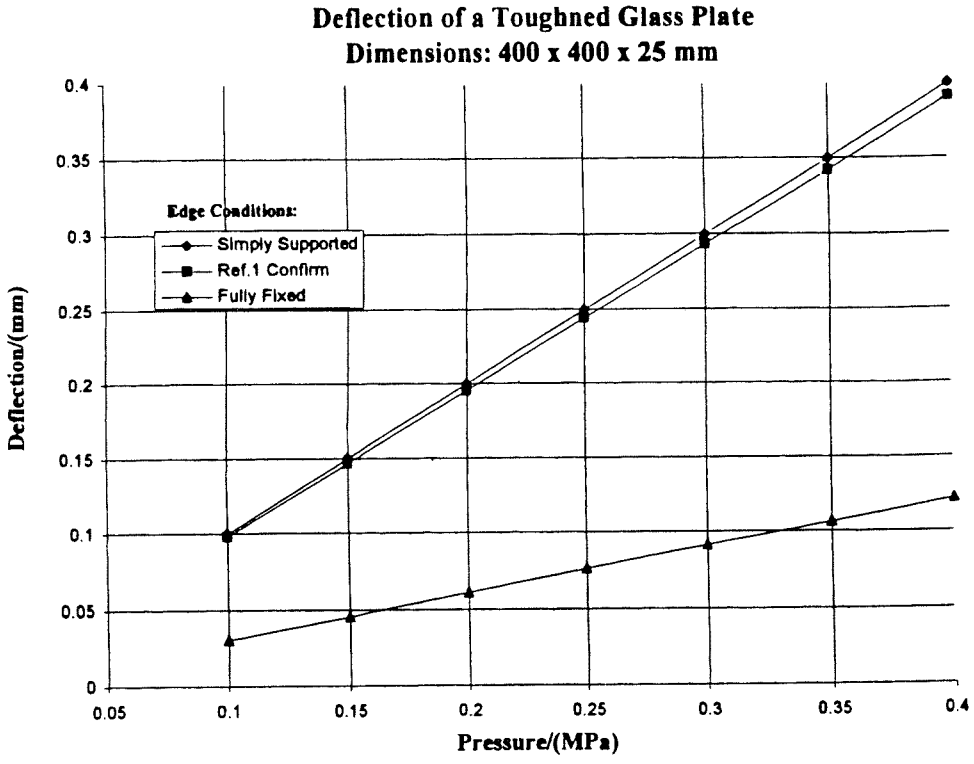

Figure C.7 Deflection of glass plate

Figure C.6 shows that the safe design stress is never exceeded. Figure C.7 shows that at high compaction (and injection pressures) the deflection of the glass plate becomes quite noticeable.

3 Pressure transfer frame

For the glass plate to be compacted to the required gap height and restrained against the injection pressure a pressure transfer frame is required. This frame is constructed from steel box sections. The production drawings are shown in Figure C.9. To compress the fibre stack the pressure transfer frame is bolted to the base plate (and grillage) with M16 bolts. To be able to apply the torque which is required to close the mould the bolts need to be lubricated with grease. Neoprene rubber strips are placed between the pressure transfer frame and the glass plate to ensure that the load is evenly spread over the glass plate.

The performance of the assembled glass plate and pressure transfer frame is estimated by assuming that the total deflection is the sum of the individual deflections of the glass plate and the pressure transfer frame. The main assumptions for the frame are that the individual beams are fully fixed and that the load is applied uniformly over the beam length. The results are illustrated in Figure C.8 and give an idea of the operating window in which useful experiments can be carried out.

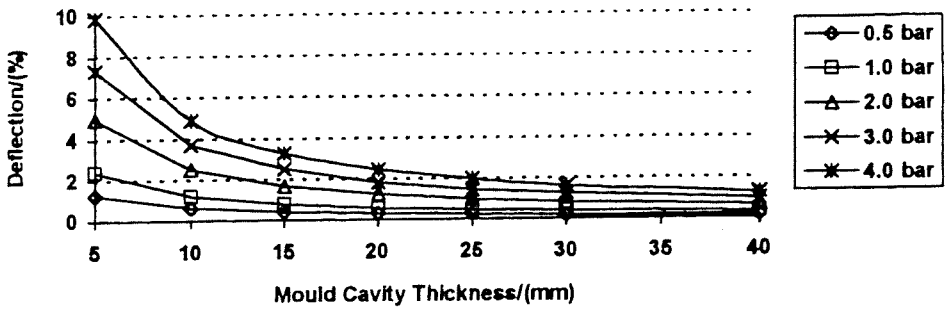

Figure C.8 Predicted radial flow mould deflection

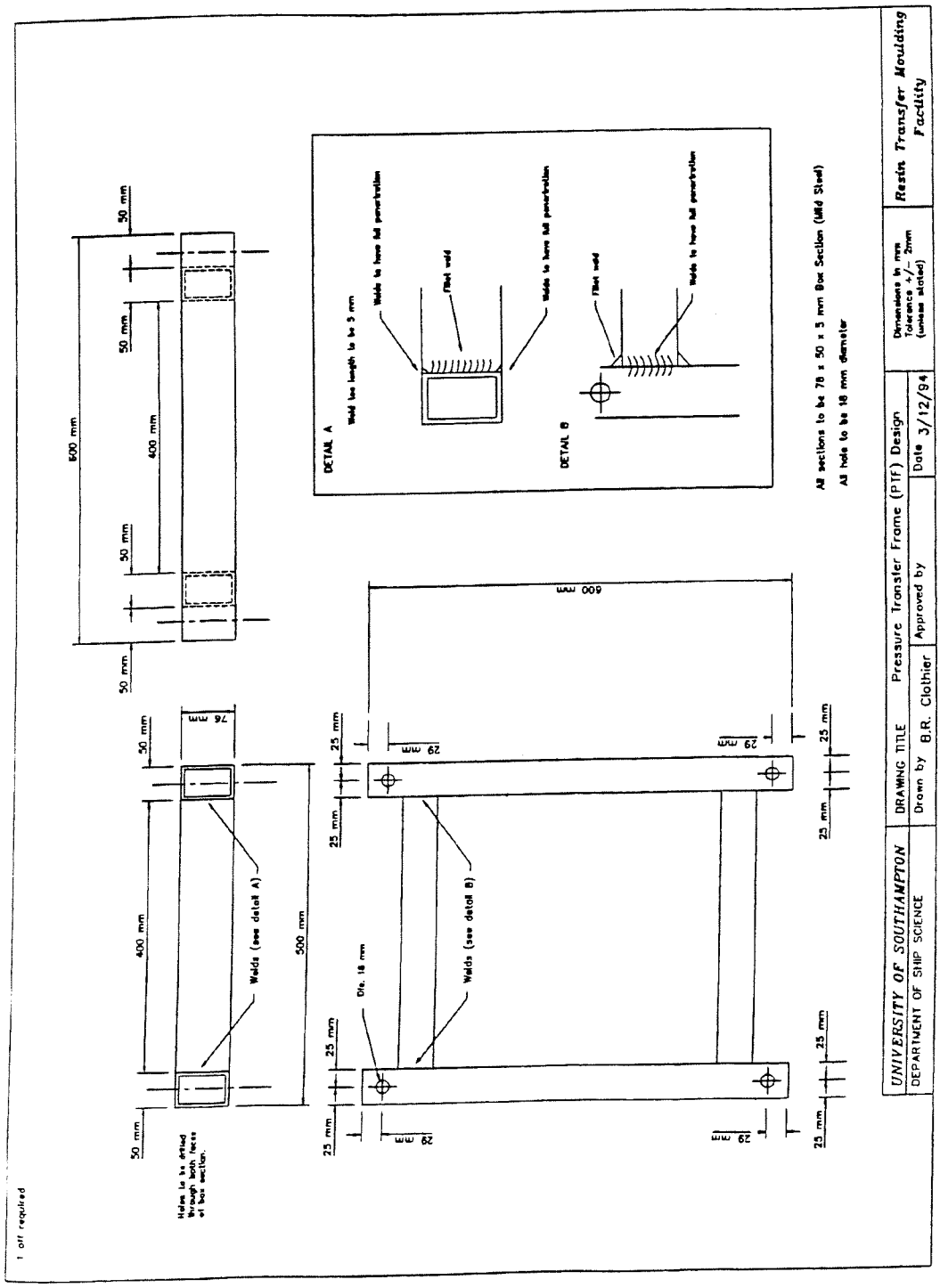

Figure C.9 Pressure transfer frame

4 Fluid supply

The test fluid, oil, is injected from a pressure vessel (an old fire extinguisher) into the mould. The maximum injection pressure is 5 bar. An existing compressed air line which was available in the laboratory was used to pressurise the pressure vessels. To ensure safe operation an adjustable safety valve, a pressure regulator for the incoming compressed air line and a

bourdon pressure gauge were fitted to the pressure vessel. To control the oil release from the pressure vessel a ball valve was fitted as well. Reinforced PVC hose was used to connect the pressure supply vessel and the mould. The pressure transducer had been suspended below the grillage with a T-piece due to space constraints in the grillage.

5 Commissioning experiments

The pressure transducer at the inlet port was calibrated by the manufacturer across its full pressure range of -1 to 5 bar. The calibration of the thermistors used in the flow experiments is discussed in Weitzenböck et al. (1995b).

A number of initial experiments were conducted to commission the test rig. The permeability results are discussed in the main text. During these initial experiments the deflection of the glass plate was measured during compaction and during the injection. The deflection of the glass plate was monitored at its centre point. The measurements were done using a dial gauge accurate to 0.02mm. The dial gauge had a magnetic base which was attached to the pressure transfer frame. This was found to be the most acceptable arrangement even though there were still some sources of error which affected the measurements (distortion of the pressure transfer frame, compaction of padding between glass plate and pressure transfer frame). Table C.1 shows the measured deflection after compaction. For higher fibre volume fractions these deflections are quite noticeable. It is therefore important, as already shown in Figure C.8, to select the correct mould thickness and fibre volume fraction to minimise the effect of the glass plate deflection. No additional deflection was measurable while the fluid was injected (at pressures up to 2.8 bar).

Run No.	V_f [%]	Thickness of cavity (mm)	Deflection of glass plate (mm)
5	45.5	4.65	0.140
6	22.7	4.65	0.130
7	22.7	4.65	0.320
8	45.5	4.65	0.730
9	29.5	20.5	0.376
11	29.8	25.1	0.445
12	29.8	25.1	0.541

Table C.1 Deflection of glass plate during commissioning experiments

D Results from permeability experiments

In the following three appendices experimental results of all the permeability experiments carried out in the Ship Science Laboratory of the University of Southampton are listed. This is in particular the flow front radii or x,y coordinates of the flow front and the time the flow front took to get to this position. Furthermore the fibre volume fraction, viscosity and inlet pressure are also listed. For all experiments Shell Vitrea M100 oil was used.

E Permeability experiments - initial experiments

The material tested was a continuous filament mat from Vetrotex (U750-450). For experiments all 7 the measurements where carried out in the reference coordiante system except for experiment 12 where the coordiante system was rotated by 15°. The inlet radius was 0.00525 m. The viscosity was 0.333 Pa s.

time [s]	$r_{f,I}$ [m]	$r_{f,II}$ [m]	$r_{f,III}$ [m]
65	0.100	0.101	0.101
130.1	0.133	0.131	0.132
194.8	0.156	0.156	0.158
259.1	0.176	0.177	0.178

Table E.1 Experiment 5 with V_f = 45.5 % and P_o = 91 kPa

time [s]	$r_{f,I}$ [m]	$r_{f,II}$ [m]	$r_{f,III}$ [m]
8.4	0.083	0.083	0.081
17.3	0.118	0.123	0.125
26.5	0.152	0.154	0.157
35.5	0.175	0.178	0.181

Table E.2 Experiment 6 with V_f = 22.7 % and P_o = 214 kPa

time [s]	$r_{f,I}$ [m]	$r_{f,II}$ [m]	$r_{f,III}$ [m]
17.8	0.097	0.098	0.099
35.1	0.135	0.134	0.135
51.9	0.162	0.161	0.162
68.8	0.183	0.181	0.178

Table E.3 Experiment 7 with V_f = 22.7 % and P_o = 114 kPa

time [s]	$r_{f,I}$ [m]	$r_{f,II}$ [m]	$r_{f,III}$ [m]
30.5	0.096	0.095	0.092
59.6	0.135	0.134	0.130
88.7	0.165	0.164	0.160
117.9	0.190	0.189	0.184

Table E.4 Experiment 8 with V_f = 45.5 % and P_o = 255 kPa

I - direction		*III* - direction	
time [s]	$r_{f,I}$ [m]	time [s]	$r_{f,III}$ [m]
21	0.052	15	0.044
95	0.104	90	0.099
227	0.156	212	0.150

Table E.5 Experiment 9 with V_f = 29.5 % and P_o = 167 kPa

I - direction		*III* - direction		*z*- direction	
time [s]	$r_{f,I}$ [m]	time [s]	$r_{f,III}$ [m]	time [s]	z_f [m]
17.5	0.042	13.3	0.038	0.5	0.0017
72.3	0.072	66	0.070	1.3	0.0099
				4.8	0.0174
				11.0	0.0244

Table E.6 Experiment 11 with V_f = 29.8 % and P_o = 124 kPa

I - direction		*II* - direction		*III* - direction		*z*- direction	
time [s]	$r_{f,I}$ [m]	time [s]	$r_{f,II}$ [m]	time [s]	$r_{f,III}$ [m]	time [s]	z_f [m]
3	0.022	2.6	0.022	1.8	0.021	16.5	0.024
12.5	0.035	13.4	0.036	8.1	0.035		

Table E.7 Experiment 12 with V_f = 29.8 % and P_o = 127 kPa

F Permeability experiments - three-dimensional flow

The material tested was a twill fabric from Vetrotex (RC600). For experiments 1, 4 and 7 the measurements where carried out in the reference coordiante system while for experiments 2,3 and 5 the coordiante system was rotated by 15°. For the two-dimensional flow the inlet diameter was 0.00635 m (the size of the hole cut into the fabric) while for three-dimensional flow the inlet diameter is 0.00525 m.

I - direction			*II* - direction			*III* - direction		
time [s]	$x_{f,I}$ [m]	$y_{f,I}$ [m]	time [s]	$x_{f,II}$ [m]	$y_{f,II}$ [m]	time [s]	$x_{f,III}$ [m]	$y_{f,III}$
10.5	0.036	0.000	41.7	0.030	0.030	35.9	-0.001	0.041
49.3	0.062	0.000	121.1	0.048	0.046	141.5	-0.001	0.063
109.6	0.086	0.000	256.6	0.066	0.063	362.2	0.001	0.088
223.8	0.109	0.000	469.3	0.083	0.084	665.0	0.002	0.113
453.5	0.138	-0.001	729.3	0.103	0.100	985.0	-0.001	0.136
654.8	0.161	0.001						

Table F.1 Experiment 1 with V_f = 50.4 %, P_o = 110 kPa and μ = 0.216 Pa s

I - direction			*II* - direction			*III* - direction		
time [s]	$x_{f,I}$ [m]	$y_{f,I}$ [m]	time [s]	$x_{f,II}$ [m]	$y_{f,II}$ [m]	time [s]	$x_{f,III}$ [m]	$y_{f,III}$
13.18	0.034	0.009	43.06	0.021	0.036	57.12	-0.008	0.034
71.4	0.057	0.016	206.74	0.035	0.058	182.35	-0.015	0.055
202.56	0.084	0.021	484.88	0.044	0.079	428.2	-0.02	0.08
418.75	0.105	0.03	922.75	0.059	0.102	665.69	-0.03	0.096
844.97	0.132	0.033	1492.9	0.073	0.125	1299.8	-0.032	0.121
1333.3	0.1565	0.0405						

Table F.2 Experiment 2 with V_f = 60.5 %, P_o = 106 kPa and μ = 0.2264 Pa s

I - direction			*II* - direction			*III* - direction		
time [s]	$x_{f,I}$ [m]	$y_{f,I}$ [m]	time [s]	$x_{f,II}$ [m]	$y_{f,II}$ [m]	time [s]	$x_{f,III}$ [m]	$y_{f,III}$
8.6	0.036	0.009	13.2	0.026	0.034	9.5	-0.008	0.039
42.4	0.062	0.015	50.5	0.032	0.056	41.7	-0.016	0.060
99.3	0.086	0.021	112.3	0.042	0.076	110.5	-0.024	0.085
188.9	0.111	0.030	206.7	0.057	0.099	214.0	-0.029	0.112
297.7	0.136	0.035	328.0	0.071	0.120	333.3	-0.033	0.137
463.6	0.161	0.043	486.6	0.083	0.143	493.0	-0.041	0.162

Table F.3 Experiment 3 with V_f = 50.4 %, P_o = 200 kPa and μ = 0.2293 Pa s

I - direction			*II* - direction			*III* - direction		
time [s]	$x_{f,I}$ [m]	$y_{f,I}$ [m]	time [s]	$x_{f,II}$ [m]	$y_{f,II}$ [m]	time [s]	$x_{f,III}$ [m]	$y_{f,III}$
12.63	0.0395	0	33.06	0.03	0.029	56.57	0	0.044
51.08	0.0635	0	116.93	0.049	0.046	211.63	0.001	0.071
124.73	0.089	0	293.25	0.07	0.066	456.81	0.001	0.098
205.46	0.1125	0	493.06	0.083	0.088	758.3	0.001	0.119
438.25	0.141	-0.001	831.63	0.104	0.101			
672.23	0.165	0						

Table F.4 Experiment 4 with V_f = 60.5 %, P_o = 195 kPa and μ = 0.2437 Pa s

I - direction		*II* - direction		*III* - direction		*z*- direction	
time [s]	$r_{f,I}$ [m]	time [s]	$r_{f,II}$ [m]	time [s]	$r_{f,III}$ [m]	time [s]	z_f [m]
74.21	0.03189	106.89	0.03191	76.52	0.02912	0.77	0.00182
302.2	0.05701	588.64	0.05445	471.76	0.05289	65.37	0.00545
959.28	0.08271	1546.71	0.07889	1397.61	0.07980	356.8	0.00909
2253.41	0.10867						

Table F.5 Experiment 5 with V_f = 51.6 %, P_o = 101 kPa and μ = 0.2164 Pa s

I - direction		*II* - direction		*III* - direction		*z*- direction	
time [s]	$r_{f,I}$ [m]	time [s]	$r_{f,II}$ [m]	time [s]	$r_{f,III}$ [m]	time [s]	z_f [m]
2.2	0.0305	4.4	0.0310	4.4	0.0300	1.1	0.0018
4.4	0.0535	6.59	0.0600	6.59	0.0566	8.79	0.0055
7.14	0.0810	12.63	0.0820	10.44	0.0810	31.31	0.0091
10.99	0.1060	28.01	0.1090	18.13	0.1060	65.91	0.0127
18.13	0.1320	52.18	0.1350	40.1	0.1310	114.8	0.0159
28.56	0.1581	116.44	0.1600	106.56	0.1570	186.75	0.0191

Table F.6 Experiment 7 with V_f = 51.6 %, P_o = 185 kPa and μ = 0.2271 Pa s

G Permeability experiments - two-dimensional flow

The fabric tested was a quasi-unidirectional non crimp fabric E-LPb 567 from Tech Textiles. For experiments 2, 3, 4 and 8 the measurements where carried out in the reference coordiante system while for experiments 1, 5, 6 and 7 the coordinate system was rotated by 15°. The inlet diameter r_o is 0.00635 m.

I - direction			*II* - direction			*III* - direction		
time [s]	$x_{f,I}$ [m]	$y_{f,I}$ [m]	time [s]	$x_{f,II}$ [m]	$y_{f,II}$ [m]	time [s]	$x_{f,III}$ [m]	$y_{f,III}$
26.81	0.026	0.0065	14.28	0.014	0.024	9.23	-0.005	0.029
230.42	0.057	0.015	95.57	0.0275	0.049	58.66	-0.0145	0.058
			258.98	0.045	0.075	190.65	-0.023	0.088
			542.61	0.059	0.102	421.34	-0.032	0.118
						685.64	-0.041	0.149

Table G.1 Experiment 1 with V_f = 49.9 %, P_o = 55 kPa and μ = 0.2509 Pa s

I - direction			*II* - direction			*III* - direction		
time [s]	$x_{f,I}$ [m]	$y_{f,I}$ [m]	time [s]	$x_{f,II}$ [m]	$y_{f,II}$ [m]	time [s]	$x_{f,III}$ [m]	$y_{f,III}$
26.14	0.024	0.002	16.47	0.02	0.0205	2.41	0.003	0.028
235.74	0.056	0.002	178.17	0.046	0.045	32.73	0	0.058
688.76	0.089	0	472.14	0.066	0.066	116.22	0	0.088
						257.27	0	0.12
						454.56	0.001	0.153

Table G.2 Experiment 2 with V_f = 49.9 %, P_o = 50 kPa and μ = 0.2315 Pa s

I - direction			*II* - direction			*III* - direction		
time [s]	$x_{f,I}$ [m]	$y_{f,I}$ [m]	time [s]	$x_{f,II}$ [m]	$y_{f,II}$ [m]	time [s]	$x_{f,III}$ [m]	$y_{f,III}$
5.6	0.028	0.0015	3.96	0.022	0.0145	0.66	-0.001	0.026
38.34	0.058	0.001	32.74	0.046	0.043	6.48	0	0.058
110.73	0.09	0	76.13	0.064	0.063	20.65	0.001	0.086
			138.08	0.0835	0.082	47.9	0.001	0.118
						90.74	0.002	0.155

Table G.3 Experiment 3 with V_f = 49.9 %, P_o = 245 kPa and μ = 0.2293 Pa s

I - direction			*II* - direction			*III* - direction		
time [s]	$x_{f,I}$ [m]	$y_{f,I}$ [m]	time [s]	$x_{f,II}$ [m]	$y_{f,II}$ [m]	time [s]	$x_{f,III}$ [m]	$y_{f,III}$
18.23	0.025	0	7.25	0.014	0.029	1.75	0	0.027
135.33	0.0545	0.001	51.85	0.0285	0.051	23.72	0.0015	0.058
362.28	0.0865	-0.002	143.68	0.043	0.0775	74.25	0	0.088
			282.75	0.057	0.102	149.17	0.002	0.117
						254.85	0.001	0.145

Table G.4 Experiment 4 with V_f = 44.3 %, P_o = 54 kPa and μ = 0.2461 Pa s

I - direction			*II* - direction			*III* - direction		
time [s]	$x_{f,I}$ [m]	$y_{f,I}$ [m]	time [s]	$x_{f,II}$ [m]	$y_{f,II}$ [m]	time [s]	$x_{f,III}$ [m]	$y_{f,III}$
6.92	0.027	0.006	1.65	0.012	0.0265	0.33	-0.0055	0.026
45.26	0.0555	0.014	17.25	0.028	0.0555	6.7	-0.014	0.056
127.54	0.086	0.0225	49.54	0.045	0.0815	21.53	-0.0215	0.085
			106.12	0.061	0.107	54.16	-0.0315	0.117
						92.5	-0.039	0.145

Table G.5 Experiment 5 with V_f = 49.9 %, P_o = 243 kPa and μ = 0.2414 Pa s

I - direction			*II* - direction			*III* - direction		
time [s]	$x_{f,I}$ [m]	$y_{f,I}$ [m]	time [s]	$x_{f,II}$ [m]	$y_{f,II}$ [m]	time [s]	$x_{f,III}$ [m]	$y_{f,III}$
2.97	0.027	0.005	0.55	0.013	0.022	0.22	-0.006	0.03
19.33	0.0575	0.014	7.03	0.0295	0.05	3.96	-0.0155	0.061
54.05	0.0865	0.022	22.19	0.0445	0.076	13.62	-0.0245	0.089
			47.24	0.061	0.101	28.34	-0.031	0.119
			81.29	0.075	0.128	49.1	-0.0395	0.145

Table G.6 Experiment 6 with V_f = 44.3 %, P_o = 245 kPa and μ = 0.2278 Pa s

I - direction			*II* - direction			*III* - direction		
time [s]	$x_{f,I}$ [m]	$y_{f,I}$ [m]	time [s]	$x_{f,II}$ [m]	$y_{f,II}$ [m]	time [s]	$x_{f,III}$ [m]	$y_{f,III}$
18.62	0.026	0.008	3.14	0.013	0.022	2.64	-0.006	0.025
127.54	0.057	0.0155	34.44	0.028	0.049	23.07	-0.014	0.057
329.89	0.086	0.022	123.09	0.046	0.0765	69.7	-0.021	0.086
			244.86	0.06	0.103	151.27	-0.03	0.116
						271.89	-0.039	0.145

Table G.7 Experiment 7 with V_f = 44.3 %, P_o = 57 kPa and μ = 0.2264 Pa s

I - direction			*II* - direction			*III* - direction		
time [s]	$x_{f,I}$ [m]	$y_{f,I}$ [m]	time [s]	$x_{f,II}$ [m]	$y_{f,II}$ [m]	time [s]	$x_{f,III}$ [m]	$y_{f,III}$
2.86	0.026	0	0.88	0.019	0.019	0.22	-0.002	0.026
24.83	0.0595	-0.001	11.21	0.0405	0.0405	3.52	0	0.058
67.56	0.091	0	34.39	0.062	0.065	11.1	0.001	0.089
			68.88	0.083	0.085	25.82	0.0015	0.12
						46.36	0.003	0.15

Table G.8 Experiment 8 with V_f = 44.3 %, P_o = 246 kPa and μ = 0.2406 Pa s

List of references

ADAMS, K. L., Miller, B. and Rebenfeld, L., (1986), Forced In-Plane Flow of an Epoxy Resin in Fibrous Networks, *Polymer Engineering and Science*, Vol. 26, No. 20, p. 1434-1441

ADAMS, K .L. and Rebenfeld, L., (1987), In-Plane Flow of Fluids in Fabrics: Structure/Flow Characterization, *Textile Research Journal*, November, p. 647-654

ADAMS, K. L., Russel, W. B. and Rebenfeld, L., (1988), Radial Penetration of a Viscous Liquid into a Planar Anisotropic Porous Medium, *International Journal of Multiphase Flow*, Vol. 14, No. 2, p. 203-215

ADAMS, K .L. and Rebenfeld, L., (1991), Permeability Characteristics of Multilayer Fiber Reinforcements. Part 1: Experimental Observations, *Polymer Composites*, June, Vol. 12, No. 3, p. 179-185

ADVANI, S. G., Bruschke, M. V. and Parnas, R. S., (1994), Resin transfer molding flow phenomena in polymeric composites, In *Flow and Rheology in Polymer Composites Manufacturing*, edited by Advani, S. G., Elsevier Science B.V., ISBN 0-444-89347-4, Chapter 12, p. 465-515

AHN, K. J., Seferis, J. C. and Berg, J. C., (1991), Simultaneous Measurements of Permeability and Capillary Pressure of Thermosetting Matrices in Woven Fabric Reinforcements, *Polymer Composites*, June, Vol. 12, No. 3, p. 146-152

AHN, S.H., Lee, W. I. and Springer, G. S., (1995), Measurement of the Three-Dimensional Permeability of Fiber Preforms Using Embedded Fiber Optic Sensors, *Journal of Composite Materials*, Vol. 29, No. 6, p. 714-733

BATCH, G. L. and Cumiskey, S., (1990), Multilayer Compaction and Flow in Composites Processing, *45th Annual Conference*, Reinforced Plastics/ Composites Institute, The Society of the Plastics Industry Inc., Washington D.C., February 12-15, session 9 - A, 11 pages

BATCHELOR, G. K., (1973), *An Introduction to Fluid Mechanics*, Cambridge University Press, ISBN 521 09817 3

BEAR, J., (1972), *dynamics of fluids in porous media*, New York, American Elsevier Publishing Company, ISBN 0-444-00114-X

BORG, S. F., (1963), *Matrix-Tensor Methods in Continuum Mechanics*, D. Van Nostrand Company, Inc., Princetown, New Jersey

BOYDE, P., Clothier, B. and Inglis A., (1995), *Design, Fabrication and Comissioning of a Resin Transfer Moulding Facility*, Master of Engineering Group Design Project Report, Faculty of Engineering and Applied Science, University of Southampton, May

BUNNEY, A., (1994), New FRP construction technology, *Shipbuilding Technology International '94*, Sterling Publications Ltd, London, ISSN 0268 8662, p. 43-46

BRÉARD, J., Saouab, A., Bouquet, G., Huberson, S and T. Charvet, (1995), Experimental Study of a Three-Dimensional Resin Flow through a Fiber Reinforcement Material, *International Conference on Materials and Energy (Enercomp 95)*, Montreal, Canada, May 8-10, p. 327-333

BRUSCHKE, M. V., (1992), *A predictive model for permeability and non-isothermal flow of viscous and shear-thinning fluids in anisotropic fibrous media*, PhD thesis, University of Delaware, Newark, DE

BRUSCHKE, M.V., Luce, T.C., Advani, S.G., (1992a), Effective In-Plane Permeability of Multi-Layered RTM Preforms, *Proceedings of the American Society for Composites*, Seventh Technical Conference, University Park, Pennsylvania, October 13-15, p. 103-112

CARLETON, P. S. and Nelson, G. S., (1994), Wetout of Glass Fiber Tows in Structural Reaction Molding I. Capillary Action and Fiber Mobility, *Journal of Reinforced Plastics and Composites*, Vol. 13, January, p. 20-37

CARRONNIER, D., Pannouillères, E., Cottu, J.-P., Gay, D. and Nardari, (1995), Mesures de la Perméabilité de Renforts Injectex®, *Mécanique Industrielle et Matériaux*, Vol. 48, No. 3, p.149-152

CARTER, E. J., Fell, A. W., Griffin, P. R. and Summerscales J., (1995), A proposed standard technique for the automated determination of the two-dimensional permeability tensor of a fabric material, *4th International Conference on Automated Composites (ICAC '95)*, Nottingham, 6-7 September

CARTER, E. J., Fell, A. W. and Summerscales J., (1995a), *Appendix 2. A Simplified Model to Calculate the Permeability Tensor of an Anisotropic Fibre Bed* ,In Griffin, P. R., Grove, S. M., Russel, P., Short, D., Summerscales, J., Guild, F. J. and Taylor, E., The effect of reinforcement architecture on the long-range flow in fibrous reinforcements, *Composites Manufacturing*, 1995, Vol. 6, No. 3-4, p. 221-235

CARTER, E. J., (1996), Advanced Composites Manufacturing Centre, School of Manufacturing and Mechanical Engineering, University of Plymouth, *Personal communication*, July

CHAN, A. W. and Hwang, S. T., (1991), Anisotropic In-plane Permeability of Fabric Media, *Polymer Engineering and Science*, August, Vol. 31, No. 16, p. 1233-1239

CHAN, A. W., Larive, D. E. and Morgan, R. J., (1993), Anisotropic Permeability of Fiber Preforms: Constant Flow Rate Measurement, *Journal of Composite Materials*, Vol. 27, No. 10, p. 996-1008

CHIBANI, M. and Gauvin, R., (1991), New Parameter to Model the Permeability of Fiber Mats, *Proceedings of the 8th International Conference on Composite Materials (ICCM-8)*, Honolulu, July 15-19, session 29 - I, 10 pages

CHICK, J. P., Rudd, C. D., Van Leeuwen, P. A. and Frenay, T. I., (1996), Material Characterization for Flow Modeling in Structural Reaction Injection Molding, *Polymer Composites*, February, Vol. 17, No. 1, p. 124-135

COREY, A. T., (1977), *Mechanics of Heterogeneous Fluids in Porous Media*, Water Resources Publications, Fort Collins, Colorado, ISBN 0-918334-17-9

DAVÉ, R., (1990), A Unified Approach to Modeling Resin Flow During Composite Processing, *Journal of Composite Materials*, Vol. 24, January, p. 22-41

DELIUS, A., CAD/CAM Information Strategy in Small Shipyards, (1994), *Proceedings: 8th International Conference on Computer Applications in Shipbuilding (ICCAS 94)*, Bremen, Germany, 5-9 September, Vol. 2, p. 9.33-9.51

DIALLO, M. L., Gauvin, R. and Trochu, F., (1995), Experimental Analysis of Flow through Multi-layer Fiber Reinforcements in Liquid Composite Molding, *4th International Conference on Automated Composites (ICAC '95)*, Nottingham, 6-7 September, p. 201-210

DOUGLAS, B., A Ship Product Model as an Integrator between Vessel Build Planning and Design, (1994), *Proceedings: 8th International Conference on Computer Applications in Shipbuilding (ICCAS 94)*, Bremen, Germany, 5-9 September, Vol. 1, p. 1.35-1.45

DULLIEN, F. A., (1979), *Porous Media - Fluid Transport and Pore Structure*, 1st edition, Academic Press

DULLIEN, F. A., (1992), *Porous Media - Fluid Transport and Pore Structure*, 2nd edition, Academic Press, ISBN 0-12-223651-3

DUSCHEK, A. and Hochrainer, A., (1948), *Grundzüge der Tensorrechnung in analytischer Darstellung. I. Teil: Tensoralgebra*, Springer Verlag, Vienna

FELL, A. W. and Summerscales, J. (1996), Advanced Composites Manufacturing Centre, School of Manufacturing and Mechanical Engineering, University of Plymouth, *Personal communication*

FERLAND, P., Guittard, D. and Trochu, F., (1996), Concurrent methods for Permeability Measurement in Resin Transfer Molding, *Polymer Composites*, Vol. 17, No. 1, p. 149-158

FIRTH, G. R., CAD/CAM Design and Manufacture, (1995), *Proceedings: Computer Aided Design and Production for Small Craft (CADAP '95)*, Southampton, United Kingdom, 26-27 September, paper no. 2

FOLEY, M. F., (1991), Techno-Economic Automated Composite Manufacturing Techniques, *SAMPE Quarterly*, January, p. 61-68

FONG, L. and Lee, L. J., (1994), Preforming Analysis of Thermoformable Fiber Mats-Preforming Effects on Mold Filling, *Journal of Reinforced Plastics and Composites*, Vol. 13, July, p. 637-663

GANDHI, M. V., Thompson, B. S. and Fischer, F., (1990), Manufacturing-process-driven design methodologies for components fabricated in composite materials, *Composites Manufacturing*, March, Vol. 1, No. 1, p. 32-40

GAUVIN; R. and Chibani, M., (1986), The Modelling of Mold Filling in Resin Transfer Molding, *International Polymer Processing*, Vol. 1, p. 42-46

GAUVIN, R. and Chibani, M., (1990), Analysis of Composite Molding with Woven and Non-Woven Reinforcements, *45th Annual Conference*, Reinforced Plastics/ Composites Institute, The Society of the Plastics Industry Inc., Washington D.C., February 12-15, Session 9 - F, 6 pages

GAUVIN, R., Kerachni, A. and Fisa, B., (1994), Variation of Mat Surface Density and Its Effects on Permeability Evaluation for RTM Modelling, *Journal of Reinforced Plastics and Composites*, Vol. 13, April, p. 371-383

GAUVIN, R., Trochu, F., Lemenn, Y. and Diallo, L., (1996), Permeability Measurement and Flow Simulation Through Fiber Reinforcements, *Polymer Composites*, Vol. 17, No. 1, p. 34-42

GARCÍA, L., Fernández, V. and Torroja, J., (1994), The role of CAD/CAE/CAM in Engineering for Production, *Proceedings: 8th International Conference on Computer Applications in Shipbuilding (ICCAS 94)*, Bremen, Germany, 5-9 September, Vol. 1, p. 1.3-1.18

GEBART, B. R., Gudmundson, P., Strömbeck, L. A. and Lundemo, C. Y., (1991), Analysis of the Permeability in RTM Reinforcements, *Proceedings of the 8th International Conference on Composite Materials (ICCM-8)*, Honolulu, July 15-19, Session 15 - E, 10 pages

GEBART, B. R., (1992), Permeability of Unidirectional Reinforcements for RTM, *Journal of Composite Materials*, Vol. 26, No.8, p. 1100-1133

GEBART, B. R. and Lidström, P., (1996), Measurement of In-Plane Permeability of Anisortropic Fiber Reinforcements, *Polymer Composites*, Vol. 17, No. 1, p. 43-51

GERE, J. M. and Timoshenko, S. P., (1987), *Mechanics of Materials*, Van Nostrand Reinhold (International) Co. Ltd, ISBN 0 278 00040 1, 2nd SI edition

GPRMC (European Organisation of Reinforced Plastics / Composite Materials), (1994), *UP-Resin Handling Guide*

GREVE, B. N. and Soh, S. K., (1990), Directional permeability measurement of fiberglass reinforcements, *SAE Transactions*, Vol.99, p. 331-343

GRIFFIN, P. R., Grove, S. M., Russel, P., Short, D., Summerscales, J., Guild, F. J. and Taylor, E., (1995), The effect of reinforcement architecture on the long-range flow in fibrous reinforcements, *Composites Manufacturing*, Vol. 6, No. 3-4, p. 221-235

GROVE, D. M. and Davis T. P., (1992), *Engineering, Quality and Experimental Design*, Longman Scientific & Technical, ISBN 0-582-06687-5

HAMMAMI, A., Trochu, F., Gauvin, R. and Wirth, S., (1995), Directional Permeability Measurement of Deformed Reinforcements, *International Conference on Composite Materials and Energy (Enercomp 95)*, Montreal, Canada, May 8-10, p. 347-354

HARRISON, A. R., Sudol, M. A., Priestly, A. and Scarborough, S. E., (1995), A Low Investment Cost Composites High Roof for the Ford Transit Van using Electroformed Shell Tooling and Resin Transfer Moulding, *Proceedings: 4th International Conference on Automated Composites (ICAC' 95)*, Nottingham, United Kingdom, 6-7 September, p. 511-525

HIRT, D. E., Adams, K. L., Prud'homme, R. K. and Rebenfeld, L., (1987), In-Plane Radial Fluid Flow Characterization of Fibrous Material, *Journal of Thermal Insulation*, January, Vol. 1, p. 153-172

KIM, Y. R., McCarthy, S. P., Fanucci, J. P., Nolet, S. C., Koppernaes, C., (1990), Resin Flow through Fiber Reinforcements during Composite Processing, *Proceedings: 22nd International SAMPE Technical Conference*, November 6-8, p. 709-723

KINCAID, D. R., Respess, J. R., Young, D. M. and Grimes, R. G., (1982), Algorithm 586 ITPACK 2C: A FORTRAN Package for Solving Large Sparse Linear Systems by Adaptive Accelerated Iterative Methods, *ACM Transactions on Mathematical Software*, Vol. 8, No. 3, September, p. 302-322

KÖTTE, R., (1991), *Verfahrensanalyse des Resin-Transfer-Molding-Processes (RTM)*, (Analysis of the Resin-Transfer-Molding Process), Ph.D. thesis, RWTH Aachen, Verlag TÜV Rheinland, Köln, ISBN 3-8249-0033-5

LAFONTAINE, P., Hébert, L.-P. and Gauvin, R., (1984), Material Characterization for the Modeling of Resin Transfer Molding, *39th Annual Conference*, Reinforced Plastics/ Composites Institute, The Society of the Plastics Industry Inc., January 16-19

LEKAKOU, C., Johari, M. A. K., Norman, D. and Bader, M. G., (1996), Measurement techniques and effects on in-plane permeability of woven cloths in resin transfer moulding, *Composites: Part A*, Vol. 27A, p. 401-408

McGEEHIN, P., Long, A. C., Rudd, C. D., Middleton, V. and Owen, M. J., (1994), The Effect of Forming on the Processing and Performance of Random Fibre Mats, *6th International Conference on Fibre Reinforced Composites (FRC'94)*, University of Newcastle upon Tyne, U. K., 29-31 March, Paper 13, 17 pages

MICHAELI, W., Hammes, V., Kirberg, K., Kötte, R., Osswald, T. A. and Specker, O., (1989), Prozeßsimulation beim RTM-Verfahren, *Kunststoffe*, Vol. 79, No. 8, p. 739-742

MOON, P. and Eberle Spencer, D., (1969), *Partial Differential Equations*, Library of Congress Number 79-78603

MORRIS, D. J. and Rudd, C. D. (1996), Department of Mechanical Engineering, University of Nottingham, *Personal communication*

PARNAS, R. S. and Salem, A. J., (1993), A Comparison of the Unidirectional and Radial In-Plane Flow of Fluids Through Woven Composite Reinforcements, *Polymer Composites*, Vol. 14, No. 5, p. 383-394

PARNAS, R. S., Howard, J. G., Luce, T. L. and Advani, S. G., (1995), Permeability Characterization: Part 1. A Proposed Standard Reference Material for Permeability, *Polymer Composites*, Vol. 16, No. 6, p. 429-445

PARNAS, R. S., (1996), National Institute of Standards and Technology, Gaithersburg, USA, *Personal communication*

PEARCE, N. and Summerscales, J., (1995), The Compressibility of a Reinforcement Fabric, *Composites Manufacturing*, Vol. 6, No. 1, p. 15-21

RAO, N. R., Falkowski, D. E. and Spencer, R. D., (1993), RTM Body Panels for Viper Sports Car, *48th Annual Conference*, Composites Institute, The Society of the Plastics Industry Inc., 8-11 February, Session 3-A, 4 pages

RUDD, C. D., Bulmer, L. J., Longbottom, A. C., Owen, M. J., Rice, E. V., Harrison, A. and Kendall, K. N., (1992), Integrated Design for RTM Components, *Proceedings of the 8th Advanced Composites Conference*, Chicago, Illinois, USA, 2-5 November, p. 215-229

RUDD, C. D., Middleton, V., Owen, M. J., Long, A. C., McGeehin, P. and Bulmer, L. J., (1994), Modelling the processing and performance of preforms for liquid moulding processes, *Composites Manufacturing*, Vol. 5, No. 3, p. 177-186

RUDD, C. D., Morris, D. J., Chick, J. P. and Warrior, N. A., (1995), Material Characterisation for SRIM, *4th International Conference on Automated Composites (ICAC '95)*, Nottingham, 6-7 September, p. 211-218

SMITH, C. S., (1990), *Design of Marine Structures in Composite Materials*, Elsevier Science Publishing Ltd, ISBN 1-85166-416-5

STEENKAMER, D. A., McKnight, S. H., Wilkins, D. J. and Karbhari, V. M., (1995), Experimental characterization of permeability and fibre wetting for liquid moulding, *Journal of Materials Science*, Vol. 30, p. 3207-3215

STIGANT, A. S., (1964), *Applied Tensor Analysis for Electrical Students*, Macdonald & Co. (Publishers) Ltd, London

SUMMERSCALES, J., (1993), A model for the effect of fibre clustering on the flow rate in resin transfer moulding, *Composites Manufacturing*, Vol. 4, No. 1, p. 27-31

TADMOR, Z., Broyer, E. and Gutfinger, C., (1974), Flow Analysis Network (FAN) - A Method for Solving Flow Problems in Polymer Processing, *Polymer Engineering and Science*, September, Vol. 14, No. 9, p. 660-665

THE NAVAL ARCHITECT, (1995), New production process for latest batch of Sandown minehunters, November, ISSN 0306 0209, p. 633-634

TOLL, S. and Månson, J.-A. E., (1994), An Analysis of the Compressibility of Fibre Assemblies, *6th International Conference on Fibre Reinforced Composites (FRC'94)*, University of Newcastle upon Tyne, U. K., 29-31 March, Paper 25, 10 pages

TREVINO, L., James Lee, L., Rupel, K. and Liou, M., (1990), Permeability and Compressibility Measurements of Fiber Mats in Resin Transfer Molding and Structural RIM, *45th Annual Conference*, Reinforced Plastics/ Composites Institute, The Society of the Plastics Industry Inc., Washington D.C., February 12-15, session 9 - E, 7 pages

TREVINO, L., Rupel, K., Young, W. B., Liou, M. J. and James Lee, L., (1991), Analysis of Resin Injection Molding in Molds With Preplaced Fiber Mats. I: Permeability and Compressibility Measurements, *Polymer Composites*, Vol. 12, No. 1, p. 20-29

TROCHU, F., Hoareau, C., Gauvin, R., Vincent, M., (1993), Experimental Analysis and Computer Simulation of Resin Transfer Molding Through Multilayer Fiber Reinforcement, In *Proceedings of the 9th International Conference on Composite Materials (ICCM-9)*, Madrid, 12-16 July, Vol III, p. 481-488

TUCKER III, C. L. and Dessenberger, R. B., (1994), Resin transfer molding flow phenomena in polymeric composites, In *Flow and Rheology in Polymer Composites Manufacturing*, edited by Advani, S. G., Elsevier Science B.V., ISBN 0-444-89347-4, Chapter 8, p. 257-323

VERHEUS, A. S., Peeters, J. H. A., (1993), The role of reinforcement permeability in resin transfer moulding, *Composites Manufacturing*, Vol. 4, No. 1, p. 33-38

WANG, T. J., Perry, M. J. and Lee, L. J., (1992), Analysis of Permeability and Void Formation in Resin Transfer Molding, *ANTEC'92*, p. 756-760

WANG, T. J., Wu, C. H. and Lee, L. J., (1994), In-Plane Permeability Measurement and Analysis in Liquid Composite Molding, *Polymer Composites*, August, Vol. 15, No. 4, p. 278-288

WEITZENBÖCK, J. R., Shenoi, R. A. and Wilson, P. A., (1995a), Characterization of Resin Flow Through Thick Laminates in Resin Transfer Moulding, *10th International Conference on Composite Materials (ICCM/10)*, Whistler, Canada, 14-18 August, Vol. III, p. 301-308

WEITZENBÖCK, J. R., Shenoi, R. A. and Wilson, P. A., (1995b), Flow Front Measurement in RTM, *4th International Conference on Automated Composites (ICAC '95)*, Nottingham, 6-7 September, Vol. 2, p. 307-314

WEITZENBÖCK, J. R., Shenoi, R. A. and Wilson, P. A., (1996), Measurement of Three-Dimensional Permeability, *4th International Conference on Flow Processes in Composites Moulding (FPCM'96)*, Aberystwyth, 9-11 September

WOERDEMAN, D. L., Phelan, F. R. and Parnas, R. S., (1995), Interpretation of 3-D Permeability Measurements for RTM Modeling, *Polymer Composites*, Vol. 16, No. 6, p. 470-480

WONG, P.Z., (1994), Flow in Porous Media: Permeability and Displacement Patterns, *MRS Bulletin*, May, p. 32-38

WU, C. H., Wang, T. J. and Lee, L. J., (1993), Permeability Measurement and its Application in Liquid Composite Molding, *48th Annual Conference*, Composites Institute, The Society of the Platics Industry Inc., 8-11 February, Session 8-E, 10 pages

WU, C. H., Wang, T. J. and Lee, L. J., (1994), Trans-Plane Fluid Permeability Measurement and Its Applications in Liquid Composite Molding, *Polymer Composites*, Vol. 15, No. 4, p. 289-298

YOUNG, W. B., Rupel, K., Han, K., James Lee, L. and Liou M. J., (1991), Analysis of Resin Injection Molding in Molds With Preplaced Fiber Mats. II: Numerical Simulation and Experiments of Mold Filling, *Polymer Composites*, Vol. 12, No. 1, p. 30-38

YOUNG, W.-B. and Wu, S. F., (1995), Permeability Measurement of Bidirectional Woven Glass Fibers, *Journal of Reinforced Plastics and Composites*, October, Vol. 14, p. 1108-1120

ZIENKIEWICZ, O. C. and Taylor, R. L., (1991), *The Finite Element Method - Vol. 2*, 4th edition, McGraw-Hill Book Company (UK) Ltd, ISBN 0-07-084175-6

ZIJL, W. and Stam, J. M., (1995), Modeling Permeability in Imperfectly Layered porous Media. I. Derivation of Block-scale Permeability Tensor for Thin Grid-Blocks, *Mathematical Geology*, Vol. 24, No. 8, p. 865-883